Etude expérimentale et théorique su spectre d'absorption de la vapeur d'eau vers 800nm et de la bande a^{1}ÎgøX^{3}Ôgñ de l'oxygène vers 1.27 micron par spectroscopie d'absorption à très haute sensibilité

Olga Leshchishina

Olga Leshchishina. Etude expérimentale et théorique su spectre d'absorption de la vapeur d'eau vers 800nm et de la bande a^{1}ÎgøX^{3}Ôgñ de l'oxygène vers 1.27 micron par spectroscopie d'absorption à très haute sensibilité. Physique [physics]. Université de Grenoble; Institute of atmospheric optics (Tomsk, Russia), 2011. Français. NNT : 2011GRENY029 . tel-00716403

HAL Id: tel-00716403
https://theses.hal.science/tel-00716403

Submitted on 10 Jul 2012

UNIVERSITÉ DE GRENOBLE

THÈSE

Pour obtenir le grade de

DOCTEUR DE L'UNIVERSITÉ DE GRENOBLE

Spécialité: **Physique de la Matière Condensée et du Rayonnement**

Arrêté ministériel: 7 août 2006

Préparée dans la cadre d'une cotutelle avec L'INSTITUT D'OPTIQUE ATMOSPHÉRIQUE DE TOMSK

Présentée par

Olga LESHCHISHINA

Thèse codirigée par **Alain CAMPARGUE** et **Olga NAUMENKO**

préparée au sein du **Laboratoire Interdisciplinaire de Physique**
dans **l'École Doctorale de Physique**

Étude expérimentale et théorique du spectre d'absorption de la vapeur d'eau vers 800 nm et de la bande $a^1\Delta_g - X\,^3\Sigma_g^-$ de l'oxygène vers 1.27 micron par spectroscopie d'absorption à très haute sensibilité

Thèse soutenue publiquement le **26.08.2011**,
devant le jury composé de:

Mme. Laurence RÉGALIA
Maître de conférences, Université de Reims Champagne Ardenne (Rapporteur)
Mr. Andrey A. VIGASIN
Directeur de Recherche, Institut de Physique Atmosphérique, Moscou Russie (Rapporteur)
Mr. Erik KERSTEL
Professeur des Universités, Université Grenoble 1 (Président)
Mr. Aleksandr Z. FAZLIEV
Directeur de Recherche, Institut d'Optique Atmosphérique, Tomsk Russie (Examinateur)
Mme. Olga V. NAUMENKO
Directeur de Recherche, Institut d'Optique Atmosphérique, Tomsk Russie (Examinateur)
Mr. Alain CAMPARGUE
Directeur de Recherche CNRS, Université Grenoble 1 (Examinateur)

To my parents

Acknowledgments

First of all, I would like to thank my thesis supervisors Alain Campargue and Olga Vasil'evna Naumenko, for their friendly way of supervising, their patience and for giving me the opportunity to learn from them. I was lucky to have such supervisors.

I am very grateful to the members of jury Laurence Régalia, Andrey Alekseevitch Vigasin, Erik Kerstel and Aleksand Zaripovitch Fazliev, especially to the rapporteurs Laurence Régalia and Andrey Alekseevitch Vigasin for taking time to read and evaluate this work and for their comments and suggestions regarding the manuscript.

I am very thankful to all the members of group LAME of LIPHY in Grenoble and laboratory of theoretical spectroscopy of IAO in Tomsk for their help, friendship and nice atmosphere in the lab. I would like also to thank PhD students of LIPHY for all the lunch breaks we shared.

I am very grateful to all of my friends in Grenoble and in Russia, especially Karina, Steve, Sveta, Natasha, Sergey, Nastya, Olivier, Olga, Vika, Alisa for their friendship and support.

I am thankful to French Foreing Office for the financial support and to CROUS of Grenoble for their help.

My warmest gratitude to my husband Vasil for his moral and English support, without that I would never have succeeded.

Finally, I would like to thank my parents, for their patience, encouragement and support. It is to them I would like to dedicate this thesis.

Résumé

La spectroscopie moléculaire à haute résolution spectrale est un des outils expérimentaux les plus puissants et fiables pour étudier la structure de la matière. Dans la plupart des cas, l'analyse de spectres moléculaires est la seule source fiable pour estimer des paramètres moléculaires et étudier l'interaction intermoléculaire. La spectroscopie moléculaire est devenue une approche bien établie et efficace pour étudier les propriétés globales de l'atmosphère terrestre, notamment l'évolution des concentrations des espèces moléculaires mineures.

La détermination des paramètres de raie spectraux (position, intensité, profil de raies) est l'étape indispensable pour aboutir à la liste de raies expérimentale utilisée pour l'attribution quantique des transitions. Durant les dernières décennies en raison d'un progrès considérable dans les techniques expérimentales, la sensibilité et la précision des spectromètres ont été nettement améliorées.

Cette thèse est consacrée à deux espèces atmosphériques majeures – la vapeur d'eau et l'oxygène – pour lesquelles nos connaissances sont encore insuffisantes pour répondre à certaines demandes des sciences atmosphériques. Le mémoire est structuré en deux parties. La première partie (Chapitres 1 et 2) concerne la molécule d'oxygène. Elle présente l'étude spectroscopique de la bande $a^1\Delta_g - X^3\Sigma_g^-$ de O_2 vers 1.27 micron qui joue un rôle important dans la chimie et la physique atmosphérique.

Après une introduction générale, *le premier chapitre* de la thèse fournit un aperçu des bases théoriques de la spectroscopie de la molécule diatomique pour ce qui concerne O_2. Des aspects importants de molécules diatomiques telles que leur symétrie et les différents moments angulaires qui peuvent se poser sont examinés.

Le deuxième chapitre contient la première contribution originale de cette thèse - il présente l'étude approfondie du système $a^1\Delta_g - X^3\Sigma_g^-$ très faible de la molécule d'oxygène grâce à l'exploitation de spectres enregistrés en utilisant la technique CW-CRDS de très haute sensibilité. Cette étude a été initialement motivée par la première détection de transitions quadrupolaires électriques dans des spectres solaires atmosphériques en décembre 2004, montrant la nécessité d'améliorer les paramètres spectraux de la bande considérée à partir de nouvelles mesures en laboratoire. Le spectre d'absorption de la bande $a^1\Delta_g - X^3\Sigma_g^-$ des six isotopologues de l'oxygène vers 1.27 micron a été enregistré à température ambiante et à 80 K par la technique CW-CRDS. La bande (0-0) permise par le dipôle magnétique est observée pour les espèces $^{16}O_2$, $^{16}O^{18}O$, $^{16}O^{17}O$, $^{17}O^{18}O$, $^{18}O_2$ et $^{17}O_2$. La sensibilité expérimentale atteinte a permis de détecter pour la première fois au laboratoire (*i*) des transitions quadrupolaires

électriques extrêmement faibles dans la bande (0-0) de $^{16}O_2$, $^{18}O_2$, $^{16}O^{17}O$ et $^{17}O_2$, (*ii*) la bande chaude (1-1) de $^{16}O_2$, $^{18}O_2$, $^{16}O^{17}O$ et $^{17}O_2$, (*iii*) la structure hyperfine des transitions de $^{16}O^{17}O$, $^{17}O^{18}O$ et $^{17}O_2$. Ces mesures combinées avec des données micro-ondes et Raman disponibles dans la littérature ont permis de déterminer les meilleures constantes spectroscopiques à ce jour, y compris les paramètres de couplage hyperfin de ^{17}O pour l'état $a^1\Delta_g$ des six isotopologues de l'oxygène.

La seconde partie (Chapitres 3 à 4) porte sur l'analyse du spectre de la vapeur d'eau et plus précisément ses isotopologues $D_2{}^{16}O$, $HD^{16}O$ et $H_2{}^{18}O$. L'étude du spectre de la vapeur d'eau et de ses composés isotopiques présente un réel intérêt pour la compréhension du bilan énergétique de l'atmosphère terrestre. Un des problèmes importants notamment pour la vapeur d'eau et ses isotopologues est l'attribution correcte des transitions rovibrationnelles surtout pour des niveaux très excités.

Le troisième chapitre présente les bases théoriques de la spectroscopie rovibrationnelle. Il commence par l'approche générale pour la séparation de mouvement nucléaire et électronique (approximation de Born-Oppenheimer) et termine par la dérivation des hamiltoniens effectifs. Les aspects principaux de méthodes variationnelles pour les calculs globaux sont soulignés. Le logiciel dédié utilisé pour l'identification du spectre est brièvement décrit.

Le quatrième chapitre expose la seconde contribution originale de la thèse - il est consacré à l'étude systématique de l'isotopologues de l'eau: $D_2{}^{16}O$, $HD^{16}O$ et $H_2{}^{18}O$ par la technique d'absorption intracavité laser (ICLAS) de très haute sensibilité et la technique de spectrométrie par Transformation de Fourier associée à une cellule multipassage de 50 m dans le visible et le proche infrarouge. Les études sont présentées par région spectrale et isotopologue allant de 8800 à 14020 cm^{-1} pour D_2O, 9100-9650 cm^{-1} puis 13020-14115 cm^{-1} pour $HD^{16}O$ et enfin 12580 à 14100 cm^{-1} pour $H_2{}^{18}O$. L'analyse des spectres basée sur les calculs variationnels de haute précision a fourni une quantité importante de nouveaux niveaux d'énergie pour chacun des isotopologues considérés. Les niveaux d'énergie expérimentaux obtenus dans cette étude et disponibles dans la littérature ont permis de calculer des positions de raies au niveau de la précision expérimentale dans la gamme 6100-15200 cm^{-1} qui s'étend bien au-delà de la gamme des enregistrements présents.

Les résultats présentés dans cette thèse ont fait l'objet d'onze publications dans les journaux internationaux à comité de lecture et ont été présenté à plusieurs conférences internationales.

Contents

List of Figures

List of Tables

Introduction

High resolution molecular spectroscopy is one of the most powerful and reliable experimental tools that allows one to obtain information about the structure of matter. Each type of motion of a molecule corresponds to particular energy levels and can be investigated by a suitable type of molecular spectroscopy. In many cases, the analysis of molecular spectra is the only reliable source when determining molecular parameters and studying intermolecular interaction. Moreover, spectroscopy is a well-established and efficient approach to study the global properties of the terrestrial atmosphere, notably the evolution of the concentrations of the minor molecular species. The experimental determination of the spectral line parameters provides an important starting point for theoretical models of molecular absorption and emission at different wavelength, pressures and temperatures. A first necessary step in the theoretical treatment of an experimental line list is quantum assignment of the absorption lines. In the recent years due to a significant progress in experimental techniques, the sensitivity and precision of spectrometers were much improved. This in turn makes high demands of the experimental data processing methods and of theoretical calculation accuracy.

The present thesis is devoted to two major atmospheric species – water and oxygen – for which the present status of our knowledge is not sufficient to fulfil the needs of atmospheric sciences.

O_2 is the dominant molecule in the thermochemistry and is the second most abundant constituent in the Earth's atmosphere. The dissociation, predissociation and band systems of molecular oxygen play an important role in the aurora, airglow and nightglow [1]. Molecular oxygen is an important constituent of stellar atmospheres including that of the sun and possibly of planetary atmospheres.

Atmospheric spectra of oxygen are used to deduce information about properties and other species in the atmosphere. For example, one could determine ozone concentrations in the mesosphere and thermosphere by monitoring emission of the products of ozone photolysis, in particular from the electronically excited $a^1\Delta_g$ and $b^1\Sigma_g^+$ states of O_2 [2]–[3], since both states are formed in the atmosphere by solar-UV photolysis of ozone by means of Hartley bands.

Our study is focused on the 1.27 μm $a^1\Delta_g - X^3\Sigma_g^-$ band of O_2 that plays an important role in the atmospheric chemistry and physics. On the Earth, this band is observed from the ground in absorption against the solar background [4] and in emission from the twilight airglow [5]. In addition to being the signature of O_3 production, the 1.27 μm band of O_2 is also important when studying the heating of the upper atmosphere. The $a^1\Delta_g - X^3\Sigma_g^-$ absorption band is also used in the field of remote sensing in relation to high-accuracy measurements of atmospheric greenhouse gases such as CO_2 and CH_4. One reason is that due to the uniform mixing of oxygen, the oxygen lines are often used as a benchmark for intensity calibration of atmospheric spectra taken by satellite instruments. Another reason is that taking the ratio of the column abundance of CO_2 or CH_4 to that of O_2 cancels many common systematic errors, especially the ones that are instrument-related [6]. The quality of the spectroscopic parameters of the $a^1\Delta_g - X^3\Sigma_g^-$ band has then a direct impact on the results of several atmospheric studies. The improvement of the existing parameters for atmospheric applications is then a strong motivation of our study of oxygen.

The very weak $a^1\Delta_g - X^3\Sigma_g^-$ system of molecular oxygen was extensively studied by high sensitivity CW-Cavity Ring Down Spectroscopy. This study was initially motivated by the first detection of electric quadrupole transitions in the atmospheric solar spectrum, showing the necessity to improve the spectral parameters of the $a^1\Delta_g - X^3\Sigma_g^-$ band of molecular oxygen from the new laboratory measurements [7]. The spectra were obtained between 7640 and 7917 cm^{-1} with “natural” oxygen and with samples highly enriched in ^{18}O and ^{17}O. The magnetic dipole-allowed (0-0) band was observed for $^{16}O_2$, $^{16}O^{18}O$, $^{16}O^{17}O$, $^{17}O^{18}O$, $^{18}O_2$ and $^{17}O_2$ species. The $a^1\Delta_g - X^3\Sigma_g^-$ (0-0) bands of $^{16}O_2$, $^{18}O_2$, $^{16}O^{17}O$ and $^{17}O_2$ show extremely weak quadrupole transitions, which are accompanied by the $a^1\Delta_g - X^3\Sigma_g^-$ (1-1) hot bands. The combination of the high sensitivity CRDS technique with a cryogenic cell at 80 K allowed for the first observation of the partly resolved hyperfine structure of the $a^1\Delta_g - X^3\Sigma_g^-$ band of the three ^{17}O containing isotopologues $^{16}O^{17}O$, $^{17}O^{18}O$ and $^{17}O_2$.

These measurements combined with microwave and Raman data available in the literature allowed us to determine the best to date spectroscopic constants including ^{17}O hyperfine coupling parameters for the $a^1\Delta_g$ and $X^3\Sigma_g^-$ states of the six oxygen isotopologues $^{16}O_2$, $^{16}O^{18}O$, $^{16}O^{17}O$, $^{17}O^{18}O$, $^{18}O_2$ and $^{17}O_2$.

The second main topic of this thesis is the study of the spectrum of the minor isotopologues of water – $H_2{}^{18}O$, $HD^{16}O$ and $D_2{}^{16}O$.

Water vapour is of crucial importance for the understanding of the energy balance of the Earth’s atmosphere. It is the most important absorber of both incoming and outgoing radiation. In particular, it is responsible for about 70% of the known atmospheric absorption of sunlight. However, there is a major problem in our understanding of atmosphere’s radiation balance because the calculated average atmospheric absorption based on known spectroscopic parameters is about 25% less than that observed. One of hypotheses proposed to account for this observed discrepancy relates to weak water lines missing in the spectroscopic databases applied for evaluation of the attenuation of the solar radiation by the Earth's atmosphere. The total effect of myriad of these weak lines may be significant and should be taken into account in the spectroscopic studies of the atmosphere [8], [9].

Weak transitions often involve highly excited upper rovibrational states. In the frame of the traditional scheme, some approximations used to derive the effective Hamiltonian are not valid for such states because of the strong non-rigidity effects. Indeed, for molecules such as $H_2{}^{16}O$, the "soft" bending vibration ν_2 breaks out the small amplitude vibration assumption, which results in divergence of energy level calculations even for low values of $J \sim 10$ [10], [11]. As a consequence, the usual perturbation treatment has poor convergence characteristics [12], calling for more sophisticated, variational techniques for the interpretation of the rovibrational spectra of water isotopologues.

A recent break-through in the H_2O spectral studies has been achieved by using global variational calculations and high-quality *ab initio* potential energy and dipole moment surfaces [13], [14] to provide rovibrational line positions and intensities. This achievement gives new opportunities to tackle this problem directly. This theoretical approach results in detailed linelists with very high accuracy (both for line position and line strength) for wide spectral regions stretching from the microwave to the near UV and including the weak lines. New representations of the effective rotational Hamiltonian based on summations of the divergent series have been recently developed [10]-[12], [15]-[17] allowing for improving the description and prediction of the highly excited energy levels of water isotopologues.

The importance of accounting for $H_2{}^{18}O$, $H_2{}^{17}O$ and HDO in the atmospheric absorption is evident since their rovibrational lines, being shifted relative to the lines of the parent molecule, may be located at windows and micro windows of atmospheric transparency and therefore they influence noticeably the amount of solar radiation reaching the Earth surface. This is particularly true for the monodeuterated species, $HD^{16}O$, that has an isotopic relative abundance of about 3×10^{-4}, since some of its absorption bands are highly shifted from those of $H_2{}^{16}O$. Atmospheric HDO spectra are also being extensively measured because this species can be used to trace the transport of water vapour into the stratosphere [18]-[19].

Moreover, knowledge of water molecule isotopic species is useful at the solution of some astrophysics problems, for example the relative contents of $H_2{}^{17}O$ and $H_2{}^{18}O$ is of interest for determination of cold star evolution.

Information relative to the dideuterated water, D_2O, is important for many applications, such as studying the planetary atmospheres and interstellar molecules, characterizing the isotope effects on the main properties of the water molecule, and evaluating the adiabatic and nonadiabatic corrections to Born-Oppenheimer approximation in modelling the potential energy surface of water.

Though the "strong part" of water vapour spectrum is substantially understood, there are serious problems in recording, assigning and modelling of the weak lines connected with transitions on highly excited rovibrational energy states. The exhaustive analyses of the published experimental transitions of the main isotopologues of the water vapour have been recently undertaken within the IUPAC-sponsored project [20]-[21], where the lack of high-sensitive measurements for the $H_2{}^{17}O$ and $H_2{}^{18}O$ molecules above 9000 cm^{-1} and for $HD^{16}O$ between 9000 and 9600 cm^{-1} was confirmed. The previous ICLAS studies available between 13000 and 14000 cm^{-1} were found to suffer from small calibration problems, and a higher sensitivity could be achieved using a Ti:Sapphire lasers instead of dyes. The studies of $D_2{}^{16}O$ absorption spectra above 9000 cm^{-1} are sparse and all of them are based on FTS. It is worth noting that the high sensitivity achieved (noise equivalent absorption $\alpha_{\min} \sim 10^{-9}$ cm^{-1}) in the 11400 – 14000 cm^{-1} region with a Titanium Sapphire laser, allowed detecting transitions with minimum line strength values of the order of 5×10^{-28} cm/molecule, i.e. at least two orders of magnitude smaller than by FTS.

For the identification of these very weak lines of $D_2{}^{16}O$, $HD^{16}O$, $H_2{}^{18}O$ in separate regions of the 8800 – 14100 cm^{-1} range, we used the global variational calculations based on high quality *ab initio* potential energy and dipole moment surfaces together with calculations in the effective Hamiltonian framework. As a result, the extensive and accurate sets of rovibrational energy levels for $D_2{}^{16}O$, $HD^{16}O$ and $H_2{}^{18}O$ isotopologues were derived. This new information on the assigned transitions and energy levels has already been or will be included in the line list recommended by the IUPAC-sponsored Task Group.

All the experimental energy levels derived in this study together with the available literature data were used to generate transition wavenumbers as a difference between the experimentally determined upper and lower energy levels, while the intensities were variational ones. As a result, extensive, detailed and high-accuracy linelists have been generated for all considered isotopologues in the 6000 – 15000 cm^{-1} region. These line lists can have applications to various atmospheric and astrophysics problems, and can be used for newly recorded spectrum assignment, further optimization of variational PES, etc.

Outline of the Thesis

The thesis consists of Introduction, four Chapters (The O_2 study is presented in Chapters 1 and 2, the water vapour spectrum analysis is presented in Chapters 3 and 4) and Conclusion. Supplementary information is provided in six Appendix sections.

Chapter I provides an overview of the theoretical fundamentals of diatomic molecule spectroscopy in relation with O_2. Important aspects of diatomic molecules such as their symmetry and the various angular momenta which can arise are examined.

Chapter II contains the first original contribution of this thesis – it presents the extensive study of the very weak $a^1\Delta_g - X^3\Sigma_g^-$ system of molecular oxygen using high sensitivity CW-Cavity Ring Down Spectroscopy. The results of the investigation of the $a^1\Delta_g - X^3\Sigma_g^-$ band of the six isotopologues of oxygen – $^{16}O_2$, $^{16}O^{18}O$, $^{16}O^{17}O$, $^{17}O^{18}O$, $^{18}O_2$ and $^{17}O_2$ are described.

Chapter III deals with the theoretical essentials of the rovibrational spectroscopy, starting with the separation of nuclear and electronic motion, and finishing with the derivation of effective Hamiltonians. The main aspects of global variational calculation are emphasized as well. It also provides a brief description of the expert system used for the spectrum identification.

Chapter IV presents the second original contribution of this thesis – it is devoted to the systematic investigation of the water isotopologues ($D_2{}^{16}O$, $HD^{16}O$, $HD^{18}O$, $H_2{}^{18}O$ and $H_2{}^{17}O$) by high sensitivity Intracavity Laser Absorption Spectroscopy and Fourier Transform spectroscopy in the visible and near-infrared range.

The results presented in this thesis were published as eleven journal articles (listed below) and presented at several international conferences. The results of the investigation of the $a^1\Delta_g - X^3\Sigma_g^-$ very weak system of molecular oxygen presented at the 22nd International Conference on High Resolution Molecular Spectroscopy were awarded Pliva Prize.

1. O.V. Naumenko, O. Leshchishina, A. Campargue. High sensitivity absorption spectroscopy of the HDO by ICLAS-VECSEL between 9100 and 9640 cm^{-1}. J. Mol. Spectrosc. 236, (2006), 58-69.

2. O.V. Naumenko, O. Leshchishina, S. Shirin, A. Jenouvrier, S. Fally, A.C. Vandaele, E. Bertseva and A. Campargue. Combined analysis of the high sensitivity Fourier Transform and ICLAS-VECSEL absorption spectra of D_2O between 8800 and 9520 cm^{-1}. J. Mol. Spectrosc. 238, (2006), 79-90.

3. O.V. Naumenko, F. Mazzotti, O. Leshchishina, J. Tennyson, A. Campargue. Intracavity laser absorption spectroscopy of D_2O between 11400 and 11900 cm^{-1}. J. Mol. Spectrosc. 242, (2007), 1-9.

4. O.V. Naumenko, O.M. Leshchishina, S. Béguier, A. Campargue. Intracavity laser absorption spectroscopy of D_2O between 12850 and 13380 cm^{-1}. J. Mol. Spectrosc. 252, (2008), 52-59.

5. A. Campargue, O.M. Leshchishina, O.V. Naumenko. $D_2{}^{16}O$: ICLAS between 13600 and 14020 cm^{-1} and normal mode labelling of the vibrational states. J. Mol. Spectrosc. 254, (2009), 1-9.

6. O.V. Naumenko, S. Béguier, O.M. Leshchishina, A. Campargue. ICLAS of HDO between 13020 and 14115 cm^{-1}. Journal of Quantitative Spectroscopy and Radiative Transfer. 111, (2010), 36-44.

7. O. Leshchishina, S. Kassi, I.E. Gordon, L.S. Rothman, L. Wang, A. Campargue. High sensitivity CRDS of the $a^1\Delta_g - X^3\Sigma_g^-$ band of oxygen near 1.27 μm: Extended observations, quadrupole transitions, hot bands and minor isotopologues. Journal of Quantitative Spectroscopy and Radiative Transfer. 111, (2010), 2236-2245.

8. S. Kassi, O. Leshchishina, I. E. Gordon, S. Yu, A. Campargue. Hyperfine structure of the $a^1\Delta_g - X^3\Sigma_g^-$ transitions of $^{16}O^{17}O$, $^{17}O^{18}O$ and $^{17}O_2$ by CRDS at 80 K. Chem Phys Letter. 502, (2011), 37-41.

9. O. Leshchishina, S. Kassi, I.E. Gordon, S. Yu, A. Campargue. The $a^1\Delta_g - X^3\Sigma_g^-$ band of $^{16}O^{17}O$, $^{17}O^{18}O$ and $^{17}O_2$ by high sensitivity CRDS near 1.27 μm. Journal of Quantitative Spectroscopy and Radiative Transfer. 112, (2011), 1257-1265.

10. O.M. Leshchishina, O.V. Naumenko, A. Campargue. High sensitivity ICLAS of $H_2{}^{18}O$ in the 12580–13550 cm^{-1} transparency window. Journal of Quantitative Spectroscopy and Radiative Transfer. 112, (2011), 913-924.

11. O. M. Leshchishina, O. V. Naumenko, A. Campargue. High sensitivity ICLAS of $H_2{}^{18}O$ between 13540 and 14100 cm^{-1}. J. Mol. Spectrosc. 268, (2011), 28-36.

References for Introduction

[1] F. E. Roach. Forbidden transitions in the upper atmosphere. Mem. Soc. Roy. Sci. Liege, Collect in 8°, Ser. 5. 17, 1969;175.

[2] D. Stranges, X. Yang, J. D. Chesko, and A. G. Suits. Production of O_2 Herzberg states in the deep UV photodissociation of ozone. J. Chem. Phys. 102, 1995; 6067.

[3] J. J. Valentini, D. P. Gerrity, D. L. Phillips, J. C. Nieh, and K. D. Tabor. CARS spectroscopy of $O_2(^1\Delta_g)$ from the Hartley band photodissociation of O_3: Dynamics of the dissociation. J. Chem. Phys. 86, 1987; 6745.

[4] L. Herzberg, G. Herzberg. Fine Structure of the Infrared atmospheric oxygen bands. Astrophys. J. 105, 1947; 353.

[5] R. P. Lowe. Interferometric spectra of the Earth's airglow (1.2 to 1.6 μm). Philos. Trans. R. Soc. London Ser. A 264, 1969; 163.

[6] R. A. Washenfelder, G. C. Toon, J.-F. Blavier, Z. Yang, N. T. Allen, P. O. Wennberg, et al. Carbon dioxide column abundances at the Wisconsin Tall Tower site. Journal of Geophysical Research D 111, 2006; 22305.

[7] I. E. Gordon, S. Kassi, A. Campargue, G. C. Toon. First identification of the $a^1\Delta_g$ - $X\,^3\Sigma_g^-$ electric quadrupole transitions of oxygen in the solar and laboratory spectra. J. Quant. Spectrosc. Radiat. Transfer 111, 2010; 1174.

[8] R. C. M. Learner et al. The contribution of unknown weak water vapor lines to the absorption of solar radiation. Geophys. Res. Lett. 26, 1999; 3609.

[9] B. A. Voronin, I. M. Nasretdinov, A. B. Serebrennikov, T. Yu. Chesnokova. Simulation of solar radiation transfer with the allowance for weak water vapour absorption lines under various aerosol conditions. Atmospheric and Oceanic Optics. 16, 2003, 272.

[10] Vl. G. Tyuterev. The generating function approach to the formulation of the effective rotational Hamiltonian. Simple closed form model describing strong centrifugal distortion in water type molecules. J. Mol. Spectrosc. 151, 1992; 97.

[11] Vl.G. Tyuterev, I. Starikov, S.A. Tashkun, S.N. Mikhailenko. Calculation of high rotational energies of water molecule using the generation function model. J. Mol. Spectrosc. 170, 1995; 38.

[12] O. L. Polyansky. One-dimensional approximation of the effective rotational Hamiltonian of the ground state of the water molecule. J. Mol. Spectrosc. 112, 1985; 79.

[13] H. Partridge, D. W. Schwenke. The determination of an accurate isotope dependent potential energy surface for water from extensive ab initio calculations and experimental data. J Chem Phys. 106, 1997; 4618.

[14] D. W. Schwenke, H. Partridge Convergence testing of the analytic representation of an ab initio dipole moment function for water: improved fitting yields improved intensities. J Chem Phys. 113, 2000; 6592.A.V. Burenin. Optimum rational perturbation theory series when treating rotational spectra of nonlinear molecules. J. Mol. Spectrosc. 140, 1990; 54.

[15] V.I. Starikov, S.A. Tashkun, Vl.G. Tyuterev. Description of vibration-rotation energies of nonrigid triatomic molecules using the generating function method. Bending states of water molecule. J. Mol. Spectrosc. 151, 1992;130-147.

[16] Vl.G. Tyuterev, A.V. Burenin, V.I. Perevalov, V.I. Starikov. General method for the reduction of the effective rotational Hamiltonian of molecules. Rotational approximants and Padé approximants. Rus. Phys. J. 28, 1985; 633.

[17] A.V. Burenin. On the convergence of rational series when treating spectra of quantum systems. J. Mol. Spectrosc. 136, 1989; 140.

[18] V.N. Payne, D. Noone, A. Dudhia, C. Piccolo, R.G.Grainger. Global satellite measurements of HDO and implications for understanding the transport of water vapour in to the stratosphere. J Quart Roy Meteor Soc. 133, 2007; 1459.

[19] J. Steinwagner, M. Milz, T. von Clarmann, N. Glatthor, U. Grabowski, M. Höpfner, et al. HDO measurements with MIPAS. Atmos Chem Phys. 7, 2007; 2601.

[20] J. Tennyson, P. F. Bernath, L.R. Brown, A. Campargue, M.R. Carleer, A.G. Császár, et al. Critical evaluation of the rotational-vibrational spectra of water vapor. Part I. Energy levels and transition wavenumbers for $H_2{}^{17}O$ and $H_2{}^{18}O$. J Quant Radiat Transfer. 110, 2009; 573.

[21] J. Tennyson, P.F.Bernath, L R. Brown, A. Campargue, M.R. Carleer, A.G. Császár et al. IUPAC Critical Evaluation of the Rotational-Vibrational Spectra of Water Vapor. Part II. Energy Levels and Transition Wavenumbers for $HD^{16}O$, $HD^{17}O$ and $HD^{18}O$. J Quant Radiat Transfer. 111, 2010; 2160.

Chapter I: Rovibronic spectroscopy of diatomic molecules

1. Introduction

High resolution molecular spectroscopy allows us to understand the nature of the nuclear and electronic motions within a molecule by analysing the experimental spectrum. In this Chapter, the very weak $a^1\Delta_g - X^3\Sigma_g^-$ band of oxygen is studied by high sensitivity CW-Cavity Ring Down Spectroscopy. To understand the spectrum of molecular oxygen, it is necessary to consider the properties of isotopic species and the structure of the electronic states. Since O_2 is a diatomic molecule, we describe theoretical fundamentals of diatomic molecule spectroscopy in this chapter.

2. The Born-Oppenheimer approximation

Since a molecule consists of positively charged nuclei and negatively charged electrons that move relative to each other, a full mechanical description of the molecule is very complicated. The central approximation in molecular spectroscopy is the separation of electronic and nuclear motions. The physical basis of this separation is as follows. Both the electrons and nuclei move in the electric field of the same intensity. However, the electron mass m is about 1836 times smaller than the nucleus mass M. Consequently, the electrons move much faster than the nuclei and the electronic motion can be separated from the nuclear motion. The electronic wave functions adjust instantaneously to the positions of the nuclei and determine the potential well in which the nuclei vibrate. One can say that by defining the system of energy levels in this way, we obtain the electron terms of the molecule. Thus unlike atoms, where the energy levels are definite numbers, here the electron terms are the functions of parameters, such as internuclear distances in the molecule. The validity of this approximation was established by Born and Oppenheimer [1] in 1927. They expanded the molecular energy in powers of $(m/M)^{1/2}$. Thus the separation of nuclear and electronic motion corresponds to selecting the larger terms of the series expansion and neglecting those that are smaller by $(m/M)^{1/2}$ or more.

In the Born–Oppenheimer approximation framework*,* augmented with an assumption that the electronic wavefunction is composed of molecular orbitals (MOs) and each MO is a linear combination of atomic orbitals (LCAO), one can obtain an approximate solution of the electronic Schrödinger equation for a diatomic molecule [2]. Thus, the electronic structure of diatomic molecules can be derived, provided that the shapes of the molecular orbitals are represented as linear combinations of atomic orbitals.

There are certain situations, particularly with polyatomic molecules, when the separation of the nuclear and electronic motion cannot be made satisfactory, but for most diatomic molecules the Born-Oppenheimer approximation is acceptable. The discussion of the diatomic molecule energy levels structure presented in this Chapter is therefore based upon the Born-Oppenheimer approximation.

3. Rotational structure and vibrational structure

A molecule, like an atom, possesses electronic energy levels determined by the configuration of orbitals. Superimposed on that electronic structure there exists a structure of vibrational and rotational levels.

An appropriate model of a rotating molecule is a non-rigid rotor, which consists of two point masses connected by a massless spring. As a starting point, one can assume that the molecule consists of two atoms rigidly connected to each other, which means that the internuclear separation remains constant [2]-[3]. The rotational energy levels are then given by:

$$F(J) = \frac{h}{8\pi^2 cI} J(J+1) = BJ(J+1), \tag{1.1}$$

where B (cm^{-1}) is the *rotational constant* with $I=\mu R^2$, $\mu = \frac{m_1 m_2}{m_1 + m_2}$ is the reduced mass and R is the internuclear distance, J represents the rotational quantum number $J = 0, 1, 2\ldots$ The rotational energy levels therefore have energies 0, $2B$, $6B$, $12B\ldots$

As a result of centrifugal forces in a rotating molecule, the internuclear distance and hence the moment of inertia will increase with rotation. This effect is known as *centrifugal distortion*. The rotational term values are therefore given by the power series

$$F(J) = BJ(J+1) - DJ^2(J+1)^2 + HJ^3(J+1)^3 + \ldots, \tag{1.2}$$

where D, H, etc., are the centrifugal distortion constants; it is necessary to go beyond the cubic term when very high J values are involved. The coefficients B, D, H etc., are usually determined by analysing the experimental spectrum.

The next stage in the development of the internal dynamics of a diatomic molecule is to establish that the molecule is not rigid. Indeed, the harmonic oscillator cannot be a correct representation for a real molecule because when the atoms are at infinite distance apart, the attractive force between them must be zero and the potential energy then has a constant value. A potential energy function that often resembles the shape of bound electronic state potentials is that proposed by Morse [4] in 1929 by the form:

$$V(R) = D_e(1 - e^{-a(R-R_e)})^2, \tag{1.3}$$

where D_e is the energy of dissociation, R_e is the equilibrium distance between nuclei and a is a constant. This function is represented by the curve in Figure 1.1. A mass point that moves under the influence such as that shown in Figure 1.1 is called an *anharmonic oscillator*. Solution of the Schrödinger equation using the Morse potential gives the term value expression

$$G(\upsilon) = \omega_e(\upsilon + \frac{1}{2}) - \omega_e x_e(\upsilon + \frac{1}{2})^2, \tag{1.4}$$

in which υ is the vibrational quantum number that runs over values $\upsilon = 0, 1, 2, 3\ldots$, ω_e is the fundamental vibrational frequency and $\omega_e x_e$ is the anharmonicity constant. Note that the vibrational energy expression (1.4) for the Morse oscillator has exactly two terms. The presence of the quadratic term in (1.4) makes the vibrational spacing decrease as υ increases, with the levels essentially converging to the dissociation asymptote (Figure 1.1).

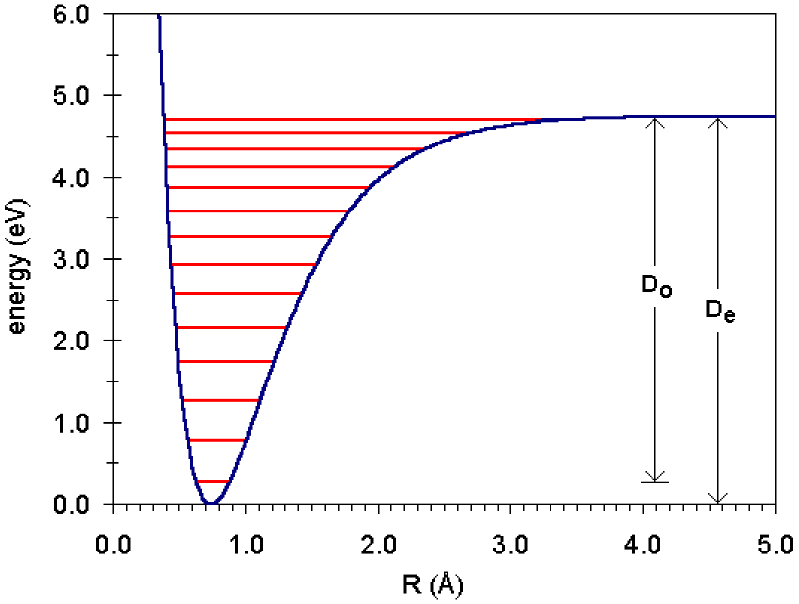

Figure 1.1. The schematic representation of the Morse potential function. The equilibrium energy of dissociation D_e is measured from the bottom of the potential well and D_0 is the dissociation energy measured from υ=0.

As the internuclear distance R changes, the dependence of the rotational constants B and D on the vibrational state should be taken into account. The mean values of the rotational constants B_υ and D_υ for the vibrational level υ are given by

$$\begin{aligned} B_\upsilon &= B_e - \alpha_e(\upsilon + 1/2) + \gamma_e(\upsilon + 1/2)^2 + \ldots, \\ D_\upsilon &= D_e + \beta_e(\upsilon + 1/2) + \ldots, \end{aligned} \tag{1.5}$$

where α_e, γ_e are rotation-vibration interaction constants, and $\beta_e(\upsilon + 1/2)$ is the correction term for the effects of vibration on the centrifugal stretching constant. The vibrational constants ω_e and $\omega_e x_e$ are related to the rotational constants B_e, α_e and D_e through the following relations:

$$\omega_e = \frac{a}{2\pi}\sqrt{2D_e/\mu},$$
$$\omega_e x_e = B_e\left(\frac{\alpha_e\omega_e}{6B_e^2}+1\right)^2, \tag{1.6}$$

in the assumption of the Morse potential function. Also, this assumption leads to the prediction for the dissociation energy

$$D_e = \frac{\omega_e^2}{4\omega_e x_e}. \tag{1.7}$$

The energies of the rovibrational levels are then expressed as:

$$E(\upsilon,J) = \omega_e(\upsilon+\frac{1}{2}) - \omega_e x_e(\upsilon+\frac{1}{2})^2 + B_e J(J+1) - D_e J^2(J+1)^2 - \alpha_e(\upsilon+\frac{1}{2})J(J+1) + \dots \tag{1.8}$$

Another procedure that is often used for representing the rovibrational energy levels within a certain electronic state was proposed by Dunham [6] in 1932:

$$E(\upsilon,J) = \sum_{lm} Y_{lm}(\upsilon+\frac{1}{2})^l (J(J+1))^m. \tag{1.9}$$

In this procedure the parameters Y_{lm}, known as Dunham's constants, are fit to the experimentally determined energy levels. These parameters have to be considered as mathematical representation, rather than constants with a physical meaning.

Nevertheless, the Dunham constants can be related to the molecular parameters B_e, D_e, ω_e, as follows $Y_{01} \approx B_e$, $Y_{02} \approx -D_e$, $Y_{03} \approx H_e$, $Y_{11} \approx -\alpha_e$, $Y_{12} \approx -\beta_e$, $Y_{21} \approx \gamma_e$, $Y_{10} \approx \omega_e$, $Y_{20} \approx -\omega_e x_e$, $Y_{30} \approx \omega_e y_e$ [7]. The equalities are approximate because they are only valid up to higher–order terms of the form $(B_e/\omega_e)^2$ in the Dunham treatment [7].

Note that the various isotopic forms of a molecule have different spectroscopic constants because the reduced mass μ is different. If the spectroscopic constants have been determined for one isotopic species of a molecule, their approximate values for the other species may be found from the following relations:

$$\omega_e \propto \frac{1}{\sqrt{\mu}}, \quad B_e \propto \frac{1}{\mu}, \quad D_e \propto \frac{1}{\mu^2}, \quad \alpha_e \propto \frac{1}{\mu^{3/2}}. \tag{1.10}$$

These relations allowed us to predict the line positions and perform the first assignment of the $a^1\Delta_g - X^3\Sigma_g^-$ ($\upsilon'' = 1 \rightarrow \upsilon' = 1$) hot band of $^{16}O^{17}O$ and $^{17}O_2$ oxygen isotopologues. We provide further details on this in Section 5 of Chapter II.

4. Angular momenta in diatomic molecules

Between the two positively charged nuclei of a diatomic molecule, there is a strong electric field possessing a rotational symmetry around the internuclear axis. The nonzero orbital electronic angular momentum **L** is strongly coupled to the internuclear axis by the electrical forces of the chemical bound. As a result, the vector **L** is not fixed in space, but precess rapidly about the internuclear axis. However, the components of the orbital angular momentum Λ are resolved along the bond axis and have definite quantized values. Thus the electronic states are defined by the quantum numbers Λ. Furthermore, the spins of individual electrons form a resultant spin vector **S**, whose magnitude is defined by the spin quantum number S. The axial components of **S** are designated by $\Sigma = S, S-1, \ldots, -S,$ where Σ can have $2S+1$ possible values. Thus $2S+1$ substates belong to an electronic state of a given Λ value. The number $2S+1$ is called the multiplicity of the electronic state. It is written as a left superscript of the term symbol, which is denoted as $^{2S+1}\Lambda_{\Omega}$, where $\Omega = \Lambda + \Sigma$. The exceptional case is $S > |\Lambda| > 0$, when there is a notation problem in labelling the $2S+1$ spin components, so $\Omega = |\Lambda| + \Sigma$ is used instead of $|\Omega|$. The symbols of the molecular terms are Σ, Π, Δ… for $\Lambda = 0, 1, 2$… The electronic states of diatomic molecules are also labelled with letters: *X* is reserved for the ground state, *A*, *B*, *C* etc., are used for excited states of the same multiplicity ($2S+1$) as the ground state, in the order of increasing energy. States with a multiplicity different from that of the ground state are labelled with *a*, *b*, *c* and so on, in order of increasing energy. Figure 1.2 shows the energy level diagram of the low-lying electronic states of O_2, where this convention is illustrated [2].

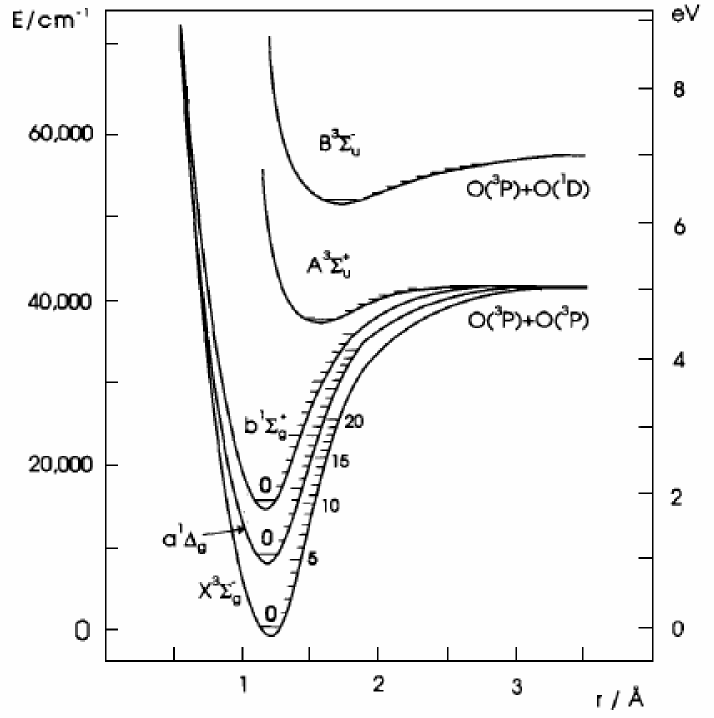

Figure 1.2. Potential energy diagram for the low-lying electronic states of the O_2 molecule (adapted from Ref. [2]).

The motion of the nuclei and electrons in the molecule, the resultant spin and even the spins of individual electrons are not totally independent of one another; certain interactions exist among them. There is an interaction between the magnetic fields of the moving electrons and nuclei on the one hand, and the resultant spin (and also the spins of the individual electrons) on the other hand. In actual molecules, the angular momenta may be presented and coupled in a complicated way by gyroscopic and magnetic forces. Individual angular momenta then lose their identity and only certain sums resulting from effective couplings are constants of motion which can be determined from the observed spectra. The presence of the various angular momenta introduces a number of phenomena and problems, such as coupling schemes and interactions which may not only shift but also split electronic energy levels. The angular momenta and their projection on molecular axis are presented in Table1.

Table 1.1. Angular momenta in a diatomic molecule.

Angular momentum, quantum number	Definition	Projection on molecular axis (in units of ħ)
Electronic orbital, *L*	$\vec{L} = \Sigma \vec{l}_i$	Λ
Electronic spin, *S*	$\vec{S} = \Sigma \vec{s}_i$	Σ
Rotational, *R*	$\vec{R}$	–
Total orbital, *N*	$\vec{N} = \vec{R} + \vec{L}$	Λ
Total molecular, *J*	$\vec{J} = \vec{N} + \vec{S}$	$\Omega = \Lambda + \Sigma$

5. Coupling of electron and rotational motions: Hund's coupling cases

As mentioned in previous Section, the molecular angular momenta may interact or couple together in various ways. Besides the interaction between the magnetic fields of the moving electrons and nuclei with the resultant spin – that is *spin-orbit interaction*; there is a weaker *spin-spin interaction* among the spins of the individual electrons (exclusive of nuclear spin). The latter produces energy differences between levels with different |Σ|. There is also an even weaker *spin-rotation interaction* that is due to the rotation of the molecule. In general, the Hamiltonian operator can be presented as:

$$H = H_{el} + H_{vib} + H_{rot} + H_{so} + H_{ss} + H_{sr} + H_{LD}, \tag{1.11}$$

where

$$H_{so} = A(\vec{L} \cdot \vec{S}), \tag{1.12}$$

$$H_{ss} = \frac{2}{3}\lambda(3S_z^2 - \vec{S}^2), \tag{1.13}$$

$$H_{sr} = \gamma(\vec{N} \cdot \vec{S}), \tag{1.14}$$

the last term in (1.11) H_{LD} is the Λ-doubling interaction and *A, λ*, *γ* are the spin-orbit, spin-spin, spin-rotational coupling constants [2], [5], [8], respectively.

Various possible ways of coupling the angular momenta were introduced by Hund [9] in 1926. Hund's coupling cases are idealised situations which help us to understand the pattern of rotational levels and the resulting spectra. Although molecules do not follow such an ideal description exactly, Hund's coupling cases are very good approximations to the actual states of many linear molecules. We limit our consideration to Hund's coupling cases (*a*) and (*b*), as they dominate in $a^1\Delta_g$ and $X^3\Sigma_g^-$ electronic states of oxygen, respectively.

Hund's coupling case (a)

In Hund's case (*a*), illustrated by the gyroscopic diagram shown in Figure 1.3a, rotation is assumed to have little influence upon the conditions existing in the molecule, i.e. *A* is large $A \gg BJ$. The orbital angular momentum **L** is strongly coupled to the inter-nuclear axis by electrostatic forces, while the electron spin angular momentum **S** is strongly coupled to **L** through spin-orbit coupling. The parallel components Λ and Σ remain quantized even in the rotating molecule, so that Ω = Λ+Σ is well-defined. A vector **Ω** pointing along the axis is coupled to the angular momentum of the rotating nuclei **R** to form the resulting total angular momentum **J**. Its quantum number can take the values: $J = \Omega, \Omega+1, \Omega+2 \ldots$ consequently, the levels with $J < \Omega$ cannot occur. There are $2S+1$ well-separated fine structure states with rotational energy levels given by $BJ(J+1)$ for each of them. Each *J* is doubly degenerated, corresponding to ±Λ (or *e/f* parity). The Hund's cases can be defined more rigorously by their "good" quantum numbers, for the Hund's case (a) they are *Λ*, *S*, *Σ*, *Ω* and *J*.

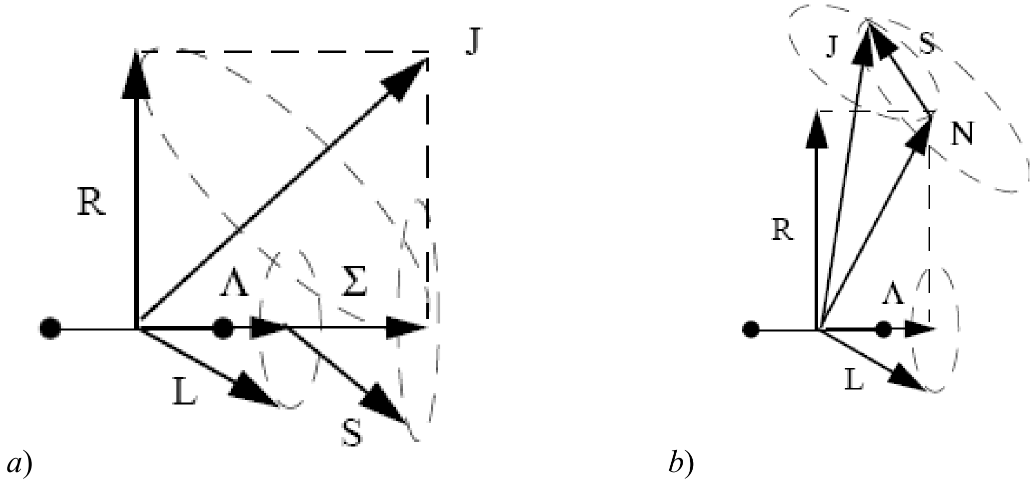

a) *b*)

Figure 1.3. Vector coupling diagram for Hund's cases *a* and *b*.

Hund's coupling case (b)

Hund's case (*b*) can be appropriate in the situation when the spin vector **S** is not coupled to the internuclear axis (Λ = 0) or this coupling is very weak, i.e. $A \ll BJ$. As it is shown in Figure 1.3b, **L** and **R** first couple to form a resultant **N,** and then **N** is coupled to **S** to form the total angular momentum **J.** Thus the "good" quantum numbers are *Λ*, *S*, *N*, and *J.* The rotational energy levels for $^{2S+1}\Lambda$ states are given by $BN(N+1)$ and there are 2(2S+1) and 2S+1 degenerate levels for $\Lambda \neq 0$ and for $\Lambda = 0$, respectively.

Cases (*a*) and (*b*) are the most widely observed, but there are many molecules that obey coupling which is intermediate between cases (a) and (b) [5].

Hund's coupling case (a_β) and ($b_{\beta J}$)

For the molecules with nonzero nuclear spin, the coupling of this nuclear spin to the various angular momenta of the molecule should be considered. The nuclear spin may be coupled with different strength to the several molecular vectors, providing additional coupling possibilities. One may distinguish the following important cases of Hund's coupling case (*a*) → (a_α), (a_β) and Hund's case (*b*) → (b_β). The subscript α indicates that the nuclear spin is most strongly coupled to the molecular axis. The subscript β denotes the quantization only in the laboratory coordinate system, consequently the hyperfine components will be expected to have Landé-type spacing, which is proportional to the large value of **F** [10].

In this thesis we deal with (a_β) and ($b_{\beta J}$) coupling cases, the corresponding vector coupling schematic diagrams are shown in Figure 1.4. In order to indicate the vector to which **I** is coupled, the subscript J is added to the notation of the coupling scheme b_β.

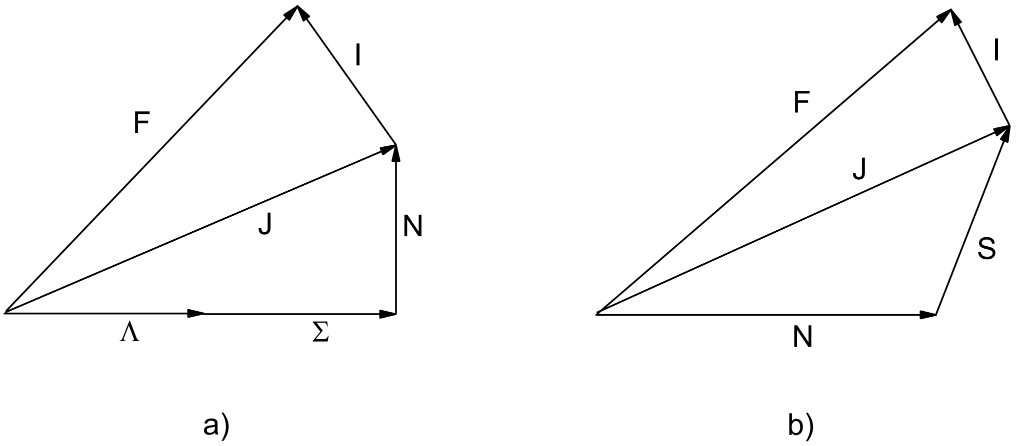

Figure 1.4. The vector model of cases (*a*) and (*b*) nuclear coupling: a) case a_α; b) case b_β

The situation described as case (a_β) is a straightforward extension of Hund's case (*a*) in which the nuclear spin angular momentum **I** is coupled to **J** to form **F (**Figure 1.4a**)**. In the case ($b_{\beta J}$), the total angular momentum **J**, which is the resultant of **N** and **S** coupling, is coupled with **I** to form **F (**Figure 1.4b**)**.

6. The symmetry of diatomic energy levels: Parity

Parity plays an important role in molecular physics when determining the selection rules for allowed transitions in the system [2], [8], [11]. Total parity is defined as the inversion in the laboratory frame, denoted by the symmetry operator E^*. All rovibronic energy levels have a parity (+) or (-), defined by the equation

$$E^*\psi = E^*(\psi_{el}\psi_{vib}\psi_{rot}) = \pm\psi \, . \tag{1.15}$$

Note that the effects of E^* on the electronic, vibrational and rotational parts of the total wavefunction need to be determined separately [2]. Because of *J*-dependent phase factor, the total parity changes sign for each *J*-level in a rotational ladder. To avoid this alternation, another parity concept, the so-called *e/f* convention has been established [12]. This *e/f* parity is rotationless parity describing the total parity with the rotational part removed. For an integer *J,*

$$E^*\psi = +(-1)^J\psi \qquad \text{for } e, \tag{1.16}$$

and

$$E^*\psi = -(-1)^J\psi \qquad \text{for } f, \tag{1.17}$$

where ψ is the total rovibronic wavefunction.

For homonuclear molecules, there are additional symmetry labels. The *g* (gerade) and *u* (ungerade) are used to classify just the electron orbital part of the total wavefunction. Moreover, the *s* (for symmetric) and *a* (for asymmetric), can be used to classify the rotational energy levels. Note that in a homonuclear molecule the symmetry of the nuclear spin wave function plays a role. The permutation of two identical nuclei is described by the operator P_{12} in the laboratory frame. There are two possible ways in which the total wave function can transform under P_{12}:

$$P_{12}(\psi\psi_{nuc}) = +(\psi\psi_{nuc}) \qquad \text{for bosons (\textit{integral} spin),} \tag{1.18}$$

and

$$P_{12}(\psi\psi_{nuc}) = -(\psi\psi_{nuc}) \qquad \text{for fermions (\textit{half-integral} spin),} \tag{1.19}$$

in which wavefunction ψ includes electron spin, orbital, vibrational and rotational parts and ψ_{nuc} is a nuclear spin wavefunction.

Thus all “+” rotational energy levels have *s* symmetry for *g* electronic states or *a* symmetry for *u* electronic states. Similarly, all “–“ rotational levels have *a* symmetry for *g* electronic states and *s* symmetry for *u* electronic states. The symmetry of oxygen energy levels is described in the following Section.

7. O_2 energy levels structure and selection rules

The electronic ground state of O_2 is $X^3\Sigma_g^-$. In the $X^3\Sigma_g^-$ state, Hund's coupling case (*b*) dominates [5] and the total angular momentum *J* is *J* = *N*+*S*. Each rotational level with quantum number *N* splits into three spin components denoted by F_1 (*J* =*N*+1), F_2 (*J* = *N*) and F_3 (*J* =*N*-1), since the total electron spin *S* in the ground state is equal to 1. The nuclear spin of ^{16}O and ^{18}O nuclei is $I = 0$, so only symmetric nuclear spin wavefunctions ψ_{nuc} are possible. The ^{16}O and ^{18}O nuclei follow Bose-Einstein statistics, so the total wave function must be symmetric under the interchange operator. Thus the symmetric states *s* (odd *N*) must be combined with symmetric nuclear spin wavefunctions, the *a* states (even *N*) combine with anti-symmetric nuclear spin wave functions, but the latter do not exist. As a consequence, the *a* levels with even *N* are absent for $^{16}O_2$ and $^{18}O_2$ isotopologues, as shown in Figure 1.5.

The excited electronic state $a^1\Delta_g$ obeys Hund's coupling case (*a*). This $a^1\Delta_g$ state is a singlet state (the total electron spin *S* = 0), and *J* is always equal to *N*. Because the projection of orbital angular momentum onto the molecular axis is not zero ($\Lambda = 2$), each rotational level is split into two through double orbital degeneracy called Λ-doubling. As $I = 0$ for ^{16}O and ^{18}O nuclei, for each value of *J* only one Λ-doublet component is allowed by the exclusion principle, namely, the one that has positive parity. Thus all the rotational levels of O_2 in its $a^1\Delta_g$ state have positive parity. The other Λ-doublet component is missing for $^{16}O_2$ and $^{18}O_2$ molecules. The heteronuclear species $^{16}O^{18}O$, $^{16}O^{17}O$ and $^{17}O^{18}O$ do not show this particular behaviour since the additional inversion symmetry. All the rotational levels are allowed for heteronuclear isotopologues (see Figure 1.5).

In the $^{17}O_2$ isotopomer the situation is also different, because ^{17}O nuclei have a non-zero nuclear spin $I = 5/2$ and follow *Fermi-Dirac* statistics. There exist $(2I+1)^2 = 36$ possible quantum states of which 21 are symmetric and 15 are anti-symmetric under the interchange of the two particles. Thus both *a* and *s* levels are allowed for the $^{17}O_2$ isotopologue. Figure 1.5 illustrates the parity of $^3\Sigma_g^-$ and $a^1\Delta_g$ states of O_2, where forbidden rotational levels of $^{16}O_2$ and $^{18}O_2$ are depicted by a dashed line.

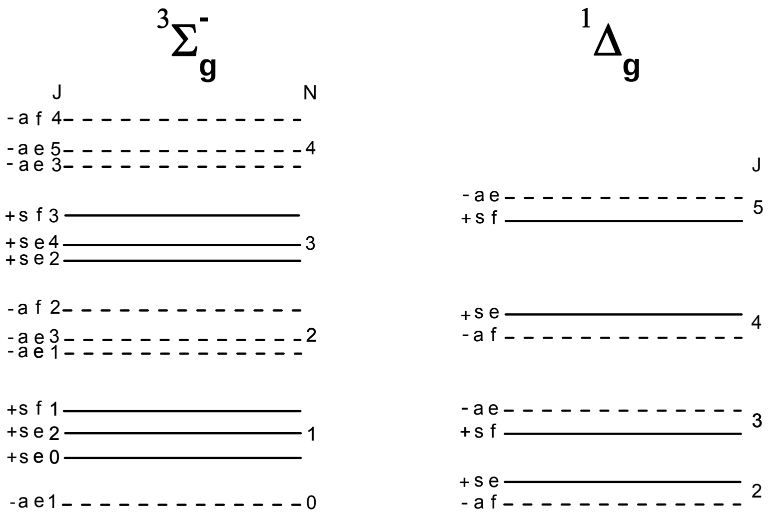

Figure 1.5. The parity of the O_2 $^3\Sigma_g^-$ and $a^1\Delta_g$ rotational energy levels. Dashed lines represent the missing rotational energy levels of $^{16}O_2$ and $^{18}O_2$ isotopologues (see text for details). All depicted rotational levels are allowed for heteronuclear isotopologues and $^{17}O_2$.

If one or both nuclei have nuclear angular momentum consequent nuclear hyperfine structure may be observed, since magnetic and electric interaction involving this moment will occur. Thus there exist two types of hyperfine effects − the *magnetic hyperfine* and the *electric quadrupole*. The predominant hyperfine structure is due to interaction between the nuclear magnetic moment and magnetic fields originating from electronic motion. Effects of nuclear quadrupole moments are smaller and give small deviation from the expected magnetic hyperfine intervals. However, for most molecules in the ground state, the magnetic fields due to various electrons almost completely cancelled, giving zero or only very small magnetic fields at the nucleus. The electric quadrupole effects become the dominating source of hyperfine structure for these molecules. Indeed, the majority of molecules have a $^1\Sigma_g^-$ ground state in which electronic angular momentum is considered zero. However, even for these molecules there are weak interactions involving nuclear magnetic moments. These include interaction between magnetic moments of two nuclei, interaction between a nuclear magnetic moment and magnetic field produced by molecular rotation and magnetic polarization of a molecule by a nuclear magnetic moment. When a molecule has an electronic angular momentum, the magnetic field associated with this momentum interacts strongly with the nuclear moments, giving the magnetic hyperfine structure comparable in size with that found in atoms. The interaction is either due to electronic angular momentum **L** or to spin angular momentum **S**. Oxygen molecule is a notable example of a molecule that has two parallel electron spins in its $X^3\Sigma_g^-$ ground state. Consequently, it is paramagnetic and has large magnetic hyperfine structure. As it is shown below, the hyperfine structure in the $a^1\Delta_g$ state is even larger than that of the ground state.

As mentioned in Section 5 of the current Chapter, the coupling of the nuclear spin to the other angular momenta can be represented by a vector diagram in which **I** is added vectorially to the other angular momenta to give a resultant total angular momentum **F**. The fine structure components are further split into hyperfine components **F = J + I,** with $F = J+I, J+I-1, \ldots |J-I|$. If $J>I$, the lowest value of F is $J-I$, but if $J<I$, the lowest value of F is $I-J$. The set of possible values for F is called a Clebsch-Gordan series. There are different ways of coupling the nuclear spin to the other angular momenta, which are discussed in Section 5 in terms of subdivisions of Hund's coupling cases and which we limit to cases a_β and $b_{\beta J}$.

In the ground $X^3\Sigma_g^-$ state the coupling between **S** and **N**, which gives rise to the fine structure of the O_2 molecule, is approximately 60000 MHz, whereas the coupling between **I** and **S** which gives rise to the magnetic hyperfine structure is only of order of 100 MHz. The coupling of **I** to **N**, which depends on the electric quadrupole interaction, is only a few MHz. Thus the $X^3\Sigma_g^-$ state represents a rather good case $b_{\beta J}$, shown in Figure 1.4b.

In the singlet $a^1\Delta_g$ state, the hyperfine structure arises from the interaction between the nuclear magnetic moment and the magnetic fields produced by an electronic angular momentum. Indeed, the coupling between **Λ** and **I** is approximately 200 MHz and therefore dominates. The nuclear quadrupole interaction is of the same order of magnitude as in the ground state [13]. Consequently, the a_β representation is appropriate for the $a^1\Delta_g$ state (Figure 1.4a). Thus the hyperfine splitting of the $a^1\Delta_g$ state is larger than that of the ground state. This is consistent with earlier magnetic resonance studies on the $^{16}O^{17}O$ and $^{17}O^{18}O$ isotopomers in the $a^1\Delta_g$ state by Arrington et al. [14].

To predict the fine and hyperfine structures of molecular transitions the information on selection rules is required. The $a^1\Delta_g - X^3\Sigma_g^-$ transitions are forbidden by the selection rules for dipole radiation and can appear only as magnetic dipole or electric quadrupole radiation. The magnetic dipole transitions of the $a^1\Delta_g - X^3\Sigma_g^-$ band follow the $\Delta J = 0, \pm 1$ and $+ \leftrightarrow +, - \leftrightarrow -$ selection rule leading to the observation of 9 branches represented by the $\Delta N(N)\Delta J(J)$ notation: $P(N)Q(J)$, $R(N)Q(J)$, $Q(N)Q(J)$ corresponding to $\Delta J = 0$ and $S(N)R(J)$, $P(N)P(J)$, $Q(N)P(J)$, $R(N)R(J)$, $O(N)P(J)$, $Q(N)R(J)$ with $\Delta J = \pm 1$. Quadrupole transitions with $\Delta J = \pm 2, \pm 1, 0$ and $+ \leftrightarrow +, - \leftrightarrow -$ are allowed, which leads to 15 possible branches $T(N)S(J)$, $S(N)S(J)$, $R(N)S(J)$, $P(N)O(J)$, $O(N)O(J)$, $N(N)O(J)$ with $\Delta J = \pm 2$, $S(N)R(J)$, $R(N)R(J)$, $P(N)P(J)$, $O(N)P(J)$, $Q(J)R(N)$, $Q(J)P(N)$ with $\Delta J = \pm 1$ and $R(N)Q(J)$, $Q(N)Q(J)$, $P(N)Q(J)$ with $\Delta J = 0$. The $\Delta J = \pm 1$ and 0 transitions coincide with much stronger magnetic dipole transitions and therefore are not observable. The rotational energy level diagram of the $a^1\Delta_g$ and $X^3\Sigma_g^-$ states of $^{16}O_2$

species together with allowed magnetic dipole and electric quadrupole transitions is shown in Figure 1.6.

Selection rules for the hyperfine structure are exactly the same as for the fine structure assuming either type of interaction is very small compared with the separation between major energy levels. The aforementioned selection rules for the fine structure then become $\Delta J = 0, \pm 1$, $\Delta F = 0, \pm 1$, $\Delta I = 0$ for the hyperfine structure. The hyperfine structure of rotational transitions almost never involves J greater than 10, since it is usually not prominent enough to be observed. For such large values of J, the most intense components of the hyperfine structure are those with $\Delta J = \Delta F$ and for these the hyperfine splitting is very small. Relative intensities of these transition components involving large J are approximately proportional to $2F + 1$ [7]. The experimental observation of the hyperfine structure of the rotational transitions of $a^1\Delta_g - X^3\Sigma_g^-$ band of ^{17}O containing oxygen isotopologues is presented further in Chapter II.

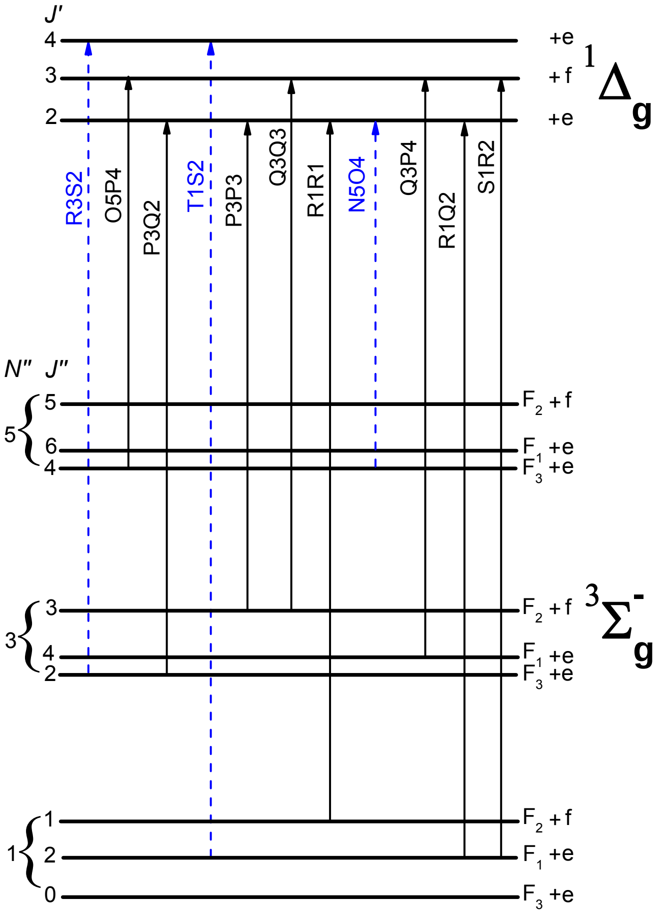

Figure 1.6. Schematic energy level diagram for the $a^1\Delta_g - X^3\Sigma_g^-$ transitions of $^{16}O_2$. The $a^1\Delta_g - X^3\Sigma_g^-$ transitions are noted *ΔNNΔJJ*. Dashed blue arrows indicate electric quadrupole transitions, while black solid arrows correspond to magnetic dipole transitions.

References for Chapter I

[1] M. Born and J.R. Oppenheimer. Zur Quantentheorie der Molekeln. Ann. Phys. 389, 1927; 457.

[2] P.F. Bernath. *Spectra of Atoms and Molecules*. Oxford University Press, Oxford, 1995.

[3] W. Gordy and R.L. Cook. *Microwave Molecular Spectroscopy*. Interscience, New York, 1970.

[4] P. M. Morse. Diatomic molecules according to the wave mechanics. II. Vibrational levels. Phys. Rev. 34, 1929; 57.

[5] G. Herzberg. *Spectra of Diatomic Molecules*. Van Nostrand, New York, 1950.

[6] J.L. Dunham. The Energy Levels of a Rotating Vibrator. Phys. Rev. 41, 721, 1932.

[7] C.H. Townes and A. L. Schawlow. *Microwave Spectroscopy*. Dover, New York, 1975.

[8] J.M. Brown and A. Carrington. *Rotational Spectroscopy of Diatomic Molecules*. Cambridge University Press, Cambridge, U.K., 2003.

[9] F. Hund. Zur deutung einiger erscheinungen in den molekelspektren. Z. Phys. 36, 657, 1926.

[10] T.M. Dunn. *Nuclear hyperfine structure in the electronic spectra of diatomic molecules.* Molecular spectroscopy – Modern Research, Academic Press, New York, 231, 1978.

[11] H. Lefebre-Brion and R.W. Field. *Perturbations in the Spectra of Diatomic Molecules*. Academic Press, New York, 1986.

[12] J.M. Brown, J. T. Hougen, K.-P. Huber, J. W. C. Johns, I. Kopp, H. Lefebvre-Brion, A.J. Merer, D. A. Ramsay, J. Rostas and R. N. Zare. The labelling of parity doublet levels in linear molecules. Mol. Spectrosc. 55, 1975; 500.

[13] B.F. Minaev and V. A. Minaeva. MCSCF response calculations of the excited states properties of the O_2 molecule and a part of its spectrum. Phys. Chem. Chem. Phys. 3, 2001; 720.

[14] C.A. Arrington, A. M. Falick, R. J. Myers. Electron paramagnetic resonance spectrum of O_2 ($a^1\Delta_g$) − Its ^{17}O hyperfine coupling and electronic and rotational g values. J. Chem. Phys. 55, 1971; 909.

Chapter II: The $a^1\Delta_g - X\,^3\Sigma_g^-$ system of oxygen by very high sensitivity CW-Cavity Ring Down Spectroscopy

1. Introduction

This chapter is devoted to the extensive study of the very weak $a^1\Delta_g - X^3\Sigma_g^-$ system of molecular oxygen using high sensitivity CW-Cavity Ring Down Spectroscopy (CW-CRDS). This study was initially motivated by the first detection of electric quadrupole transitions in the atmospheric solar spectrum, showing the necessity to improve the spectral parameters of the $a^1\Delta_g - X^3\Sigma_g^-$ band of molecular oxygen from the new laboratory measurements [1]. The spectra were obtained between 7640 and 7917 cm^{-1} with "natural" oxygen and with samples highly enriched in ^{18}O and ^{17}O. The magnetic dipole-allowed (0-0) band was observed for $^{16}O_2$, $^{16}O^{18}O$, $^{16}O^{17}O$, $^{17}O^{18}O$, $^{18}O_2$ and $^{17}O_2$ species. The (0-0) bands of $^{16}O_2$, $^{18}O_2$, $^{16}O^{17}O$ and $^{17}O_2$ show extremely weak quadrupole transitions, which are accompanied by the $a^1\Delta_g - X^3\Sigma_g^-$ (1-1) hot bands. These measurements allowed us to determine the best to date spectroscopic constants of the $a^1\Delta_g - X^3\Sigma_g^-$ band of the six isotopologues of oxygen – $^{16}O_2$, $^{16}O^{18}O$, $^{16}O^{17}O$, $^{17}O^{18}O$, $^{18}O_2$ and $^{17}O_2$. The combination of the high sensitivity CRDS technique with a cryogenic cell at 80 K allowed for the first observation of the partly resolved hyperfine structure of the $a^1\Delta_g - X^3\Sigma_g^-$ band of the three ^{17}O containing isotopologues $^{16}O^{17}O$, $^{17}O^{18}O$ and $^{17}O_2$.

The current chapter is organized as follows. We start with an introductory part, which consists of four subsections. General information on oxygen molecule is given in Subsection 1.1. Subsection 1.2 outlines the importance of $a^1\Delta_g - X^3\Sigma_g^-$ band of molecular oxygen near 1.27 µm in atmospheric studies. Then we describe the state of the art of the $a^1\Delta_g - X^3\Sigma_g^-$ band investigations and the present status of the HITRAN data for the $a^1\Delta_g - X^3\Sigma_g^-$ band in Subsections 1.3 and 1.4, respectively. In Section 2 we proceed with description of the experimental technique that was used to record the presently investigated high sensitivity absorption spectrum of the $a^1\Delta_g - X^3\Sigma_g^-$ band. The details of our experimental setup for room and 80K temperature recordings are given in Sections 3 and 4, respectively. The assignment of the CRDS spectra is described in Section 5. Next we present spectroscopic parameter derivation, which is split into two parts. Section 6 considers the $^{16}O_2$, $^{16}O^{18}O$ and $^{18}O_2$ isotopologues. Section 7 is devoted to a more complex case of ^{17}O containing isotopologues that requires taking into account the hyperfine structure. We discuss our results in Section 8 and draw conclusions in Section 9.

1.1. General information on the O_2 molecule

Molecular oxygen is the second most abundant constituent in the Earth's atmosphere. There are six stable oxygen isotopic species: $^{16}O_2$, $^{16}O^{18}O$, $^{16}O^{17}O$, $^{17}O^{18}O$, $^{18}O_2$ and $^{17}O_2$. The three most abundant oxygen isotopic species in terrestrial atmosphere are $^{16}O_2$, $^{16}O^{18}O$ and $^{16}O^{17}O$ with corresponding abundances – 0.995, 3.991×10^{-3} and 7.422×10^{-4}, as shown in Table 2.1. As mentioned in Section 7 of Chapter I, O_2 is one of the few paramagnetic molecules with an even number of electrons, its ground state has a permanent magnetic moment due to unpaired electrons with parallel spins. Because of the lack of permanent electric dipole momentum, oxygen molecule can interact with an electromagnetic field only via its magnetic dipole or by its electric quadrupole moment.

Table 2.1. Relative abundance of isotopic species of the O_2 molecule adopted for HITRAN.

Isotopologue	Abundance
$^{16}O_2$	0.995262
$^{16}O^{18}O$	3.99141×10^{-3}
$^{16}O^{17}O$	7.42235×10^{-4}
$^{17}O^{18}O$	1.558×10^{-6}
$^{18}O_2$	4.203×10^{-6}
$^{17}O_2$	1.444×10^{-7}

Calculated from isotopic abundances adopted for HITRAN.

The lowest electron configuration of O_2 is $(1s\sigma_g)^2$ $(1s\sigma_u)^2$ $(2s\sigma_g)^2$ $(2s\sigma_u)^2$ $(2p\sigma_g)^2$ $(2p\pi_u)^4$ $(2p\pi^*{}_g)^2$. It gives rise to the ground electronic state $X\,^3\Sigma_g^-$ and the two first excited states $a^1\Delta_g$ and $b^1\Sigma_g^+$. These low-lying excited electronic states $a^1\Delta_g$ and $b^1\Sigma_g^+$ are located at 7918.1 cm^{-1} and 13195 cm^{-1} above the ground state, as shown in Figure 1.2 Chapter I. They are metastable, since electric-dipole transitions from the ground state are triply forbidden by spin, orbital angular momentum and parity selection rules.

The $a^1\Delta_g$ and $b^1\Sigma_g^+$ excited electronic states give rise to near-infrared and visible spectra. Although the line intensities are usually small, the high mixing ratio and long optical path in the terrestrial atmosphere compensate to produce meaningful absorption [2].

1.2. Atmospheric interest of the $a^1\Delta_g - X\,^3\Sigma_g^-$ band near 1.27 μm

Atmospheric spectra of oxygen are used to deduce information about properties and other species in the atmosphere. For example, one could determine ozone concentrations in the mesosphere and thermosphere by monitoring emission of the products of ozone photolysis, in particular from the electronically excited $a^1\Delta_g$ and $b^1\Sigma_g^+$ states of O_2 [3]–[4], since both these states are formed in the atmosphere by solar–UV photolysis of ozone by means of Hartley bands.

The 1.27 μm $a^1\Delta_g - X\,^3\Sigma_g^-$ band of O_2 plays an important role in the atmospheric chemistry and physics. On the Earth this band is observed from the ground in absorption against the solar background [5] and in emission from the twilight airglow [6]. In addition to being the signature of O_3 production, the 1.27 μm band of O_2 is also important when studying the heating of the upper atmosphere. The role of the heating due to absorption of solar radiation by molecular oxygen in the $b^1\Sigma_g^+ - X^3\Sigma_g^-$ and $a^1\Delta_g - X^3\Sigma_g^-$ bands was examined by Mlynczak and Marshall [7]. This study demonstrated that together these O_2 bands contribute approximately 10% to the diabatic (i.e., solar plus exothermic chemical reaction) heating of the middle mesosphere. The $a^1\Delta_g - X^3\Sigma_g^-$ band accounts for ~10% of the O_2-contributed heating at the tropopause.

To use the 1.27 μm O_2 band for the atmospheric modelling, one must have accurate spectroscopic parameters. Moreover, the knowledge of accurate spectroscopic parameters of the $a^1\Delta_g - X^3\Sigma_g^-$ band of oxygen is very important in the field of remote sensing in relation to high–accuracy measurements of atmospheric greenhouse gases such as CO_2 and CH_4. One reason is that due to the uniform mixing of oxygen, the oxygen lines are often used as a benchmark for intensity calibration of atmospheric spectra taken by satellite instruments. Another reason is that taking the ratio of the column abundance of CO_2 or CH_4 to that of O_2 cancels many common systematic errors, especially the ones that are instrument-related [8].

1.3. Previous studies of the $a^1\Delta_g - X^3\Sigma_g^-$ band

Electronic transitions of oxygen have been a subject of over one hundred theoretical, laboratory and field studies for over a century. The $b^1\Sigma_g^+ - X^3\Sigma_g^-$ atmospheric system has been investigated in details but studies of the infrared system $a^1\Delta_g - X^3\Sigma_g^-$ are much less numerous, because it is about 100 times weaker. The fine structure of the atmospheric oxygen $a^1\Delta_g - X^3\Sigma_g^-$ band was first resolved by G. Herzberg in 1934, who photographed this band in the solar spectrum under high dispersion [9]. Details on the solar $a^1\Delta_g - X^3\Sigma_g^-$ (0−0) and (1−0) bands were given later by G. Herzberg and L. Herzberg [5]. The vibrational and rotational constants of the $a^1\Delta_g$ state of O_2 were evaluated [5]. In this pioneering work, relative accuracy of the observed line positions was ±0.03 cm^{-1} in the (0−0) band and ±0.07 cm^{-1} in the (1−0) band, respectively. Despite the obvious importance of the 1.27 μm band in the atmospheric studies, the number of laboratory measurements of the absorption spectrum of $a^1\Delta_g - X^3\Sigma_g^-$ band of O_2 is limited, mainly because of the small intensity of this magnetic dipole-allowed band. The very long radiative lifetime of the $a^1\Delta_g$ state of $\tau_{1/2}$ ~ 45 min reflects the weakness of this band [10]. Table 2.2 summarizes the high resolution spectroscopy of the O_2 $a^1\Delta_g - X^3\Sigma_g^-$ band over the last thirty years [11]−[17]. A detailed summary of previous studies of O_2 $a^1\Delta_g - X^3\Sigma_g^-$ and $b^1\Sigma_g^+ - X^3\Sigma_g^-$ transitions up to 1998 is given in Ref. [18].

Table 2.2. Summary of hig resolution spectroscopic experiments of $a^1\Delta_g - X^3\Sigma_g^-$ (0−0) band of O_2 in the past 30 years.

Investigation	Year	Technique	
C. Amiot and J. Vergès [11]	1981	FTS	Afterglow discharge
L.-B. Lin et al. [12]	1988	FTS	Path length of 20.25 m
Y. T. Hsu et al. [13]	1992	FTS	Path length of 18.75 m
W. R. Pendleton et al. [14]	1996	FTS	Twilight atmospheric emission
W. J. Lafferty et al. [15]	1998	FTS	Path length of 84 m
S. M. Newman et al. [16]	1999	FTS, CRDS	Path length of 32 to > 256 m
S.-L. Cheah et al. [17]	2000	FTS	Path length of 6 and 107 m
Current study	2010	CW-CRDS	

FTS: Fourier Transform Spectroscopy; CRDS: Cavity Ring Down Spectroscopy.

1.4. Status and deficiencies of the $a^1\Delta_g - X^3\Sigma_g^-$ band HITRAN line list

Due to their importance, magnetic dipole transitions in the $a^1\Delta_g - X^3\Sigma_g^-$ band were tabulated in the HITRAN database [19] since its inception [20]. Hence these parameters have been continuously updated as HITRAN was evolving. The intensities of the $a^1\Delta_g - X^3\Sigma_g^-$ (0-0) band for $^{16}O_2$ in HITRAN, however, were found to be inadequate for atmospheric retrievals such as the ones in Ref. [6]. The new list of $^{16}O_2$ intensities recently adopted for HITRAN, which proved to be more accurate in application to atmospheric retrievals [8] was derived by Orr-Ewing based on experimental results from Newman et al. [16]. In order to further improve the quality of retrievals, Washenfelder et al. [8] applied an empirical scaling to HITRAN2008 intensities of $^{16}O^{18}O$ that originated from Ref. [18]. These intensity improvements have served as a basis for an interim update of the HITRAN oxygen file that was placed on the HITRAN website in November 2009 [21].

Figure 2.1 illustrates the $a^1\Delta_g - X^3\Sigma_g^-$ near-infrared atmospheric band system and the $b^1\Sigma_g^+ - X^3\Sigma_g^-$ band system in visible region as provided by the current version of HITRAN [19]. The O_2 $a^1\Delta_g - X^3\Sigma_g^-$ system consists of the (0−1), (0−0) and (1−0) bands at 1.58 μm, 1.27 μm, and 1.07 μm, respectively. The $b^1\Sigma_g^+ - X^3\Sigma_g^-$ system is about 100 times stronger. It consists of (1−1) band at 771 nm and bands at 762 nm, 688 nm, 629 nm, which are referred to as *A*, *B*, and *γ* atmospheric bands of molecular oxygen.

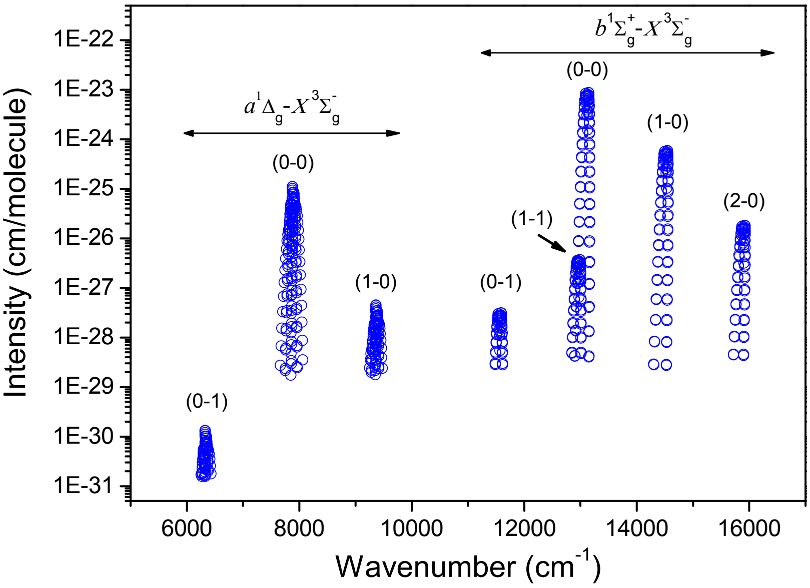

Figure 2.1. Overview of the $^{16}O_2$ $a^1\Delta_g - X^3\Sigma_g^-$ and $b^1\Sigma_g^+ - X^3\Sigma_g^-$ band systems.

Despite recent updates, there is still significant room for improvement of spectral parameters of the $a^1\Delta_g - X^3\Sigma_g^-$ band. For instance, the $^{16}O^{18}O$ line intensities in the $a^1\Delta_g - X^3\Sigma_g^-$ band have limited quality because of the lack of proper experimental input parameters for this species in HITRAN. Furthermore, no electric quadrupole lines in the $a^1\Delta_g - X^3\Sigma_g^-$ band near 1.27 μm were identified before our work due to their anticipated weakness. Indeed, the theoretical predictions of the emission probability for the electric quadrupole component in the classic work of Klotz et al. [22] gives a value of 5×10^{-7} s^{-1} which is significantly lower than the value measured for the magnetic dipole component 2.19×10^{-4} s^{-1} [16]. However, even this value is still larger than the one predicted in the same paper for the quadrupole transitions for the A-band (1.55×10^{-7} s^{-1}), which were recently observed by Long et al. [23] using frequency-stabilized cavity ring-down spectroscopy (FS-CRDS) technique. Thus, considering that $a^1\Delta_g - X^3\Sigma_g^-$ transitions are located at lower wavenumbers, one would expect their electric quadrupole band intensity to be at least one order of magnitude stronger than that of the *A*-band (see Eq. (19) in Ref. [24]).

The electric quadrupole transitions in the $a^1\Delta_g - X^3\Sigma_g^-$ band of $^{16}O_2$ near 1.27 μm were detected for the first time in atmospheric solar spectra acquired with a ground based Fourier transform spectrometer (FTS) in Park Falls, WI [1]. This spectrum, shown in Figure 2.2, was measured in December 2004 at a solar zenith angle of 82.45°, thus representing an airmass of 7. In Figure 2.2a the solar spectrum was fitted using the latest official release of HITRAN database [19], while in Figure 2.2b it was fitted using a superior O_2 line list provided by Prof. Andrew Orr-Ewing, based on the work of Newman et al. [25] with some minor adjustments described in

Ref. [8]. In Figure 2.2b one can see that there are several lines that are not accounted for in the reference line lists. These missing lines in Figure 2.2b are, in fact, electric quadrupole lines of the $a^1\Delta_g - X\,^3\Sigma_g^-$ band [1].

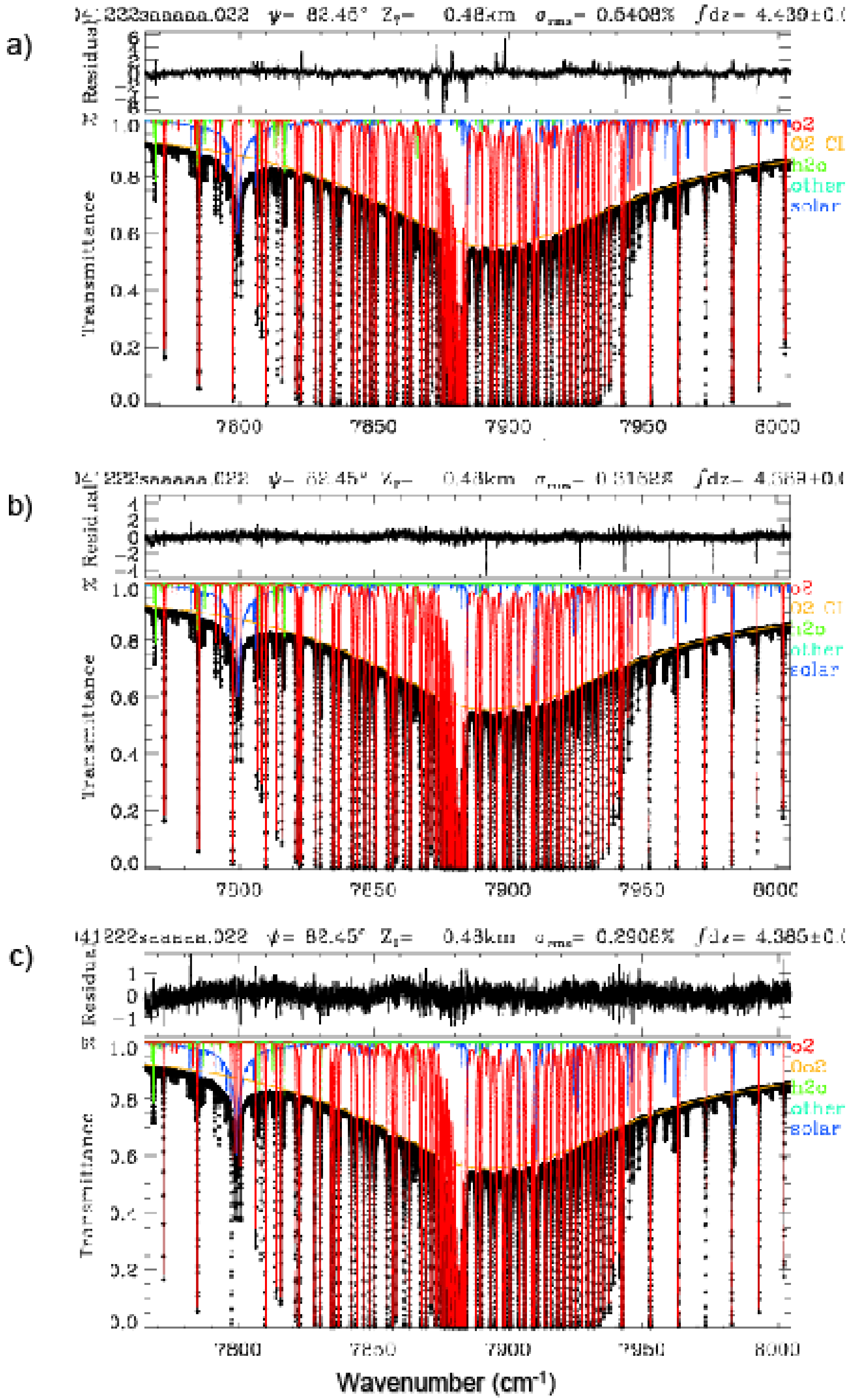

Figure 2.2. Solar FTS spectrum of the $a^1\Delta_g - X\,^3\Sigma_g^-$ band of oxygen measured in December 2004 from Park Falls, WI (442 m asl) at a solar zenith angle of 82.45°. a) Fitted using the HITRAN2008 $a^1\Delta_g - X\,^3\Sigma_g^-$ magnetic dipole (M1) transitions; b) using updated HITRAN file (07_hit09.par) [21] of M1 transitions based on Ref. [25]; c) adding the calculated electric quadrupole line list. In each panel, ♦- symbols represent the measured spectrum, and the black line represents the calculation. The residual trace at the top of each panel represents their difference (Measured-Calculated). The various coloured lines represent the various contributions to the calculated transmittance. The O_2 collision induced absorption (orange curve) is fitted separately from the discrete O_2 absorption (red curve). Note that the RMS residual in panel c) is almost a factor of 2 better than that in panel a). The spectrum, acquired in 75 s of integration time, was one of over 300 measured on this day. It represents an effective atmospheric path length of over 50 km (adapted from Ref. [1]).

In order to fit the solar spectrum with better residuals than those in Figure 2.2b one has to include reliable reference data not only for electric quadrupole line positions but also for their intensities. The intensities that can be estimated directly from the solar spectrum cannot be very accurate due to the overlap with interfering absorptions (e.g. H_2O, O_2 magnetic dipole, solar absorptions) and the difficulty of evaluating the effective path length at high solar zenith angles. In order to provide quantitative intensity information for electric quadrupole transitions high-sensitivity CW-Cavity Ring Down Spectroscopy experiments were carried out in our laboratory in the 7717-7917 cm^{-1} region. The measurements of the isolated electric quadrupole lines provided necessary input parameters for calculations of the electric quadrupole lines with the intensity greater than 10^{-30} cm/molecule. This calculated line list was then included into the fit of the solar spectrum in Figure 2.2, yielding improved residuals (Figure 2.2c). This discovery of the missing quadrupole lines became the cornerstone of the extensive experimental investigations of the weak $a^1\Delta_g - X^3\Sigma_g^-$ system for the six isotopologues of oxygen – $^{16}O_2$, $^{16}O^{18}O$, $^{16}O^{17}O$, $^{17}O^{18}O$, $^{18}O_2$ and $^{17}O_2$ that are presented in this thesis.

In the derivation of the current $a^1\Delta_g - X^3\Sigma_g^-$ line positions of $^{16}O_2$ in HITRAN, the $X^3\Sigma_g^-$ spectroscopic constants from Rouillé et al. [26] and $a^1\Delta_g$ rotational constants determined from the microwave spectrum by Hillig et al. [27] were used [18]. Ref. [18] states that the term energy of $a^1\Delta_g$ was taken from Krupenie [28]. However, although none of the subsequent HITRAN papers have elaborated on this, the term values of Krupenie were adjusted in HITRAN to match unpublished FTS spectrum measured by Brault [29]. The effective term values were 7883.75639 cm^{-1} for $\upsilon = 0$ and 9367.20879 cm^{-1} for $\upsilon = 1$. In HITRAN 2008, the line positions of $^{16}O^{18}O$ were calculated using ground-state constants of Mizushima and Yamomoto [30] and excited-state rotational constants reported by Herzberg and Herzberg [4]. Just like for the principal isotopologue, the term values of Krupenie [28] were adjusted to match unpublished FTS spectrum [29] (the effective value was 7885.06858 cm^{-1}).

In spite of the extensive studies available for the molecular oxygen, the extent of high precision measurements remains limited, and the modelling of a variety of atmospheric phenomena, such as ozone photodissociation or atmospheric absorption in the near-infrared, relies on the accuracy and precision of available spectroscopic data. Although the resulting HITRAN line positions have not received criticism from the users and the quality of the input constants (especially for $^{16}O_2$) is quite reasonable, it seems that direct measurements of $a^1\Delta_g - X^3\Sigma_g^-$ band may provide means of obtaining a more consistent set of line positions. Moreover, line positions reported in the most recent measurements by Cheah et al. [17] differ from those in HITRAN by more than 0.01 cm^{-1}. The authors of Ref. [17] stated that their line positions were superior to the corresponding ones in HITRAN. This disagreement between data also calls for additional experimental studies.

In order to attend the problems listed above and extend the observations, spectra of the $a^1\Delta_g - X\,^3\Sigma_g^-$ electronic transitions have been recorded by CW-CRDS and are reported in this thesis. CW-CRDS technique used in our spectra recordings is described in the next Section. The experimental details and obtained spectra will be presented followed by the spectrum assignment and spectroscopic parameters derivation of the $a^1\Delta_g$ and $X\,^3\Sigma_g^-$ states for each of the oxygen isotopologues under consideration.

2. Principles of the CW-Cavity Ring Down Spectroscopy technique

The CW-Cavity Ring Down Spectroscopy (CW-CRDS) technique was used to study the $a^1\Delta_g - X\,^3\Sigma_g^-$ band of molecular oxygen near 1.27 µm. CW-CRDS is one of the most powerful and versatile absorption techniques. It is based on the measurements of the decay rate of light intensity inside an optical cavity. The ringdown cavity comprises two high reflectivity mirrors (typically reflecting more than 99.99%) placed at distance *l* facing each other. Figure 2.3 illustrates the basic principle of a CW-CRDS setup.

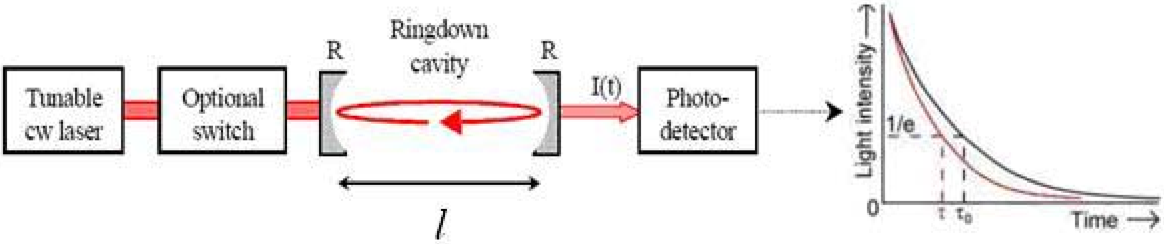

Figure 2.3. Schematic diagram of a typical ringdown setup. τ_0 and τ are the ring down time of the empty cavity and the cavity with a sample inside, respectively (adapted from Ref. [31]).

The transmitted wave decays exponentially in time. The decay rate is proportional to the both fixed cavity losses, such as absorption by the dielectric coating or scattering on the surface and absorption by the medium of interest within the cavity. Light from the laser is first injected into the ringdown cavity through one of the mirrors, effectively trapping the light within the cavity. The light reflects back and forth between the two highly reflective mirrors multiple times up to a total path length of many kilometres. Once the photodetector external to the cavity “sees” a preset level of light energy, the light source is shuttered. On each successive pass, a small amount of light emits through the mirror and produces an easily detectable signal. Thus the decay constant, also called the ring down time τ is measured as a function of laser wavelength to obtain the spectrum of cavity optical losses. The transmitted intensity $I(t)$ is an exponential decay of the initial intensity I_0:

$$I(t) = I_0 \exp(-t/\tau) \tag{2.1}$$

Considering the surface and diffraction losses on the mirrors L and the frequency dependent absorption coefficient of the sample α, the decay rate of the trapped photons is

$$\frac{1}{\tau} = (T + L + \alpha(\nu)l)\frac{c}{l} = \frac{1}{\tau_0} + c\alpha(\nu) \tag{2.2}$$

where T is transmittivity (of the order of 10^{-5} or less), l is the cavity length and c is the speed of light. The first term on the right hand side $(1/\tau_0)$ of Equation 2.2 is the contribution of minor losses. It depends smoothly on the wavelength and gives the baseline of the absorption spectrum that can be measured when the cavity is empty. Thus by scanning the laser wavelength, the sample absorption coefficient is obtained directly in units of cm^{-1} by dividing the decay rate $1/\tau$ by speed of light (Equation 2.2). The key advantages of CRDS over traditional absorption spectroscopic techniques is long effective path length $l_{eff} = c\tau$ and insensitivity to laser power fluctuation, thus offering great sensitivity. Moreover, it uses small sample volumes (typically<500 cm^3) and can use laser sources having very narrow line width and achieving high spectral resolution (<10^{-4} cm^{-1}). The CW-CRDS disadvantage is that scanning is time consuming due to small spectral step size.

The fibered distributed feedback (DFB) laser CW-CRDS spectrometer used to record the high sensitivity absorption spectrum of $a^1\Delta_g - X^3\Sigma_g^-$ oxygen band presented in this thesis has been developed in our laboratory by D. Romanini et al. [32]−[33] and continuously improved in the last years by Samir Kassi, who was the main responsible of the spectra recordings. The following Section gives a brief overview of the CW-CRDS spectrometer. Further details on the experimental setup can be found in Refs. [34]−[36].

3. Experimental details and sample composition

The high-sensitivity CW-CRDS absorption spectra of the O_2 isotopologues were recorded in the 7640-7917 cm^{-1} region. Three samples were used: the first one contained oxygen with an isotopic composition near natural abundance (hereafter referred to as ^{16}O sample), the second one (^{18}O sample) was highly enriched in ^{18}O (Cambridge Isotope laboratories, >95 % of $^{18}O_2$) and the third one was highly enriched in ^{17}O (^{17}O sample). The stated atomic composition of the ^{17}O sample (from Sigma Aldrich) was ^{17}O: 55.8%, ^{16}O: 43.4% and ^{18}O: 0.8 %. The pressure value of the recordings was fixed to 50.0 Torr in case of the ^{16}O and ^{18}O samples and to 30.0 Torr for the ^{17}O sample. In order to avoid saturation of the strongest lines, additional spectra of the ^{18}O and ^{17}O samples were recorded at 5.0 Torr in the 7876-7900 cm^{-1} and 7839-7917 cm^{-1} region, respectively.

As mentioned in the previous Section, the fibered distributed feedback laser CW-CRDS spectrometer was used in our recordings. In brief, each DFB laser diode has a typical tuning range of about 40 cm^{-1} by temperature tuning from -5°C to 60°C. The whole 5850-7917 cm^{-1} is accessible by using a series of 65 DFB lasers. For the present experiment, nine DFB laser diodes were needed to cover the 7640-7917 cm^{-1} region of interest. The electro-polished stainless steel ringdown cell (l = 2 m, inner diameter Φ= 11 mm) was fitted by a pair of super-mirrors. The reflectivity of these mirrors (about 99.997 %) corresponds to empty cell ring down times of about $\tau = 200\,\mu\text{s}$. About one hundred ringdown events were averaged for each spectral data point; the complete temperature scan of one DFB laser (15000 spectral points) required about 70 minutes. The achieved noise equivalent absorption (detection limit) was about $\alpha_{\min} \sim 4\times10^{-11}$ cm^{-1} over the whole spectrum, which is equivalent to 1% absorbance after more than one thousand kilometres. The pressure measured by a capacitance gauge (MKS 100 Torr full range with 0.1% accuracy) and the ringdown cell temperature were monitored during the spectrum recording. Figure 2.4 shows the overview of the spectra of the ^{16}O and ^{18}O samples recorded at a pressure of 50.0 Torr and a temperature of 300.2 K together with spectra of the ^{17}O highly enriched sample recorded at 30.0 Torr and 296 K. The spectrum does not cover the high energy part of the $a^1\Delta_g - X^3\Sigma_g^-$ band above 7917 cm^{-1}, as we could not purchase the fibered DFB laser for this spectral region.

Each 40 cm^{-1} wide spectrum recorded with one DFB laser was calibrated independently on the basis of wavelength values provided by a Michelson-type wavemeter (Burleigh WA-1650, 60 MHz resolution and 100 MHz accuracy). The calibration was further refined by stretching the whole spectrum in order to match the accurate positions of reference lines (see Ref. [35] for details). The magnetic dipole line positions of the $a^1\Delta_g - X^3\Sigma_g^-$ band of ^{16}O$_2$ as provided in the recent HITRAN [19] were used for calibration. The typical uncertainty of the line positions is estimated to be less than 1×10^{-3} cm^{-1}. The spectra of the ^{18}O sample were calibrated against ^{16}O^{18}O lines observed in the spectra of the ^{16}O sample. In that way the calibration of the three spectra was consistent with the HITRAN line list of O$_2$. The line positions of ^{16}O^{18}O from HITRAN were not used for calibration because the quality of the constants used to generate that list was inferior to those used for the principal isotopologue.

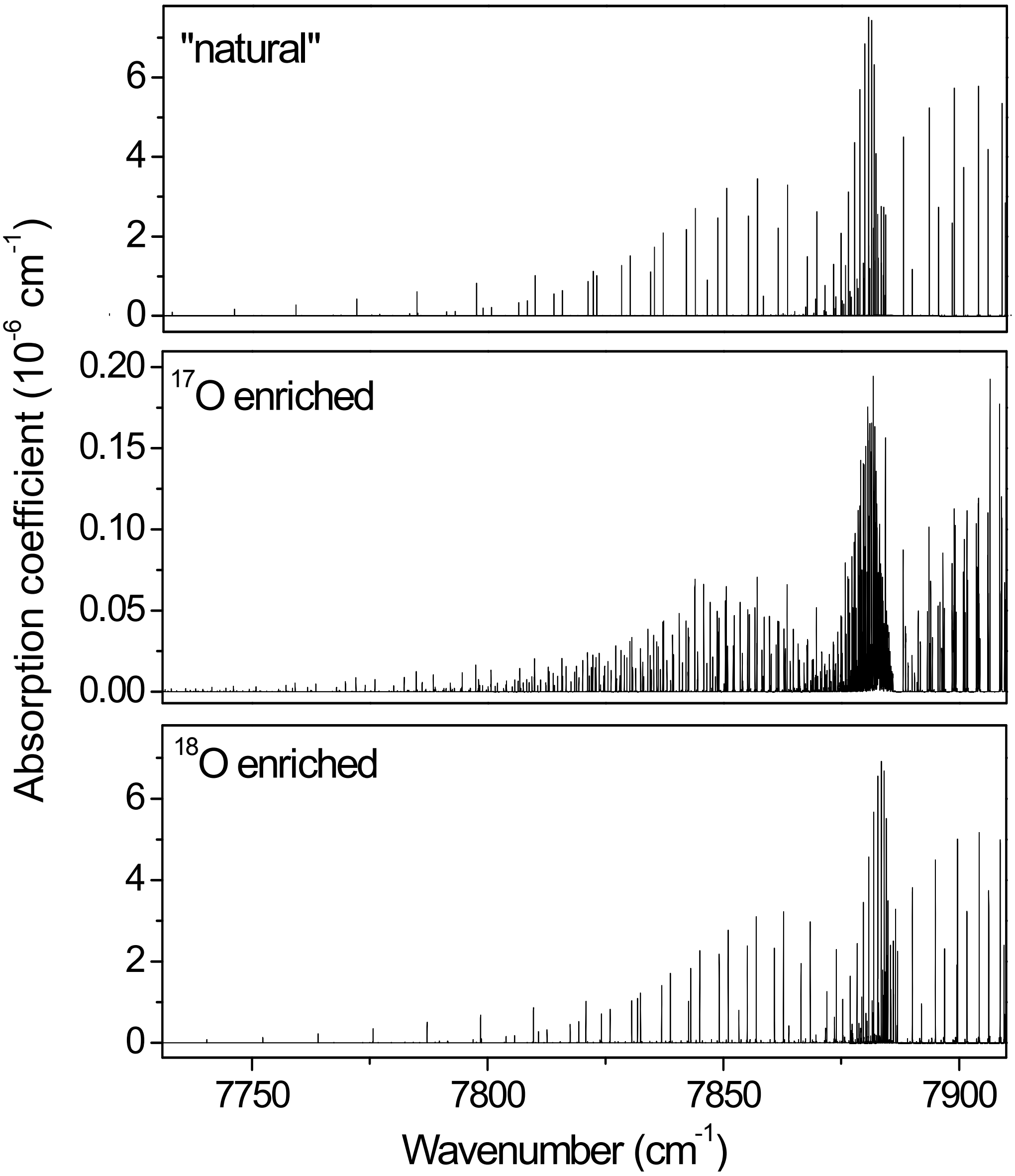

Figure 2.4. Overview of the $a^1\Delta_g - X\,^3\Sigma_g^-$ band of oxygen recorded by CW-CRDS (P=50.0 and 30.0 Torr, T=300.2 and 296 K). The upper, middle and lower panels correspond to O_2 with an isotopic composition near natural abundance sample, highly ^{17}O-enriched and highly ^{18}O-enriched samples, respectively.

The line centres and intensities were determined by using an interactive least squares multi-line fitting program FITYK[1] assuming a line profile of Voigt type. At 30.0 or 50.0 Torr, the pressure broadening has a significant contribution to the observed line profile and a Voigt function was adopted for the fitting. The DFB linewidth is about one thousandth of the Doppler broadening and thus negligible. The local baseline (assumed to be a linear function of the wavenumber) and the three parameters of each Voigt profile (line centre, integrated absorbance, HWHM of the Lorentzian component) were fitted. The HWHM of the Gaussian component was fixed to its theoretical value. In Figure 2.5, the spectrum of the $^{18}O_2$ Q(19)R(18) magnetic dipole transition at 7880.215 cm^{-1} is presented with the corresponding residuals. For such well isolated lines, the uncertainty on the retrieved intensity value is estimated to be less than 2%.

---

[1] FITYK program version v0.8.6, http://sourceforge.net/projects/fityk/

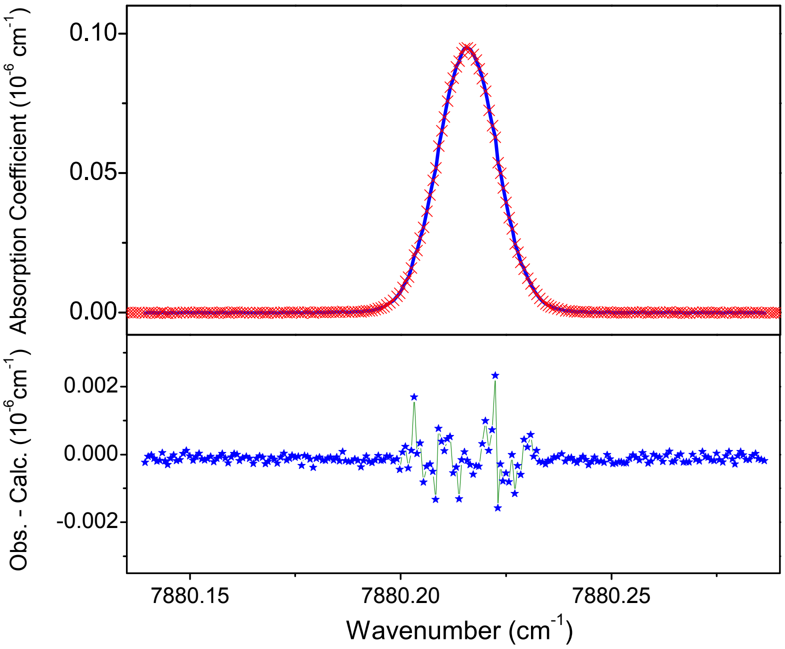

Figure 2.5. Spectrum of the $^{18}O_2$ Q(19)R(18) magnetic dipole transition at 7880.215 cm^{-1} (P= 5.0 Torr, T= 298 K). The upper panel shows the measured (x) and fitted (solid) line profiles; the lower panel shows the residuals of the fit.

As pointed out in Section 7 of Chapter I, in the case of the ^{17}O containing isotopologues, the situation becomes more complicated because ^{17}O has a nuclear spin $I = 5/2$. Coupling of the nuclear spin to electron spin in the $X\,^3\Sigma_g^-$ state and to the electronic angular momentum in the $a^1\Delta_g$ state gives rise to a magnetic hyperfine structure in the ^{17}O containing species. As a result of the Doppler broadening at room temperature, the magnetic hyperfine structure could not be resolved and it manifested itself only as a broadening of the ^{16}O^{17}O, $^{17}O_2$ and ^{17}O^{18}O transitions. Figure 2.6 shows an example of the unresolved hyperfine structure of two ^{17}O^{18}O transitions in the spectrum of ^{18}O sample which appear significantly broader than the nearby ^{16}O^{18}O transitions.

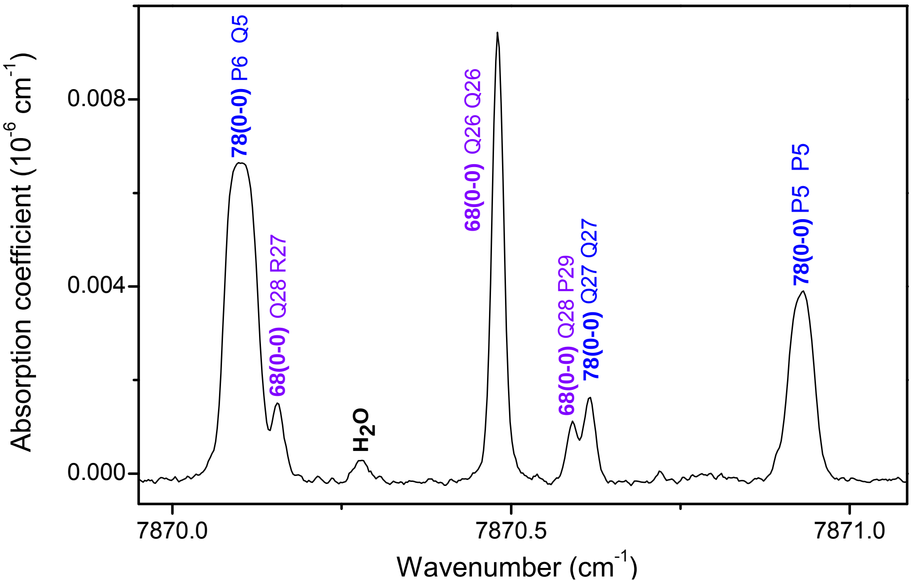

Figure 2.6. Apparent line broadening due to the unresolved hyperfine structure of two ^{17}O^{18}O transitions. The ^{17}O^{18}O lines are significantly broader than the nearby ^{16}O^{18}O line.

For the ^{17}O containing isotopologues, the determination of the line centres and line intensities was difficult because of the superposition of many hyperfine (hf) components which are only partly resolved, especially in the spectrum of the ^{17}O sample. The line profile analysis was adapted according to the impact of the hf structure on the observed line profile:

(i) In the case of the high rotational transitions of the ^{17}O isotopologues, showing negligible hf structure, the transitions were considered as single lines and the same program was used to fit the line profile.

(ii) The most challenging situation is the case where the lines show a wide, generally asymmetric and mostly unresolved profile due to the hf structure. To minimize the negative effect of the unresolved hf structure, the line centres were determined as an average value over the line profile of the wavenumbers weighted by the corresponding absorption coefficient, the line intensities being obtained from the integrated absorption coefficient.

Overall, 376, 649 and 843 lines were measured in the spectrum of ^{16}O, ^{18}O and ^{17}O samples, respectively. Some lines due to impurities (mostly H_2O but also N_2O, CO_2 and HF) were also identified.

On the basis of the HITRAN intensity values, we checked that the abundance of the $^{16}O^{18}O$ species in the ^{16}O sample was close to its “natural” value (3.77×10^{-3} against 3.99×10^{-3} [19]). The relative abundances of the $^{16}O^{18}O$ and $^{16}O_2$ species in the ^{18}O sample and ^{17}O sample were calculated to be 4.9×10^{-2} and 1×10^{-3} and $7.02(92)\times10^{-3}$ and 0.184(7), respectively.

In order to estimate the relative concentration of the $^{16}O^{17}O$ and $^{17}O^{18}O$ species, we assumed that the band strength was the same as that of the $^{16}O^{18}O$ species. The estimated values of 7.9×10^{-4} and 1.1% were obtained for $^{16}O^{17}O$ in the ^{16}O sample and for $^{17}O^{18}O$ in the ^{18}O sample, respectively. In the ^{17}O sample, this assumption leads to the values of 0.469(30) and $9.6(18)\times10^{-3}$ for $^{16}O^{17}O$ and $^{17}O^{18}O$, respectively. From these estimated molecular concentrations we derived the following atomic composition of the ^{17}O sample: ^{17}O: 56.9%, ^{16}O: 42.2%, ^{18}O: 0.83 % which is in very good agreement with the stated atomic composition (^{17}O: 55.8%, ^{16}O: 43.4%, ^{18}O: 0.8 %). Note that the concentration of impurities was negligible: in the ^{17}O sample, H_2O and CO_2 relative concentrations were calculated to be less than 1.5×10^{-4} and 10^{-4} respectively. In the ^{16}O and the ^{18}O samples, the relative concentration of H_2O was calculated to be less than 3×10^{-5}. Table 2.3 summarizes the observations and composition for the three samples and provides the number of lines corresponding to the different bands together with their intensity range.

Table 2.3. Summary of the CW-CRDS observations of the $a^1\Delta_g - X\,^3\Sigma_g^-$ system of O_2.

Isotopologue	HITRAN notation	Abundance	Band	Number of lines	Intensity range[a] (×10^{-26} cm/molecule)
^{16}O sample					
$^{16}O_2$	66	0.995	(0-0)	97	3.9×10^{-4} – 11.0
			(0-0) elec. quad.	23	1.0×10^{-4} – 1.9×10^{-2}
			(1-1)	79	1.1×10^{-4} – 6.4×10^{-3}
$^{16}O^{18}O$	68	3.8×10^{-3}	(0-0)	127	4.3×10^{-4} – 1.9×10^{-2}
$^{16}O^{17}O$	67	7.9×10^{-4}	(0-0)	50	1.6×10^{-4} – 5.8×10^{-3}
^{18}O sample					
$^{18}O_2$	88	0.94	(0-0)	138	2.0×10^{-4} – 10.1
			(0-0) elec. quad.	22	1.9×10^{-4} – 6.0×10^{-3}
			(1-1)	95	1.1×10^{-4} – 8.1×10^{-3}
$^{16}O^{18}O$	68	4.9×10^{-2}	(0-0)	202	1.6×10^{-4} – 3.4×10^{-1}
$^{17}O^{18}O$	78	~1×10^{-2}	(0-0)	139	3.3×10^{-4} – 6.4×10^{-2}
$^{16}O_2$	66	~1×10^{-3}	(0-0)	53	1.1×10^{-4} –1.3×10^{-2}
^{17}O sample					
$^{16}O^{17}O$	67	0.469(30)	(0-0)	206	3.79×10^{-4} – 3.55
			(0-0) elec. quad.	12	3.77×10^{-4} – 4.93×10^{-3}
			(1-1)	68	1.35×10^{-4} –1.71×10^{-3}
$^{17}O_2$	77	0.330(30)	(0-0)	209	2.04×10^{-4} – 2.96
			(0-0) elec. quad.	8	2.66×10^{-4} – 6.82×10^{-4}
			(1-1)	39	1.36×10^{-4}– 1.61×10^{-3}
$^{16}O_2$	66	0.184(7)	(0-0)	89	2.95×10^{-4} – 1.89
			(0-0) elec. quad.	5	3.93×10^{-4} – 5.02×10^{-4}
			(1-1)	24	2.75×10^{-4} – 7.84×10^{-4}
$^{17}O^{18}O$	78	$9.6(18)\times10^{-3}$	(0-0)	105	3.5×10^{-4} – 4.7×10^{-2}
$^{16}O^{18}O$	68	$7.02(92)\times10^{-3}$	(0-0)	78	2.53×10^{-4} – 3.86×10^{-2}

[a] The given intensity values include the relative abundance in the considered sample.

4. Spectrum of the $a^1\Delta_g - X\,^3\Sigma_g^-$ band of $^{16}O^{17}O$, $^{17}O^{18}O$ and $^{17}O_2$ isotopologues at 80 K

Due to the Doppler broadening, the hyperfine structure cannot be fully resolved at room temperature and shows up only as an additional broadening of the transitions of the ^{17}O containing isotopologues (Figure 2.6). In order to decrease the Doppler broadening by a factor of 2, the spectrum of the ^{17}O sample in the 7876-7893 cm^{-1} region was recorded at 80±2 K, hereafter referred as liquid nitrogen temperature (LNT) [37]. This spectral section corresponds to the low rotational transitions, which exhibit the most resolved hyperfine structure. The pressure value of the LNT recordings was fixed to 1.5 Torr.

The cryogenic cell used for the CW-CRDS recordings at liquid nitrogen temperature is described in Refs. [38]-[41]. It was developed and extensively used to characterize the absorption spectrum of methane at low temperature in the 1.7 and 1.26 μm region [38]-[41]. Briefly, it is based on an original design (see Fig. 1 of Ref. [38]) which dispenses with an external vacuum jacket by exploiting the fact that a low pressure gas sample constitutes itself a good thermal insulation. The cryostat is a 1.42 m long hollow cylinder both filled and completely surrounded by the sample gas volume. The liquid nitrogen filling the tube constitutes its single suspension point which, combined with an almost perfect cylindrical geometry, helps to eliminate stress normally present in a double-jacket cell configuration. The distance between the highly reflective mirrors and the cryostat ends is about 0.5 cm. A sensitivity equivalent to that achieved at room temperature (noise equivalent absorption $\alpha_{\min} \sim 10^{-10}$ cm^{-1}) was obtained. Coinciding temperature values (80±2 K) were obtained from the Doppler profile of methane absorption lines [38]-[39] and the rotational intensity distribution of the $3\nu_2$ band of CH_3D [41].

Figure 2.7 shows the different line profiles obtained for the R1R1 transitions of the $^{16}O_2$, $^{16}O^{17}O$ and $^{17}O_2$ isotopologues (Note that we use *ΔNN"ΔJJ"* notation). While the $^{16}O_2$ line appears as a single line with a Doppler limited profile, the $^{16}O^{17}O$ and $^{17}O_2$ lines are split in different hf components. The comparison between the 296 K and 80 K spectra shown in Figure 2.7 and Figure 2.8 illustrates the much better resolution of the hf structure at 80 K due to the reduction of the Doppler broadening (HWHM of 0.008 and 0.004 cm^{-1} at 296 K and 80 K, respectively).

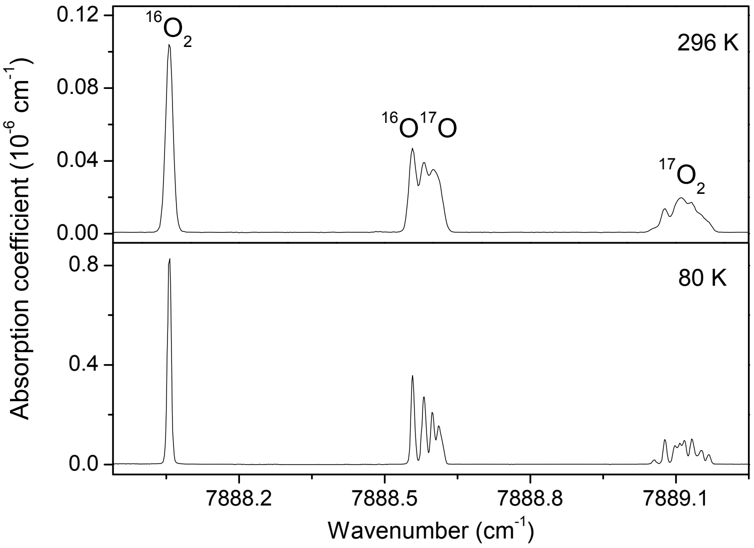

Figure 2.7. The R1R1 transition of $^{16}O_2$, $^{16}O^{17}O$ and $^{17}O_2$ at 296 and 80 K. Spectra recorded at room temperature (P=5.0 Torr) and liquid nitrogen temperature (P=1.5 Torr) are shown on the upper and lower panels, respectively.

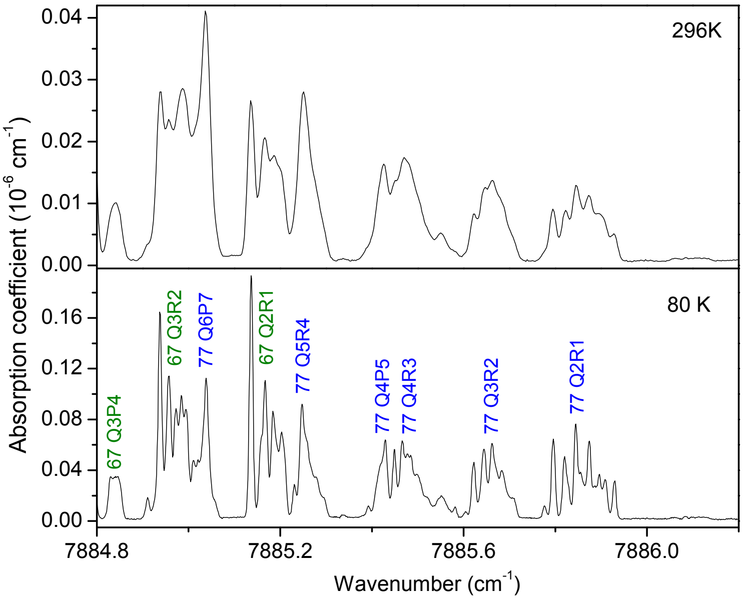

Figure 2.8. Partly resolved hyperfine structure of $^{16}O^{17}O$ and $^{17}O_2$ transitions at 296 K and 80 K in the region of the QR and QP branches. The spectra recorded at 296 K (P=5.0 Torr) and 80 K (P=1.5 Torr) are shown on the upper and lower panels, respectively.

A detailed analysis of the hf structure was performed only for the few first rotational transitions recorded at LNT because these transitions show the most resolved hf structure. Eight, six and four hf manifolds of $^{16}O^{17}O$, $^{17}O_2$ and $^{17}O^{18}O$ respectively were treated in this way. The line centres and intensities were determined using the same interactive least squares multi-line fitting program FITYK[2] as for high rotational transitions of the spectrum at room temperature.

The hyperfine structure affecting the $X\,^3\Sigma_g^-$ ground state of $^{17}O_2$, $^{16}O^{17}O$ and $^{17}O^{18}O$ was previously reported from microwave, millimetre and electron paramagnetic resonance spectroscopy (EPR) measurements [42] - [44], [46] - [47]. The observation of the ground state hyperfine structure by absorption spectroscopy in the near-infrared or visible region is particularly difficult as the Doppler width is significantly larger than hf splitting. Recently, Long et al. [44] could measure the ground hyperfine structure from an excess of the broadening of some transitions of the $b^1\Sigma_g^+ - X\,^3\Sigma_g^-$ band near 760 nm. The sub-Doppler hyperfine structure could be evidenced from a detailed study of the line profile recorded by frequency–stabilized CRDS [44]. It is important to note that the evidenced extra broadening of the $b^1\Sigma_g^+ - X\,^3\Sigma_g^-$ band transitions is due to the ground state hyperfine structure as the $b^1\Sigma_g^+$ upper electronic state is a singlet Σ state with negligible hyperfine structure, as mentioned in Section 7 of Chapter I.

In the present study devoted to the $a^1\Delta_g - X\,^3\Sigma_g^-$ band, the situation is different as the nuclear spin can couple to the electronic angular momentum of the $a^1\Delta_g$ upper state. Our spectra (for instance, Figure 2.7) show that the observed hf splitting is significantly larger than the Doppler broadening and then that the hf structure of the $a^1\Delta_g$ upper state is larger than that of the ground state. This is consistent with earlier EPR measurements of $^{16}O^{17}O$ and $^{17}O^{18}O$ species in the $a^1\Delta_g$ state [45].

5. Spectrum assignment

The assignments of the (0–0) band of $^{16}O_2$ were performed by comparison with the assignments provided in the HITRAN database. The maximum deviations between the HITRAN line positions and our observations are of the order of 3×10^{-3} cm^{-1} for the highest rotational transitions. The HITRAN intensity cutoff was fixed to 2×10^{-29} cm/molecule. Five transitions with intensities below this intensity cutoff were detected in our ^{16}O spectra.

The first assignments of the (0–0) band of $^{18}O_2$ were performed from a rough simulation (see Eq. 1.10) based on the $^{16}O_2$ band with the frequency axis scaled according to the ratio of the B rotational constants [48]. The assignments were then iteratively extended during the fit of the spectroscopic parameters, as described in the following Section 6.

---

[2] FITYK program version v0.8.6, http://sourceforge.net/projects/fityk/

The assignments of the $^{16}O^{18}O$ (0−0) band were obtained by comparison with the 2009 update of HITRAN database [19] and then iteratively extended during the fitting of the spectroscopic parameters. The assignments of the corresponding bands of the $^{16}O^{17}O$ and $^{17}O^{18}O$ isotopologues were performed by analogy with the $^{16}O^{18}O$ band, taking into account the change of the rotational constants [42], [48] (see Eq. 1.10).

In the first stage, assignments of the $a^1\Delta_g - X^3\Sigma_g^-$ (0−0) band of $^{17}O_2$ were performed from a rough simulation (see Eq. 1.10) based on the $^{16}O^{18}O$ band with the frequency axis shifted and scaled according to the ratio of the B rotational constants [43] and then iteratively extended during the fit of the spectroscopic parameters, as depicted in Section 7.

As mentioned in Section 7 of Chapter I, the electric quadrupole transitions follow the $\Delta J = \pm2, \pm1, 0$ selection rule, leading to 15 possible branches, but the $\Delta J = \pm1$ and 0 transitions coincide with much stronger magnetic dipole transitions and are not observable. Moreover, the *S*(*N*)*S*(*J*) and *O*(*N*)*O*(*J*) branches were found to be too weak to be detected in the present recordings, leaving only four observed branches for quadrupole transitions: *T(N)S(J), R(N)S(J), P(N)O(J)* and *N(N)O(J).*

As the quadrupole transitions reach upper levels, which are accessed through magnetic dipole transitions, their positions can be accurately predicted [1]. Overall, twenty three, twenty two, twelve and eight quadrupole transitions were identified for the $^{16}O_2$, $^{18}O_2$, $^{16}O^{17}O$ and $^{17}O_2$ species, respectively. Their measured line intensities range between 1×10^{-30} and 1.9×10^{-28} cm/molecule (see Table 2.3).

The achieved experimental sensitivity ($\alpha_{\min} \sim 10^{-10}$ cm^{-1}) allowed for the first detection of the (υ''= 1→ υ'= 1) hot band of $^{16}O_2$, $^{18}O_2$, $^{16}O^{17}O$ and $^{17}O_2$ which has a relative intensity of about 5×10^{-4} compared to the (0-0) band. The assignment of the $^{16}O_2$ hot band was performed on the basis of predictions obtained by means of the constants that are used in HITRAN for the $X\ ^3\Sigma_g^-$ ($\upsilon = 1$) [49] and $a^1\Delta_g$ ($\upsilon = 1$) [29] levels. The first assignments of the $^{18}O_2$ (1−1) band were performed by analogy with $^{18}O_2$ (0−0) band, taking into account the change of the rotational constants [50].

Unlike $^{16}O_2$, $^{18}O_2$ and $^{17}O_2$, to the best of our knowledge, no Raman data are available in the literature for the $^{16}O^{17}O$ isotopologue. Thus we were not able to predict line positions of the $^{16}O^{17}O$ hot band considering the change of the rotational constants, since no constants of $\upsilon = 1$ level of $X\ ^3\Sigma_g^-$ and $a^1\Delta_g$ states of the $^{16}O^{17}O$ are available. However, as pointed out in Chapter I, if the spectroscopic constants were obtained for one isotopic species of a molecule, their approximate values for the other species can be obtained from the mass-dependent relations (see Equation 1.10). Indeed, the spectrum of the other oxygen isotopologues may be predicted by determining B, D, and λ constants of $^{16}O_2$, since $B_i = \rho^2 B$, $D_i = \rho^4 D$, $\nu_i = \rho\nu$ and λ is approximately independent of the isotopic mass, where the subscript i refers to the heavier isotopic molecule and where $\rho = \sqrt{\mu / \mu^i}$ and μ is the reduced mass [51]. The vibrational frequency ν, the B and D rotational constants of the $^{16}O^{17}O$ and $^{17}O_2$ in the $a^1\Delta_g$ and $X\,^3\Sigma_g^-$ states were predicted using the $^{16}O_2$ corresponding values. The difference between the observed and calculated energy term values increases smoothly with the reduced mass of O_2 isotopologues up to vaule of 1.26 cm^{-1} for $^{18}O_2$. We used this dependence to correct the predicted energy term value of the $X\,^3\Sigma_g^-$ $(\upsilon = 1)$ of $^{16}O^{17}O$. This correction value was interpolated from the known (obs.-calc.) term value differences for the other isotopologues. As shown in Table 2.4, the agreement between the observed and estimated values of the molecular constants of the $\upsilon = 1$ levels of the $X\,^3\Sigma_g^-$ and $a^1\Delta_g$ states of the $^{16}O^{17}O$ and $^{17}O_2$ isotopologues is very satisfactory.

Thus the first assignments of the $^{16}O^{17}O$ and $^{17}O_2$ hot bands were performed on the basis of predictions obtained using the computed rovibrational constants. The assignments of these weak transitions were made possible thanks to the good accuracy of these predicted spectra: the maximum deviations between predicted and measured line positions were of the order of 30×10^{-3} cm^{-1}. Finally, we were able to assign the 39 and 69 transitions of the very weak $a^1\Delta_g - X\,^3\Sigma_g^-$ (1-1) hot band of $^{16}O^{17}O$ and $^{17}O_2$, respectively.

Table 2.4. Constants of the υ =1 levels of the $X\,^3\Sigma_g^-$ and $a^1\Delta_g$ states of $^{16}O^{17}O$ and $^{17}O_2$.

Parameters	$^{16}O^{17}O$				$^{17}O_2$			
	$X\,^3\Sigma_g^-$							
	υ =0		υ =1		υ =0		υ =1	
	Observed	Predicted	Observed	Predicted	Observed	Predicted	Observed	Predicted
E			1533.55[b]	1533.2327[a]			1510.3649(44)	1509.7202
B	1.3953322(27)	1.395212	1.380238(40)	1.37987	1.3529818(11)	1.352749	1.338575(56)	1.33787
D	$4.5615(21)\times10^{-6}$	4.5586×10^{-6}	$4.533(78)\times10^{-6}$	4.558×10^{-6}	$4.2893(19)\times10^{-6}$	4.285×10^{-6}	$4.26(14)\times10^{-6}$	4.284×10^{-6}
	$a^1\Delta_g$							
B	1.3760896(29)	1.376089	1.359745(42)	1.37596	1.3343330(13)	1.33408	1.318697(58)	1.31874
D	$4.8107(24)\times10^{-6}$	4.8053×10^{-6}	$4.783(81)\times10^{-6}$	4.823×10^{-6}	$4.5235(20)\times10^{-6}$	4.517×10^{-6}	$4.43(13)\times10^{-6}$	4.534×10^{-6}

[a] The predicted energy term value of the $X\,^3\Sigma_g^-$ (υ =1) was extrapolated from that of $^{16}O_2$ isotopologue using above mentioned dependence of the vibrational frequency versus the reduced mass.

[b] The best estimate was obtained from predicted value after correction (see text).

The overview of the $a^1\Delta_g - X\,^3\Sigma_g^-$ transitions assigned to $^{16}O_2$, $^{18}O_2$, $^{17}O_2$, $^{16}O^{17}O$ and $^{17}O^{18}O$ is presented in Figure 2.9. Note that the abundance of $^{17}O^{18}O$ in the ^{17}O spectra is almost the same as in the ^{18}O spectra, where we were able to detect 45 additional lines which are hidden by much stronger $^{16}O^{17}O$ lines in the ^{17}O recordings. As summarized in Table 2.3, a total of 376, 649 and 843 transitions of the different oxygen isotopologues were measured in the ^{16}O, ^{18}O and

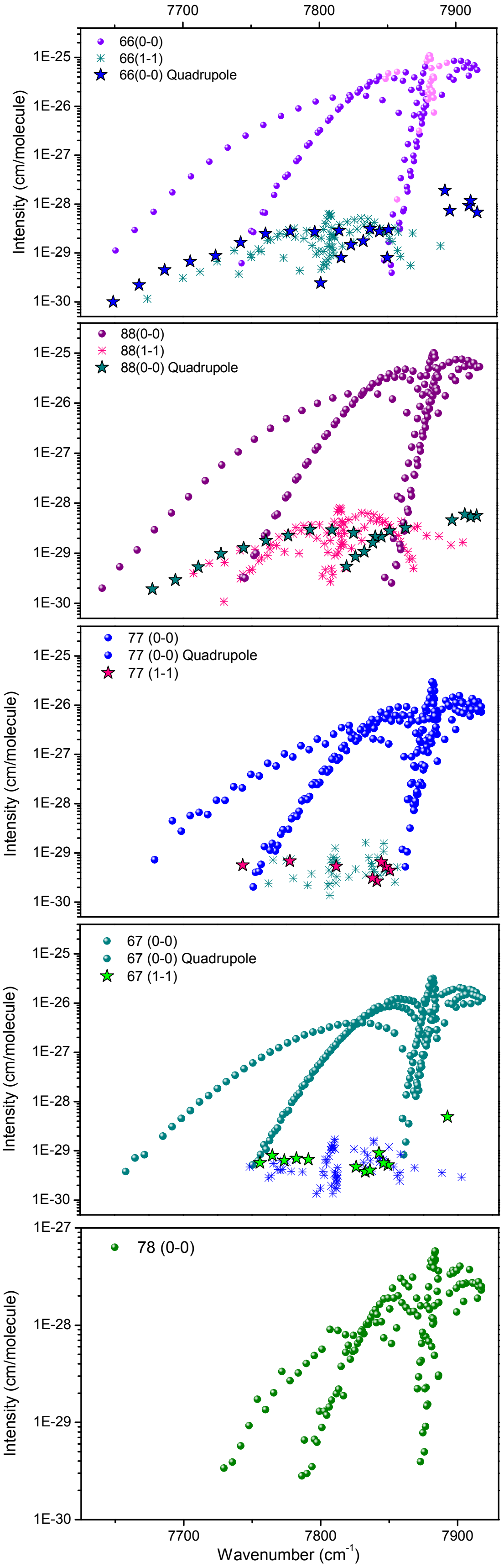

Figure 2.9. Overview of the line lists of $^{16}O_2$, $^{18}O_2$, $^{17}O_2$, $^{16}O^{17}O$ and $^{17}O^{18}O$ (from upper to lower panel, sequentially). Circles, asterisks and stars correspond to the $a^1\Delta_g - X\ ^3\Sigma_g^-$ (0–0) band, (1–1) hot band and electric quadrupole transitions, respectively. For completeness, a few lines of the $^{16}O_2$ (0–0) band (light full circles), which were saturated in the CRDS spectrum, have been replaced by the corresponding HITRAN values. In the ^{17}O sample, the relative abundances were estimated to be 0.469, 0.330 and 9.6×10^{-3} for $^{16}O^{17}O$, $^{17}O_2$ and $^{17}O^{18}O$, respectively. Note that for $^{17}O^{18}O$ the intensity scale is different.

^{17}O spectra, respectively. Their intensities span about 5 orders of magnitude between 1×10^{-30} and 1×10^{-25} cm/molecule.

The global line lists of ^{16}O, ^{18}O and ^{17}O spectra including line positions and the experimental values of the intensities corresponding to the relative abundances listed in Table 2.3 are provided as Supplementary Material of Refs. [52]–[53].

6. Spectroscopic parameter derivation: $^{16}O_2$, $^{18}O_2$ and $^{16}O^{18}O$

The present and the following Sections are devoted to the determination of the spectroscopic constants for $^{16}O_2$, $^{18}O_2$, $^{16}O^{18}O$ and ^{17}O containing isotopologues, respectively**.** Comparison of our resulting parameters with those available in the literature is given in Section 8.

The SPFIT software [54] was used to fit all the measured transitions. The ground $X\,^3\Sigma_g^-$ electronic state is represented by the effective Hamiltonian that accounts for the molecular rotation, fine structure and spin-rotation coupling with the first and the second centrifugal distortion terms:

$$H_{eff} = B\mathbf{N}^2 - D\mathbf{N}^4 + H\mathbf{N}^6 + \left[\lambda + \lambda_D\mathbf{N}^2 + \lambda_H\mathbf{N}^4\right]\frac{2}{3}\left(3S_z^2 - \mathbf{S}^2\right) + \left[\gamma + \gamma_D\mathbf{N}^2 + \gamma_H\mathbf{N}^4\right]\mathbf{N}\cdot\mathbf{S} \quad (2.1)$$

where B, λ and γ are rotational, spin-spin and spin-rotation interaction constants, respectively, while the other constants are their 1st and 2nd order centrifugal distortion terms. The rotational energies in the $a^1\Delta_g$ state were fit to a simple expression:

$$F_\upsilon(J) = T_\upsilon + B_\upsilon J(J+1) - D_\upsilon[J(J+1)]^2 + H_\upsilon[J(J+1)]^3. \quad (2.2)$$

One should note that theoretically the second order Λ–doubling term should be added to this equation (see for instance Eq. (2) from the work of Drouin et al. [48]). Nevertheless, although the Λ-doubling splitting of the rotational levels increases as $\sim J^{2\Omega}$ and for some of the isotopologues the lines with $J' \leq 43$ were observed, this splitting could not be evidenced in our experiments. This is in agreement with the findings of Drouin et al. [48] where the microwave (MW) transitions within the $a^1\Delta_g$ state involving $J \leq 23$ were measured. Although Drouin et al. did use the second order Λ-doubling constant in the fit, they found it to be largely undetermined, which (taking into account that these MW measurements [48] are very precise) leads to the conclusion that this constant is negligible.

In our work the energy origin is taken for the hypothetical $N = 0$ $J = 0$ level of the ground $X\,^3\Sigma_g^-$ state. As shown in Figure 2.10**,** the lowest energy level of $^{16}O_2$ will be 0.24584 cm^{-1} above this origin, whereas for $^{18}O_2$ and $^{16}O\,^{18}O$ it will be 0.07516 and 0.47795 cm^{-1} below this origin. If the hyperfine structure is ignored, the lowest energy level will be below this origin by value of 0.46452 cm^{-1}, 0.47975 cm^{-1} and 0.49403 cm^{-1} for $^{16}O\,^{17}O$, $^{17}O_2$ and $^{17}O\,^{18}O$, respectively.

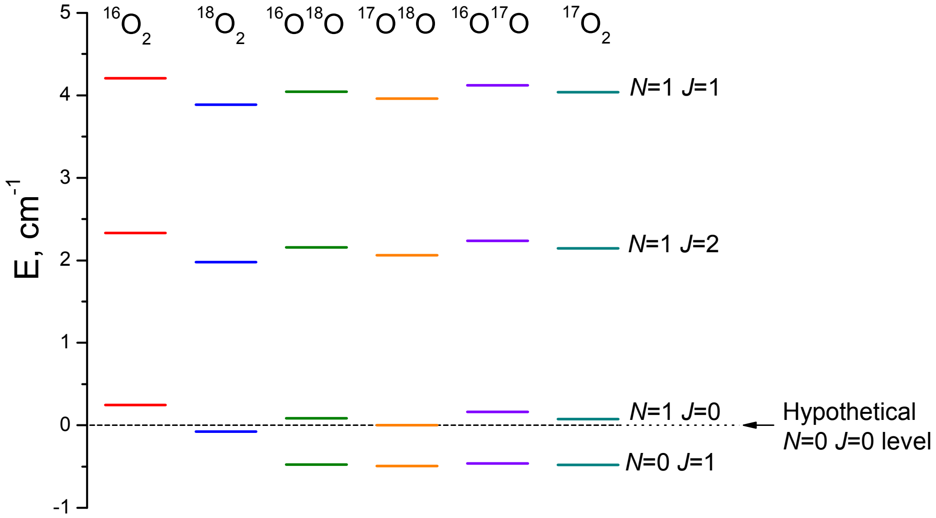

Figure 2.10. The energy origin of the $X\,^3\Sigma_g^-$ ground state for the six oxygen isotopologues.

6.1. $^{16}O_2$

The lines of the $a^1\Delta_g - X\,^3\Sigma_g^-$ (0−0) and (1−1) bands measured in this work were fitted together with lines from supplementary material of the work devoted to THz measurements by Drouin et al. [48].

In addition to transitions within the $\upsilon = 0$ ground and $a^1\Delta_g$ electronic states measured by Drouin et al, their supplementary file includes microwave measurements in the $X\,^3\Sigma_g^-$ state by Tretyakov et al. [55], Endo and Mizushima [56], Golubiatnikov and Krupnov [57], Zink and Mizushima [58] and Park et al. [59] as well as MW measurements in the $a^1\Delta_g$ state by Hillig et al. [27]. We have also included MW measurements in the $X\,^3\Sigma_g^-$ ($\upsilon = 1$) [56] and $a^1\Delta_g$ (υ= 1) [60] states. In order to connect all four vibrational states ($X\,^3\Sigma_g^-$ $\upsilon = 0,1$ and $a^1\Delta_g$ $\upsilon = 0,1$) observed in our work, stimulated Raman measurements of the fundamental band in the $X\,^3\Sigma_g^-$ state by Rouillé et al. [49] and Millot et al. [61] were also included. Note that there are also incoherent Raman measurements [62] available in the literature. However, the data available in Ref. [62] do not exceed those from Rouillé et al. [49], while the experimental uncertainty in Ref. [62] is larger. The reported experimental uncertainty was used for OO and SS branches from Ref. [49]. However, the 0.001 cm^{-1} uncertainty reported there for the QQ branch lines seems to be underestimated. The reason is that in the QQ branch of the stimulated Raman spectra the fine structure of the rotational levels is not resolved, unlike the OO and SS branches. We therefore assigned the line centres reported for the QQ branches to all three components of the transition using the option of SPFIT to include blended lines and weight them with calculated relative intensities. The results of the fit are given in Table 2.6.

Table 2.6. Spectroscopic parameters of the $\upsilon = 0$ and 1 levels of the $X\,^3\Sigma_g^-$ and $a^1\Delta_g$ states of $^{16}O_2$ and $^{18}O_2$.

<table>
<tr><th rowspan="3">Parameters</th><th colspan="6">$X\,^3\Sigma_g^-$</th></tr>
<tr><th colspan="3">$^{16}O_2$</th><th colspan="3">$^{18}O_2$</th></tr>
<tr><th colspan="2">$\upsilon = 0$</th><th>$\upsilon = 1$</th><th>$\upsilon = 0$</th><th colspan="2">$\upsilon = 1$</th></tr>
<tr><td>E^a</td><td colspan="2">-</td><td>1556.389914(147)</td><td></td><td colspan="2">1468.4442(33)</td></tr>
<tr><td>B</td><td colspan="2">1.437675974(19)</td><td>1.42186406(64)</td><td>1.278008448(57)</td><td colspan="2">1.2647600(12)</td></tr>
<tr><td>D</td><td colspan="2">4.840356(76)×10^{-6}</td><td>4.83954(42)×10^{-6}</td><td>3.82252(39)×10^{-6}</td><td colspan="2">3.82558(727)×10^{-6}</td></tr>
<tr><td>H</td><td colspan="2"></td><td></td><td>-5.20(494)×10^{-13}</td><td colspan="2"></td></tr>
<tr><td>λ</td><td colspan="2">1.984751193(50)</td><td>1.98957881(13)</td><td>1.9845955423(417)</td><td colspan="2">1.989117019(166)</td></tr>
<tr><td>λ_D</td><td colspan="2">1.946930(325)×10^{-6}</td><td>2.11277(98)×10^{-6}</td><td>1.721382(233)×10^{-6}</td><td colspan="2">1.85292(127)×10^{-6}</td></tr>
<tr><td>λ_H</td><td colspan="2">9.71(30)×10^{-12}</td><td></td><td>7.719(242)×10^{-12}</td><td colspan="2">1.614(213)×10^{-11}</td></tr>
<tr><td>γ</td><td colspan="2">-8.42537356(584)×10^{-3}</td><td>-8.445758(19)×10^{-3}</td><td>-7.48670002(457)×10^{-3}</td><td colspan="2">-7.5038322(130)×10^{-3}</td></tr>
<tr><td>γ_D</td><td colspan="2">-8.1183(223)×10^{-9}</td><td>-8.349(79)×10^{-9}</td><td>-6.4111(160)×10^{-9}</td><td colspan="2">-6.4108(267)×10^{-9}</td></tr>
<tr><td>γ_H</td><td colspan="2">4.84(153)×10^{-14}</td><td></td><td>-3.80(113)×10^{-14}</td><td colspan="2"></td></tr>
<tr><td></td><th colspan="6">$a^1\Delta_g$</th></tr>
<tr><td></td><th colspan="2">$\upsilon = 0$</th><th>$\upsilon = 1$</th><th>$\upsilon = 0$</th><th colspan="2">$\upsilon = 1$</th></tr>
<tr><td>T</td><td colspan="2">7883.756645(113)</td><td>9367.208821(267)</td><td>7886.409277(117)</td><td colspan="2">9286.2239(33)</td></tr>
<tr><td>B</td><td colspan="2">1.417839039(38)</td><td>1.40072433(17)</td><td>1.260409499(56)</td><td colspan="2">1.2460722(28)</td></tr>
<tr><td>D</td><td colspan="2">5.102256(243)×10^{-6}</td><td>5.1211(41)×10^{-6}</td><td>4.029678(664)×10^{-6}</td><td colspan="2">4.04700(827)×10^{-6}</td></tr>
<tr><td>H</td><td colspan="2">-2.395(283)×10^{-12}</td><td>-4.97(313)×10^{-12}</td><td>-1.855(617)×10^{-12}</td><td colspan="2"></td></tr>
<tr><td rowspan="2">Number of lines</td><td colspan="3">Total: 378</td><td colspan="3">Total: 359</td></tr>
<tr><td>MW: 85</td><td>Raman: 94</td><td>This work: 199</td><td>MW: 78</td><td>Raman: 26</td><td>This work: 255</td></tr>
<tr><td>rms</td><td>3.48×10^{-2} MHz</td><td>2.48×10^{-3} cm^{-1}</td><td>1.13×10^{-3} cm^{-1}</td><td>2.48×10^{-2} MHz</td><td>68.1×10^{-3} cm^{-1}</td><td>7.7 ×10^{-4} cm^{-1}</td></tr>
</table>

[a] The energy origin is taken for the hypothetical $N = 0$ $J = 0$ level of the symmetric species of the ground $X\,^3\Sigma_g^-$ state (see Figure 2.10). The lowest energy level of $^{16}O_2$ will be 0.24584 cm^{-1} above this origin, whereas for $^{18}O_2$ it will be 0.07516 cm^{-1} below (see Figure 2.10).

Table 2.6 includes the *rms* values of the fit corresponding to the different experimental sources (MW, Raman and this work): $rms = \sqrt{\dfrac{\sum_i (\sigma_{obs} - \sigma_{calc})_i^2}{N - p}}$, where the summation applies to the N experimental data of a given source and p is the number of fitted parameters. The *rms* value for our data is 1.13×10^{-3} cm^{-1} which is in agreement with our experimental uncertainty.

6.2. $^{18}O_2$

In the same manner as the principal isotopologue, $^{18}O_2$ line positions of the $a^1\Delta_g - X\,^3\Sigma_g^-$ (0-0) and (1-1) bands observed in this work were fitted together with line positions from supplementary material of work by Drouin et al. [48], which also contains measurements within the $\upsilon = 0$ state of $X\,^3\Sigma_g^-$ by Endo and Mizushima [63] and Steinbach and Gordy [64]. In addition we have included the measurements within the $X\,^3\Sigma_g^-$ $(\upsilon = 1)$ state [63] and within the $a^1\Delta_g$ $(\upsilon = 0)$ state [60]. Raman measurements of the fundamental band in the $X\,^3\Sigma_g^-$ state by Edwards et al. [50] were also included to connect vibrational levels in both electronic states. Unlike the

Raman measurements of $^{16}O_2$ by Rouillé et al. [49], the fine structure was not resolved by Edwards et al. not only for the QQ branch but also for the OO and SS branches. We therefore assigned large uncertainties (up to 0.05 cm^{-1}) to the Raman line centers. This resulted in a less accurate determination of the absolute energy term values of $X\ ^3\Sigma_g^-\ (\upsilon = 1)$ and $a^1\Delta_g\ (\upsilon = 1)$ states than for $^{16}O_2$. The results of the fit are summarized in Table 2.6. The *rms* values of the Raman data and of our near-infrared data (6.8×10^{-2} and 7.7×10^{-4} cm^{-1}, respectively) reflect the accuracy of the two experimental sources.

6.3. $^{16}O^{18}O$

$^{16}O^{18}O$ transitions were observed in the spectrum of each of the three samples. However, the spectrum of the ^{18}O sample had more $^{16}O^{18}O$ lines as a result of a higher relative concentration (see Table 2.3). These were used as a primary source of the measured data. We did, however, add a few $^{16}O^{18}O$ lines from the $^{16}O_2$ spectra when the corresponding transitions were blended in the $^{18}O_2$ spectra. Once again, the supplementary material of work by Drouin et al. [48] was employed in the fit together with our measurements. For $^{16}O^{18}O$, that file also contains measurements within the $X\ ^3\Sigma_g^-\ (\upsilon = 0)$ state by Amano and [65], Mizushima and Yamomoto [30], Steinbach and Gordy [66] and Crownover et al. [67]. We have also added the MW measurements within $a^1\Delta_g\ (\upsilon = 0)$ state by Cohen et al. [60]. The results of the fit are summarized in Table 2.7.

Table 2.7. Spectroscopic parameters of the $\upsilon = 0$ level of the $X\,^3\Sigma_g^-$ and $a^1\Delta_g$ states of $^{16}O^{18}O$.

Parameters	$\mathbf{^{16}O^{18}O}$	
	$X\,^3\Sigma_g^-$	
B		1.3578522686(414)
D		$4.31692(53)\times10^{-6}$
$\boldsymbol{\lambda}$		1.984674291(162)
$\boldsymbol{\lambda_D}$		$1.833535(842)\times10^{-6}$
$\boldsymbol{\lambda_H}$		$9.50(81)\times10^{-12}$
$\boldsymbol{\gamma}$		$-7.956001(11)\times10^{-3}$
$\boldsymbol{\gamma_D}$		$-7.318(15)\times10^{-9}$
	$a^1\Delta_g$	
$\boldsymbol{T^a}$		$7885.06789(13)^b$
B		1.33913493(10)
D		$4.552623(674)\times10^{-6}$
Number of lines	MW: 85	This work: 208
rms	6.73×10^{-2} MHz	0.69×10^{-3} cm^{-1}

[a] The energy origin is taken for the level $N = 0$, $J = 0$ of the ground $X\,^3\Sigma_g^-$ state. The lowest energy level of $^{16}O^{18}O$, is 0.47795 cm^{-1} below this origin (see Figure 2.10).

[b] The term value used in HITRAN was 7885.06858 cm^{-1} based on the unpublished FTS data of Brault [29].

The results of the fit of the spectroscopic parameters of the $^{16}O_2$, $^{16}O^{18}O$ and $^{18}O_2$ isotopologues are provided as Supplementary Material of Ref. [52]. These supplementary files include the complete set of wavenumber values used to refine the parameters together with the corresponding fitted values and the references.

7. Spectroscopic parameter derivation: $^{16}O^{17}O$, $^{17}O^{18}O$ and $^{17}O_2$

As mentioned in Chapter I, while ^{16}O and ^{18}O isotopes of oxygen have a nuclear spin $I = 0$, ^{17}O has a non-zero nuclear spin $I = 5/2$. The coupling of this nuclear spin to electron spin in the $X\,^3\Sigma_g^-$ state and to the electronic angular momentum in the $a^1\Delta_g$ state gives rise to a magnetic hyperfine structure. Thus this Section comprises two parts. Firstly, we describe the form of hyperfine interaction in the $X\,^3\Sigma_g^-$ and $a^1\Delta_g$ states in detail. Secondly, we derive the spectroscopic parameters for the $X\,^3\Sigma_g^-$ and $a^1\Delta_g$ states of $^{16}O^{17}O$, $^{17}O^{18}O$ and $^{17}O_2$ from a global fit including hyperfine coupling parameters.

7.1. The hyperfine structure of the $a^1\Delta_g - X\,^3\Sigma_g^-$ transitions

The Hamiltonian for the three ^{17}O isotopologues can be expressed as [42]−[43]:

$$H = H_{RFS} + H_{HFS} \tag{2.3}$$

where H_{RFS} corresponds to the rotational and fine structure terms and H_{HFS} to the hyperfine term.

The expression of H_{RFS} in the ground $X\,^3\Sigma_g^-$ and upper $a^1\Delta_g$ electronic states is given by Equations 2.1 and 2.2, respectively.

The general expression of the hyperfine structure Hamiltonian can be written as:

$$H_{HFS} = aI_zL_z + b_F I\cdot S + c(I_zS_z - \frac{1}{3}I\cdot S) + \frac{eQq(3I_z^2 - I^2)}{4I(2I-1)}, \tag{2.4}$$

where the first term describes the interaction of the electronic orbital moment with the nuclear spin, the second and third terms represent the isotropic (Fermi contact interaction) and anisotropic parts of the electron spin-nuclear spin coupling, respectively. The fourth term represents the electric quadrupole interaction due to asymmetric charge distribution around the nucleus. The hyperfine coupling constants are defined by:

$$\begin{aligned} a &= 2g_I\mu_0\mu_I\left(\frac{1}{r^3}\right)_{av}, \\ b_F &= \frac{16\pi}{3}g_I\mu_0\mu_I\psi^2(0), \\ c &= 3g_I\mu_0\mu_I\left(\frac{3\cos^2\vartheta - 1}{r^3}\right)_{av}, \end{aligned} \tag{2.5}$$

where g_I is the nuclear *"g"* factor, μ_0 is the Bohr magneton, μ_N is the nuclear magneton, r being the distance between he unpaired electron and the ^{17}O nucleus and θ being the angle between the **r** vector and the internuclear axis, $\psi^2(0)$ is the probability of the electron to be found at the nucleus and the averaging is over space coordinates for the states in question. The constant a refers only to electrons with orbital angular momentum. The Fermi contact parameter b_F describes the contribution from the electron density at the nucleus, whilst c is associated with angular spin distributions.

The evaluation of the energy resulting from the equation (2.4) depends on the coupling scheme which implies the particular case of interaction. In the $X\,^3\Sigma_g^-$ ground state, the interaction between nuclear magnetic moment of ^{17}O and the magnetic field associated with spin angular momentum **S** gives rise to the magnetic hyperfine structure which follows ($b_{\beta J}$) coupling case, shown in Figure1.4(b) (Section 5 of Chapter I). In this state $\Lambda = 0$ and therefore the first term vanishes in Equation 2.4. The two other terms lead to the hf splitting of each (N, J) rotational level in different components:

$$\begin{aligned} W(F_1) &= \frac{\mathbf{IJ}}{(N+1)}\left\{b_F + c\frac{2N}{(2N+3)}\right\}, \\ W(F_2) &= \frac{\mathbf{IJ}}{\mathrm{N}(N+1)}\left(b_F + \frac{2}{3}c\right), \\ W(F_3) &= \frac{\mathbf{IJ}}{N}\left\{-b_F + c\left(\frac{2N+2}{2N-1}\right)\right\}, \end{aligned} \tag{2.6}$$

where $\mathbf{IJ} = 1/2[F(F+1)-I(I+1)-J(J+1)]$ with $F= J+I, J+I-1, \ldots|J-I|$ and F_1, F_2 and F_3 correspond to $J=N+1$, $J=N$ and $J=N-1$, respectively. Note that Equation 2.6 ignores small contribution due to quadrupole coupling.

As mentioned in Section 7 of Chapter I, the selection rules for $^{16}O^{17}O$, $^{17}O^{18}O$ and $^{17}O_2$ magnetic dipole transitions are $\Delta J = 0, \pm 1$ and $\Delta F = 0, \pm 1$. For the high J values, only the hyperfine transitions with $\Delta F = \Delta J$ are significant and the intensities are proportional to $(2F+1)$ [68]. The allowed transitions of the R1R1 line together with the corresponding experimental spectrum of $^{16}O^{17}O$, $^{17}O^{18}O$ and $^{17}O_2$ are included in Figure 2.11 and Figure 2.12. Since the hyperfine coupling terms are identical for $^{16}O^{17}O$ and $^{17}O^{18}O$, the observed hf structures are very similar, as shown in Figure 2.11. Only the strongest of the 39 hyperfine components are represented in Figure 2.12 for clarity.

In the case of the $^{16}O^{17}O$ and $^{17}O^{18}O$ species, $I = 5/2$ and then $F= J + 5/2, J + 3/2, \ldots |J-5/2|$. The rotational levels are then split into six components for $J > 2$. Figure 2.11 shows the hyperfine splitting in the lower ($N'' = J'' = 1$) and upper ($N' = J' = 2$) states of the R1R1 transition of $^{16}O^{17}O$ and $^{17}O^{18}O$. The hyperfine energy levels were calculated using Equations 2.6 and 2.7 for upper and lower states, respectively.

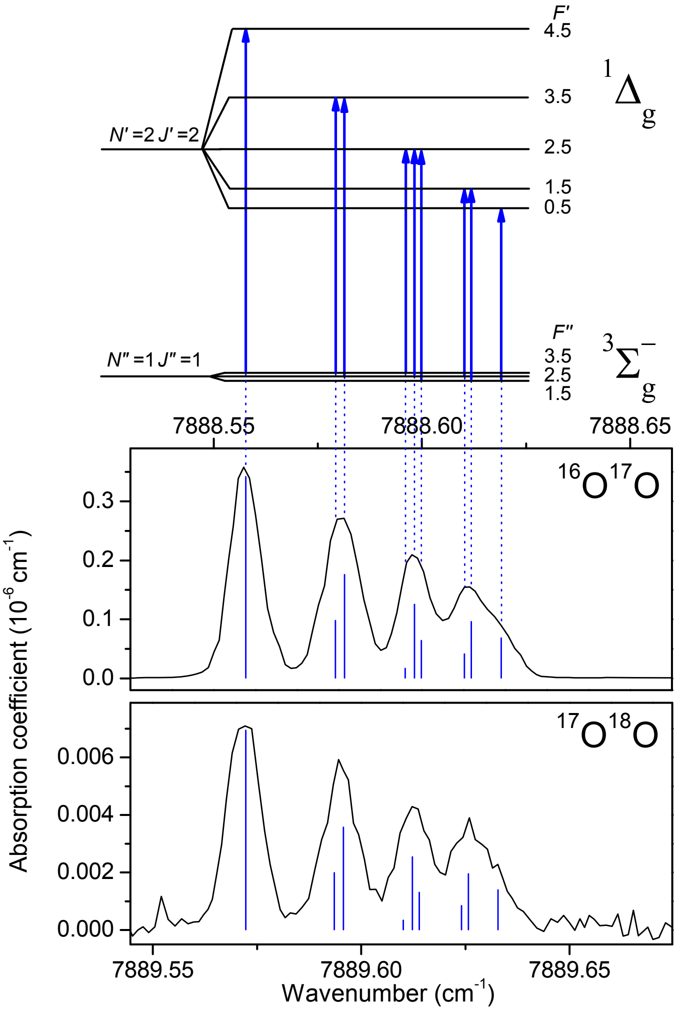

Figure 2.11. Energy diagram and spectrum of the hyperfine structure of the R1R1 transition $^{16}O^{17}O$ and $^{17}O^{18}O$ in the spectrum recorded at 80K. Note that the Λ-doubling is unresolved in the present experiment. The stick spectrum corresponds to the calculated hf structure.

In the case of the $^{17}O_2$ isotopologue, the vectorial addition of the two nuclear spins ($I_1 = I_2 = 5/2$) leads to six values of the total nuclear spin $I_{tot} = I_1 + I_2, \ldots, |I_1 - I_2| = 5, 4, 3, 2, 1, 0$. In the $X\,^3\Sigma_g^-$ ground state the even and odd values of N'' can only be associated with odd and even values of I''_{tot}, respectively, because of the nuclear spin function symmetry [42]. Figure 2.12 shows the hyperfine splitting in the lower and upper states of the R1R1 transition. The N'' =1 level can be associated only with I'' = 0, 2, 4 and then F'' = 1, 2, 3, 4 and 5, while in the N' = 2, upper state, the six I' values (0-5) are possible and then F' varies from zero to seven.

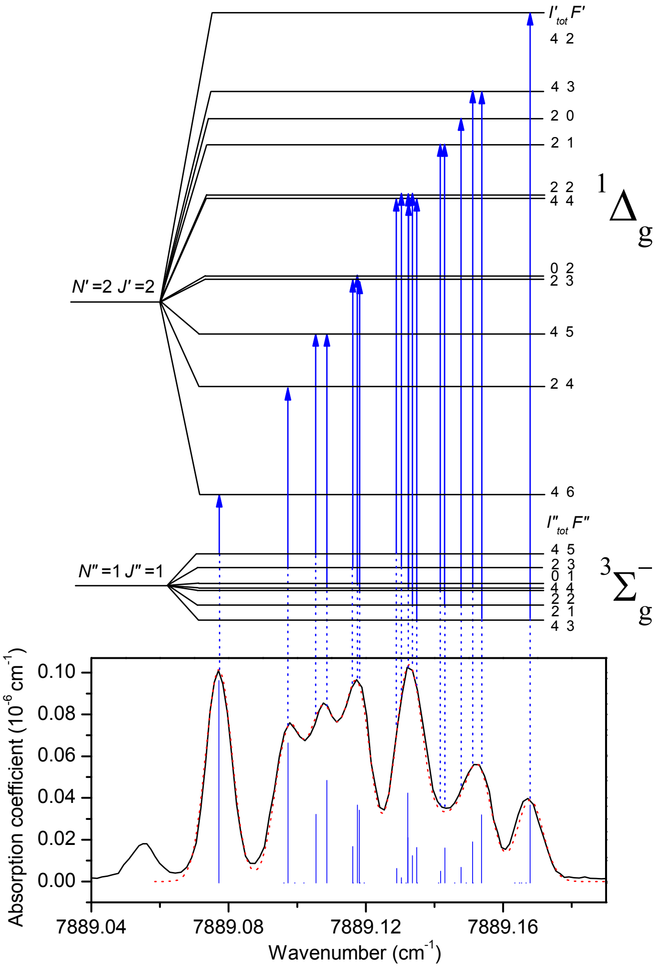

Figure 2.12. Energy diagram and spectrum at 80 K of the hyperfine structure of the R1R1 transition of $^{17}O_2$. The black solid line corresponds to the experimental spectrum while the red dashed line is a simulation based on the calculated hf structure (stick spectrum). Note that the energy scale of the hyperfine levels corresponds to the wavenumber scale of the spectrum. The line on the left hand side of the spectrum is a $^{16}O^{18}O$ transition. The upper state hf levels with odd I_{tot}, to which no transitions are allowed from the lower N''=J''=1, are ignored in this figure for clarity.

The $a^1\Delta_g$ upper state is a singlet state ($S = 0$), so that only the first and fourth interaction terms remain in Equation 2.4. This $a^1\Delta_g$ state obeys the Hund's electronic case (a) coupling. The magnetic hyperfine structure for the $a^1\Delta_g$ is given by the coupling case a_β, shown in Figure1.4(a) in Chapter I, and the dominant magnetic part of the hyperfine operator simplifies to yield the hyperfine energy [69]:

$$W = a\Lambda\Omega \mathbf{IJ} / J(J+1), \tag{2.7}$$

with $\Lambda = \Omega + \Sigma$, which is equal to $\Lambda = 2$, as $\Sigma = 0$. From this expression, it is obvious that the hyperfine component separations decrease when J increases i.e. that, in the different branches, transitions from the first rotational levels are expected to show the most resolved hf structure. As an example, Figure 2.13 and Figure 2.14 illustrate the evolution of the hf structure with an increasing rotational excitation for $^{16}O^{17}O$ and $^{17}O_2$, respectively: the hf structure is partly resolved for the first N, J rotational levels but shows up as a small extra broadening for N, J values larger than 10. It is worth mentioning that Λ-doubling could not be resolved in the present experiment.

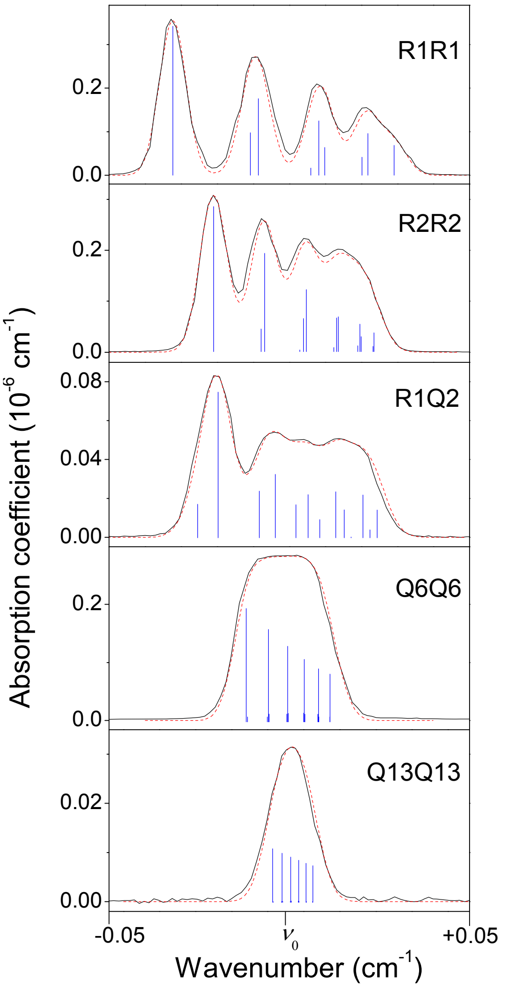

Figure 2.13. The hyperfine structure of different $^{16}O^{17}O$ transitions (T=80 K, P=1.5 Torr). The wavenumber values (ν_0) that correspond to the centre of the spectral range of each panel are the following: R1R1 - 7888.5906, R2R2 – 7891.2606, R1Q2 – 7890.4704, Q6Q6 – 7882.3106 and Q13Q13 – 7879.6066 cm^{-1}. Black solid line corresponds to the experimental spectrum while red dashed line is a simulation based on the calculated stick spectrum (in blue).

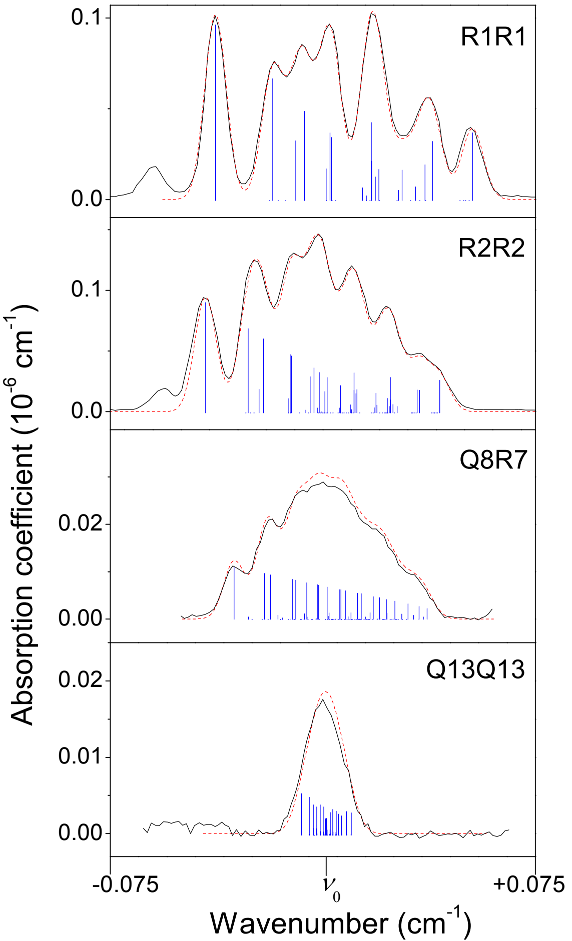

Figure 2.14. The hyperfine structure of different $^{17}O_2$ transitions (T=80 K, P=1.5 Torr). The wavenumber values (ν_0) that correspond to the centre of the spectral range of each panel are the following: R1R1 – 7889.1152, R2R2 – 7891.7151, Q8R7 – 7884.4304 and Q13Q13 – 7880.4153 cm^{-1}. On the two upper panels the features on the left hand side are $^{16}O^{18}O$ transitions. Black solid line corresponds to the experimental spectrum while red dashed line is a simulation based on the calculated stick spectrum (in blue).

7.2. Band-by-band fit

Our detailed experimental investigation of the $a^1\Delta_g - X^3\Sigma_g^-$ system of the three ^{17}O containing oxygen isotopologues – $^{16}O^{17}O$, $^{17}O^{18}O$ and $^{17}O_2$ – was performed in two steps.

Firstly, we used the $^{16}O^{17}O$ transitions observed in the spectrum of the ^{16}O sample and transitions of $^{17}O^{18}O$ in the ^{18}O spectrum, respectively [52]. These transitions were very weak because of the low relative concentration (Table 2.3), which increased the experimental uncertainty of line centres determination. Furthermore, as mentioned in Section 3 of the current Chapter, the line profiles of some transitions of $^{16}O^{17}O$ and $^{17}O^{18}O$ were observed to be broadened due to an unresolved hyperfine structure (see Figure 2.6). Therefore, the hyperfine splitting of the energy levels is sufficient to broaden the line profile, but insufficient to be completely resolved under our experimental conditions. In order to minimize the negative effect of unresolved hyperfine structure, the line positions were taken as the average value over the line profile of the wavenumbers weighted by the corresponding absorption coefficient. As a consequence, the uncertainties assigned to the $^{16}O^{17}O$ and $^{17}O^{18}O$ transitions were increased up to 3×10^{-3} cm^{-1}.

The MW lines from Cazzoli et al [42] were fit together with electronic transitions. It was found that the value of centrifugal distortion constant D reported by Cazzoli et al. is not accurate enough, since it is an estimate based on isotopic scaling of the well known value for $^{16}O_2$. As a result of the combined fit, the centrifugal distortion constant D in the ground state was particularly improved. This is proved by the results of the fit that included only the data from Ref. [42] (see Table 5 in Ref. [52]). The ground state constants were then fixed to the values obtained in the results of the new fit and the fit of only electronic transitions measured in our work was performed. In such a way we determined previously unavailable constants for the $a^1\Delta_g$ state of $^{16}O^{17}O$ and $^{17}O^{18}O$, which are listed in Table 4 in Ref. [52] and are not reproduced here.

Secondly, the spectra of ^{17}O highly enriched sample were recorded both at room (RT) and at liquid nitrogen temperatures, thus we were able to extend the observations of $^{16}O^{17}O$, $^{17}O^{18}O$ and $^{17}O_2$ isotopologues taking into account the hyperfine structure. The narrowing by a factor of 2 of the Doppler width at 80 K compared to room temperature was decisive to (partly) resolve and interpret the hf structure. In the first iteration, we focused on the derivation of the hyperfine coupling constants and the LNT data set was combined with the MW measurements from Cazzoli et al. [42]–[43]. As mentioned in Section 4 of the current Chapter, only the lowest rotational transitions of the LNT spectra were used as the hf structure of higher rotational transitions is mostly unresolved. In case of blended lines, we assigned all the underlying components of sufficient intensity (more than 1%) to one line center and weighted them according to their calculated relative intensities. The rotational part of the Hamiltonian in the ground $X\,^3\Sigma_g^-$ and upper $a^1\Delta_g$ electronic states were fit to Equations 2.1 and 2.2, respectively. Since only few low rotational transitions were considered, the centrifugal distortion constants could not be determined and were held fixed to the values determined in first stage of our study for $^{16}O^{17}O$ and $^{17}O^{18}O$ isotopic species and to the values from Ref. [70] for $^{17}O_2$. Then we completed the input data with the RT data set. Using the SPFIT option which allows one to exclude these lines from the fit of the hf parameters, the global fit including all the transitions of the (0-0) band and (1-1) hot band, was performed and provided both the hf coupling constants and the rotational constants (including the centrifugal distortion constants).

As mentioned above, the RT line positions were taken as an average value over the line profile. In consequence, the uncertainties assigned to the $^{17}O_2$, $^{16}O^{17}O$ and $^{17}O^{18}O$ transitions were increased up to 10×10^{-3} cm^{-1} for some low J values.

The $^{17}O_2$ lines of the $a^1\Delta_g - X\,^3\Sigma_g^-$ (0-0) band measured in this work were fitted together with MW lines from Cazzoli et al. [43]. The lines of the $a^1\Delta_g - X\,^3\Sigma_g^-$ (1-1) band together with Raman measurements of the fundamental band in the $X\,^3\Sigma_g^-$ state [50] were fitted separately, because even the fine structure was not resolved by Edwards et al. [50]. In this fit we fixed the constants of the $\upsilon = 0$ levels of the $X\,^3\Sigma_g^-$ and $a^1\Delta_g$ states to their fitted values and excluded the hf parameters. Raman line centres were included in the fit with large uncertainties (0.015 cm^{-1}).

Unlike $^{17}O_2$, to the best of our knowledge no Raman data are available in the literature for the $^{16}O^{17}O$ species. Thus we were not able to determine the absolute energy term values of the $X\,^3\Sigma_g^-$ (υ =1) and $a^1\Delta_g$ (υ =1) states. The $^{16}O^{17}O$ lines of the $a^1\Delta_g - X\,^3\Sigma_g^-$ (0-0) and (1-1) bands were fitted separately and the energy term value of the $X\,^3\Sigma_g^-$ (υ =1) level was fixed to the corrected calculated value (1533.55 cm^{-1}), as mentioned in Section 5 of this Chapter.

Due to the low abundance of $^{17}O^{18}O$ in the ^{17}O sample (about 1%), the $^{17}O^{18}O$ transitions are very weak which increased the experimental uncertainty in the line position values. The $^{17}O^{18}O$ lines from the ^{17}O spectra were used as the primary source of the input data of the fit and then were completed by 45 lines which were previously measured in the ^{18}O enriched spectrum and are blended or hidden in the ^{17}O spectra.

The results of the fit are given in Table 2.7. The corresponding *rms* values relative to our data (2.07×10^{-3}, 2.08×10^{-3} and 2.39×10^{-3} cm^{-1} for $^{17}O_2$, $^{16}O^{17}O$ and $^{17}O^{18}O$, respectively) are satisfactory, considering the large uncertainty in some line centres.

Note that we have tried to fit the quadrupole coupling constant of the $a^1\Delta_g$ (last term in Eq. 2.4) but it could not be well determined. The corresponding constant in the ground state of

$^{16}O^{17}O$ and $^{17}O^{18}O$ is about -8 MHz and according to the calculations of Minaev and Minaeva [71] it should be similar in the excited state and then too small to be determined from our near-infrared spectra.

We have superimposed to the spectra of Figure 2.12−Figure 2.14 a simulation of the hyperfine structure calculated with the fitted parameters values. The simulated spectra were obtained by affecting a Doppler line profile (at 80 K) to the stick spectrum provided by the SPFIT software [54]. It leads to a very good agreement between the measured and calculated spectra.

The results of the fit of the spectroscopic parameters of the $^{16}O^{17}O$, $^{17}O^{18}O$ and $^{17}O_2$ isotopologues are provided as Supplementary Material of Refs. [52], [53]. The supplementary files include the complete set of wavenumber values measured in this work together with microwave and Raman measurements when available and the corresponding (obs.-calc.) values. The files relative to the $^{16}O^{17}O$ and $^{17}O^{18}O$ species in [52] include the results of the new fit of Cazzoli et al microwave measurements [42].

Table 2.7. Spectroscopic parameters (cm^{-1}) of the $\upsilon = 0$ and $\upsilon = 1$ levels of the $X\,^3\Sigma_g^-$ and $a^1\Delta_g$ states of $^{16}O^{17}O$, $^{17}O^{18}O$ and $^{17}O_2$.

Parameters	$X\,^3\Sigma_g^-$				
	$^{16}O^{17}O$		**$^{17}O^{18}O$**	**$^{17}O_2$**	
	$\upsilon = 0$	**$\upsilon = 1$**	**$\upsilon = 0$**	**$\upsilon = 0$**	**$\upsilon = 1$**
E		[a]			1510.3649(44)
B	1.3953322(27)	1.380238(40)	1.3154953(23)	1.3529818(11)	1.338575(56)
D	$-4.5615(21)\times10^{-6}$	$-4.533(78)\times10^{-6}$	$-4.0535(39)\times10^{-6}$	$-4.2893(19)\times10^{-6}$	$-4.26(14)\times10^{-6}$
λ	1.98471099(30)	1.98849(82)	1.98463272(69)	1.98466915(12)	1.9860(12)
λ_D	$1.8885(37)\times10^{-6}$		$1.7835(95)\times10^{-6}$	$1.82771(88)\times10^{-6}$	
γ	$-8.176545(78)\times10^{-3}$	$-8.207(63)\times10^{-3}$	$-7.70714(12)\times10^{-3}$	$-7.927372(21)\times10^{-3}$	$-8.23(11)\times10^{-3}$
γ_D	$-6.99(58)\times10^{-9}$		$-7.3(12)\times10^{-9}$	$-7.199(88)\times10^{-9}$	
b_F	$-1.82607(31)\times10^{-3}$		$-1.82610(70)\times10^{-3}$	$-1.826529(78)\times10^{-3}$	
c	$4.67255(79)\times10^{-3}$		$4.6729(20)\times10^{-3}$	$4.67116(21)\times10^{-3}$	
eQq	$-2.713(80)\times10^{-4}$		$-2.74(16)\times10^{-4}$	$-2.769(13)\times10^{-4}$	
	$a\,^1\Delta_g$				
	$\upsilon = 0$	**$\upsilon = 1$**	**$\upsilon = 0$**	**$\upsilon = 0$**	**$\upsilon = 1$**
T	7884.45452(11)	7812.63054(91) [b]	7885.78877(16)	7885.15500(12)	9324.8176(48)
B	1.3760896(29)	1.359745(42)	1.2973722(28)	1.3343330(13)	1.318697(58)
D	$-4.8107(24)\times10^{-6}$	$-4.783(81)\times10^{-6}$	$-4.2743(47)\times10^{-6}$	$-4.5235(20)\times10^{-6}$	$-4.43(13)\times10^{-6}$
a	$-7.250(65)\times10^{-3}$		$-7.055(87)\times10^{-3}$	$-7.069(42)\times10^{-3}$	
Number of lines [c]	Total: 345		Total: 180	Total: 793	
	MW: 59 This work [d]: 218	This work: 68	MW: 30 This work [d]: 155	MW: 516 This work [d] : 215	Raman: 23 This work: 39
rms [f]	4.48×10^{-2} MHz 2.08×10^{-3} cm^{-1}	2.49×10^{-3} cm^{-1}	5.58×10^{-2} MHz 2.39×10^{-3} cm^{-1}	7.11×10^{-2} MHz 2.07×10^{-3} cm^{-1}	9.75×10^{-3} cm^{-1} 3.03×10^{-3} cm^{-1}

[a] The energy term value of $X\,^3\Sigma_g^-$ ($\upsilon = 1$) was estimated to be $E = 1533.55$ cm^{-1} using the corresponding value of $^{16}O_2$ and the mass dependence of the vibrational frequency.

[b] Difference between the energy term values of the υ=1 levels in the ground X $^3\Sigma_g^-$ and excited $a^1\Delta_g$ states.

[c] Microwave (MW) and Raman data were taken from Refs. [42] – [43] and Ref. [50], respectively.

[d] The hyperfine components were not counted; one hf manifold was considered as one line.

[f] $rms = \sqrt{\dfrac{\sum_i (\sigma_{obs} - \sigma_{calc})_i^2}{N - p}}$, where the summation applies to the N experimental data of a given source and p is the number of fitted parameters.

8. Discussion

In the present Section we compare the spectroscopic parameters of the $a^1\Delta_g - X\,^3\Sigma_g^-$ band of oxygen obtained in our work to the values available in the literature. The first part is devoted to rotational and fine-structure parameters and second one deals with hyperfine coupling parameters.

Rotational and fine-structure parameters

In Table 2.8, the $a^1\Delta_g$ state constants of $^{16}O_2$ are compared with those from Amiot and Vergès [11], Rothman [72], Cheah et al. [17], Drouin et al. [48] and with the constants used to generate the most recent HITRAN line list [19].

Table 2.8. Comparison of the spectroscopic parameters of the $\upsilon = 0$ and 1 levels of the $a^1\Delta_g$ state of $^{16}O_2$.

Parameters	**$a^1\Delta_g$ state of $^{16}O_2$**					
	This work	**Amiot and Vergès [11]**	**Rothman [72]**	**Cheah et al. [17]**[c]	**Drouin et al. [48]**[c]	**HITRAN**[d]
T_0	7883.756645(113)[a]	7883.76179(28)[a]	7882.4288(3)[b]	7888.107842(86)[b]		7883.75639[a]
B_0	1.417839039(38)	1.41784020(82)	1.4178442(19)	1.41780381(90)	1.417798185(45)	1.41779818[c]
D_0	5.102256(243)×10^{-6}	5.1769(56)×10^{-6}	5.1074(24)×10^{-6}	5.11144(139) ×10^{-6}	5.10196(34) ×10^{-6}	5.10210[c]
H_0	-2.395(283)×10^{-12}	1.589(89)×10^{-10}			-2.79(41)×10^{-12}	
T_1	9367.208821(267)[a]		9365.881(28)[b]			9367.20879[a]
B_1	1.40072433(17)		1.40051(42)			1.4007253
D_1	5.1211(41)×10^{-6}		4.35(1.22)×10^{-6}			5.1263×10^{-6}
H_1	-4.97(313)×10^{-12}					

[a] The energy origin is taken for the hypothetical $N = 0$, $J = 0$ level of the ground $X\,^3\Sigma_g^-$ state.

[b] The energy origin is taken for the level $N = 0$, $J = 0$ of the ground $X\,^3\Sigma_g^-$ state (see text for details).The difference between the $N = 1$, $J = 0$ and hypothetical $N = 0$, $J = 0$ levels is 0.24584 cm^{-1} (see Figure 2.10).

[c] They used Hamiltonian contains $[J(J+1) - \Omega^2]$ rather than just $J(J+1)$ used in this work (Eq.2.2).

[d] Constants taken from the program that was used to generate the most recent HITRAN line list. The rotational constants in the v=0 state are those from Hillig et al. [27], rotational constants in the v=1 state and all term values are based on the unpublished FTS data of Brault [29].

It is worth mentioning that in Ref. [72], experimental values from Amiot and Vergès [11] were fit together with (0-0) band higher rotational levels observed in the Venus spectra of Ref. [73] and (1-0) transitions from the Liège Atlas data [74]. Significant differences can be immediately noted in term energies (T) of $a^1\Delta_g$ determined in Refs. [17], [72] and the ones determined in Ref. [11]. The values from Ref. [17] were derived using a different Hamiltonian than Eq. (2.2) of the present work. Cheah et al. [17] used $[J(J+1) - \Omega^2]$ whereas we used just $J(J+1)$. Also, Cheah et al. [17] and Rothman [72] have taken the zero point energy for the first existing energy level in the symmetric species of oxygen of the ground state ($N = 1$, $J = 0$), whereas in this work and the work of Amiot and Vergès [11], the hypothetical $N = 0$, $J = 0$ level for these species was taken as zero (see Figure 2.10). Another interesting observation is that the distortion constants H in this work and Ref. [11] are not only significantly different in magnitude but also in sign. Finally, one can note that the line positions from Ref. [17] are systematically larger than ours by ~ 0.02 cm^{-1} with a maximum deviation of 0.050 cm^{-1} for one line of the QQ branch. It is difficult to explain this discrepancy but the line positions measured here agree well if calibrated using HITRAN water (present as impurities in our samples) or HITRAN oxygen lines, which provides confidence in our measurements.

Table 2.9 gives the comparison of the spectroscopic parameters for the $X\ ^3\Sigma_g^-$ state of $^{16}O^{18}O$ and $^{18}O_2$ obtained in this work to those published by Drouin et al. [48], Mizusima and Yamamoto [30], Endo and Mizusima [63]. It is not surprising that the parameter values and the corresponding uncertainties agree very well as we included these measurements in our fit procedure. The values of B and D constants for the $a^1\Delta_g$ upper state obtained in our study are compared with those obtained by Cohen et al. [60] in Table 2.9, as well. The improvements are significant, since only a few pure rotational transitions of $^{16}O^{18}O$ and $^{18}O_2$ in their $a^1\Delta_g$ $\upsilon = 0$ state were measured in work of Cohen et al. [60].

Table 2.9. Comparison of the spectroscopic parameters (MHz) in the $X\,^3\Sigma_g^-$ and $a^1\Delta_g$ states of $^{16}O^{18}O$ and $^{18}O_2$.

Parameters	$X\,^3\Sigma_g^-$					
	$^{16}O^{18}O$			**$^{18}O_2$**		
	This work	**Drouin et al. [48]**	**Mizusima [30]**	**This work**	**Drouin et al. [48]**	**Endo [63]**
$\boldsymbol{B}$	40707.38680(124)	40707.38657(126)	40707.3856(48)	38313.72940(172)	38313.72938(168)	38313.761(39)
$\boldsymbol{D}\times10^3$	129.4163(159)	129.4142(161)	129.48(40)	114.5964(117)	114.5983(104)	118.0(27)
$\boldsymbol{\lambda}$	59499.0385(49)	59499.0375(49)	59499.0427(52)	59496.6776(13)	59496.6776(12)	59496.6831(39)
$\boldsymbol{\lambda_D}\times10^3$	54.967(25)	54.9777(253)	54.9537(262)	51.606(7)	51.6058(70)	51.573(18)
$\boldsymbol{\lambda_H}\times10^9$	285(24)	272.1(243)	294.8(248)	231.4(72)	231.4(73)	257(14)
$\boldsymbol{\gamma}$	-238.51490(32)	-238.51530(32)	-238.51483(52)	-224.44562(14)	224.44562(14)	224.4411(31)
$\boldsymbol{\gamma_D}\times10^6$	-219.40(44)	-217.77(44)	-219.38(45)	-192.22(48)	-192.23(48)	193.8(33)
$\boldsymbol{\gamma_H}\times10^9$		1.305[a]		-1.14(34)	-1.14(34)	
	$a^1\Delta_g$					
	This work	**Cohen et al. [60]**		**This work**	**Cohen et al. [60]**	
$\boldsymbol{B}$	40146.25470(311)	40145.1629(23)		37916.553(36)	37785.1581(23)	
$\boldsymbol{D}\times10^3$	136.4706(205)	136.381(21)		114.706(216)	120.766(21)	

[a] This parameter was fixed.

Hyperfine coupling constants

Our fitted values of the hyperfine coupling constants for the $a^1\Delta_g$ state are reproduced in Table 2.10 in MHz units and compared with the values determined by Arrington et al. from a fit of EPR spectra [45]. Since in theory there is no isotopic dependence for this parameter, these authors performed a global fit for the two species and determined the coupling constant to be -424±1 MHz which is almost exactly 2 times greater than our values (-217.3±1.9 and -211.5±2.6 MHz, for $^{16}O^{17}O$ and $^{17}O^{18}O$, respectively). This factor of 2 difference is merely due to the difference in the definition of the coupling constant in the work of Arrington et al. [45], where the value of Λ (Λ =2 in this case) is absorbed into the constant.

Table 2.10. The hf coupling parameter (MHz) of the $a^1\Delta_g$ state of $^{16}O^{17}O$, $^{17}O^{18}O$ and $^{17}O_2$.

	$^{16}O^{17}O$	$^{17}O^{18}O$	$^{17}O_2$
This work [a]	-217.35(195)	-211.50(261)	-211.93(126)
[45] [a]	-424(1)[a]	-424(1)[a]	

[a] The difference by a factor of 2 compared to our values is due to a difference in the definition (see text for details).

The ground-state hyperfine structure of $^{16}O^{17}O$, $^{17}O^{18}O$ and $^{17}O_2$ has been previously investigated in the microwave and millimeter ranges [42]−[44], [46]−[47]. The comparison with the hf coupling constants of $^{16}O^{17}O$ and $^{17}O^{18}O$ in the ground state obtained by Cazzoli et al. [42] is not straightforward as they used different parameters for the Hamiltonian corresponding to the magnetic part of the hyperfine splitting:

$$H_{HFS} = b\mathbf{I}\cdot\mathbf{S} + cI_zS_z \tag{2.8}$$

The minor difference with our Eq. (2.4) is that the isotropic and anisotropic contributions are not completely separated and therefore Eq. (2.8) yields less valuable physical information. Nevertheless, to make direct comparison we have fitted the CRDS and MW data using the magnetic contribution as given in Eq. (2.8). The results of this fit are given in Table 2.11 together with the values from Cazzoli et al. [42]. There appears to be a good agreement in all the constants except *c* which is slightly different. The reason for this discrepancy is unclear, but one can note that our value of *c* for $^{16}O^{17}O$ is close to the one reported by Gerber from EPR spectroscopy measurements [47]. Also, we have fitted only the MW lines from Ref. [42] and the discrepancy with the value of *c* reported in [42] remained, while the residuals in our fit were smaller.

Table 2.11. Comparison of the hyperfine coupling parameters of the $X^3\Sigma_g^-$ state of $^{16}O^{17}O$, $^{17}O^{18}O$ and $^{17}O_2$.

Parameter (MHz)	$^{16}O^{17}O$	$^{17}O^{18}O$	$^{17}O_2$
b[a] (This work)	-101.4356(34)	-101.4416(62)	-54.7580(24)
b [42], [43]	-101.441(5)	-101.46(1)	-54.758(3)
c (This work)	140.095(23)	140.090(59)	140.0378(62)
c [42], [43]	139.73(3)	139.68(6)	140.037(9)[b]
c [47]	140.123(36)	...	...
eQq (This work)	-8.13(24)	-8.23(47)	-8.302(39)
eQq [42], [43]	-8.3(3)	-7.8(5)	-8.29(3)

[a] For comparison purpose, the hyperfine parameters of $^{16}O^{17}O$ and $^{17}O^{18}O$ were fitted using the same hf Hamiltonian that was used in Ref. [42] (Eq. (2.8)). In consequence, the obtained *b* values differ from those included in Table 2.7. The value given for $^{17}O_2$ is the b_F value listed in Table 2.7 (Eq.(2.4)).

[b] The value given here is three times the value of Ref [42] due to a difference in the definition.

In the work of Cazzoli et al. [43] devoted to $^{17}O_2$ the corresponding part of the Hamiltonian is given as:

$$H_{HFS} = \alpha\, \mathbf{I}\cdot\mathbf{S} + \beta(3I_zS_z - \mathbf{I}\cdot\mathbf{S}), \qquad (2.9)$$

where the isotropic and anisotropic parts are separated. This expression is similar to our Eq. (2.4) where our b_F and c constants correspond to α and 3β, respectively. The comparison of our hyperfine parameters obtained using Eq. (2.4) with those given in Ref. [43] is also given in Table 2.11 and shows a very good agreement.

9. Conclusions

This work allows one to significantly extend the available reference spectroscopic data for the $a^1\Delta_g - X^3\Sigma_g^-$ band of oxygen near 1.27 µm, which is very important in the field of remote sensing. Indeed, the obtained results provide information for improving the HITRAN line list both in terms of accuracy and completeness. In Ref. [1], it was shown that it is important to include $a^1\Delta_g - X^3\Sigma_g^-$ electric quadrupole transitions of $^{16}O_2$ into HITRAN in order to improve atmospheric retrievals. The intensities of many of these transitions are actually above the HITRAN intensity cutoff (2×10^{-29} cm/molecule). The intensities of the $a^1\Delta_g - X^3\Sigma_g^-$ (1-1) band of $^{16}O_2$ and the $a^1\Delta_g - X^3\Sigma_g^-$ (0-0) band of $^{16}O^{17}O$ measured in this work are comparable with those of the $^{16}O_2$ electric quadrupole transitions and therefore also need to be accounted for. Therefore parameters determined here will be used to generate line lists and complete the present HITRAN line list by including bands discussed above and lowering the intensity cut off.

We compared the intensity values of the $^{16}O_2$ lines in the "natural" sample with intensities of this species provided in HITRAN [19]. In Figure 2.15 the ratios of the intensities are plotted versus CRDS line intensities. They are in very good agreement for the strongest lines but a smooth deviation increasing with rotational quantum numbers is evidenced.

The line intensities for $^{16}O^{18}O$ measured here, constitute an important contribution to the HITRAN database, where so far their values required significant improvement. The lack of proper experimental input parameters for $^{16}O^{18}O$ was the main reason for the limited quality of line intensities in the $a^1\Delta_g - X^3\Sigma_g^-$ band for this species in HITRAN.

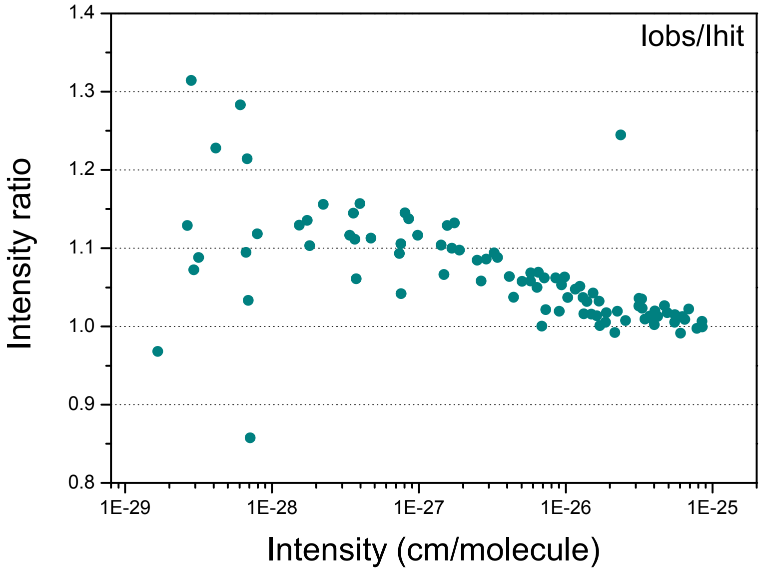

Figure 2.15. Ratio of the $^{16}O_2$ line intensities measured in this work and provided in HITRAN.

It is important to mention that *if* we assume that the abundance of $^{16}O^{18}O$ in the "natural" sample is that adopted in HITRAN (3.99×10^{-3}), our intensity values are found to be systematically lower by about 10% as shown in Figure 2.16. Consequently, we belive that $^{16}O^{18}O$ HITRAN intensity values should be corrected. (We estimated that they should be multiplied by 0.914).

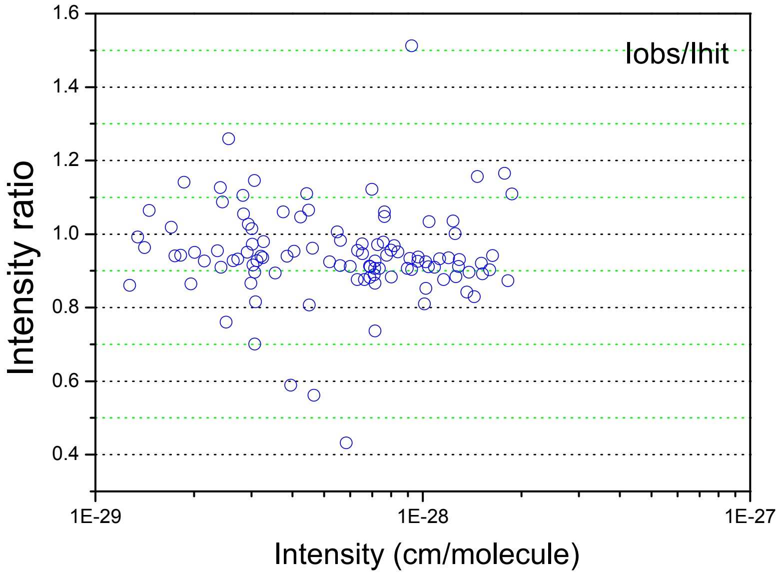

Figure 2.16. Ratio of the $^{16}O^{18}O$ line intensities measured in this work and provided in HITRAN [19].

Thus we came to a conclusion that the CRDS intensity values measured in this work could be used for the improvement of the $^{16}O_2$ and $^{16}O^{18}O$ dipole moment parameters.

The spectroscopic knowledge of the $a^1\Delta_g - X^3\Sigma_g^-$ band of the three ^{17}O containing oxygen isotopologues – $^{16}O^{17}O$, $^{17}O^{18}O$ and $^{17}O_2$ – has been considerably extended from our CRDS spectra at room temperature and at 80 K. The combination of the high sensitivity CRDS technique with a cryogenic cell at 80 K allowed for the first observation of the partly resolved hyperfine structure of the $a^1\Delta_g - X\,^3\Sigma_g^-$ band of the $^{16}O^{17}O$, $^{17}O^{18}O$ and $^{17}O_2$ isotopologues. The observed structure results from the hyperfine splittings of both the $X\,^3\Sigma_g^-$ ground state and the $a^1\Delta_g$ upper state which have a different origin: the hyperfine splitting of the $X\,^3\Sigma_g^-$ levels is due to the coupling of the ^{17}O nuclear spin to the electronic spin while that of the $a^1\Delta_g$ upper states is larger and results from the coupling of the ^{17}O nuclear spin to the electronic orbital angular momentum. The hyperfine coupling parameters in the excited state have been determined from a global fit of the line positions. The simulation of the hf structure calculated using these parameters leads to a very satisfactory reproduction of the measured hyperfine structure (Figure 2.12 − Figure 2.14).

Overall, the spectroscopic fit of the line positions measured in this work combined with microwave and Raman measurements available in the literature provides the best to date set of spectroscopic constants for the $X\,^3\Sigma_g^-$ and $a^1\Delta_g$ states. The $a^1\Delta_g$ parameters for the $^{17}O^{18}O$ species were determined for the first time. Also, improved ground state constants (in particular centrifugal distortion) were obtained for the $^{16}O^{17}O$ and $^{17}O^{18}O$ isotopologues. For the $^{17}O_2$ isotopologue, the $a^1\Delta_g$ parameters including the hyperfine coupling parameter were determined for the first time. The new observation of electric quadrupole transitions in the $a^1\Delta_g - X\,^3\Sigma_g^-$ system of $^{16}O^{17}O$ and $^{17}O_2$ species is reported together with the first determined spectroscopic constants for the $a^1\Delta_g$ $\upsilon = 1$ state of these species.

References for Chapter II

[1] I.E. Gordon, S. Kassi, A. Campargue, G.C. Toon. First identification of the $a^1\Delta_g - X^3\Sigma_g^-$ electric quadrupole transitions of oxygen in the solar and laboratory spectra. J. Quant. Spectrosc. Radiat. Transfer 111, 2010; 1174.

[2] L.S. Rothman and A. Goldman. Infrared electric quadrupole transitions of atmospheric oxygen. Appl. Opt. 20, 1981; 2182.

[3] D. Stranges, X. Yang, J. D. Chesko, and A. G. Suits. Production of O_2 Herzberg states in the deep UV photodissociation of ozone. J. Chem. Phys. 102, 1995; 6067.

[4] J.J. Valentini, D. P. Gerrity, D. L. Phillips, J. C. Nieh, and K. D. Tabor. CARS spectroscopy of $O_2(^1\Delta_g)$ from the Hartley band photodissociation of O_3: Dynamics of the dissociation. J. Chem. Phys. 86, 1987; 6745.

[5] L. Herzberg, G. Herzberg. Fine structure of the infrared atmospheric oxygen bands. Astrophys J. 105, 1947; 353.

[6] R. P. Lowe. Interferometric spectra of the Earth's airglow (1.2 to 1.6-µm). Philos. Trans. R. Soc. London Ser. A 264, 1969; 163.

[7] M. G. Mlynczak and B. T. Marshall. A re-examination of the role of the solar heating in the O_2 atmospheric and infrared atmospheric bands. Geophys. Res. Lett.23, 1996; 657.

[8] R. A. Washenfelder, G. C. Toon, J.-F. Blavier, Z. Yang, N. T. Allen, P. O. Wennberg, et al. Carbon dioxide column abundances at the Wisconsin Tall Tower site. Journal of Geophysical Research D 111, 2006; 22305.

[9] G. Herzberg. Photography of infrared solar spectrum to wavelength 12900 Å. Nature (London) 133, 1934; 759.

[10] R. M. Badger, A. C. Wright, and R. F. Whitlock. Absolute intensities of the discrete and continuous absorption bands of oxygen gas at 1.26 and 1.065 and the radiative lifetime of the $a^1\Delta_g$ state of oxygen. J.Chem.Phys.43, 1965; 4345.

[11] C Amiot, J Vergès. The magnetic dipole $a^1\Delta_g$ - $X\ ^3\Sigma_g^-$ transition in the oxygen afterglow. Can J Phys 59, 1981; 1391.

[12] L.-B. Lin, Y.-P. Lee, and J. F. Ogilvie. Line strengths of the band $a^1\Delta_g$ - $X\ ^3\Sigma_g^-$ of $^{16}O_2$. J. Quant. Spectrosc. Radiat. Transfer 5, 1988; 375.

[13] Y. T. Hsu, Y. P. Lee, and J. F. Ogilvie, Intensities of lines in the band a $a^1\Delta_g$ (v′=0) - $X\ ^3\Sigma_g^-$ (v″=0) of $^{16}O_2$ in absorption. Spectrochem. Acta 48A, 1992; 1227.

[14] W. R. Pendleton, Jr., D. J. Baker, R .J. Reese, and R. R. O'Neil. Decay of O_2 ($a^1\Delta_g$) in the evening twilight airglow: implications for theradiative lifetime. Geophys. Res. Lett. 23, 1996; 1013.

[15] W. J. Lafferty, A. M. Solodov, C. L. Lugez, G.T. Fraser. Rotational line strengths and self-pressure-broadening coefficients for the 1.27 μm, $a^1\Delta_g - X\,^3\Sigma_g^-$ (0, 0) Band of O_2. Appl Opt 37, 1998; 2264.

[16] S. M. Newman, I. C. Lane, A. J. Orr-Ewing, D. A. Newnham, J. Ballard. Integrated absorption intensity and Einstein coefficients for the O_2 $a^1\Delta_g - X\,^3\Sigma_g^-$ (0, 0) transition: A comparison of cavity ringdown and high resolution Fourier transform spectroscopy with a long-path absorption cell. J Chem Phys 110, 1999; 10749.

[17] S.-L. Cheah, Y.-P. Lee, J. F. Ogilvie. Wavenumbers, strengths, widths and shifts with pressure of lines in four bands of gaseous $^{16}O_2$ in the systems $a^1\Delta_g - X\,^3\Sigma_g^-$ and $b^1\Sigma_g^+ - X^3\Sigma_g^-$. J Quant Spectrosc Radiat Transfer 64, 2000; 467.

[18] R. R. Gamache, A. Goldman, L. S. Rothman. Improved spectral parameters for the three most abundant isotopomers of the oxygen molecule. J Quant Spectrosc Radiat Transfer 59, 1998; 495.

[19] L.S. Rothman, I.E. Gordon, A. Barbe, D. C. Benner, P. F. Bernath, M. Birk, et al. The HITRAN 2008 molecular spectroscopic database. J Quant Spectrosc Radiat Transfer 110, 2009; 533.

[20] R. A. McClatchey, W. S. Benedict, S. A. Clough, D. E. Burch, R. F Calfee, K. Fox, et al. *AFCRL Atmospheric absorption line parameters compilation*; 1973.

[21] http://www.cfa.harvard.edu/hitran/updates.html#Oxygen%20update

[22] R. Klotz, C. M. Marian, S. D. Peyerimhoff, B. A. Hess, R.J. Buenker. Calculation of spin-forbidden radiative transitions using correlated wavefunctions: Lifetimes of $b^1\Sigma^+$, $a^1\Delta$ states in O_2, S_2 and SO. Chem Phys 89, 1984; 223.

[23] D. A. Long, D. K. Havey, M. Okumura, H. M. Pickett C. E. Miller, J. T. Hodges. Laboratory measurements and theoretical calculations of O_2 *A* band electric quadrupole transitions. Phys Rev A 80, 2009; 042513.

[24] M. Simecková, D. Jacquemart, L. S. Rothman, R. R. Gamache, A. Goldman. Einstein *A*-coefficients and statistical weights for molecular absorption transitions in the *HITRAN* database. J. Quant. Spectrosc. Radiat. Transfer 98, 2006; 130.

[25] S. M. Newman, A. J. Orr-Ewing, D. A. Newnham, J. Ballard. Temperature and pressure dependence of line widths and integrated absorption intensities for the O_2 $a^1\Delta_g - X\,^3\Sigma_g^-$ (0, 0) transition. J Phys Chem A. 104, 2000; 9467.

[26] G. Rouillé, G. Millot, R. Saint-Loup, H. Berger. High-resolution stimulated Raman spectroscopy of O_2. J Mol Spectrosc 154, 1992; 372.

[27] K. W. Hillig, C. C. W. Chiu, W. G. Read, E. A. Cohen. The pure rotation spectrum of $a^1\Delta_g$ O_2. J Mol Spectrosc 109, 1985; 205.

[28] P. H. Krupenie. The Spectrum of Molecular Oxygen J Phys Chem Ref Dat 1, 1972; 423.

[29] J. Brault, private communication, 1982.

[30] M. Mizushima, S. Yamamoto. Microwave absorption lines of $^{16}O^{18}O$ in its ($X\,^3\Sigma_g^-$, v=0) state. J Mol Spectrosc 148, 1991; 447.

[31] I. Debecker, A. K. Mohamed and D. Romanini. High-speed cavity ringdown spectroscopy with increased spectral resolution by simultaneous laser and cavity tuning. Optics Express 13, 2005; 2906.

[32] D**.** Romanini, A. A. Kachanov, N. Sadeghi and F. Stoeckel. CW cavity ring down spectroscopy. Chem Phys Letter 264,1997; 316.

[33] D**.** Romanini, A. A. Kachanov, and F. Stoeckel. avity ringdown spectroscopy: broad band absolute absorption measurements. Chem Phys Letter 270; 1997, 546.

[34] P. Macko, D. Romanini, S. N. Mikhailenko, O.V. Naumenko, S. Kassi, A. Jenouvrier, et al. High sensitivity CW-cavity ring down spectroscopy of water in the region of the 1.5 μm atmospheric window. Journal of Molecular Spectroscopy 227, 2004; 90.

[35] J. Morville, D. Romanini, A.A. Kachanov, M. Chenevier. Two schemes for trace detection using cavity ringdown spectroscopy. Appl Phys D78, 2004; 465.

[36] B.V. Perevalov, S. Kassi, D. Romanini, V.I. Perevalov, S.A. Tashkun, A. Campargue. CW-cavity ringdown spectroscopy of carbon dioxide isotopologues near 1.5 μm. J Mol Spectrosc 238, 2006; 241.

[37] S. Kassi, O. Leshchishina, I.E. Gordon, S. Yu, A. Campargue. Hyperfine structure of the $a^1\Delta_g - X\,^3\Sigma_g^-$ transitions of $^{16}O^{17}O$, $^{17}O^{18}O$ and $^{17}O_2$ by CRDS at 80 K. Chem Phys Letter, 502, 2011; 37.

[38] S. Kassi, B. Gao, D. Romanini, A. Campargue. The near-infrared (1.30-1.70 μm) absorption spectrum of methane down to 77 K. Phys. Chem. Chem. Phys. 10, 2008; 4410.

[39] S. Kassi, D. Romanini, A. Campargue. Mode by Mode CW-CRDS at 80 K: Application to the 1.58 μm transparency window of CH_4. Chem. Phys. Lett. 477, 2009; 17.

[40] L. Wang, S. Kassi, A. Liu, S. Hu, A. Campargue. The 1.58 μm transparency window of methane (6165- 6750 cm^{-1}): empirical line list and temperature dependence between 80 K and 296 K . J Quant Spectrosc Radiat Transfer. 112, 2011; 937.

[41] L. Wang, S. Kassi, A. Liu, S. Hu, A. Campargue. High sensitivity absorption spectroscopy of methane at 80 K in the 1.58 μm transparency window: Temperature dependence and importance of the CH_3D contribution J. Mol. Spectrosc. 261, 2010; 41.

[42] G. Cazzoli, C. Degli Esposti, P.G. Favero, G.Severi. Microwave spectra of $^{16}O^{17}O$ and $^{18}O^{17}O$. Nuovo Cimento B Serie 62,1981; 243.

[43] G. Cazzoli, C. Degli Esposti, B.M. Landsberg. Millimetre wave spectrum of $^{17}O_2$. Magnetic hyperfine structure and quadrupole coupling constants. Nuovo Cimento D Serie 3, 1984; 341.

[44] D. A. Long, D. K. Havey, M. Okumura, C. E. Miller, J. T. Hodges. Cavity ring-down spectroscopy measurements of sub-Doppler hyperfine structure. Phys. Rev. 81, 2010; 064502.

[45] C. A. Arrington, A. M. Falick, R. J. Myers. Electron Paramagnetic Resonance Spectrum of O_2 ($a^1\Delta_g$) - Its ^{17}O Hyperfine Coupling and Electronic and Rotational g Values. J. Chem. Phys. **55**, 1971; 909.

[46] S. L. Miller, C.H. Townes. The microwave absorption spectrum of $(^{16}O)_2$ and $O^{16}O^{17}$. Phys. Rev 90, 1953; 537.

[47] P. Gerber. Hyperfeinstruktur des Elektronenspinresonanzspektrums von molekularem Sauerstoff in der Gasphase, Helv. Phys. Acta, 45, 1972; 655.

[48] B.J. Drouin, S. Yu, C. E. Miller, H.S.P. Müller, F. Lewen, S. Brünken, et al. Terahertz spectroscopy of oxygen, O_2, in its $^3\Sigma_g^-$ and $^1\Delta$ electronic states: THz Spectroscopy of O_2. J Quant Spectrosc Radiat Transfer 111, 2010; 1167.

[49] G. Rouillé, G. Millot, R. Saint-Loup, H. Berger. High-resolution stimulated Raman spectroscopy of O_2. J Mol Spectrosc 154, 1992; 372.

[50] H. G. M Edwards., D. A. Long, K. A. B. Najm, M. Thomsen. The vibration-rotation Raman spectra of $^{18}O_2$, $^{17}O^{18}O$, $^{17}O_2$ and $^{16}O_2$. J Raman Spectrosc 10, 1981; 60.

[51] H. D. Babcock, L. Herzberg. Fine structure of the red system of atmospheric oxygen bands. Astrophys. J. 108, 1948; 167.

[52] O. Leshchishina, S. Kassi, I. E. Gordon, L. S. Rothman, L. Wang, A. Campargue. High sensitivity CRDS of the $a^1\Delta_g - X\ ^3\Sigma_g^-$ band of oxygen near 1.27 μm: extended observations, quadrupole transitions, hot bands and minor isotopologues J. Quant. Spectrosc. Radiat. Transfer 111, 2010; 2236.

[53] O. Leshchishina, S. Kassi, I.E. Gordon, S. Yu, A. Campargue. The $a^1\Delta_g - X\ ^3\Sigma_g^-$ band of $^{16}O^{17}O$, $^{17}O^{18}O$ and $^{17}O_2$ by high sensitivity CRDS near 1.27 μm. J. Quant. Spectrosc. Radiat. Transfer, 112, 2011; 1257.

[54] H. M. Pickett The fitting and prediction of vibration-rotation spectra with spin interactions. J Mol Spectrosc. 148, 1991; 371.

[55] M. Y. Tretyakov, M. A. Koshelev, V. V. Dorovskikh, D. S. Makarov, P. W. Rosenkranz. 60-GHz oxygen band: precise broadening and central frequencies of fine-structure lines, absolute absorption profile at atmospheric pressure, and revision of mixing coefficients. J Mol Spectrosc 231, 2005; 1.

[56] Y. Endo, M. Mizushima. Microwave Resonance Lines of $^{16}O_2$ in its Electronic Ground State ($X\,^3\Sigma_g^-$). Jpn J Appl Phys 21, 1982; L379.

[57] G.Y. Golubiatnikov, A. F. Krupnov. Microwave study of the rotational spectrum of oxygen molecule in the range up to 1.12 THz. J Mol Spectrosc 217, 2003; 282.

[58] L. R. Zink, M. Mizushima. Pure rotational far-infrared transitions of $^{16}O_2$ in its electronic and vibrational ground state. J Mol Spectrosc 125, 1987; 154.

[59] K. Park, I. G. Nolt, T.C. Steele, L. R. Zink, K. M. Evenson, K. V. Chance, et al. Pressure broadening of the 50.873 and 83.469 cm^{-1} molecular oxygen lines. J Quant Spectrosc Radiat Transfer 56, 1996; 315.

[60] E. A. Cohen, M. Okunishi, J. J. Oh. The isotope effect of the O_2 $a^1\Delta_g$ rotational constant. J Mol Struct 352-353, 1995; 283.

[61] G. Millot, B. Lavorel, G. Fanjoux. Pressure Broadening, Shift, and Interference Effect for a Multiplet Line in the Rovibrational Anisotropic Stimulated Raman Spectrum of Molecular Oxygen. J Mol Spectrosc 176, 1996; 211.

[62] S. Brodersen, J. Bendtsen. The incoherent Raman spectrum of $^{16}O_2$ molecular constants from all experimental data. J Mol Spectrosc 219, 2003; 248.

[63] Y. Endo, M. Mizushima. Microwave Absorption Lines of $^{18}O_2$ in Its Electronic Ground State ($X\,^3\Sigma_g^-$). Jpn J Appl Phys 22, 1983; L534.

[64] W. Steinbach, W. Gordy. Millimeter and submillimeter wave spectrum of $^{18}O_2$. Phys Rev A. 8, 1973; 1753.

[65] T. Amano, E. Hirota. Microwave spectrum of the molecular oxygen in the excited vibrational state. J Mol Spectrosc 53, 1974; 346.

[66] W. Steinbach, W. Gordy. Microwave spectrum and molecular constants of $^{16}O^{18}O$ Phys Rev A. 11, 1975; 729.

[67] R. L. Crownover, F. C. De Lucia, E. Herbst. The submillimeter-wave spectrum of $^{16}O^{18}O$. Astrophys J 349, 1990; L29.

[68] C. H. Townes and A. L. Schawlow, *Microwave Spectroscopy*, Dover, New York, 1975.

[69] R.A. Frosh, H.M. Foley. Magnetic hyperfine structure in diatomic molecules Phys. Rev. 88, 1952; 1337.

[70] http://physics.nist.gov/PhysRefData/MolSpec/Diatomic/Html/Tables/O2.html

[71] B.F. Minaev, V.A. Minaeva. MCSCF response calculations of the excited states properties of the O_2 molecule and a part of its spectrum. Phys. Chem. Chem. Phys. 3, 2001; 720.

[72] L. S. Rothman. Magnetic dipole infrared atmospheric oxygen bands. Appl Opt 21, 1982; 2428.

[73] P. Connes, G. Michel. High-Resolution Fourier Spectra of Stars and Planets. Astrophys J 190, 1974; L29.

[74] J. W. Swensson, W. S. Benedict, L. Delbouille, G. Roland, in: *Mem Soc R Sci Liege Collect Special*, 1970; Vol. 5.

Chapter III: Theoretical fundamentals of rovibrational spectroscopy

1. Introduction

The second object under investigation of the present thesis is the water isotopologues – $D_2{}^{16}O$, $HD^{16}O$ and $H_2{}^{18}O$. This Chapter is devoted to description of the main approaches used in the course of the analysis of the high resolution absorption spectra of water isotopologues in the near-infrared and visible regions. In the next, Section the theoretical fundamentals of rovibrational spectroscopy are briefly described. Sections 3 and 4 present the effective Hamiltonian approach that was used for the modelling of the experimental energy levels obtained. Section 5 provides the description of the global variational calculation based on which our spectrum assignment was performed. The main aspects of the expert system used for spectrum identification are given in Section 6.

2. Separations of the electronic and nuclear motions. Rovibrational Hamiltonian

The quantum mechanical treatment of molecular rovibrational states consists in the solution of the stationary Schrödinger equation

$$H\Psi_\alpha = E_a \Psi_\alpha , \tag{3.1}$$

where H is quantum mechanical Hamiltonian operator for the molecule, E_a and Ψ_a are eigenvalues and eingenfunctions of H, respectively. E_a are the possible energy values of the stationary states with a set of quantum numbers denoted as a. Energies E_a and wave functions Ψ_a allow one to calculate the line positions and probabilities of transitions between different states of a molecule. Nonrelativistic molecular Hamiltonian in space-fixed axis system (SFS) is defined by the following expression:

$$H = \sum\nolimits_i \frac{p_i^2}{2m_e} + \sum\nolimits_N \frac{p_N^2}{2M_N} + U(x,r) \tag{3.2}$$

where p_i, m_e and p_N, M_N, are the operator of impulse and mass of i^{th} electron and N^{th} nuclei, respectively; $U(x,r)$ – Coulomb interaction potential, x and r denote sets of electronic and nuclear variables, respectively. The Schrödinger equation with the molecule Hamiltonian (3.2) depending on a large number of electronic and nuclear variables is unsolvable in analytical form even in the case of the simplest diatomic molecule H_2. Very complicated numerical methods should be developed to deal directly with Eq. (3.2). For this reason, it is desirable to separate the problem into parts by using some approximations, which reduce the dimensionality. As mentioned in Chapter I, the approximation that allows for the separation of the electronic and the nuclear motions is the famous Born-Oppenheimer approximation [1], [2].

The rovibrational transitions within the ground electronic state typically give rise to the absorption spectrum in infrared region, which is studied in Chapter IV of the thesis. Briefly, the scheme of electronic and nuclear motions separation is as follows.

In the frame of Born-Oppenheimer approximation, the problem reduces to the task that involves motion of electrons in the field of numerous fixed nuclei. Due to $M_N \gg m_e$ the second term in (3.2), which corresponds to the kinetic energy of nuclei, gives only a small corrections to the electronic energy. In this case, the solution of the Schrödinger equation with the Hamiltonian (3.2):

$$\left(\sum_i \frac{p_i^2}{2m_e} + U(x,r)\right)\Phi_n(x,r) = V_n(r)\Phi_n(x,r) \tag{3.3}$$

provides the electronic energy $V_n(r)$ as a function of nucleus coordinates *r*. In the case of diatomic molecules, these electronic energy functions form the curves called the adiabatic electronic terms for each electronic state *n* (a set of electronic quantum numbers). In the case of polyatomic molecules, the $V_n(r)$ form the surfaces in the multidimensional configuration space of nucleus coordinates.

The complete molecular wavefunction corresponding to the Hamiltonian (3.1) can be expanded into the series on complete set of functions $\Phi_n(x,r)$:

$$\Psi(x,r) = \sum_n \chi_n(r)\Phi_n(x,r), \tag{3.4}$$

where $\chi_n(r)$ are the rovibrational functions depending on *r*. If we substitute this expansion in the Schrödinger equation (3.3) we will obtain the equation system for the determination of $\chi_n(r)$:

$$\left[\sum_N \frac{p_N^2}{2M_N} + V_n(r) - E\right]\chi_n(r) = \sum_m \widehat{\Lambda}_{nm}\chi_m(r), \tag{3.5}$$

where *N* is the number of atoms in a molecule and $\widehat{\Lambda}_{nm}$ are the so called non-adiabatic operators connecting two electronic states *n* and *m*. Usually the non-adiabatic terms at the right hand side of Eq. (3.5) are small and can be significant only in the case of crossed or closely spaced electronic energy surfaces. Such situation occur for the excited electronic states, but in the case of molecules under consideration the ground electronic states of which are well separated from the excited states the non-adiabatic operators can be neglected. Therefore in this case

$$\left[\sum_N \frac{p_N^2}{2M_N} + V_n(r)\right]\chi_n(r) = E\chi_n(r). \tag{3.6}$$

Here the electronic energy $V_n(r)$ is considered as a potential energy function, which governs the nuclear motion (in the electronic state *n*).

Eq. (3.6) includes the different types of motion (for instance, translation of a molecule as a whole in the space) and still remains hard to solve analytically. It is more convenient to describe a molecule in terms of translation, rotation, and internal vibration coordinates. Simplification of Eq. (3.6) can be achieved by replacing the space-fixed coordinate system by new coordinate system suitable for the description of the individual types of motions mentioned above. In the case of absence of external fields, the translation movement can be exactly separated by a choice of the molecular-fixed coordinate system (MFS) whose origin is placed in the center of mass. The overall molecule rotation, in turn, cannot be separated exactly, but a suitable choice of the MFS orientation allows one to minimize the interaction between rotation and vibration [3].

The normal coordinates of vibration Q ($\mathrm{cm \cdot g^{1/2}}$) are usually used as internal variables. These normal coordinates Q are defined as linear combinations of the components of the vibrational displacement vectors of the atomic nuclei with respect to the MFS and satisfying certain conditions [3], [4]. As the variables describing the rotation of a molecule the Euler angles θ, φ, χ are used, which define the orientation of the MFS with respect to the SFS. Thus after making the Born-Oppenheimer approximation one arrives at the rovibrational Hamiltonian H_{VR} in the coordinates $(\theta, \varphi, \chi; Q_1, Q_2, ..., Q_{3N-6})$ for the vibrational and rotational molecular states of a given electronic state.

The rovibrational Hamiltonian of a polyatomic nonlinear molecule, assuming that in the molecule there is a equilibrium configuration (when $Q_i = 0$) with respect to which small-amplitude oscillations occur [5], [6] was obtained by Wilson and Howard [7], Darling and Dennison [8]. Later on, Watson [9] simplified this Hamiltonian and reduced to the form that is commonly used nowadays to determine the rovibrational energy levels. Watson nonrelativistic Hamiltonian in the Eckart MFS is given by:

$$H_{VR} = \frac{1}{2}\sum_{\alpha,\beta}(J_\alpha - \pi_\alpha)\mu_{\alpha\beta}(q)(J_\beta - \pi_\beta) + \frac{1}{2}\sum_k \omega_k p_k^2 + V(q) - \frac{1}{8}\sum_\alpha \mu_{\alpha\alpha}(q), \tag{3.7}$$

where J_α and $\pi_\alpha = \sum_{i,j} \xi_{ij}^\alpha (\omega_i / \omega_j)^{1/2} q_i p_i$ are the dimensionless operators associated with the total angular and vibrational angular moment components along the MFS axis ($i, j = 1,\ 2, ... 3N-6, \alpha, \beta = x, y, z$), respectively, ξ_{ij}^α are Coriolis constants, $q_k = 2\pi(\frac{c}{h}\omega_k)^{1/2} Q_k$ and $p_k = -i\frac{\partial}{\partial q_k}$ are dimensionless operators associated with the normal coordinates and conjugated momenta, respectively ; $\mu_{\alpha\beta}(q)$ are the normal coordinates dependent components of tensor of inverse inertia moment (in units of cm^{-1}); $V(q)$ is the potential energy function in the adiabatic approximation (in units of cm^{-1}). Thus, the two first terms describe nuclear rotational and vibrational movements, respectively. The last contribution is the so-called Watson term, caused by the quantum nature of the problem.

Since we assume that all nuclear vibrations in molecule are of small amplitude then the normal coordinates q_i should be regarded as small values, and functions $\mu_{\alpha\beta}(q)$ and $V(q)$ do not vary significantly during vibrations. Then these functions can be represented by their Taylor series around the equilibrium configuration:

$$\mu_{\alpha\beta}(q) = \mu^{0}_{\alpha\beta}\delta_{\alpha\beta} + \sum_{i}\mu^{i}_{\alpha\beta}q_i + \sum_{ik}\mu^{ik}_{\alpha\beta}q_i q_k + \ldots; \tag{3.8}$$

$$V(q) = \frac{1}{2}\sum_{i}\omega_i q_i^2 + \frac{1}{6}\sum_{i,j,k}\Phi_{ijk}q_i q_j q_k + \frac{1}{24}\sum_{i,j,k,l}\Phi_{ijkl}q_i q_j q_k q_l + \ldots. \tag{3.9}$$

where ω_i are the harmonic frequencies (cm^{-1}), $\mu^{ij\ldots m}_{\alpha\beta}$ are the rovibrational interaction constants and Φ_{ijk}, Φ_{ijkl} are the anharmonic constants (cm^{-1}). Hereafter the traditional spectroscopic units – wavenumbers (cm^{-1}) are used for the Hamiltonian, energy, and spectroscopic constants.

3. The effective Hamiltonian approach and its application to the rovibrational energy levels modelling

It was shown [5], [10]-[11] that each consequent term of the expansions (3.8) and (3.9) is λ times smaller than the preceding one, where $\lambda \ll 1$ is known as Born-Oppenheimer parameter [10]:

$$\lambda = (m_e / M_N)^{1/4} \sim (2\bar{B}/\bar{\omega})^{1/2}, \tag{3.10}$$

where $\bar{B}$ and $\bar{\omega}$ are the average values of rotational constants and harmonic frequencies. Thus, the Hamiltonian (3.7) could be rewritten as:

$$H = H_0 + \lambda H_1 + \lambda^2 H_2 + \lambda^3 H_3 + \ldots, \tag{3.11}$$

where

$$H_0 = \frac{1}{2}\sum\nolimits_i \omega_i\left(p_i^2 + q_i^2\right). \tag{3.12}$$

The Schrödinger equitation with Hamiltonian H_0 is exactly solvable resulting in well-known eigenvalues and eingenfunctions:

$$\begin{aligned} E_0^{vib}(\upsilon_1\upsilon_2\ldots\upsilon_{3N-6}) &= \sum_{i=1}^{3N-6}\omega_i(\upsilon_i + \frac{1}{2}), \\ \left|\upsilon_1\upsilon_2\ldots\upsilon_{3N-6}\right\rangle &= \left|\upsilon_1\right\rangle\left|\upsilon_2\right\rangle\left|\upsilon_{3N-6}\right\rangle, \end{aligned} \tag{3.13}$$

where $|\upsilon\rangle = (2\pi 2^{\upsilon}\upsilon!)^{-1/2}\exp(-q^2/2)H_{\upsilon}(q)$, $H_{\upsilon}(q)$ are the Hermite polynomials and υ_i are the vibrational quantum numbers. The perturbation operators H_1, H_2... in (3.11) include the derivatives of the inverse tensor of inertia, of the potential energy function and a combinations of the angular momentum operators.

In the frame of the traditional approach the perturbation theory is used to transform the Hamiltonian (3.7) to an effective Hamiltonian $\tilde{H}$, which should be diagonal or block-diagonal in the basis of zero order functions (3.13). The effective Hamiltonian $\tilde{H}$ possesses the same eigenvalues as the initial rovibrational Hamiltonian H, but its matrix is considerably simpler. The perturbation theory in the form of contact transformation procedure (CT) allows one to derive the effective Hamilnonian [12]:

$$\tilde{H} = U^{+}\,\mathrm{H}U = e^{i\lambda^n s_n}\ldots e^{i\lambda^2 s_2}e^{i\lambda s_1}\,\mathrm{H}\,e^{-i\lambda s_1}e^{-i\lambda^2 s_2}\ldots e^{-i\lambda^n s_n}, \tag{3.14}$$

which is presented by a block-diagonal matrix in the basis of zero-order wavefunctions $|V\rangle$ and $|V'\rangle$ ($V \equiv (\upsilon_1,\upsilon_2,\ldots,\upsilon_{3N-6}), V' \equiv (\upsilon_1',\upsilon_2',\ldots,\upsilon_{3N-6}')$). Quantities s_n here are the generators of transformation. Each block (polyad) of this matrix ties together all the vibrational states that are in resonance interaction and effective Hamiltonian $\tilde{H}$ can be represented as direct sum of the operators related to polyads (*Γ*) of interacting vibrational states:

$$\tilde{H} = \sum_{\Gamma}\sum_{VV'\in\Gamma} H_{VV'}|V\rangle\langle V'|. \tag{3.15}$$

Diagonal elements of the transformed Hamiltonian are the effective rotational Hamiltonians (ERH) corresponding to a given vibrational state *V*. These rotational Hamiltonians can be written in a general form:

$$H_{VV} = \sum_{n}\sum_{p+q+r=2n} h^{(V)}_{p\,q\,r}(J_x^p\,J_y^q\,J_z^r + J_z^r\,J_y^q\,J_x^p), \tag{3.16}$$

where only components with even total power of operators J_α ($\alpha = x, y, z$), should be retained. Coefficients $h^{(V)}_{pqr}$ called spectroscopic parameters are the functions of molecular constants and vibrational quantum numbers υ_i. The vibrational dependence of spectroscopic parameters can be expressed by the so-called serial formula:

$$h^{(V)}_{pqr} = h^{(0)}_{pqr} + \sum_i h^{(i)}_{pqr}\left(\upsilon_i + \frac{1}{2}\right) + \sum_{ij} h^{(ij)}_{pqr}\left(\upsilon_i + \frac{1}{2}\right)\left(\upsilon_j + \frac{1}{2}\right) + \ldots \tag{3.17}$$

The first coefficient $h^{(V)}_{000}$ in (3.16) is the vibrational energy and the second order terms $h^{(V)}_{200}$, $h^{(V)}_{020}$, $h^{(V)}_{002}$ are the rotational constants and those for higher order terms are known as centrifugal distortion constants.

In the case of asymmetric-top molecule, serial formulae for vibrational energy and rotational constants are frequently represented as:

$$\begin{aligned} E_V &= \sum_i \omega_i \left(\upsilon_i + \frac{1}{2}\right) - \sum_{ij} x_{ij} \left(\upsilon_i + \frac{1}{2}\right)\left(\upsilon_j + \frac{1}{2}\right) + \ldots, \\ B_\alpha &= B_\alpha^e - \sum_i a_\alpha^i \left(\upsilon_i + \frac{1}{2}\right) + \ldots \end{aligned} \tag{3.18}$$

where x_{ij} are the anharmonic spectroscopic constants, B_x^e, B_y^e, B_z^e are equilibrium rotational constants and a_x^i, a_y^i, a_z^i are vibration-rotation constants.

For further details of the rovibrational Hamiltonian decomposition the reader is referred to Refs. [10], [11]. The CT was applied for the first time by Van Vleck [13] and then it have been widely used to solve a variety of problems in molecular spectroscopy [5]. The CT is aimed at simplification of the calculation procedure of rovibrational energy levels. This is achieved by means of total (in case of isolated vibrational states) or block (in case of accidental resonances) diagonalization of the matrix representation of the rovibrational Hamiltonian (3.7) in the basis of zero-order wave functions (3.18).

In practice, spectroscopic constants in Eqs. (3.16) and (3.17) are frequently determined by fitting to the experimental line positions or energy levels. For the inverse problem effective Hamiltonians of the form (3.16) is not correct, because of an infinite number of different sets of constants could be found which result in exactly the same energy levels. Indeed, any unitary transformation of the type

$$\begin{aligned} H'_{VV} &= e^{i\left(\sigma_x J_x + \sigma_y J_y + \sigma_z J_z + \ldots\right)} H_{VV} e^{-i\left(\sigma_x J_x + \sigma_y J_y + \sigma_z J_z + \ldots\right)} = \\ &= e^{i\left(\sigma_x J_x + \sigma_y J_y + \sigma_z J_z + \ldots\right)} \left[\sum_{r,p,q} h_{rpq}^{(V)} \left\{ J_x^r J_y^p J_z^q + J_z^q J_y^p J_z^r \right\} \right] e^{-i\left(\sigma_x J_x + \sigma_y J_y + \sigma_z J_z + \ldots\right)} = \\ &= \sum_{r,p,q} h_{rpq}^{\prime(V)} \left\{ J_x^r J_y^p J_z^q + J_z^q J_y^p J_z^r \right\}, \end{aligned} \tag{3.19}$$

leads to the effective Hamiltonian of the same operator form and having exactly the same eigenvalues, but with the new spectroscopic constants $h_{rpq}^{\prime(V)}$ depending on the choice of constants σ_α. Watson [14] suggested the transformations of the type (3.19) which results in the reduced effective Hamiltonian with spectroscopic constants unambiguously determined from the experimental energy levels.

Both the reduction procedure and the exact form of reduced effective Hamiltonian depend on the molecular symmetry, energy levels degeneracy etc. In the case of isolated vibrational states of asymmetric type molecule Watson's A-reduced Hamiltonian has the form [14]:

$$\begin{aligned} H_{VV} = E_V &+ (A^V - \tfrac{B^V+C^V}{2})J_z^2 + \tfrac{B^V+C^V}{2}J^2 + \tfrac{B^V+C^V}{2}J_{xy}^2 - \Delta_K^V J_z^4 - \Delta_{JK}^V J_z^2 J^2 - \Delta_J^V J^4 + H_K^V J_z^6 + \\ &+ H_{KJ}^V J_z^4 J^2 + H_{JK}^V J_z^2 J^4 + J_J^V J^6 + L_K^V J_z^8 + L_{KKJ}^V J_z^6 J^2 + L_{KJK}^V J_z^4 J^4 + L_{JKK}^V J_z^2 J^6 + L_J^V J^8 + \ldots \qquad (3.20) \\ &+ h_K^V \{J_z^4, J_{xy}^2\} + h_{JK}^V \{J_z^2, J_{xy}^2\} J^2 + 2h_J^V J^4 J_{xy}^2 + \ldots , \end{aligned}$$

where

$$J^2 = J_x^2 + J_y^2 + J_z^2,\ J_{xy}^2 = J_x^2 - J_y^2 = \frac{1}{2}(J_+^2 + J_-^2),\ \{A, B\} = AB + BA, \qquad (3.21)$$

where $J_+ = J_x - iJ_y,\ J_- = J_x + iJ_y$ are the spherical components of total angular momentum

In Eq. (3.20) E_V is the vibrational energy, A^V, B^V and C^V are three rotational constants, and $\Delta_k^V, \Delta_{Jk}^V, \Delta_J^V, \delta_k^V, \delta_J^V, H_k^V, \ldots$ are the centrifugal distortion constants for a given vibrational state V. The numerical diagonalization of operator (3.20) in the basis of symmetric rigid rotor functions $|JK\rangle$ defined by relations:

$$\begin{aligned} &J^2 |JK\rangle = (J^2 + J)|JK\rangle; \\ &J_z |JK\rangle = K|JK\rangle; \qquad (3.22) \\ &(J_x \pm iJ_y)|JK\rangle = (J(J+1) + K(K \pm 1))^{1/2} |JK \pm 1\rangle, \end{aligned}$$

allows one to calculate rovibrational energy levels.

Thus, the problem of diagonalization of the total rovibrational Hamiltonian (3.7) is reduced to the problem of eigenvalues determination of a matrix of finite dimension.

When describing a real molecule spectrum, it is usually impossible to consider some vibrational states as isolated because of resonances. In the rovibrational theory, there are two kinds of resonances: regular and accidental ones. The regular resonances are caused by the presence of equivalent bonds in the molecule and they are naturally taken into account by solving Schrödinger equation. The accidental resonances are the results of near degeneracy of two (or more) vibrational states. For the resonance interaction to take place, except for proximity or coincidence of vibrational states, the rovibrational Hamiltonian should include the terms that bind these states. Thus taking into account the resonance interactions implies the need to construct the effective Hamiltonian for the group of resonating states – polyad.

For many XY_2 molecules of the symmetry point group C_{2V}, for example, H_2O, the resonance effects originate from the proximity of $\omega_1 \sim 2\omega_2 \sim \omega_3$, where $\omega_1, \omega_2, \omega_3$ are the fundamental frequencies of molecular vibrations of symmetry species A_1, A_1, and B_1, respectively. The group of resonating vibrational states includes those with the same value of the so called polyad quantum number $p = 2\upsilon_1 + \upsilon_2 + 2\upsilon_3 = 0,\ 1,\ 2,\ 3 \ldots$, where υ_1, υ_2 and υ_3 are the vibrational quantum numbers. For $p = 0$ and 1 these groups consist of isolated states (000) and (010), respectively; for $p = 2$ and 3 they contain three states, the so called first and second triad

{(020), (100), (001)} and {(030), (110), (011)}. The higher vibrational states form two hexads (6 states), two decades (10 states), etc. The polyads of resonating states for the water molecule are schematically shown in Figure 3.1.

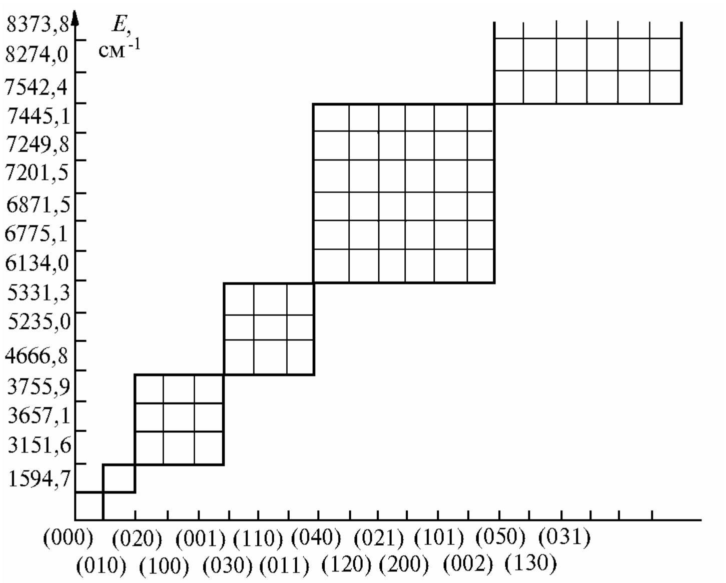

Figure 3.1. Polyad of interacting vibrational states for the $H_2{}^{16}O$ molecule (adapted from Ref. [15]).

The resonance interactions for water-type molecule can be classified as follows [3], [5], [16]:

1. Anharmonic resonance or Fermi-type resonance – is the resonance between the vibrational states of the same symmetry: $A_1 \leftrightarrow A_1$ or $B_1 \leftrightarrow B_1$, i.e. interaction between two states with even $\Delta\upsilon_3 = \upsilon_3 - \upsilon_3'$, $\upsilon_3 \in V$, $\upsilon_3' \in V'$. Without loss of generality, the corresponding non-diagonal operator $H^F_{VV'} = \langle V|H|V'\rangle$ can be presented by the following formula [17]-[20]:

$$H^F_{VV'} = \sum_{\ell mp} F^{(VV')}_{2\ell m 2p} J^{2\ell} \left\{ J_+^{2p} \left(J_z + p\right)^m + \left(-1\right)^m \left(J_z + p\right)^m J_-^{2p} \right\} \tag{3.23}$$

In the present work we use the following expression for Fermi-type interaction [21]:

$$H^F_{VV'} = F_0^{(VV')} + F_K^{(VV')} J_z^2 + F_{xy}^{(VV')}(J_x^2 - J_y^2) - F_{xyK}^{(VV')} \left\{ J_z^2, (J_x^2 - J_y^2) \right\} - 2F_{xyJ}^{(VV')} J^2 (J_x^2 - J_y^2) + \dots \tag{3.24}$$

$H^F_{VV'}$ has nonvanishing matrix element with $\Delta J = 0,\ \Delta K = 0,\ \pm 2$.

2. Coriolis-type resonance – resonance interaction between two vibrational states of different symmetry: $A_1 \leftrightarrow B_1$, i.e. interaction between two states with odd $\Delta\upsilon_3 = \upsilon_3 - \upsilon_3'$. Without loss of generality, the corresponding non-diagonal operator $H^C_{VV'} = \langle V|H|V'\rangle$ is given by [17]-[20]:

$$H^C_{VV'} = \sum_{\ell mp} C_{2\ell m 2p+1} J^{2\ell} \left\{ J_+^{2p+1} \left(2J_z + 2p + 1\right)^m + (-1)^{m+1} \left(2J_z + 2p + 1\right)^m J_-^{2p+1} \right\}. \tag{3.25}$$

For a molecule such as H_2O, operator (3.25) can be reduced to the form [21], which has been used in this thesis:

$$H_{VV'}^{C} = C_{y}^{VV'}(iJ_y) + C_{yK}^{VV'}\left\{iJ_y, J_z^2\right\} + C_{yJ}^{VV'}(iJ_y)J^2 + C_{yKK}^{VV'}\left\{iJ_y, J_z^4\right\} + \ldots \tag{3.26}$$

$H_{VV'}^{C}$ has nonvanishing matrix element with $\Delta J = 0,\ \Delta K = 0,\ \pm 1$.

Since $\Delta J = 0$ for all the nonvanishing matrix elements, the whole Hamiltonian matrix breaks up into blocks corresponding to different values of J. For a given J, there are $(2J+1)$ different values of K, i.e. $-J \le K \le J$. In order to simplify the diagonalization process, it is useful to work in a symmetry-adapted basis in which the Hamiltonian matrix splits into four submatrices, which correspond to the four different symmetry species $+s, -s, +a$ and $-a$ for the rovibrational levels of a molecule of the group C_{2V}. In this symmetry-adapted basis, the wave functions $\left|VJK\gamma\right\rangle$, of the basis are given by

$$\left|VJK\gamma\right\rangle = \psi_V S(JK\gamma), \tag{3.27}$$

where $\gamma = 0,\ 1,\ \psi_V$ is the vibrational wavefunction and $S(JK\gamma)$ is the symmetry-adapted rotational wavefunction [15], [16]. The S functions can be classified into four different rotational basis $E^{+},\ E^{-},\ O^{+}$ and O^{-} according to the values of K and γ. The symmetry Γ of the overall wave function $\left|VJK\gamma\right\rangle$ is defined by the symmetry of the vibrational wave function, Γ_V, and the rotational basis.

By diagonalization of the Hamiltonian submatrix in the symmetry-adapted basis of rovibrational functions for a given J and overall symmetry Γ we obtain the eigenvalues $E_{JK_aK_c}^{V}$ and eingenfunctions $\left|VJK_aK_c\right\rangle$, where $0 \le K_a,\ K_c \le J$ and $K_a + K_c = J$ or $K_a + K_c = J + 1$. For the asymmetric top molecules the quantum numbers K_a and K_c characterize the J component along the inertia axes a and c in the two limiting cases of asymmetric top: prolate and oblate ones, respectively. Thus, the observed energy levels are identified by the quantum numbers $(\upsilon_1\upsilon_2\upsilon_3, JK_aK_c)$.

By using effective Hamiltonian in polynomial form (3.16) or (3.20) for the description rotational structure of vibrational states of a molecule such as $H_2{}^{16}O$ a number of problems take place. In the recent years due to the great progress of experimental techniques, the higher and higher sensitivity can be achieved and accordingly weak lines connected with transitions on highly excited rovibrational energy states can be measured. However, for these states some approximations used to derive effective Hamiltonian are not valid because of strong non-rigidity effects. Indeed, for the molecules, such as $H_2{}^{16}O$, the “soft” bending vibration ν_2 breaks out the small amplitude vibration assumption, that results in divergence of energy level calculations even for low values of $J \sim 10$ [8], [11].

One more feature is associated with an abnormal dependence of the rotational level structure on the high bending state. This is reflected in the fact that spectroscopic parameters of $h_{pqr}^{(V)}$ undergo an abnormally strong dependence on the vibrational quantum number υ_2, and this dependence can not be described by serial formula (3.17) or (3.18). For the water molecule power series expansion of the rotational Hamiltonian (3.16) becomes slowly convergent or even divergent, which leads to the necessity to include very high powers of operators J_α in effective Hamiltonian [8]-[26].

Because of the divergence of the EH in the form of series (3.16) one has to use the special methods of series summation. Nowadays a number of summation methods have been proposed [27]-[32], which resulted in significant improvement of rotational energy level calculations. In this thesis, the effective rotational Hamiltonian presented by Padé-Borel approximants, which was proposed by Polyansky [32] is used. The Padé-Borel approximation has been already applied for rovibrational spectra analysis of different molecules such as H_2O, HDO, D_2O [33]–[34]. It was shown that this method of summation significantly improves the calculation of the energy levels of molecules with large non-rigidity effects. Matrix elements of the rotational Hamiltonian (3.20) when using Padé-Borel approximants:

$$PB^{[1,1]}(\lambda) = \int_0^\infty e^{-t} P^{[1,1]}(\lambda t)\,dt \tag{3.28}$$

are presented in the form

$$\begin{aligned}\langle JK|H_{vv}|JK\rangle &= E_v + \int_0^\infty \frac{c_0 c_1 + \left(c_1^2 - c_0 c_2\right)t}{c_1 - c_2\,t} e^{-t}dt,\\ \langle JK|H_{vv}|JK \pm 2\rangle &= \langle JK|J_{xy}^2|JK \pm 2\rangle \int_0^\infty \frac{b_0 b_1 + (b_1^2 - b_0 b_2)t}{b_1 - b_2 t} e^{-t}dt,\end{aligned} \tag{3.29}$$

where the formal parameter λ is set equal to 1 in final computations

$$\begin{aligned} c_0 &= \left[A - \frac{B+C}{2}\right]K^2 + \frac{B+C}{2}J(J+1)\\ c_1 &= -\Delta_K K^4 - \Delta_{JK} K^2 J(J+1) - \Delta_J J^2 (J+1)^2\\ 2c_2 &= H_K k^6 + H_{KJ} k^4 J(J+1) + H_{JK} k^4 J^2 (J+1)^2 + H_J J^3 (J+1)^3 + L_K k^8 + \ldots \end{aligned} \tag{3.30}$$

$$\begin{aligned} b_0 &= \frac{B-C}{2}\\ b_1 &= -\delta_k\left[K^2 + \left(K \pm 2\right)^2\right] - 2\delta_J J(J+1)\\ 2b_2 &= h_k\left[K^4 + \left(K \pm 2\right)^4\right] + h_{jk}\left[K^2 + \left(K \pm 2\right)^2\right]J\left(J+1\right) + 2h_J J^2\left(J+1\right)^2 + \ldots \end{aligned} \tag{3.31}$$

The integrals in Eq. (3.29) can be evaluated in closed form by using the integral exponent representation [35]:

$$Ei(-x) = -\int_{x}^{\infty} e^{-t} t^{-1} dt . \tag{3.32}$$

4. Effective vibrational Hamiltonian

For the variety of water vapour spectroscopy problems, it is important to know the vibrational spectroscopic parameters such as the harmonic frequencies ω_λ, the anharmonic constants $x_{\lambda\mu}$, $y_{\lambda\mu\eta}$, the Fermi-resonance parameter F, the Darling-Dennison resonance parameter Γ^{DD}, etc. On the one hand, these parameters allow one to calculate the vibrational band origins; on the other hand, they could be used to determine the potential energy function parameters. These spectroscopic constants are the parameters of the pure vibrational Hamiltonian (rotation is not included).

Labelling of the vibrational states is an important problem for $H_2{}^{16}O$ and its isotopologues. The normal mode labelling is traditionally used in the literature and accepted in the most popular spectroscopic databanks like HITRAN [36] and GEISA [37]. In the frame of the effective Hamiltonian model the consistent approach to obtain the normal mode labelling of the vibrational states could be developed. It was firstly proposed for the $H_2{}^{16}O$ molecule [38], and later applied to the H_2S vibrational states [39]. This method has been presently applied for the modelling of the vibrational states of the $D_2{}^{16}O$ and $H_2{}^{18}O$ molecules (Chapter IV).

Vibrational energies can be obtained by diagonalization of the matrix representation of the effective vibrational Hamiltonian:

$$H = \sum_{VV' \in a} H_{VV'} \left| V \right\rangle \left\langle V' \right| , \tag{3.33}$$

where a includes all the vibrational states of the same symmetry having the same polyad number of $p = 2\upsilon_1 + \upsilon_2 + 2\upsilon_3 = 0,\ 1,\ 2,\ 3...$, where υ_1, υ_2 and υ_3 are the vibrational quantum numbers; $\left| V \right\rangle = \left| \upsilon_1 \upsilon_2 \upsilon_3 \right\rangle$, $\left| V' \right\rangle = \left| \upsilon_1' \upsilon_2' \upsilon_3' \right\rangle$ are the vibrational wave functions taken as a product of the harmonic functions. The diagonal operators have the following form:

$$\begin{aligned} H_{VV} = &\sum_{\lambda}^{3} \omega_\lambda \left(\upsilon_\lambda^i + 1/2 \right) + \sum_{\lambda,\mu\geq\lambda}^{3} x_{\lambda\mu} \left(\upsilon_\lambda^i + 1/2 \right)\left(\upsilon_\mu^i + 1/2 \right) + \\ &+ \sum_{\lambda,\mu\geq\lambda,\nu\geq\mu}^{3} y_{\lambda\mu\nu} \left(\upsilon_\lambda^i + 1/2 \right)\left(\upsilon_\mu^i + 1/2 \right)\left(\upsilon_\nu^i + 1/2 \right) + \\ &+ \sum_{\lambda,\mu\geq\lambda,\nu\geq\mu,\eta\geq\nu}^{3} z_{\lambda\mu\nu\eta} \left(\upsilon_\lambda^i + 1/2 \right)\left(\upsilon_\mu^i + 1/2 \right)\left(\upsilon_\nu^i + 1/2 \right)\left(\upsilon_\eta^i + 1/2 \right) \end{aligned} , \tag{3.34}$$

and non-diagonal couplings correspond to the Fermi-type interaction:

$$H_{VV'} = F \left\{ \left(\upsilon_1 + \frac{1}{2} \pm \frac{1}{2} \right)\left(\upsilon_2 + \frac{1}{2} \mp \frac{1}{2} \right)\left(\upsilon_2 + \frac{1}{2} \mp \frac{3}{2} \right) \right\}^{1/2} , \tag{3.35}$$

where $\left|V\right\rangle = \left|\upsilon_1\upsilon_2\upsilon_3\right\rangle$, $\left|V'\right\rangle = \left|\upsilon_1' \pm 1\ \upsilon_2' \mp 2\ \upsilon_3'\right\rangle$ and to the Darling-Dennison-type resonance interaction:

$$H_{VV'} = \left\{\Gamma_{DD} + \gamma_1\left(\upsilon_1 + \frac{1}{2} \pm 1\right) + \gamma_2\left(\upsilon_2 + \frac{1}{2}\right) + \gamma_3\left(\upsilon_3 + \frac{1}{2} \mp 1\right)\right\} \times$$
$$\times \left\{\left(\upsilon_1 + \frac{1}{2} \pm \frac{1}{2}\right)\left(\upsilon_1 + \frac{1}{2} \pm \frac{3}{2}\right)\left(\upsilon_3 + \frac{1}{2} \mp \frac{3}{2}\right)\left(\upsilon_3 + \frac{1}{2} \mp \frac{1}{2}\right)\right\}^{1/2}, \tag{3.36}$$

where $\left|V\right\rangle = \left|\upsilon_1\upsilon_2\upsilon_3\right\rangle$, $\left|V'\right\rangle = \left|\upsilon_1' \pm 2\upsilon_2'\upsilon_3' \mp 2\right\rangle$.

The resulting wave functions provided by the diagonalization of the Hamiltonian matrix are a linear combination of the basis harmonic oscillator functions:

$$\left|u_1u_2u_3\right\rangle = \sum_{\upsilon_1\upsilon_2\upsilon_3 \in a} C_{u_1u_2u_3}^{\upsilon_1\upsilon_2\upsilon_3} \left|\upsilon_1\upsilon_2\upsilon_3\right\rangle, \tag{3.37}$$

where $\sum\limits_{\upsilon_1\upsilon_2\upsilon_3 \in a} \left|C_{u_1u_2u_3}^{\upsilon_1\upsilon_2\upsilon_3}\right|^2 = 1$ in accordance with the normalization of the basis functions, and the u_1, u_2, u_3 represent the approximate vibrational quantum numbers of the resulting vibrational energy level. $P_n = \left|C_{u_1u_2u_3}^{\upsilon_1\upsilon_2\upsilon_3}\right|^2$ are known as the mixing coefficients of the resulting wave function, where $n = 1$ corresponds to the largest contribution in Eq. (3.37) and the terms with $n = 2,\ 3...$ are ranked in the decreasing order of the mixing coefficients. In the proposed procedure, the approximate vibrational quantum numbers u_1, u_2, u_3 are chosen to coincide with those of the $\left|\upsilon_1\upsilon_2\upsilon_3\right\rangle$ basis function (Eq. 3.37) which has the maximal value of the mixing coefficient P_1.

It is worth noting, that for the highly excited states the EH-wavefunctions seem to be greatly mixed without pronounced maximum, what prevents establishing the unambiguous labelling, still one can trace, which basic functions contribute to the resulting wave function.

5. Global variational calculations. Main characteristic features and applications to the rovibrational spectra analysis

The traditional method just described in the two previous Sections faces with the certain problems both when describing highly excited rovibrational state of the water molecule and by considering abnormal dependence of spectroscopic parameters on the deformation (bending) vibration. That is why in recent years the alternative approaches have been actively developed. Among these methods, developed for the calculation of rovibrational energy levels of the water molecule, variational methods are becoming commonly used.

The variation method, which allows one to approximate the ground state energy of a system without solving the Schrödinger equation, is based on the variation theorem [40]:

For a system, whose Hamiltonian operator H is time independent and whose lowest energy eigenvalue is E_1 and ψ is any normalized, well-behaved function of the system's particles coordinates that satisfies the boundary conditions of the problem, then

$$\int \psi^* H \psi d\tau \geq E_1 \tag{3.38}$$

The variation theorem allows one to calculate an upper bound for the system's ground state energy. In this linear variational method, the required wave function is expanded in terms of complete, orthonormal set of eingenfunctions of *H,* the stationary-state eingenfunctions $\{\phi_i\}$:

$$\psi = \sum_{i=1}^{m} c_i \phi_i \,, \tag{3.39}$$

where *m* define the dimension of the basic set $\{\phi_i\}$ and c_i are constants. The function ψ is called a *trial variational function*, and the integral in (3.38) is called the *variational integral*. In order to arrive at a good approximation to the ground state energy E_1, one tries many trial variation functions and look for the one that gives the lowest value of the variational integral. As evident from (3.38), the lower value of the variational integral, the better the approximation one has to E_1. The ground state wavefunction gives the minimum value of the variational integral. Thus, the lower the value of the variational integral, the closer the trial variational function will approach the true ground state wavefunction. In practice, one usually puts several parameters into the trial function ψ, and then varies these parameters so as to minimize the variational integral. Successful use of the variation method depends on the ability to make a good choice for the trial function.

The practical realization of this method requires large computational resources and so it is now applied mostly for the triatomic molecules containing the least quantity of internal vibrational coordinates. The H_{VR} form depends on the set of internal coordinates, which is usually choosen in such a way as to provide a simple geometrical interpretation. In the case of the triatomic molecules the valence [41], Radau [42] and hyperspherical [41] coordinates are used. The description of these coordinates and the corresponding kinetic energy operator forms are given in Ref. [41]-[43].

Nowadays, a great number of programs for the rovibrational energy calculation by linear variational method are developed, the exhaustive review is given in Ref. [44]. Partridge and Schwenke (PS) [1]-[14] used the Hamiltonian presented in Radau coordinates and evaluated the potential energy function by means of the high accuracy *ab initio* calculations for the large set of nuclear configurations. This potential energy function was then optimized by the fit to experimental data available in HITRAN-92. Not only the dominant isotopic species $H_2{}^{16}O$, but also $HD^{16}O$, $H_2{}^{16}O$, $D_2{}^{16}O$, $H_2{}^{17}O$ and $H_2{}^{18}O$ isotopologues were considered, which allowed for taking into account the adiabatic corrections. Thus, the PS potential energy surface (PES) is mass-dependent.

The *ab initio* calculation of the dipole moment surface (DMS) for water, which allows one to define the dipole moment of the molecule at any nuclear configuration was also performed in Ref. [1]-[14]. As a result, a good agreement between the experimental and calculated values of line position and intensities for 30000 lines was obtained with the *rms* deviation less than 0.08 cm^{-1} for the line centres. It is worth noting, that such a kind of calculations which allows one to describe the whole rovibrational spectrum from a united set of constants of the PES and DMS were performed for the water molecule for the first time.

The PS PES [1]-[14] was further improved by Shirin et al. [47]-[49] (for the $H_2{}^{16}O$, $H_2{}^{17}O$ and $H_2{}^{18}O$ and D_2O molecules) by means of the DVR3D nuclear motion program suite [50]. Recently, the high accuracy variational linelist was computed by Voronin, Tolchenov and Tennyson (VTT) [51] for the HDO molecule using the spectroscopically determined HDO PES of Yurchenko et al. [52], the so-called CVR dipole moment surface [53], and the DVR3D nuclear motion program suite [50].

In our study, we used all of these variational calculations for the identification of the observed rovibrational spectra of water isotopologues, as each of them has specific advantages, as shown in Chapter IV. The spectrum assignment procedure relies on well-known features of variational calculation: the smooth and slow variation of deviations of the observed levels from their calculated values for the energy levels of a particular vibrational state having the same K_a and increasing J values [54]. Though the (obs.-calc.) values may reach up to several cm^{-1}, which leads to tens of experimental lines as possible candidates for the considered assignment, the existence of evident (obs.-calc.) tendencies combined with intensity matching still provides reliable assignments. As one example, the residuals of the observed [55] minus calculated by VTT [51] energy levels of $HD^{16}O$ for the (000) state with $K_a = 1-5$ are shown in Figure 3.2.

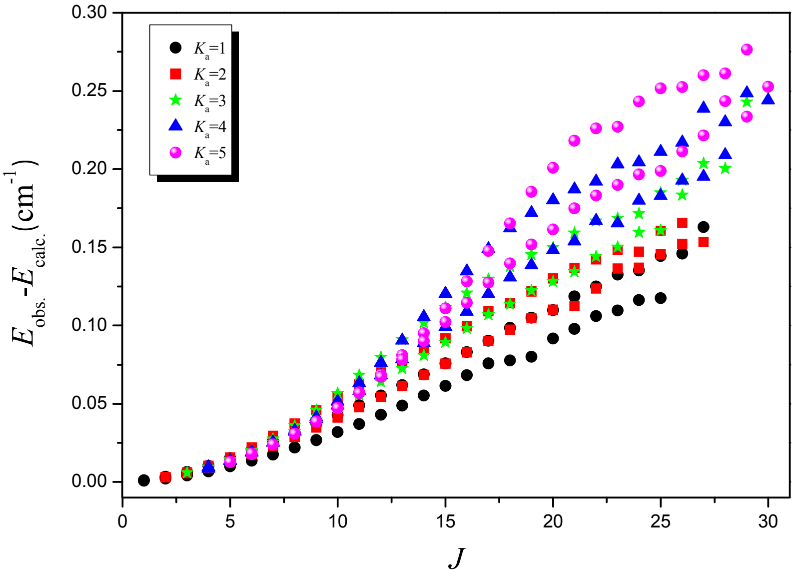

Figure 3.2. Residuals of observed (IUPAC TG [55]) minus calculated (VTT [51]) energy levels of $HD^{16}O$ for the ground vibrational state and K_a between 1 and 5. (adapted from Ref. [55]).

Despite the fact that the variational calculations do not require knowledge of "resonance interactions", the traces of perturbations caused by the occurrence of the close values of the energy levels are distinctly seen in variational calculations. Indeed, the (obs.-calc.) tendencies for the highly excited vibrational states investigated in our study are not particularly smooth as they can be strongly perturbed by nearby states. Examples of the (obs.-calc.) trend perturbations due to resonance interactions for the HDO molecule are clearly seen in Figure 3.3.

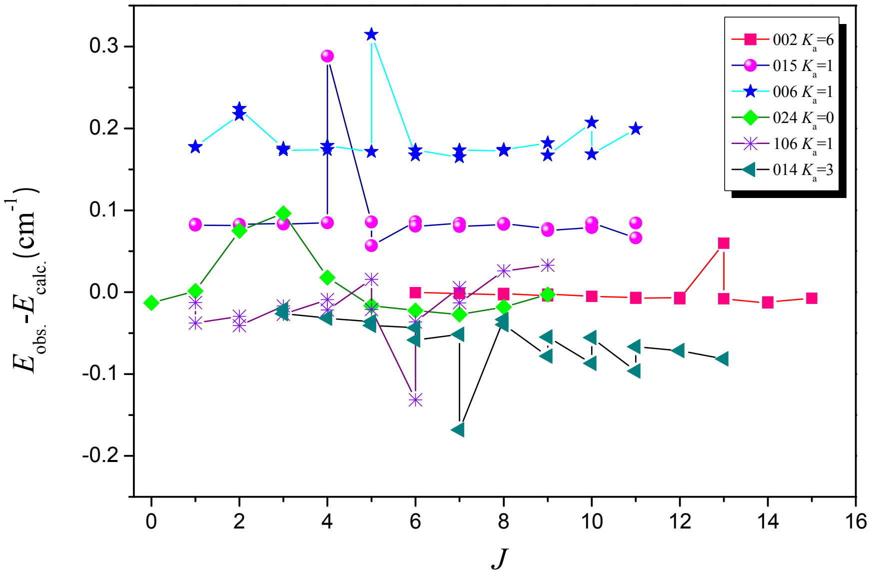

Figure 3.3. Variation of the differences between the observed (IUPAC TG [55]) and calculated (VTT [51]) values for the HDO energy levels of the (002), (015), (006), (024), (106) and (014) vibrational states with K_a=0, 1, 3, 6 as a function of the rotational quantum number J.

Thus, in the case of transitions reaching upper levels in close resonance, the accuracy of variational calculation can be considerably decreased for positions and especially for intensities. These intensity distortions are caused by inaccurate evaluation of the wavefunctions of interacting energy levels and do not depend on the dipole moment function. For instance, in case of HDO, intensity perturbation by several orders of magnitude can occur when interacting levels coincide within 1 cm^{-1} [56]. One example of the intensity distortion was described in Ref. [57], where in the course of the FTS spectrum of HDO analysis it was found that the whole (330)-(000) band of 31 lines is significantly perturbed due to resonance coupling with the (013)-(000) band. Half of line intensities of the (330)-(000) band was observed strongly underestimated, while the other half-overestimated to nearly the same extent, yielding a good average $I_{\text{obs}} / I_{\text{calc}}$ ratio of 1.17. Figure 3.4 shows the observed to calculated intensity ratios for mostly unperturbed (005)-(000) band and for the highly perturbed (330)-(000) band observed in Ref. [57]. Accurate experimental intensities, such as those available in the present study, provide an opportunity to study intensity redistribution between lines involving resonance partners.

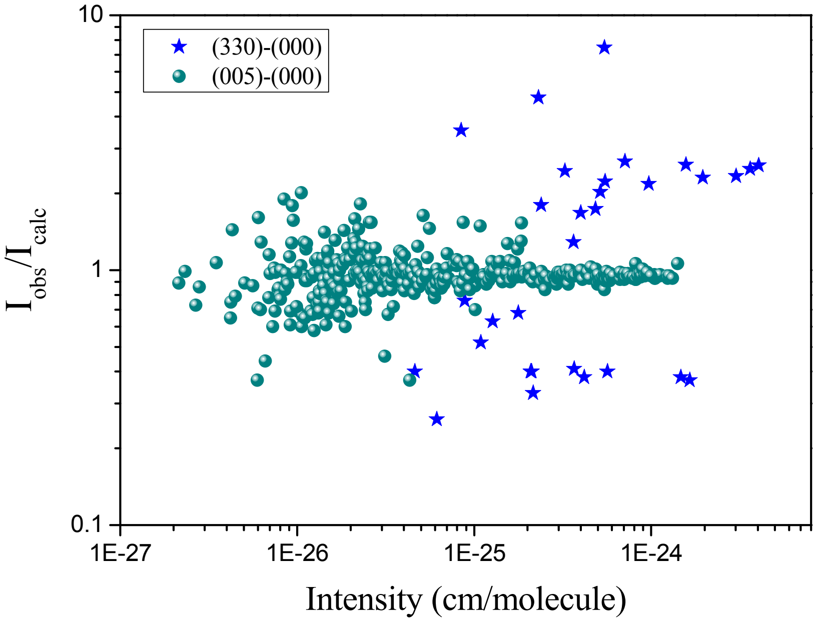

Figure 3.4. Ratio of the observed to calculated line intensities for largely unperturbed (005)-(000) band and for highly perturbed (330)-(000) band (adapted from Ref. [57]).

The spectrum assignment implies not only the evaluation of upper and lower energy state involved in the transitions, but also the association of each rovibrational level with the set of quantum numbers, hereafter called as labelling.

In our study for the labelling of the rovibrational energy levels, the usual quantum numbers used by spectroscopists are adopted. In the case of the vibrations of water, it is the standard normal coordinates labelling ($\upsilon_1\ \upsilon_2\ \upsilon_3$). In this notation υ_1, υ_2 and υ_3 stand for the symmetric stretching, bending, and antisymmetric stretching quantum numbers, respectively. In order to label the rotational states the standard asymmetric top quantum numbers $J\ K_a\ K_c$ are used. Thus, the rovibrational levels of each isotopologue are identified uniquely by six labels altogether ($\upsilon_1\ \upsilon_2\ \upsilon_3,\ J\ K_a\ K_c$).

It is worth noting, that all of the labels except J described above are only approximate ones and methods to identify the most appropriate labels for highly excited energy states of water are still a matter of active research [58]. Rigorous labels, if the hyperfine coupling associated with the nuclear spins is neglected, are the total rotational angular momentum, J, and the total parity, p. There is an additional quantum number specifying ortho and para states, provided the very weak coupling [59] between such states is neglected. The number $q = (K_\mathrm{a} + K_\mathrm{c} + \upsilon_3)$ is even for para states and odd for ortho ones. One more number n is added to completely specify each energy level. n is the position of a given energy level in the block of Hamiltonian matrix for a given combination of J; p and q. This labelling is a natural one for energy levels obtained from variational computations but is of only limited usefulness when analyzing experimental data since these rarely give a complete set of levels. One of the advantages of the presently used PS variational calculations [1]-[14] is that the matching algorithm for the two sets of quantum numbers (rigorous J; p, q. and approximate $\upsilon_1\ \upsilon_2\ \upsilon_3$, $J\ K_\mathrm{a}\ K_\mathrm{c}$) is included in the program suite [60]. However, when J increases the algorithm performance deteriorates, which leads to the superfluous attribution of the energy levels to the same J-multiplet of a given vibrational state ($N > 2J + 1$, for given J) and their deficiency for the other vibrational state ($N < 2J + 1$). Thus, the labelling could be not unique, i.e. for the one vibrational state there is more than one set of energy levels. For example, for H_2O this labelling procedure can give the same assignment to a whole set of rotational sublevels belonging to different vibrational states such as the ($\upsilon_1\upsilon_2\upsilon_3$) and ($\upsilon_1 - 2\ \upsilon_2\ \upsilon_3 + 2$) states. These states are separated by more than 700 cm^{-1} and do not interact in effective Hamiltonian representations.

Thus, for deeper understanding of the intramolecular dynamics and reliable rovibrational labelling, the resonance interactions between the analyzed states have to be considered. Indeed, knowledge of resonance interaction scheme, which is naturally determined in the course of energy levels modelling in the frame of effective Hamiltonian (EH) approach, allows one to overcome the ambiguities of assignment and avoid the errors when using the variational calculations. That is why in the course of our study the calculations within an EH approach were performed to confirm the rovibrational labelling. This reflects the relationship and complementarity of the two types of calculations.

6. Expert system for identification of high resolution rovibrational spectra

Modern experimental setups like Fourier transform spectrometers allow measuring thousands of spectral lines in a relatively short period of time, while the theoretical analysis of this information may last much longer. High resolution rovibrational (RV) spectra of the asymmetric top molecules have no expressed characteristic features like the symmetric top or diatomic molecules, where the systems of equidistant lines can be easily traced. Consequently, the assignment of the asymmetric top molecules RV transitions relies in a large extent of the preliminary calculation of the line position and intensity.

Rydberg-Ritz combination rule

The Rydberg -Ritz combination rule represents a powerful tool of the molecular spectra identification. According to this rule, the analyzed experimental spectrum contains the systems of lines whose centres by pairs obey the relationship

$$\left\| \nu_{n_1}^{\mathrm{e}} - \nu_{n_2}^{\mathrm{e}} \right| - \left| \nu_{fi_1}^{c} - \nu_{fi_2}^{c} \right\| \le \Delta\nu_{n_1} + \Delta\nu_{n_2} \tag{3.40}$$

where $\nu_{n_1}^{\mathrm{e}}$, $\nu_{n_2}^{\mathrm{e}}$, $\nu_{fi_1}^{c}$, $\nu_{fi_2}^{c}$ are the calculated and measured line centres; n_1 and n_2 are the line numbers; $\Delta\nu_{n_1}$, $\Delta\nu_{n_2}$ are measurements errors; i_1 and i_2 are the quantum numbers of the initial levels of the transitions $f \leftarrow i_1$ and $f \leftarrow i_2$, respectively. Here, it is supposed that the energy of the initial levels (to be certain, we consider it as a ground vibrational state) is previously determined with higher accuracy than $\Delta\nu_n$. Hereafter, the group of lines obeying combination difference (CD) criterion (3.40) is called as a CD-group. Note that the differences in (3.40) are independent of errors in calculation of the upper levels, i.e. even the calculation of poor accuracy can be applied. Figure 3.5 shows an example of formation of the CD-group. The systems of lines obeying the combination rule can be easily found in the experimental spectrum, however, if the analyzed spectrum is crowded, a number of the suitable systems of lines can be large, and additional criteria are needed to choose the correct variant.

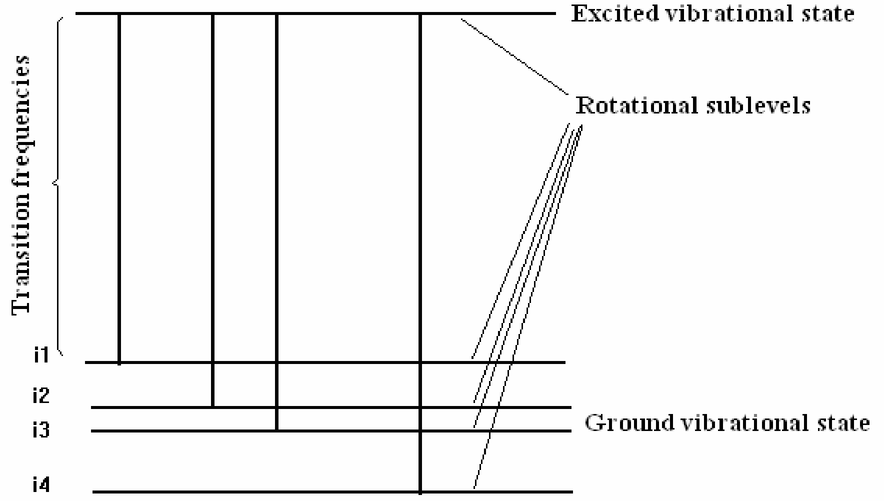

Figure 3.5. The schematic illustration of the formation of the CD-group of lines.

The informative indicators applied for recognition of the CD-group

The expert system was created in Institute of Atmospheric Optics (Tomsk, Russia) [61], [62], which can search and identify lines included in the combination difference. In what follows, we outline the main ideas employed to develop the Expert system as well as give a short description of its operating and built in service, omitting the mathematical aspects which can be found in [61], [62]. This expert system uses the pattern recognition theory [63]-[65] to discriminate the correct variant among many realizations of the combination rule. Such a problem is a typical one for the pattern recognition theory and mathematical statistics methods and algorithms can be naturally applied to the spectrum analysis facilitation. The only correct variant of CD is chosen by a researcher using a number of indicators, i.e. definite combination of the line characteristics.

To apply the pattern recognition theory it is necessary to specify the objects (i.e. the characteristic features) to be recognized and their indicators. The analysis shows that to make the line assignment it is necessary to use simultaneously the Rydberg-Ritz combination rule, which is the only accurate one free of model limitations, along with the calculated lines characteristics (their positions and intensities). This provides reliability and generality of the recognition rules. Thus, the pattern recognition problem reduces to determination of the similarity of the observed and calculated characteristics within the array of lines satisfying approximately the combination rule. It is obvious that in order to obtain a flexible system the use of algorithms with training to recognition is desirable in this case.

Each line under consideration has definite characteristic that can serve as an indicators for comparison of different variants of the CD's and choosing the best one. The following characteristics have been found to be expedient: (*1*) deviation of the measured line frequency from the calculated one; (*2*) deviation of the measured line intensity from the calculated one; (3) accuracy of the combination rule fulfilment for a given line; (*4*) deviation of the measured line intensity from the calculated average (over the total set) value; (5) proportionality, on the average, of the measured and calculated line intensity; (6) the ratio of the summed intensity for all the experimental lines found to the calculated total intensity; (7) accuracy of the combination rule fulfilment throughout the group. These indicators were found to work very efficiently: two choices of the correct variant provided by the researcher are usually enough to teach system to find the correct variant automatically without the error.

The input and output information and operating the Expert system

To start the expert system, it is necessary to input the experimental linelist consisting of line positions and intensities (absorption, transmittance) and the rotational, centrifugal distortion, resonance parameters, which are used to calculate upper and lower energy levels and then the wavenumbers of transitions falling into analyzed spectral region. Three types of the effective rotational Hamiltonians are available in the system: well known Watson - type operator and two modern representations of the rotational Hamiltonian's matrix elements through the Pade-Borel approximants [12] and the generating functions [15]. All possible anharmonic and Coriolis-type interactions between the considered rovibrational states can be also accounted for.

The transformed transition moment parameters necessary to calculate transition intensity can be either inputted or evaluated by the system from the correspondence of the observed and calculated intensities. The expert system can also work with the synthetic spectrum file prepared by other program in the required format. Some additional information concerning the quality of the experimental and calculated spectra is also required like the estimated accuracy of the combination rule validity, which depend on the accuracy of the experimental line positions, and the interval in lines inside which the CDs are searched for, which depends, mainly, on the accuracy of the calculated positions.

The best variant of the CD connected to the considered upper energy level is placed on the screen, while the researcher can list all variants and choose another one. Figure 3.6 shows the best variant of CD proposed by the expert system for the (310) [845] energy level of $HD^{16}O$ molecule. On panel *B* in Figure 3.6 the current state of the database for the spectrum is shown: all, but one, of eight found experimental lines have no identification in the database. The line №1 has already one assignment, though we can add one more identification according to the expert system. Up to three assignments on the same experimental line are available. The preliminary experimental energy of the upper level averaged on the CD-group is given (10092.51198 cm^{-1}) followed by its *rms* uncertainty in 10^{-3} cm^{-1} (6.318), and number of lines used in the level determination (8).

Panel *C* in Figure 3.6 illustrates the result of acceptance of this variant of the CD: all the eight lines received their RV assignment in the database for the spectrum. The upper level is determined from the six lines and is written into the database for the energy levels with the energy of 10092.5126 cm^{-1} and sufficiently lesser *rms* uncertainty of 1.126×10^{-3} cm^{-1}. In order to derive as accurate upper level as possible, the clear outliers can be excluded from the CD, though these outliers will be kept in the database for the spectrum for completeness of assignment. Thus, the line number one, which represent the unresolved doublet, and the weakest line number ten have been excluded from a level determination, though they left assigned in the spectrum database.

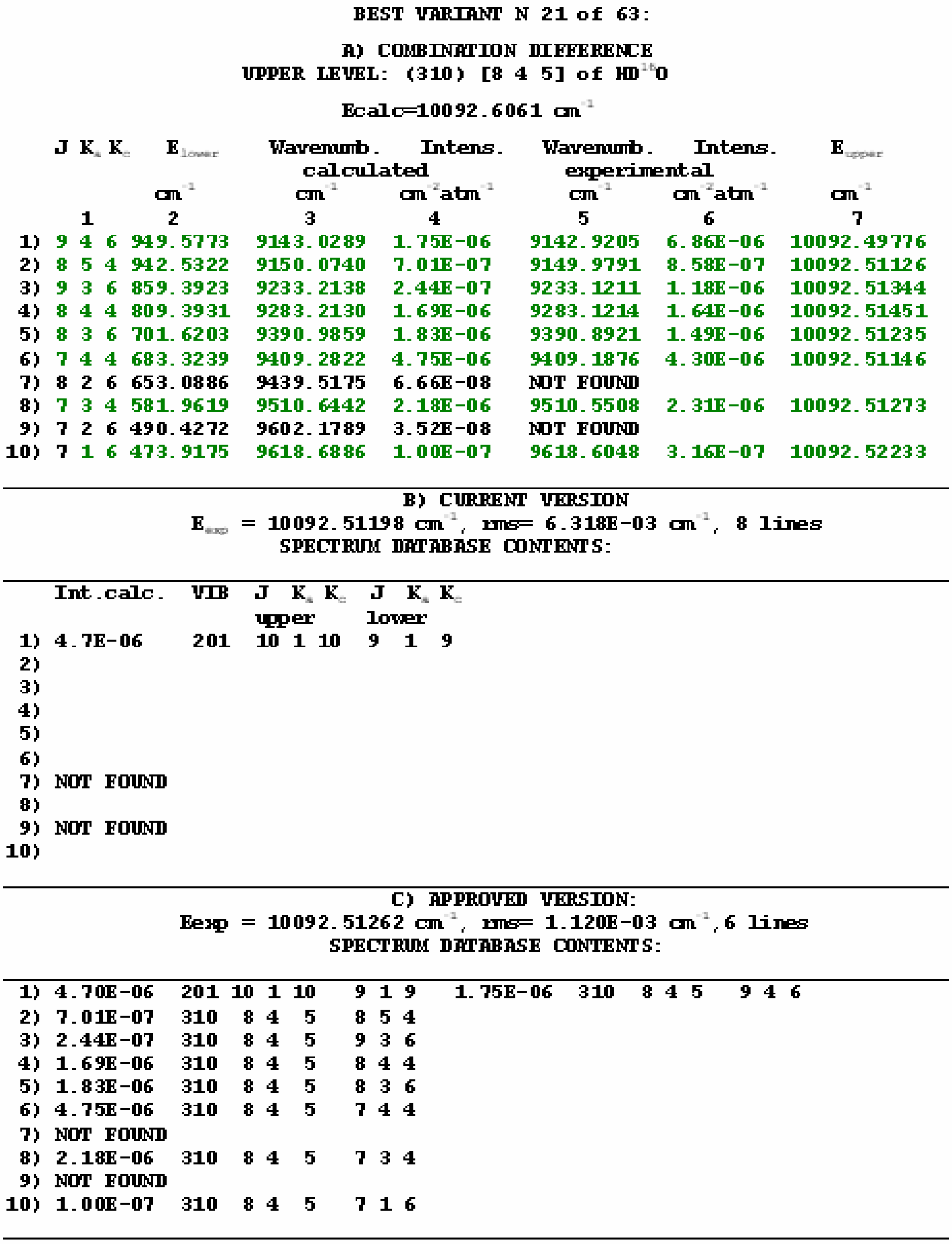

```
                         BEST VARIANT N 21 of 63:

                        A) COMBINATION DIFFERENCE
                  UPPER LEVEL: (310) [8 4 5] of HD16O

                         Ecalc=10092.6061 cm-1

    J Ka Kc   Elower     Wavenumb.   Intens.    Wavenumb.   Intens.     Eupper
                               calculated             experimental
              cm-1       cm-1        cm-2atm-1  cm-1        cm-2atm-1   cm-1
      1         2          3           4          5           6           7
 1) 9 4 6 949.5773   9143.0289  1.75E-06   9142.9205  6.86E-06  10092.49776
 2) 8 5 4 942.5322   9150.0740  7.01E-07   9149.9791  8.58E-07  10092.51126
 3) 9 3 6 859.3923   9233.2138  2.44E-07   9233.1211  1.18E-06  10092.51344
 4) 8 4 4 809.3931   9283.2130  1.69E-06   9283.1214  1.64E-06  10092.51451
 5) 8 3 6 701.6203   9390.9859  1.83E-06   9390.8921  1.49E-06  10092.51235
 6) 7 4 4 683.3239   9409.2822  4.75E-06   9409.1876  4.30E-06  10092.51146
 7) 8 2 6 653.0886   9439.5175  6.66E-08   NOT FOUND
 8) 7 3 4 581.9619   9510.6442  2.18E-06   9510.5508  2.31E-06  10092.51273
 9) 7 2 6 490.4272   9602.1789  3.52E-08   NOT FOUND
10) 7 1 6 473.9175   9618.6886  1.00E-07   9618.6048  3.16E-07  10092.52233
--------------------------------------------------------------------------------
                           B) CURRENT VERSION
           Eexp = 10092.51198 cm-1, rms= 6.318E-03 cm-1, 8 lines
                       SPECTRUM DATABASE CONTENTS:
--------------------------------------------------------------------------------
    Int.calc.   VIB  J  Ka Kc  J  Ka Kc
                     upper     lower
 1) 4.7E-06     201  10 1 10   9  1  9
 2)
 3)
 4)
 5)
 6)
 7) NOT FOUND
 8)
 9) NOT FOUND
10)
--------------------------------------------------------------------------------
                          C) APPROVED VERSION:
           Eexp = 10092.51262 cm-1, rms= 1.120E-03 cm-1,6 lines
                       SPECTRUM DATABASE CONTENTS:
--------------------------------------------------------------------------------
 1) 4.70E-06  201 10 1 10   9 1 9   1.75E-06  310  8 4 5   9 4 6
 2) 7.01E-07  310  8 4  5   8 5 4
 3) 2.44E-07  310  8 4  5   9 3 6
 4) 1.69E-06  310  8 4  5   8 4 4
 5) 1.83E-06  310  8 4  5   8 3 6
 6) 4.75E-06  310  8 4  5   7 4 4
 7) NOT FOUND
 8) 2.18E-06  310  8 4  5   7 3 4
 9) NOT FOUND
10) 1.00E-07  310  8 4  5   7 1 6
--------------------------------------------------------------------------------
```

Figure 3.6. The best variant of the CD-group proposed by the expert system for the (310) [845] energy level of the HD^{16}O molecule. *A*. The columns are as follows: (1) rotational quantum numbers of the lower state, (2) the energy of the lower state in cm^{-1}, (3) calculated transition wavenumber in cm^{-1}, (4) calculated transition intensity in cm^{-2} atm^{-1}, (5) experimental wavenumber in cm^{-1}, (6) experimental intensity in cm^{-2} atm^{-1}, (7) experimental value of the upper level in cm^{-1}. On panels *B* and *C* – current and accepted experimental energy of the upper level, respectively, is given, as well as contents of the database for spectrum before and after confirmation by the researcher.

As the rotational and vibrational excitation increases, the transitions become weaker and the CDs become poorer. Finally, only one transition coming on the upper level is available. The assignment, however, is possible in this case too, but the choice is, mostly, on the researcher, and the agreement with the calculated position and intensity remains the only criterion of the correct assignment of line. In case of strong and accurate spectrum with CD-groups of large size, the automatic mode can be run for “trained” system in the CD's regime only. This automatic mode is recommended for use on the initial stage of spectrum assignment only, and the resulting identification requires further refinement.

The contents of the energy levels and spectrum database can be outputted in the form of tables suitable for further use in computations and publications. Since its creation in 1997, the expert system [61], [62] has been successively applied for the assignment of high resolution rovibrational spectra of water vapour and its isotopologues, hydrogen sulphide and its isotopologues (see, for example Refs. [66]-[68]). It can also be applied to any triatomic molecule of the C_{2V} or C_S symmetry. This system optimally combine the efficiency in the line assignment with the opportunity to check directly every upper level derived, what add to the reliability of the resulting information. We have exploited this expert system for the identification of all the experimental spectra included in Chapter IV.

References for Chapter III

[1] M. Born and J. R. Oppenheimer. Zur Quantentheorie der Molekeln. Ann. Phys. 389, 1927; 457.

[2] P. Jensen, P. R. Bunker. The BO approximation. *Computational Molecular Spectroscopy*. (P. Jensen and P.R. Bunker, Eds).Wiley, 2000.

[3] D. Papoushek, M. R. Aliev. *Molecular Vibrational-Rotational Spectra.* Elsevier-Academia. 1982.

[4] A. D. Bykov, L. N. Sinitsa, V. I. Starikov. *Introduction in rovibrational spectroscopy of polyatomic molecules*. Tomsk. Publishing House of the IAO SB RAS, 2004.

[5] G. Amat, H. H. Nielsen, C. Torrago. *Rotation-vibration of polyatomic molecules*. New York: M.Dekker. Inc., 1971.

[6] H. H. Nielsen. The vibration-rotation energies of molecules and their spectra in the infra-red. Handbuch der Physik. 37, 1959; 173.

[7] E. Br. Wilson, J. B. Howard. The vibration-rotation energy levels of polyatomic molecules. I. Mathematical theory of semirigid asymmetrical top molecules. J. Chem. Phys. 4, 1936; 260.

[8] B. T. Darling, D.M. Dennison. The water vapor molecule. Phys. Rev. 57, 1940; 128.

[9] J. K. G. Watson. Simplification of the molecular vibration-rotation Hamiltonian. Mol. Phys. 15, 1968; 479.

[10] H. H. Nielsen. The vibration-rotation energies of polyatomic molecules. Phys. Rev. 60, 1941; 794.

[11] G. Amat, M. Goldsmith, H. H. Nielsen. Higher order rotation-vibration energies of polyatomic molecules. I-II. J. Chem. Phys. 24, 1957; 1178.

[12] Vl. G. Tyuterev. Contact transformation and dynamic variables, in "Molecular High-Resolution Spectroscopy" – Novosibirsk, Nauka, 93-115, 1976. (*in Russian*)

[13] J. N. Van Vleck. On σ-type doubling and electron spin in the spectra of a diatomic molecules. Phys. Rev. 33, 1929; 467.

[14] J. K. G. Watson. Determination of centrifugal distortion coefficients of asymmetric-top molecules. J. Chem. Phys. 46, 1967; 1935.

[15] A. D. Bykov, L. N. Sinitsa, V. I. Starikov. *Experimental and theoretical methods in spectroscopy of the water vapor*. Novosibirsk. Publishing House of SB RAS, 1999.

[16] Y. Y. Kwan. The interacting states of an asymmetric top molecule XY_2 of the group C_{2v}. Application to five interacting states: (101), (021), (120), (200) and (002) of $H_2{}^{16}O$. J. Mol. Spectrosc. 71, 1978; 260.

[17] V. I. Perevalov, Vl. G Tyuterev. Centrifigual distortion of molecules in the case of accidental resonances. Tomsk, SB RAS, 1979. (*in Russian*)

[18] V. I. Perevalov, Vl. G Tyuterev. Model with unambiguously derived parameters in simultaneous treatment of two resonating vibrational states of asymmetric top molecules. Izv. Vuzov. Physics.2, 1982;. 108. (*in Russian*)

[19] V. I. Perevalov, Vl. G Tyuterev. Centrifigual distortions of asymmetric top molecules in the case of Fermi-type resonances (contact transformations in the quasidegenerate case). Optics and spectroscopy. 51, 1981; 640. (*in Russian*)

[20] V. I. Perevalov, Vl. G Tyuterev. Reduction of the centrifugal distortion Hamiltonian of asymmetric top molecules in the case of accidental resonances: two interacting states. lower-order terms. J. Mol. Spectrosc. 96, 1982; 56.

[21] O. N. Ulenikov, A. B. Malikova, M. Koivusaari, S. Alanko, R. Anttila. high resolution vibrational-rotational spectrum of H_2S in the region of the ν_2 fundamental band. J. Mol. Spectrosc. 176, 1996; 229.

[22] Vl. G. Tyuterev. The generating function approach to the formulation of the effective rotational Hamiltonian. Simple closed form model describing strong centrifugal distortion in water type molecules. J. Mol. Spectrosc. 151, 1992; 97.

[23] Vl. G. Tyuterev, V. I. Starikov, S.A. Tashkun, S.N. Mikhailenko. Calculation of high rotational energies of water molecule using the generation function model. J. Mol. Spectrosc. 170, 1995; 38.

[24] C. Camy-Peyret, J. M. Flaud. Line positions and intensities in the$\square_2$ band of $H_2{}^{16}O$. Mol. Phys. 32, 1976; 523.

[25] E. Kyro. Centrifugal distortion analysis of pure rotational spectra of $H_2{}^{16}O$, $H_2{}^{17}O$, and $H_2{}^{18}O$. J. Mol. Spectrosc. 88, 1981; 167.

[26] V. I. Starikov, Vl. G. Tyuterev. *Intramolecular ro-vibrational interactions and theoretical methods in the spectroscopy of nonrigid molecules*. Tomsk, SB RAS, 1997. (*in Russian).*

[27] A. V. Burenin, M. Yu. Ryabikin. The method for treatment of highly excited vibration-rotational states of simple molecules: Diatomic molecule. J. Mol. Spectrosc. 136, 1989; 140.

[28] A. V. Burenin. On the convergence of rational series when treating spectra of quantum systems. J. Mol. Spectrosc. 136, 1989; 140.

[29] A. V. Burenin. Optimum rational perturbation theory series when treating rotational spectra of nonlinear molecules. J. Mol. Spectrosc. 140, 1990; 54.

[30] V. I. Starikov, S.A. Tashkun, Vl.G. Tyuterev. Description of vibration-rotation energies of nonrigid triatomic molecules using the generating function method. Bending states of water molecule. J. Mol. Spectrosc. 151, 1992;130-147.

[31] Vl. G. Tyuterev, A.V. Burenin, V.I. Perevalov, V.I. Starikov. General method for the reduction of the effective rotational Hamiltonian of molecules. Rotational approximants and Padé approximants. Rus. Phys. J. 28, 1985; 633.

[32] O. L. Polyansky. One-dimensional approximation of the effective rotational Hamiltonian of the ground state of the water molecule. J. Mol. Spectrosc. 112, 1985; 79.

[33] C. Camy-Peyret, J.-M. Flaud, J.-Y. Mandin, A. Bykov, O. Naumenko, L. Sinitsa, B. Voronin. Fourier-transform absorption spectrum of the $H_2{}^{17}O$ molecule in the 9711-11335 cm^{-1} spectral region: the first decade of resonating states. J Quant Spectrosc Radiat Transfer. 61, 1999; 795.

[34] A. Bykov, O. Naumenko, L. Sinitsa, B. Voronin, B. P. Winnewisser. The $3\nu_2$ band of $D_2{}^{16}O$. J. Mol. Spectrosc. 199, 2000; 158.

[35] H. Bateman, A. Erdélyi. *Higher transcendental functions*. Krieger Pub Co, 1981.

[36] L. S. Rothman, D. Jacquemart, A. Barbe, D. C. Benner, M. Birk, L. R. Brown, et al. The HITRAN 2004 molecular spectroscopic database. J Quant Radiat Transfer. 96, 2005; 139.

[37] N. Jacquinet-Husson, N.A. Scott, A. Chédin, L. Crépeau, R. Armante, V. Capelle, J. Orphal, A. Coustenis, C. Boonne, N. Poulet-Crovisier, A. Barbe, M. Birk, L.R. Brown, C. Camy-Peyret, C. Claveau, K. Chance, N. Christidis, C. Clerbaux, P.F. Coheur, V. Dana, et al. The GEISA spectroscopic database: Current and future archive for Earth and planetary atmosphere studies. J. Quant. Spectrosc. Radiat. Transfer. 109, 2008; 1043.

[38] A. D. Bykov, Yu. S. Makushkin, O. N. Ulenikov. The vibrational analysis of $H_2{}^{16}O$. J. Mol. Spectrosc. 99, 1983; 221.

[39] O. V. Naumenko and A. Campargue. $H_2{}^{32}S$: First observation of the $(70^{\pm},0)$ local mode pair and updated global effective vibrational Hamiltonian. J. Mol. Spectrosc. 210, 2001; 224.

[40] I. N. Levine. *Quantum chemistry.* (5th Edition), Prentice Hall, New Jersey, 1999.

[41] B.P. Johnson, W.P. Reinhardt. Adiabatic separations of stretching and bending vibrations: Applications to H_2O. J. Chem. Phys. 85, 1986; 4538.

[42] R. Islampour, M. Gharibi, M. Miralinaghi. The molecular Hamiltonian in Jacobi coordinates. Molecular Physics. 104, 2006; 1879.

[43] Z. Bacic, D. Walt, J. C. Light. A variational localised representation calculation of the vibrational levels of the water molecule up to 27000 cm^{-1}. J. Chem. Phys. 89, 1988;. 947.

[44] J. Tennyson. Variational calculations of rotation-vibration spectra. *Computational Molecular Spectroscopy.* (P. Jensen and P.R. Bunker, Eds).Wiley, 2000.

[45] H. Partridge, D. W. Schwenke. The determination of an accurate isotope dependent potential energy surface for water from extensive ab initio calculations and experimental data. J Chem Phys 106, 1997; 4618.

[46] D. W. Schwenke, H. Partridge Convergence testing of the analytic representation of an ab initio dipole moment function for water: improved fitting yields improved intensities. J Chem Phys 113, 2000; 6592.

[47] S. V. Shirin, R. I. Ovsyannikov, N. F. Zobov, O. L. Polyansky, J. Tennyson. Water line lists close to experimental accuracy using a spectroscopically determined potential energy surfaces for $H_2{}^{16}O$, $H_2{}^{17}O$ and $H_2{}^{18}O$. J Chem Phys. 128, 2008; 2243061.

[48] S. V. Shirin, N. F. Zobov, O. L. Polyansky, J. Tennyson, T. Parekunnel and P.F. Bernath. Analysis of hot D_2O emission using spectroscopically determined potentials. J. Chem. Phys. 120, 2004; 206.

[49] S. V. Shirin, N. F. Zobov and O. L. Polyansky. Theoretical line list of $D_2{}^{16}O$ up to 16000 cm^{-1} with an accuracy close to experimental. J. Quant. Spectrosc. Radiat. Transfer. 109, 2008; 549.

[50] J. Tennyson, M.A. Kostin, P. Barletta, G.J. Harris, J. Ramanlal, O. L. Polyansky, N. F. Zobov. DVR3D: a program suite for the calculation of rotation-vibration spectra of triatomic molecules. Comp. Phys. Comm. 163, 2004; 85.

[51] B. A.Voronin, J.Tennyson, R. N. Tolchenov, A. A. Lugovskoy, S. N. Yurchenko. A high accuracy computed line list for the HDO molecule. Monthly Notices of the Royal Astronomical Society. 402, 2010; 492.

[52] S. N. Yurchenko, B. A. Voronin, R. N. Tolchenov, N. Doss, O. V. Naumenko, W. Thiel, et al. Potential energy surface of HDO up to 25000 cm^{-1}. J Chem Phys 128, 2008; 044312.

[53] L. Lodi, R.N. Tolchenov, J. Tennyson, A. E. Lynas-Gray, S. V. Shirin, N. F. Zobov, et al. A high accuracy dipole surface for water. J Chem Phys 128, 2008;044304.

[54] O.L. Polyansky, N.F. Zobov, S.Viti, J. Tennyson, P. F. Bernath, L.Wallace. K band spectrum of water in sunspots. Astrophys. J. 489, 1997; 205.

[55] J. Tennyson, P.F.Bernath, L. R. Brown, A. Campargue, M. R. Carleer, A. G. Császár et al. IUPAC critical evaluation of the rotational-vibrational spectra of water vapor. Part II. Energy levels and transition wavenumbers for $HD^{16}O$, $HD^{17}O$ and $HD^{18}O$. J Quant Radiat Transfer. 111, 2010; 2160.

[56] A. Campargue, I. Vasilenko and O. Naumenko. Intracavity laser absorption spectroscopy of HDO between 11 645 and 12 330 cm^{-1}. J. Mol. Spectrosc. 234, 2005; 216.

[57] B.A. Voronin, O.V. Naumenko, M. Carleer, P.-F. Coheur, S. Fally, A. Jenouvrier, R.N. Tolchenov, A.C. Vandaele, J. Tennyson. HDO absorption spectrum above 11500 cm^{-1}: Assignment and dynamic. J. Mol. Spectrosc. 244, 2007; 87.

[58] N. F. Zobov, R. I. Ovsyannikov, S. V. Shirin, O. L. Polyansky. The assignment of quantum numbers in the theoretical spectra of the $H_2{}^{16}O$, $H_2{}^{17}O$ and $H_2{}^{18}O$ molecules calculated by variational methods in the region 0-26000 cm^{-1}. Opt. Spectrosc. 102, 2007; 348.

[59] A. Miani, J. Tennyson. Can ortho-para transitions for water be observed? J. Chem Phys 120, 2004; 2732.

[60] D.W. Schwenke. Vibrational calculations of rovibrational energy levels and transition intensities for tetratomic molecules. J. Phys. Chem. 100, 1996; 2867.

[61] A.P. Shcherbakov. Application of pattern recognition theory to identification of the rovibrational spectral lines. Atmos. Oceanic. Opt. 10, 1997, 591.

[62] A. D. Bykov, O. V. Naumenko, A. M. Pshenichnikov, L. N. Sinitsa and A. P. Shcherbakov. An expert system for identification of lines in vibrational-rotational spectra. Optics and Spectroscopy. 94, 2003; 528.

[63] L. L. Levin. *Introduction into pattern recognition theory*. State University, Tomsk, 1982.

[64] M.E. Eljashberg, L. A. Gribov, V.V. Serov. *Molecular spectral analysis and Computer*. Nauka, Moscow. 1980.

[65] M.A. Aizerman, E. I. Braverman, and L.I. Posonoer. *Potential functions method in the* computer training problems. Nauka, Moscow, 1970.

[66] J. M. Flaud, C. Camy-Peyret, A. Bykov, O.V. Naumenko, T. Petrova, A. Shcherbakov, L. N. Sinitsa. The High-resolution spectrum of water vapor between 11600 and 12750 cm^{-1}. J Mol Spectrosc. 183, 1997; 300.

[67] Y. Ding, O. Naumenko, S.-M. Hu, Q. Zhu, E. Bertseva, A. Campargue. The absorption spectrum of H_2S between 9540 and 10 000 cm^{-1} by intracavity laser absorption spectroscopy with a vertical external cavity surface emitting laser. J. Mol. Spectrosc. 217, 2003, 222.

[68] B. A. Voronin, O.V. Naumenko, M. Carleer, P.-F. Coheur, S. Fally, A. Jenouvrier, R.N. Tolchenov, A.C. Vandaele, J. Tennyson. HDO absorption spectrum above 11500 cm^{-1}: Assignment and dynamic. J. Mol. Spectrosc. 244, 2007; 87.

[69] A.D. Bykov, O. V. Naumenko, E. R. Polovtseva, S.-M. Hu, A.-W. Liu. Fourier transform absorption spectrum of D_2O in 7360-8440 cm^{-1} spectral region. J. Quant. Spectrosc. Radiat. Transfer. 111, 2010; 2197.

Chapter IV: Theoretical treatment of the high resolution absorption spectra of the $D_2{}^{16}O$, $HD^{16}O$ and $H_2{}^{18}O$ molecules in the 8800-14100 cm^{-1} spectral region

1. Introduction

The high resolution spectroscopy of water molecule and its isotopologues is of great theoretical and practical interest. Despite the fact that water molecule is one of the simplest polyatomic molecules, numerous intra-molecular interactions are evidenced in the complicated high resolution spectra of water vapour. Extensive theoretical and experimental efforts in the study of high resolution water vapour spectra, led to a significant progress. In spite of this, the necessity of having more and more precise quantitative information leads to unabated interest in the water vapour spectra analysis. The strongest absorption lines of $H_2{}^{16}O$ and its isotopologues are well known from the microwave to the visible regions. However, weak transitions involving highly excited energy levels are still not properly accounted for neither experimentally nor theoretically.

Systematic investigation of the water isotopologues by high sensitivity Intracavity Laser Absorption Spectroscopy (ICLAS) and Fourier Transform spectroscopy (FTS) has been undertaken in the visible and near-infrared range. The high resolution absorption spectra of $D_2{}^{16}O$, $HD^{16}O$, $HD^{18}O$, $H_2{}^{18}O$ and $H_2{}^{17}O$ isotopic species were recorded and analyzed in a wide spectral region. The present Chapter is devoted to this extensive investigation and consists of seven Sections. Main aspects of ICLAS method are outlined in Section 2. It is followed by the presentation of our series of studies by ICLAS and FTS of D_2O absorption spectrum in spectral range from 8800 to 14020 cm^{-1} in Section 3. The analysis of the HDO absorption spectrum by ICLAS (Vertical external cavity surface emitting lasers and Ti:Sapphire laser) between 8800 and 14115 cm^{-1} is dealt with in Section 4. Section 5 presents our series of investigations of $H_2{}^{18}O$ enriched spectrum by ICLAS in the 12580-14100 cm^{-1} range. The derivation of the “reference” list of rovibrational transitions of the $D_2{}^{16}O$, $HD^{16}O$ and $H_2{}^{18}O$ molecules is described in Section 6. Discussion of the results in Section 7 concludes the Chapter.

1.1. General characteristics of the H_2O molecule

The water molecule, containing three nuclei and ten electrons, is one of the simplest molecules and, at the same time, it is the most abundant polyatomic molecule in the universe. H_2O is a nonlinear molecule consisting of two hydrogen atoms covalently bonded to a single oxygen atom. Its electronic structure is rather simple: the ground electronic state of water is very well separated from all the excited states. The equilibrium configuration of H_2O and D_2O molecules belong to the symmetry point group C_{2V}, while that of HDO molecule is of the symmetry point group C_S.

Oxygen has three stable isotopes: ^{16}O, ^{17}O, and ^{18}O, hydrogen has two: ^{1}H and ^{2}H (D-deuterium). Hence, there are nine stable isotopic modifications of H_2O, their relative concentration in water is presented in Table 4.1.

Table 4.1. Water molecule stable isotopic species, mass of isotope (a.m.u. - atomic mass unit), relative concentration (%).

		^{16}**O**	^{17}**O**	^{18}**O**
		99.757	0.038	0.205
^{1}**H** 99.9885	H_2O	99.7317	0.0371884	0.0199983
^{2}**H** 0.0115	HDO	0.031069	1.158×10^{-5}	6.23×10^{-5}
	D_2O	2.4197×10^{-6}	9×10^{-10}	4.9×10^{-9}

$m(^{16}O) = 15,9949149$ $m(^{1}H) = 1,00782160$
$m(^{17}O) = 16,9991400$ $m(^{2}H) = 2,01409468$
$m(^{18}O) = 17,9991527$ $m(^{3}H) = 3,01603815$

Note. The mass is indicated in a carbon scale; 1 a.m.u.= $1,6605655\ 10^{-24}$ g.

As a triatomic molecule, water has only three vibrational degrees of freedom, as shown in Figure 4.1. Of the three fundamental vibrations, two can be characterized as stretching vibrations – a symmetric and an antisymmetric one for symmetrically substituted isotopologues, while at about half of the energy of the stretches there is a totally symmetric bending vibration.

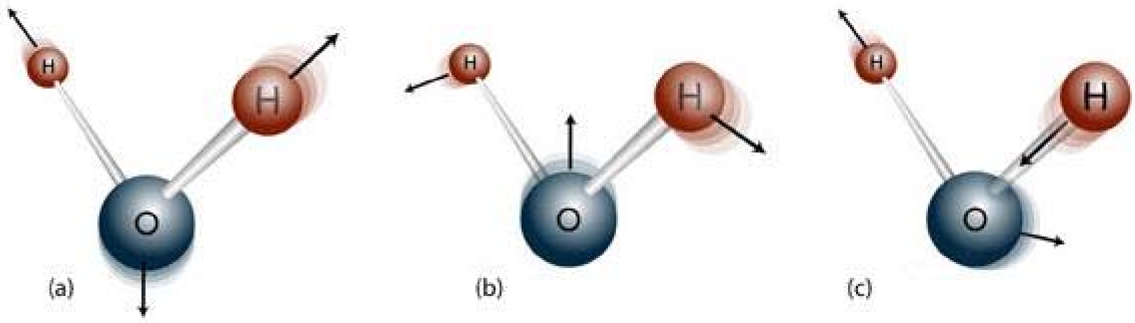

Figure 4.1. Normal mode of vibration for the H_2O molecule: (a) symmetric stretch ν_1; (b) bending vibration ν_2 and (c) antisymmetric stretch ν_3.

The fundamental frequencies ω_1, ω_2, ω_3 of the symmetrically substituted water isotopologues are such that $\omega_1 \approx 2\omega_2 \approx \omega_3$. Table 4.2 presents the fundamental frequencies of water isotopologues under consideration.

Table 4.2. Fundamental frequencies (cm^{-1}) of $H_2{}^{16}O$, $HD^{16}O$ and $D_2{}^{16}O$ molecules.

Molecule	ω_1	ω_2	ω_3
$H_2{}^{18}O$	3822	1642	3925
$HD^{16}O$	2823	1444	3888
$D_2{}^{16}O$	2763	1207	2890

Since all the three equilibrium moments of inertia are not equal, the water molecule is concerned as an asymmetric top. As a result of rather big difference between the three moment of inertia the rovibrational water spectrum is quite complex.

The nuclear dynamics of the water molecule exhibits several peculiarities. For example, due to the presence of two light hydrogen atoms, its vibrations are of large amplitude, and separation of the vibrational and rotational degrees of freedom is rather poor. It is worth noting, that substitution of H atom by D leads to a increase of the molecule mass and its moments of inertia. Therefore the stretching frequency decreases by a factor of about $\sqrt{2}$ and a given wavenumber region then corresponds to a higher stretching excitation (i.e. a smaller intensity) in D_2O compared to H_2O. In case of the HDO molecule, its intra-molecular dynamics differs significantly from that of the parent $H_2{}^{16}O$ species due to the decrease of symmetry from C_{2V} to C_S and considerable change in harmonic frequencies (Table 4.2). Due to large detuning (more than 1000 cm^{-1}) between ω_1 and ω_3 harmonic frequencies of $HD^{16}O$ (Table 4.2), the highly excited OH stretching states represent localized states.

The rovibrational spectrum of water spans over wide spectral region from MW to visible region. As a consequence of big permanent dipole moment (1.85 D) rotational transitions form the strong rotational spectrum, which extends over the range from 0.7 to 1647 cm^{-1}. Absorption spectrum of water vapour in near-infrared and visible regions is an alternation of the absorption bands and the transparency windows. Though the “strong part” of water vapour spectrum is substantially understood, there are serious problems in the recording of weak lines connected with transitions on highly excited rovibrational energy states in the near IR to UV spectral regions. In the present study to measure weak absorption lines of water vapour isotopologues $D_2{}^{16}O$, $HD^{16}O$ and $H_2{}^{18}O$, high sensitivity Intracavity Laser Absorption spectroscopy was used.

2. ICLAS

Intracavity Laser Absorption spectroscopy (ICLAS) is a technique possessing specific advantages in terms of sensitivity and spectral resolution that makes it particularly suitable for the characterization of spectral regions with weak absorption features.

Any type of laser with a homogeneously broadened gain medium and a resonator with low losses can be used for ICLAS. The basic principle is as follows. An absorbing medium with absorption lines narrower than the broadband spectrum of the laser is placed inside the cavity. When the laser is turned on, it starts to oscillate on many resonator modes simultaneously; only after many resonator round trips the spectrum of the generated light will strongly concentrate in the spectral region with the highest gain. During this evolution, weak absorption features of the sample can imprint signatures on the spectrum, because they can influence the spectrum during many round trips. A measurement of the spectrum is done some time after switching on the laser-generation time; this time should be long enough to allow for strong spectral features to develop, but also short enough to prevent too strong narrowing of the spectrum caused by the finite gain bandwidth [1]-[8]. An equivalent absorption path length of several hundred kilometres may be reached in such a configuration, resulting in detection limits as low as 10^{-10}-10^{-11} cm^{-1} [9].

In the present study, two ICLAS spectrometers were applied: experimental setup based on VeCSEL (8800-9640 cm^{-1}) and Ti:Sapphire (11400-14100 cm^{-1}) laser. A VeCSEL consists of a laser cavity with a semiconductor quantum wells structure used as the amplification medium. In this Section, the description of our ICLAS spectrometers is limited to their main characteristics. Further details on these spectrometers could be found in Refs. [10]-[14].

In our series of investigations, the experimental setup based on VeCSEL was applied to the study of D_2O and HDO absorption spectrum in the 8800-9520 cm^{-1} and 9100-9640 cm^{-1} spectral regions, respectively. The achieved sensitivity was of the order of $\alpha_{min} \sim 5\times10^{-9}$ cm^{-1}, which is less than the best performances achieved in other spectral regions (see for instance Refs. [14]-[16]) as a consequence of the poorer laser properties of the VeCSEL presently used. The spectra were recorded with generation times up to 130 μs, leading to equivalent absorption path lengths of the order of 23.4 km as the filling ratio of the laser cavity by the absorption cell was 60 %. The spectral resolution was about 0.04 cm^{-1} slightly larger than the Doppler broadening.

The ICLAS spectrometer based on a Ti:Sapphire laser was used to record the high resolution absorption spectra of D_2O, HDO and $H_2{}^{18}O$ in the 11300-14100 cm^{-1} spectral region accessible with our Ti:Sapphire laser. This ICLAS-Ti:Sapphire spectrometer allows for the detection of weak transitions with intensity down to 1-5×10^{-28} cm/ molecule. The spectra were recorded with a generation time of 190 µs corresponding to an equivalent absorption path length of 24 km. The length of the intracavity absorption cell was 65 cm which resulted in a 42% filling ratio of the Ti:Sapphire laser cavity. The cell was filled with the gas sample at pressures ranging between 2 and 20 hPa, but most of the recordings were performed at a pressure of 15.8 hPa or 18.4 hPa. The spectral resolution of the grating spectrograph was close to the Doppler line broadening. The ICLAS spectra were recorded successively within 12 cm^{-1} wide spectral section by the 3754 photodiode array placed at the exit of the spectrograph. The wavenumber calibration procedure of each individual spectrum requires the use of reference lines. For the wavenumber calibration, we used several absorption markers superimposed on the sample spectrum according to the spectral range of interest. This issue together with the line list construction is discussed in more detail in the corresponding Sections.

The ICLAS spectra analyzed in this thesis were recorded by Alain Campargue, Elena Bertseva and Fabio Mazzotti.

3. Fourier Transform and ICLAS absorption spectra of $D_2^{16}O$ in the 8800-14020 cm^{-1} spectral region

3.1 Introduction

This Section presents our series of studies of the $D_2^{16}O$ absorption spectrum by high sensitivity spectroscopy in the wide spectral range from 8800 to 14020 cm^{-1} (Figure 4.2). Information relative to the dideuterated water, D_2O, is important for many applications, such as studying the planetary atmospheres and interstellar molecules, characterizing the isotope effects on the main properties of the water molecule, and evaluating the adiabatic and nonadiabatic corrections to Born-Oppenheimer approximation in modelling the potential energy surface (PES) of water.

The D_2O spectrum in the near IR region is much less characterized than that of the monodeuterated species, HDO. By the time we started our investigations, the absorption spectrum of D_2O above 8100 cm^{-1} was the subject of a few reports: the $(\nu_1 + \nu_2/2 + \nu_3) = 3.5$ and 4 polyads near 9300 [17] and 10300 cm^{-1} [18] respectively, were investigated by Fourier Transform spectroscopy (FTS) with a 105 m path length. The 12570-12820 cm^{-1} section was recorded by ICLAS-Ti:Sapphire associated with a FTS detection scheme [19]. The 12450-12850 cm^{-1} spectral region has been probed with the high sensitivity ICLAS set up [20].

The first part of our D_2O study concerns the 8800-9520 cm^{-1} region [21], corresponding to the full coverage of the $(\nu_1 + \nu_2/2 + \nu_3) = 3.5$ polyad, which is the 2nd decade of resonating states (the 1st decade lying in the 7500−8300 cm^{-1} region has been analyzed in Refs. [22], [23]). The absorption spectrum was recorded in parallel by the Reims-Bruxelles group with high sensitivity FTS and in Grenoble by ICLAS based on Vertical external Cavity Surface Emitting Lasers (VeCSEL). An equivalent sensitivity corresponding to the detection limit $\alpha_{\min} \sim 5\times10^{-9}$ cm^{-1} was achieved in the two recordings allowing much deeper knowledge of this spectral region compared to [17].. As discussed below, the combination of the two spectra obtained by different methods proved to be a valuable help in the species and rovibrational assignment process. The analysis of the $D_2^{16}O$ absorption spectrum recorded between 10000 and 13200 cm^{-1} by the Reims-Bruxelles collaboration using a high sensitivity FTS spectrometer coupled to a long multiple reflection absorption cell of 50 m base length [24]. In the energy region above 11400 cm^{-1} the ICLAS spectrometer based on a Ti:Sapphire laser was used to record the very weak absorption spectrum of dideuterated water [25], [26], [27]. As shown in Figure 4.2, the D_2O spectrum in the 11400-11900 cm^{-1} region is dominated by two well-separated bands: the

$3\nu_1+\nu_2+\nu_3$ and the $\nu_1+\nu_2+3\nu_3$ centred at 11500.247 and 11816.636 cm^{-1} respectively, belonging to the $(\nu_1+\nu_2/2+\nu_3)=4.5$ polyad which is the first pentadecade of resonating states.

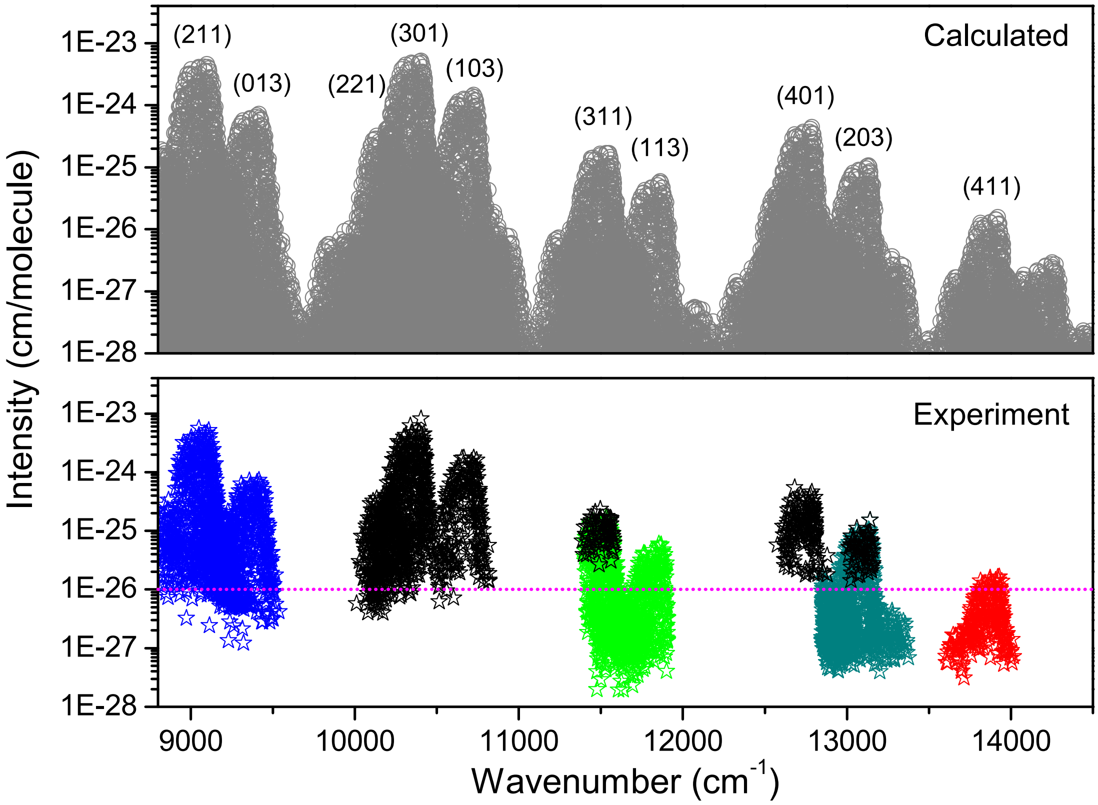

Figure 4.2. Overview of the $D_2^{16}O$ spectra in the 8800-14500 cm^{-1} region. *Upper panel*: spectrum calculated from the D_2O optimized potential energy surface of Ref. [28] and SP *ab initio* dipole moment surface [30]; *Lower panel*: spectra obtained from our FTS and ICLAS recordings [24]-[27]. The presently investigated spectral regions are marked by different colors. Red dashed line indicates typical sensitivity of FTS.

The previous experimental investigations of the D_2O absorption spectroscopy in the higher energies are limited to 12850 cm^{-1} [19], [20]. The absorption properties and intermolecular dynamics of D_2O at a high vibrational excitation are then far from being completely understood. The presently investigated 12850-14020 cm^{-1} spectral region is the highest energy range where $D_2^{16}O$ transitions are measured, it was not previously observed. For comparison, as mentioned in Section 4, the absorption spectrum of monodeuterated water, HDO, has been recorded during the last ten years by ICLAS [31], [32] and FTS [33]–[35] up to 23000 cm^{-1}. The main reasons for this difference are that, *(i)* compared to OH, the OD stretching anharmonicity is smaller and then an OD stretching overtone band is less intense than the corresponding OH band, and *(ii)* the deuterium substitution leads to a decrease of the stretching frequency by a factor of about $\sqrt{2}$; a given wavenumber region then corresponds to a higher stretching excitation (i.e. a smaller intensity) in D_2O compared to H_2O. Consequently, the decrease of the strength of the stretching overtone bands as a function of energy is faster in D_2O than in H_2O. Moreover, experimentally it is challenging to avoid a H contamination of the D_2O sample during the filling of the absorption cell, and the obtained D_2O spectrum is often obscured at high energy by the stronger HDO (and H_2O) absorption. This situation is encountered in the presently investigated 12830-14020 cm^{-1} spectral region [26], [27]. The HDO absorption in the 12850-13380 cm^{-1} region is comparable to that of D_2O, while in the 13600-14700 cm^{-1} range the HDO transitions are more than two orders of magnitude stronger than the $D_2^{16}O$ ones, as shown in Figure 4.3. A 1% H contamination is the typical maximum value that can be tolerated. In the 13600-14020 cm^{-1} spectral region, the $D_2^{16}O$ experimental spectrum is dominated by transitions of the weak (411)-(000) vibrational band centred at 13876.021 cm^{-1} (Figure 4.2). For comparison, this excitation corresponds to a vibrational energy of 18990 cm^{-1} in $H_2^{16}O$, and no experimental data are available for similar vibrational bands in $H_2^{17}O$ and $H_2^{18}O$. The results concerning this highest energy range, which are presented below, could be obtained only because laser techniques (in particular ICLAS) require small quantity of gas and make it possible to reach D_2O concentration approaching 100% in the absorption cell.

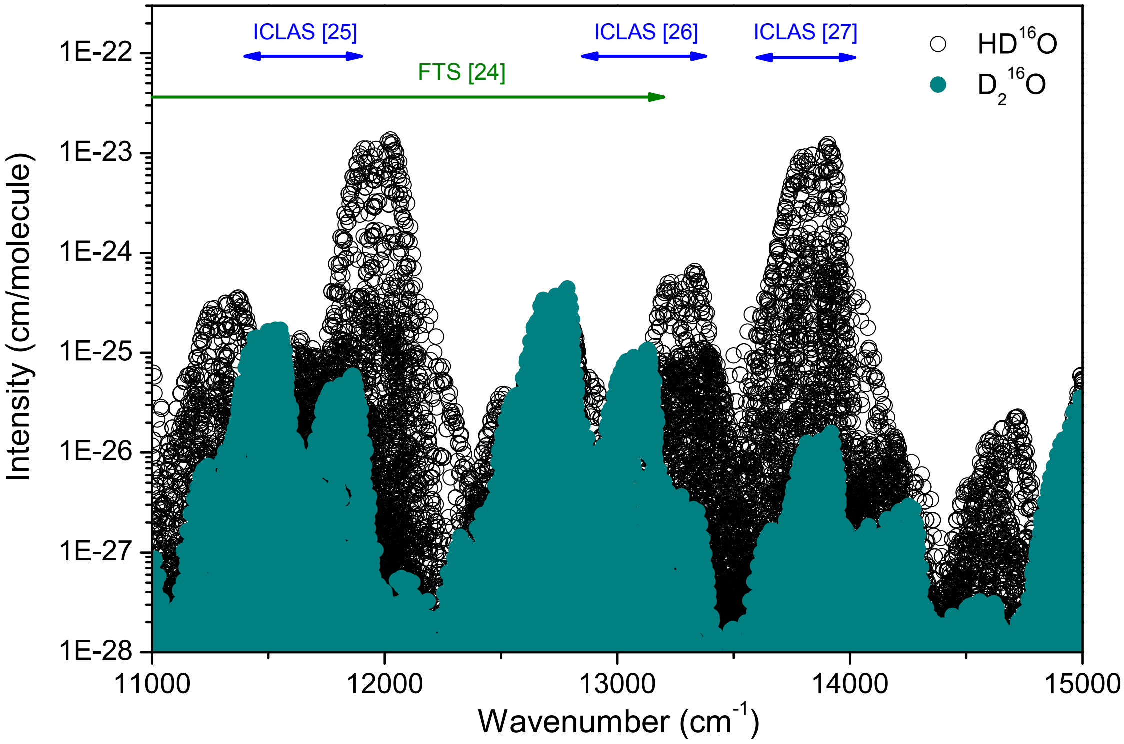

Figure 4.3. Overview of the D_2O and HDO spectra in the 11000-15000 cm^{-1} region as predicted by Shirin et al. [28] and Schwenke and Partridge [29], [30] respectively. Note the much larger intensity values for HDO in the high energy part of the present investigation. The spectral regions presently investigated by ICLAS and FTS are indicated [24]–[27].

The experimental details and line list construction for the whole spectral region under consideration are given in the subsection 3.2. Subsection 3.3 presents the line assignments and energy levels derivation. The last subsection describes the vibrational Hamiltonian parameters derivation in order to propose consistent vibrational labels of the $D_2^{16}O$ states up to 18000 cm^{-1}.

3.2 Experimental details and line list construction

To study the absorption spectrum of $D_2{}^{16}O$ in wide spectral range from 8800 to 14200 cm^{-1}, several experimental techniques having specific advantages were applied. The 8800 − 9520 cm^{-1} section was recorded by ICLAS based on VeCSEL and by high sensitivity FTS with 600 m path length. The FTS spectra were recorded by the Bruxelles-Reims group. The details of their experimental setup can be found in [36]−[38]. Our ICLAS experimental apparatus is described in Section 2 of the current Chapter. Further details of experimental recordings and wavenumber calibration of FTS and ICLAS spectra are given in our paper [21]. Figure 4.4 shows the comparison of the FTS and ICLAS spectra in a selected spectral section around 9278 cm^{-1}. The D_2O/HDO/H_2O relative fractions were estimated to be 74/23/3 and 93.7/6.0/0.3 for the FTS and ICLAS samples respectively. The contribution of HDO and H_2O absorption lines was then largely reduced in the ICLAS spectrum, which helped to observe D_2O lines when falling in close coincidence with HDO or H_2O transitions.

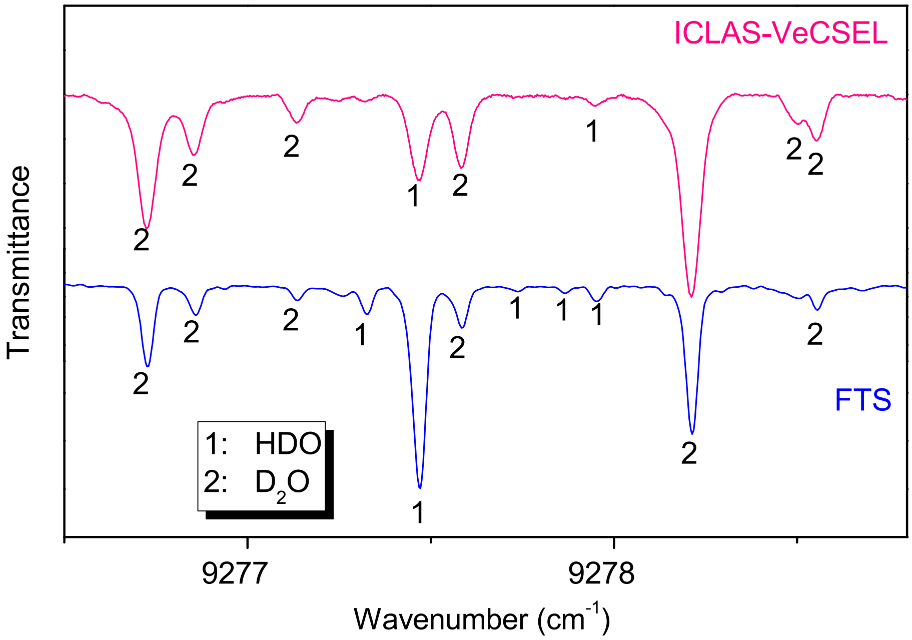

Figure 4.4. Comparison of the FTS and ICLAS-VeCSEL spectra. The experimental conditions (path length, total pressure and sample composition) were the following:FTS: 602.3 m, 13.3 hPa, D_2O/HDO/H_2O = 74/23/3; ICLAS: 20.7 km, 23.6 hPa, D_2O/HDO/H_2O ≈ 93.7/6.0/0.3.

The D_2O line list between 8800 and 9520 cm^{-1} region was obtained by combining the FTS measurements in the whole region with ICLAS data in the 9095-9510 cm^{-1} region where the two spectra are available. The FTS line intensities were adopted for strong and middle intensity lines. This led to a set of 625 FTS lines that were merged with 213, mostly weak, lines measured by ICLAS. As the relative concentration of D_2O compared to H_2O was about 15 times higher in the ICLAS sample compared to the FTS one, some of the relatively strong lines were also retrieved from the ICLAS spectrum in the case of unrecoverable overlapping with strong H_2O

lines. The weakest detected lines have an intensity value of the order of $5x10^{-27}$ cm/molecule both for FTS and ICLAS-VeCSEL (see Figure 4.2).

The strong part of the D_2O spectrum in the 10000-13200 cm^{-1} region was recorded by Reims-Brussels collaboration with the same FTS spectrometer, as described above. The weaker part of the D_2O absorption spectra above 11400 cm^{-1} was measured with ICLAS spectrometer based on a Ti:Sapphire laser described in Section 2 of present Chapter. It is worth noting that the ICLAS detection limit achieved in the 11400-14000 cm^{-1} with the Ti:Sapphire laser is 50 times better than that provided by ICLAS-VeCSEL below 10000 cm^{-1} [21] (see Figure 4.2).

Generally, the experimental procedure of the ICLAS recordings was nearly the same for each spectral section in our series of studies. It consisted in successive fillings of the cell with D_2O, recording the spectrum, evacuating the cell and recording the background spectrum. This procedure has both the advantage of increasing the signal to noise ratio and washing out natural water from the cell. Indeed, due to the rapid proton exchange between the $D_2^{16}O$ introduced in the gas phase and the H_2O molecules absorbed on the walls of the cell, D_2O replaces H_2O progressively, leading to a very high deuterium enrichment. From the relative intensity of several $HD^{16}O$ and $D_2^{16}O$ transitions we estimate the $D_2^{16}O$ concentration to be about 99%. With such deuterium enrichment, the D_2O transitions could be observed above 11400 cm^{-1}, while they are typically two orders of magnitude weaker than HDO transitions in the 13600-14020 cm^{-1} range and D_2O absorption is comparable to that of HDO only in the 12850–13380 cm^{-1} region, as shown in Figure 4.3.

It is worth pointing out that this procedure benefits from the small volume (about 200 cm^3) and small internal surfaces of the cell and from the fact that the gas consumption is very limited (0.5 g of D_2O is sufficient for more than 150 filling-emptying cycles). The small gas consumption is one of the advantages of laser techniques compared to direct absorption ones using multipass cells which require a large volume of gas.

The ICLAS spectrum was obtained by gathering the 12 cm^{-1} wide sections of the spectrum recorded successively. Each 12 cm^{-1} wide portion of the spectrum was calibrated independently using the corresponding reference line positions adopted from the literature. The accuracy of the wavenumber calibration varies within 0.004–0.005 cm^{-1} as confirmed in the next subsection by the uncertainty obtained for the energy levels retrieved from several transitions. The line centres and relative line intensities were then determined by using an interactive least squares multi-lines fitting program[5] assuming the Voigt profile for each line. Line position, integrated line absorbance, Gaussian and Lorentzian widths of each line and the corresponding

---

[5] FITYK program version v0.8.6, http://sourceforge.net/projects/fityk/

baseline (assumed to be a linear function of the wavenumber) were derived from the multiline fitting procedure. Except for the stronger lines, the Lorentzian component was found unnecessary and a purely Gaussian profile (taking into account both the Doppler broadening and the spectrograph apparatus function) was used.

The determination of absolute line intensity values requires the knowledge of the D_2O partial pressure and of the absorption path length. In our experiment, the generation time is controlled and the absorption path length is known, but an accurate determination of the D_2O pressure is more problematic. A drawback of the experimental procedure consisting in successive filling and emptying the cell, is that the pressure value decreases during the recording of an individual spectrum, as a result of the D_2O adsorption on the cell wall. We then found it more convenient and probably more accurate to normalize the relative intensity values retrieved from each elementary spectrum to the intensity values calculated in Ref. [28]. Such normalization is justified by the good agreement observed up to 13160 cm^{-1} between the calculated [28] and FTS line intensities obtained in our work [24].

The most complete list for each investigated spectral range was created simply by gathering all the line lists corresponding to the individual 12 cm^{-1} spectral window. In this global list, many lines appear several times as a consequence of several recordings of the same spectral windows and of the existence of overlapping regions. As the accuracy of the ICLAS line positions was estimated to be around 0.004 cm^{-1}, we decided to consider two lines as identical when both their wavenumber difference was less than 0.008 cm^{-1} and their intensity differed by at most a factor of 2. This global line list was then further checked and cleaned of spurious lines or irreproducible spectral features close to the noise level. The obtained list was then considered for the rovibrational analysis provided below. Note that the high sensitivity achieved (noise equivalent absorption $\alpha_{\min} \sim 10^{-9}$ cm^{-1}) in the 11400-14000 cm^{-1} region with a Titanium Sapphire laser, allowed detecting transitions with minimum line strength values of the order of 5×10^{-28} cm/molecule, i.e. two orders of magnitude smaller than the FTS or ICLAS-VeCSEL. The summary of the experimental information obtained for each spectral region under investigation is provided in Table 4.3. For the complete set of $D_2{}^{16}O$ experimental energy levels newly derived in the present study over the whole spectral region under consideration, the reader is referred to the relevant papers [21], [25]-[27]. The energy levels obtained from the analysis of the FTS spectrum between 10000 and 13200 cm^{-1} [24] have not been published yet and so are given in Appendix A.1.

Table 4.3. Summary of experimental information obtained from the investigated $D_2{}^{16}O$ absorption spectra.

Spectral range (cm^{-1})	Experimental technique	Number of $D_2{}^{16}O$ lines	Number of new rovibrational energy levels
8800-9520 [21]	ICLAS−VeCSEL, FTS	1223	577
10000-13200 [24]	FTS	1175	436
11400-11900 [25]	ICLAS	840	530
12850-13380 [26]	ICLAS	874	422
13600-14020 [27]	ICLAS	248	177

3.3 Spectrum analysis and results

3.3.1 Rovibrational assignment and energy levels derivation

Since the achievements in the theoretical modelling of the rovibrational molecular spectra of water [29]−[30], the assignment of the high resolution water vapour and its isotope substituted species spectra is generally performed on the basis of high accuracy variational line lists. In our study we used the synthetic line lists based on D_2O potential energy surface (PES) [28], [39] and Schwenke and Partridge ab initio dipole moment surface (DMS) [30].

The assignment procedure takes into account the regular and smooth tendencies in the deviations of the observed levels from their calculated values. Though the (obs.-calc.) values may reach up to several cm^{-1}, which leads to tens of experimental lines as possible candidates for the considered assignment, the existence of evident (obs.-calc.) tendencies combined with intensity matching between the observed and calculated intensities still provides reliable assignments.

As the calculations of Ref. [28] do not provide reliable rovibrational labellings, we used the rovibrational labelling provided by Ref. [40], which followed the labelling procedure adopted by Partridge and Schwenke in their original work [29]. This procedure is based on inspecting the contributions of the basis functions into the resulting wave function of the analyzed energy level. However, at high rovibrational excitation leading to a considerable mixing of the wave functions, this procedure may lead to ambiguities in the ascribing of the vibrational and rotational quantum numbers. Indeed, we faced a problem with ambiguous labelling for a number of levels. Calculations in the frame of the effective Hamiltonian approach (EH) were performed to confirm the resulting labelling. This issue is discussed in more detail in subsection 3.4.

The 8800-9520 cm^{-1} spectral region studied by FTS and ICLAS-VeCSEL

In the course of the 8800-9520 cm^{-1} spectral region analysis we compared the synthetic spectrum [39] with that of Partridge and Schwenke [29]-[30] (PS), which can also be used for D_2O assignment (see, for example, [41], [42]). As stated in [42], for low-lying vibrational states, the (obs.-calc.) deviations for PS calculation may increase up to 1.2 cm^{-1} but preserve their regular dependence on J and K_a quantum numbers up to J, K_a values around 30 thus providing reliable criteria for assignment of the hot D_2O spectra. However, it is not the case for the whole spectral region under consideration. Indeed, the (obs.-calc.) deviations for PS calculations lose their regularity and increase a lot starting at $J = 10$, (see Figure 4.5), reaching -1.53 cm^{-1} for $J = 16$. The reason for the poor accuracy of the PS calculations for D_2O may be caused by the fact that, the D_2O PES [29] was optimized by a fitting to the experimental data that included only the ground state (000) and the first triad of interacting states (020), (100), (001) from Ref. [43] along with (010) state from Ref. [44]. In contrast with PS calculations, the presently used D_2O PES from Ref. [39], shows though rather large, but regular (obs.-calc.) deviations up to $J = 17$ (Figure 4.5). For the purpose of assignment, the intensity and line position matching between theory and experiment are both important. Figure 4.6 illustrates the very satisfactory agreement between the experimental and calculated stick spectra respectively in the whole 8800-9520 cm^{-1} investigated spectral region.

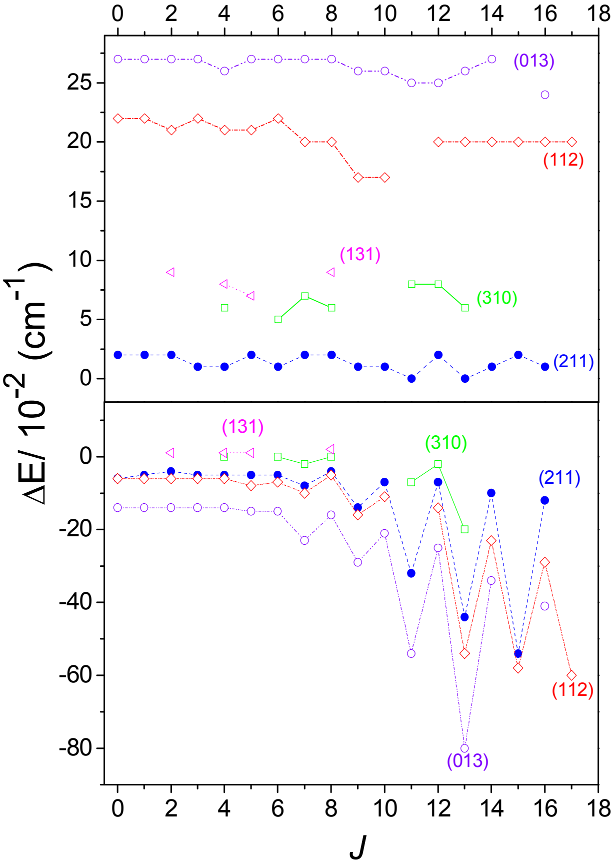

Figure 4.5. Variation of the ($E_{obs.}$-$E_{calc.}$) differences for the [*J0J*] rotational term values of the analyzed vibrational states. Note the change in the ordinate scale. *Upper panel:* rotational term values obtained from the D_2O optimized potential energy surface of Ref. [39]; *Lower panel:* calculated values from Schwenke and Partridge [29].

A summary of the quantitative information obtained from the combined study of the ICLAS and FTS spectra of D_2O recorded between 8800 and 9500 cm^{-1} is given in Table 4.4. An important set of 687 accurate energy levels belonging to eight vibrational states listed in Table 4.4 was derived by adding the ground state experimental rotational energies [41] to the observed transitions. Only separate energy levels were derived for the (032), (230) and (221) states. For the other five states, the number of energy levels is comparable or significantly exceeds that of the main isotopologue, $H_2{}^{16}O$. The band origins for the (131) and (310) states were extrapolated from the (obs.-calc.) tendency for the [*J0J*] levels (see Figure 4.5). The band origin of the (221) state, presently observed through a hot band, was derived from (221)-(000) transitions assigned in our study of FTS spectrum between 10000 and 13200 cm^{-1} [24].

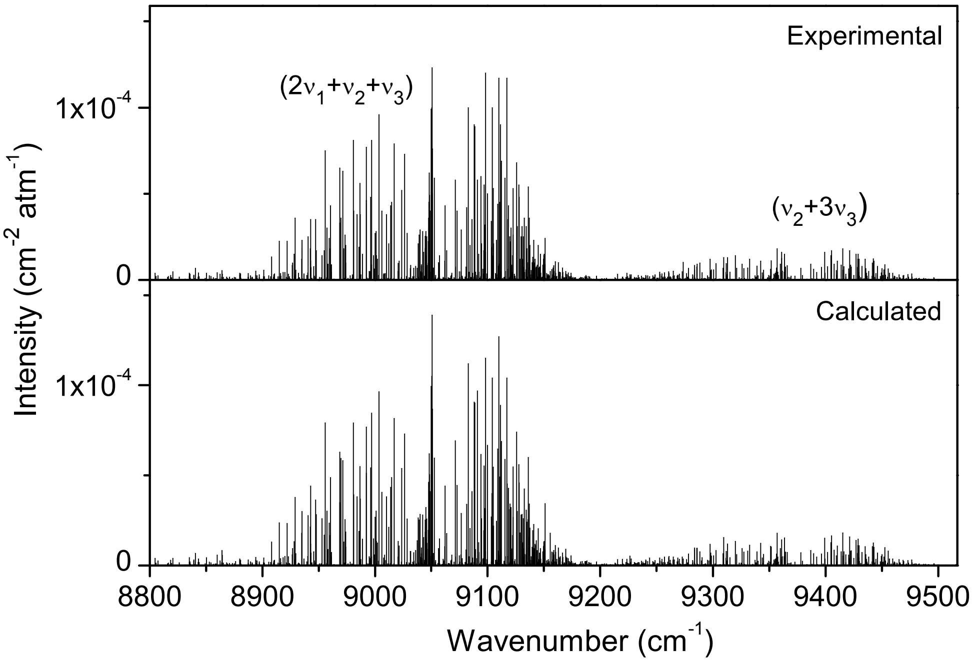

Figure 4.6. Comparison of the D_2O stick spectrum between 8800 and 9500 cm^{-1}: *Upper panel*: combined spectrum obtained from FTS and ICLAS recordings (see text); *Lower panel*: synthetic spectrum calculated from the D_2O optimized potential energy surface of Ref. [39] and SP *ab initio* dipole moment surface [30].

We included in Table 4.4 a comparison of the energy level set presently derived with that of Ref. [17] where a total of 110 levels belonging to the (211), (310), and (032) vibrational states were determined. Out of these 110 levels, 103 coincide with ours within 0.0021 cm^{-1} while seven outliers deviate from 0.009 up to 0.034 cm^{-1}. Consequently, in this region the number of newly derived energy levels is 577.

Table 4.4. Summary of the information obtained from the ICLAS and FT spectra of D_2O recorded between 8800 and 9500 cm^{-1}.

Band	Upper state vibrational term value^a (cm^{-1})			Band intensity (cm/molecule)	$J_{\max}$	$K_{a\,\max}$	Number of levels
	Calc. Ref. [39]	Observed	Ref. [17]				
(230)-(000)	8712.00		8713.31	6.9E-25	10	6	11
(131)-(000)	8792.55	8792.63^b	8788.60	5.5E-24	13	9	81
(032)-(000)	8946.90		8934.60	8.2E-25	9 [7]	5 [4]	14 [1]
(310)-(000)	9005.45	9005.50^b	9005.35	1.6E-23	14 [7]	8 [3]	102 [10]
(211)-(000)	9050.34	9050.349	9050.36	2.7E-22	16 [13]	9 [6]	175 [99]
(112)-(000)	9202.50	9202.716	9201.90	1.4E-23	17	9	139
(013)-(000)	9366.04	9366.313	9365.45	4.0E-23	16	9	157
(221)-(010)	10180.04	10180.116		1.8E-25	7	2	8
						Total:	687 [110]

The values given in brackets in the last three columns correspond to the results of Ref. [17].
^{a} Rovibrational term value of the [$J\,K_a\,K_c$]=[000] rotational level.
^{b} Values extrapolated from the [*J*0*J*] energy levels.

The 10000-13200 cm^{-1} spectral region studied by FTS

The assignment of 1175 D_2O lines observed by FTS between 10000 and 13200 cm^{-1} [24] was performed using the above mentioned high accuracy variational calculations based on an optimized PES of D_2O [39]. A set of 709 accurate rovibrational energy levels was derived belonging to ten vibrational states: (122), (203), (023), (103), (301), (401), (221), (400), (311) and (320), 436 of them being reported for the first time. Table 4.5 summarizes the obtained experimental information in this region, where variational band origins are provided by more recent study [28]. Accurate within 0.1 cm^{-1} band origins for the (400)-(000), (103)-(000), and (311)-(000) bands were derived from the (obs.-calc.) tendencies for [*J0J*] energy levels of the corresponding upper states.

Table 4.5. Summary of the experimental information retrieved from the analysis of the FTS spectrum of $D_2{}^{16}O$ between 10000 and 13200 cm^{-1}.

Band	Band origin (cm^{-1})		Number of levels	
	Calculated [28]	Observed	Total	New
(320)-(000)	10136.34		15	15
(221)-(000)	10180.11	10180.1165	114	106
(122)-(000)	10330.59		29	29
(400)-(000)	10341.02	10341.02	85	85
(301)-(000)	10358.54	10358.5603	159	69
(023)-(000)	10494.83		16	16
(103)-(000)	10679.69	10679.69*	116	116
(311)-(000)	11500.24	11500.25*	53	0
(401)-(000)	12743.02	12743.0491	73	0
(203)-(000)	13088.18	13088.324	49	0
		Total:	709	436

*Values extrapolated from the (obs.-cal.) tendency for [*J0J*] energy levels.

The 11400-11900 cm^{-1} spectral region studied by ICLAS

At the first stage of our analysis of the 11400-11900 cm^{-1} spectral range [25], we used the identification list based on the PES of Ref. [39] and the DMS of Ref. [30], which we refer to as "calculation 1". Most of the strong lines, which belong, mainly, to the (311)-(000) and (113)-(000) bands with low J and K_a values were confidently assigned in this way. However, we experienced difficulties in assigning the transitions belonging to much weaker bands or those of the strong bands with high J and K_a values, since some of the observed positions were found to deviate greatly (up to 1.2 cm^{-1}) from their predicted values. These weak transitions are generally not involved in combination differences (CD) in the ground state, and their identification relies almost entirely on the good correspondence between theory and experiment.

It was clear that new calculations were required since the available experimental D_2O energy level set used to optimize the previous D_2O PES [39] was too limited, leading to important deviations from the current observations. Thus, the new experimental energy levels obtained at the first stage of this study, as well as new data from our study [21] and from Refs. [42], [45] were combined and used by Shirin et al. [28] for a further optimization of the D_2O PES. A new synthetic spectrum [28], below referred to as "calculation 2", was generated with the new D_2O PES and again with the DMS of Ref. [30]. It was successfully applied to complete the assignment of the weak D_2O lines in the 11400−11900 cm^{-1} spectral region. In total, 530 new precise experimental energy levels were derived for the eight vibrational states, as summarized in Table 4.6. We estimate the accuracy of the observed energy levels as 0.002 cm^{-1} on average for levels confirmed by the combination difference relations. Energy levels derived from blended lines are determined with less accuracy. Note that 47 of the energy levels for the (311) vibrational state were also determined from our analysis of the FTS spectrum [24] in 10000-13200 cm^{-1} spectral range.

Table 4.6. Summary of the spectroscopic information obtained by ICLAS for D_2O in the 11400-11906 cm^{-1} region.

Vibrational state	Band origin (cm^{-1})		Intensity (cm/molecule)		I_{obs}/I_{calc}	Number of lines	Number of levels
	Observed	Calculated[a]	Observed	Calculated[a]			
330		11245.68	1.736E-26	1.616E-26	1.07	5	5
231		11289.72	9.40E-26	9.40E-26	1.00	13	9
132		11441.21	1.116E-25	1.136E-25	0.98	21	18
410	11483.6393	11483.65	6.52E-25	7.32E-25	0.89	110	85
311	11500.2475	11500.24	9.04E-24	9.40E-24	0.96	317	160
033	11605.79[b]	11605.75	1.42E-25	1.172E-25	1.21	68	45
212	11679.3894	11679.27	4.00E-25	4.24E-25	0.94	166	94
113	11816.6366	11816.58	2.892E-24	2.876E-24	1.01	256	114

[a] Calculated values limited to the observed transitions from Ref. [28].
[b] Value extrapolated from the [*J*0*J*] energy levels.

Deviations of the observed energy levels from "calculation 1" and "calculation 2" are shown in Figure 4.7 for the [*J*0*J*] energy levels of the strongest assigned bands. "Calculation 2" is much more precise, with maximum (obs.-cal.) deviation not exceeding 0.13 cm^{-1}. The pronounced deviation of the (113) [10 0 10] level at 12368.1736 cm^{-1} from the smooth behaviour of the (obs.-cal.) curve for the (113) vibrational state ("calculation 2") is caused by a strong resonance interaction with the (410) [10 5 6] level at 12369.25 cm^{-1}. The origin of the (033)-(000) band at 11605.79 cm^{-1} (Table 4.6) could be derived with estimated accuracy not worse than ± 0.05 cm^{-1}, from the (obs.-calc.) trend for the [*J*0*J*] energy levels.

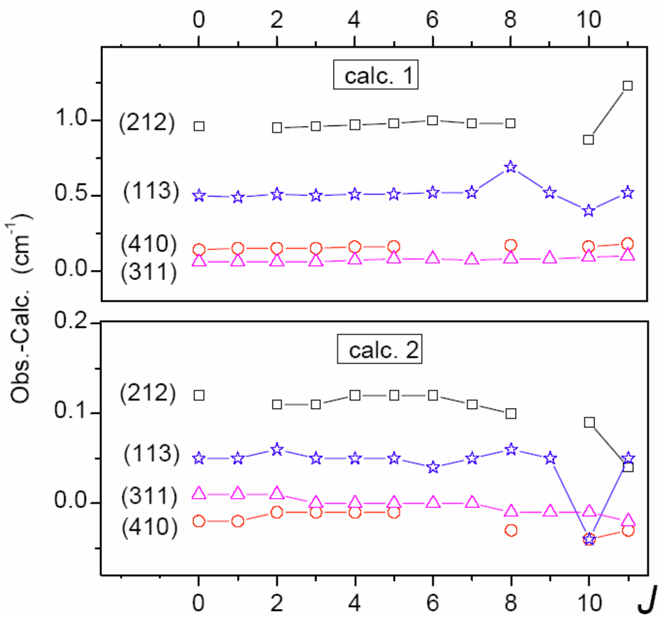

Figure 4.7. Variation of the differences between the experimental and calculated energy levels of $D_2{}^{16}O$ versus J, for the $K_a = 0$ energy of the four of the analyzed vibrational states corresponding to the stronger bands. Upper and lower panels illustrate the results of the variational calculations of Ref. [39] (calc. 1) and Ref. [28] (calc. 2) respectively. Note the different scales adopted for the ordinate axis.

The 12850-13380 cm^{-1} and 13600-14020 cm^{-1} spectral regions by ICLAS

The rovibrational assignments of our experimental spectra in the 12850-13380 cm^{-1} and 13600-14020 cm^{-1} spectral regions were performed by comparing with the results of "calculation 2" [28]. In the 12850-13380 cm^{-1} spectral range, an overall set of 529 energy levels belonging to 13 vibrational states was derived from the spectrum assignment by adding the ground state energy value [41] to the transition wavenumber. A summary of the obtained results is presented in Table 4.7.

Table 4.7. Summary of the experimental information retrieved from the analysis of the ICLAS spectrum of $D_2{}^{16}O$ between 12850 and 13375 cm^{-1}.

$\upsilon_1\ \upsilon_2\ \upsilon_3$	Band Origin (cm^{-1})		Number of levels	
	Calculated [28]	Observed	all	new
142	12530.77		10	7
420	12603.55		1	1
321	12618.92	12618.912	7	1
043	12698.51		2	0
500	12737.42	12737.397	40	18
401	12743.03	12743.035	42	0
222	12799.14	12799.25 [a]	19	17
123	12934.10	12934.20[a]	96	74
302	12988.32	12988.432	103	95
203	13008.19	13088.307	146	146
104	13263.80	13263.902	61	61
024	13112.05		1	1
091	12473.12		1	1
		Total:	529	422

[a] Value extrapolated from the [*J*0*J*] energy levels.

Overall, 177 upper rovibrational energy levels belonging to six vibrational states were derived by adding the ground state energies from Ref. [41] to the measured wavenumbers in the 13600-14020 cm^{-1} spectral range. A large set of levels could be determined for the (331), (312) and (411) states, while a few additional levels belong to the (430), (232) and (133) states. A summary of the retrieved experimental information is presented in Table 4.8.

Table 4.8. Summary of the experimental information retrieved from the analysis of the ICLAS spectrum between 13600 and 14020 cm^{-1}, all the energy levels are newly observed.

$\upsilon_1\ \upsilon_2\ \upsilon_3$	Band Origin (cm^{-1})		Number of levels
	Observed	Calculated [28]	
430		13702.64	2
331	13717.264	13717.38	44
312	13869.30*	13869.37	36
411	13876.021	13876.05	90
232		13900.32	1
133		14033.36	4

*Value extrapolated form the [*J*0*J*], [*J*1*J*] energy levels (see Figure 4.10).

An average value of 0.09 cm^{-1} is obtained for the (obs.-calc.) deviations of the energy levels. Considering that our transition wavenumbers are located at about 1000 cm^{-1} above those included into the PES's fitting [28], the extrapolation capabilities of the variational calculations of Ref. [28] were found satisfactory. As one example, the rovibrational energy levels of $D_2{}^{16}O$ newly derived from the analysis of ICLAS spectrum between 13600 and 14020 cm^{-1} are partly presented in Table 4.9. For the complete set of newly retrieved energy levels in this spectral region, the reader is referred to the relevant paper [27].

Table 4.9. $D_2{}^{16}O$ rovibrational energy levels of the (411), (331), and (312) vibrational states newly derived from the ICLAS spectrum between 13600 and 14020 cm^{-1}.

J	K_a	K_c	(411)				(331)				(312)			
			E_{obs} (cm^{-1})	σ	N	δ	E_{obs} (cm^{-1})	σ	N	δ	E_{obs} (cm^{-1})	σ	N	δ
0	0	0	13876.021		1	-0.02	13717.264		1	-0.12				
1	0	1	13887.337	1.5	2	-0.03	13729.070		1	-0.11				
1	1	1	13895.561	1.1	2	-0.02	13739.631		1	-0.08				
1	1	0	13898.102	0.2	2	-0.02	13742.388		1	-0.10				
2	0	2	13908.757		1	-0.06								
2	1	2	13915.960		1	-0.02	13760.048		1	-0.09	13910.535	0.3	2	-0.06
2	1	1	13923.568	0.3	2	-0.02	13768.307		1	-0.11	13916.850		1	-0.03
2	2	1	13947.709	1.8	2	-0.02	13800.231	0.8	2	-0.07	13941.598	5.7	1	-0.05
2	2	0	13948.244	1.1	2	-0.02	13800.700		1	-0.07	13942.084		1	-0.04
3	0	3	13942.851	2.6	3	-0.03	13785.090	7.2	1	-0.12				
3	1	3	13946.304	0.9	2	-0.02	13790.466		1	-0.10	13939.408		1	-0.06
3	1	2	13961.361	1.3	3	-0.04								
3	2	2	13982.123	0.9	2	-0.02	13834.989		1	-0.09				
3	2	1	13984.581	1.2	2	-0.03	13837.253	3.5	2	-0.09				
3	3	1	14028.943	0.7	2	-0.01					14023.338		1	-0.05
3	3	0	14029.002		1	-0.01	13894.399		1	-0.04				
4	0	4	13984.507	1.3	2	-0.04					13977.859	3.1	2	-0.15
4	1	4	13986.341	0.7	2	-0.03	13830.664		1	-0.11	13979.567		1	-0.07
4	1	3	14010.926	0.2	2	-0.04								
4	2	3	14027.612	0.7	2	-0.03	13880.971		1	-0.10				
4	2	2	14034.223	5.7	2	-0.04					14028.089		1	-0.06
4	3	2	14075.789	0.0	2	-0.03	13941.540	5.4	2	-0.05	14070.315		1	-0.04
4	4	1	14139.988	9.8	2	-0.01								
4	4	0	14139.992		1	-0.01					14134.837		1	-0.02
5	0	5	14034.973	1.5	2	-0.04	13878.720		1	-0.13				
5	1	5	14035.840	1.4	2	-0.04	13880.378		1	-0.11	14029.144		1	-0.06
5	1	4	14071.739		1	-0.06	13918.604	3.9	2	-0.15				
5	2	4	14083.988	6.8	2	-0.04					14078.721	5.7	2	-0.07
5	2	3	14097.184	0.8	2	-0.06	13950.907		1	-0.10				
5	3	3	14133.559	4.2	2	-0.02					14129.013		1	-0.07
5	3	2	14135.986		1	-0.04	14001.888	7.7	3	-0.06	14130.521		1	-0.07
5	4	2	14198.759	8.6	3	-0.02								
5	4	1	14198.824	0.2	2	-0.02	14080.753		1	0.01				
5	5	1	14281.362	1.4	2	0.01	14180.670		1	0.05	14276.556		1	0.00
5	5	0	14281.364	1.7	2	0.01	14180.670		1	0.05	14276.551		1	-0.01

N is the number of lines used for the upper energy level determination. σ (in 10^{-3} cm^{-1}) denotes the corresponding statistical error defined as the rms value of the deviation of the levels derived through several transitions. δ represents the deviation of the experimental levels from their calculated [28] values in cm^{-1}.

3.3.2 Line intensities

As mentioned above in Subsection 3.2, the experimental line intensities were derived from the relative values by normalizing to the calculated values [28]. Such an approach yields line intensity values accurate enough for further possible quantitative applications (see Refs. [20], [25], [32]). Accurate experimental intensities for D_2O absorption lines in the near-infrared region were reported only in our FTS analysis [24]. The quality of the “calculation 2” intensities based on Schwenke and Partridge DMS [28] was checked in this work [24] by the comparison with 1175 precise experimental intensities in the 10000-13160 cm^{-1} spectral region and found to be satisfactory with an average I_{obs}/I_{calc} intensity ratio of 1.09. Our ICLAS intensities are also in satisfactory agreement with the calculated values for the whole spectral region under study. As one example, Figure 4.8 displays the observed to calculated intensity ratio versus the calculated line intensity in the 11400-11900 cm^{-1} spectral region. The good agreement between the experimental and predicted intensities was a crucial criterion for the assignment of a number of lines. As usual, the largest deviations are mainly due to “shoulders” of strong lines and components of unresolved doublets, and are sometimes caused by superposition with HDO lines.

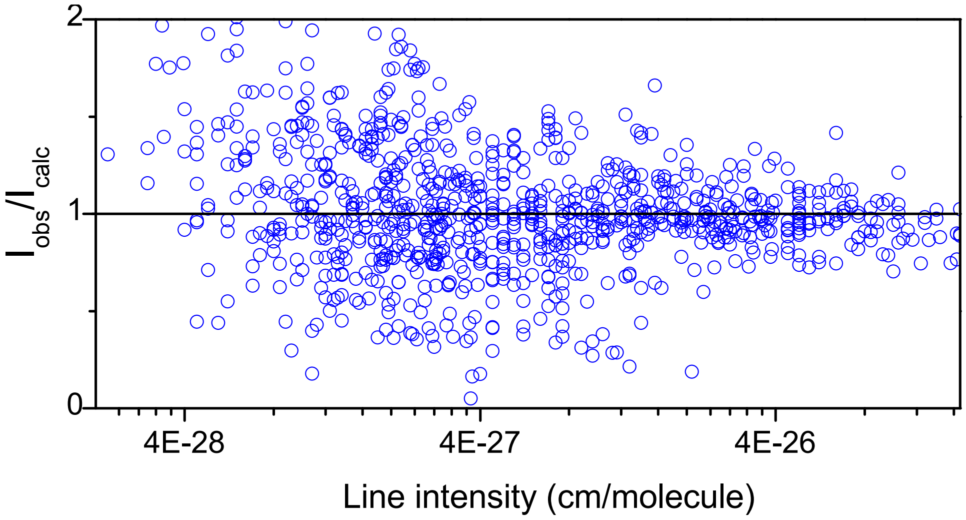

Figure 4.8. Variation of the ratio of the ICLAS D_2O line intensities in the 11400-11900 cm^{-1} spectral region to those predicted by the new variational calculations of Ref. [28], versus the calculated intensity values.

3.3.3 High-order resonance interactions and their influence on the calculated line positions and intensities

Similar to its parent species, H_2O, the D_2O molecule is known to undergo strong centrifugal distortion effects leading to divergence of the perturbation series in the Watson-type rotational Hamiltonian [42]. Another consequence is the existence of local high-order resonance interactions involving the highly excited bending states. Intensity transfers to resonance transitions coming on the highly excited bending states such as (070), (080), (090), (0 10 0), and even (0 12 0) were observed in the HDO spectrum (see Ref. [33] and references quoted therein). In the case of the $D_2{}^{16}O$ isotopologue, no significant resonance intensity redistribution towards such high bending states had been evidenced until now; the most excited $D_2{}^{16}O$ bending state analysed (from hot spectra [45]) is the (050) state. In the present analysis, the transitions reaching the (203) [826] level at 13566.084 cm^{-1} and the (091) [844] level at 13566.274 cm^{-1} were found in resonance. Approximate calculations within the effective Hamiltonian model confirmed that the upper level of the relatively strong (as far as current data are concerned) transitions at 12946.711 and 13165.012 cm^{-1} is indeed the (091) [844] upper level. As shown in Figure 4.9, the calculated intensities for the transitions reaching the (091) [844] level are underestimated by about a factor of 2, while the corresponding transitions reaching the (203) [826] state are overestimated. This abrupt distortion in the calculated intensities for transitions reaching upper energy levels in close resonance has been discussed before in the HDO spectrum [32], [33]. Since this intensity transfer is very sensitive to the relative position of the resonant levels, the observed distortions of the line intensities reflect inaccuracy of the calculated wavefunctions of the interacting energy levels, which, in turn, is a consequence of inaccuracy of the potential energy surface.

It is worth noting that the results of the calculations of Ref. [28] show significant improvement compared to those obtained by Schwenke and Partridge [29], [30]. Despite the fact that SP calculations for line position diverge greatly in the considered spectral region for $J > 10$ – (obs.-calc.) deviations may reach a value up to 40 cm^{-1}, SP calculated intensities still match the experimental values for most of the lines. However, in the case of transitions reaching the (091) state, SP line intensities are predicted more than two orders of magnitude weaker than observed and the (091) [844] – (000) [725] transition is predicted to have an intensity below our detection limit (see Figure 4.9). On the other hand, the intensities of the corresponding line-partners reaching the (203) [826] level are significantly overestimated compared to the calculations, based on the PES of Ref. [28].

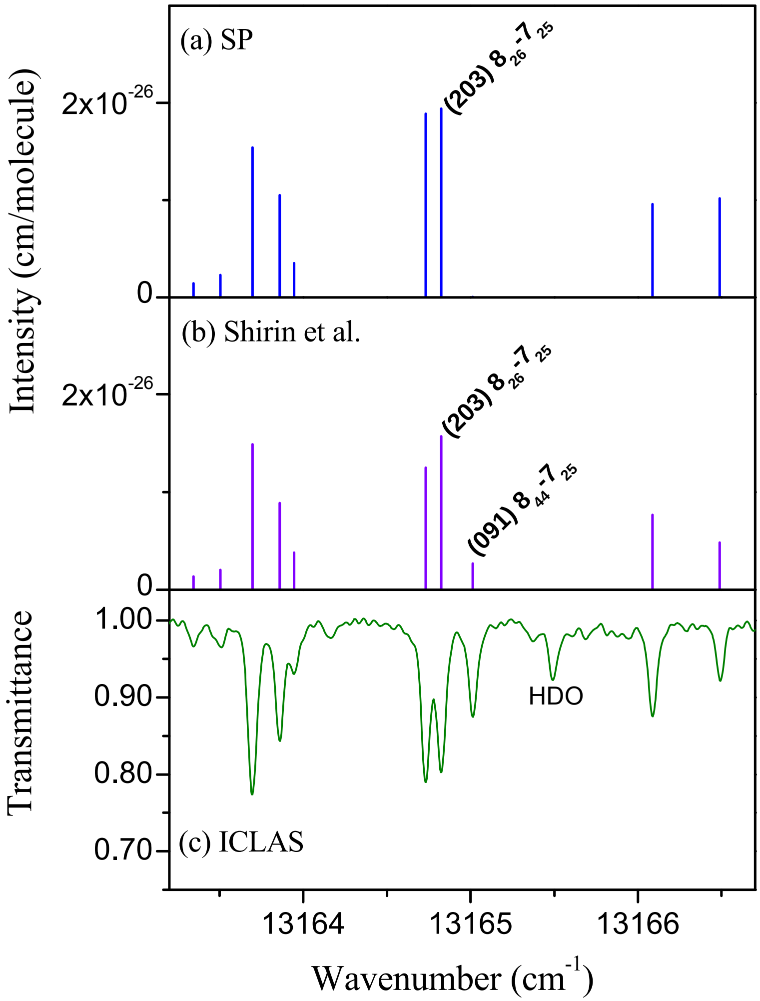

Figure 4.9. Comparison of the D_2O spectrum near 13165 cm^{-1} showing the (203) [826]–(000) [725] and (091) [844]–(000) [725] transitions with upper levels in resonance interaction. (a) Predictions of Ref. [30]; (b) Predictions of Ref. [28]; (c) ICLAS spectrum (P = 18 hPa, l_{eq} = 24 km). For an easier comparison of the line intensities, the line positions of the calculated spectra (panels (a) and (b)) were fixed to the experimental values. Note the significant deviations between the calculated and measured intensities for the (091) [844]–(000) [725] transition.

Thus, in case of close resonance, the uncertainty on the resulting variational wavefunctions may lead to important errors on the transition intensities of the weak lines. That is why it is desirable to determine all possible resonance interactions, which can influence the quality of variational intensities. The occurrences of resonance interactions also need to be considered when inspecting the (obs.-calc.) tendencies for the energy levels in the course of spectrum identification. Indeed, the distortion of the smooth behaviour of the (obs.-calc.) energy levels curve may be caused by resonance interactions. This fact is illustrated in Figure 4.10, where the deviations of the $K_a = 0$, 1 energy levels from their calculated values are shown for the (331), (312) and (411) states. A large outlier (0.41 cm^{-1}) is noted for the (411) [616] level at 14094.798 cm^{-1}. It was identified as resulting from a close resonance interaction with the [606] level of the (280) highly excited bending state, predicted at 14096.12 cm^{-1} [28]. The sharp breaking of the (obs.-calc.) tendency could have hampered the assignment of this level but our assignment to the (411) [616] was confidently supported from a ground state combination difference relation of two relatively strong lines. One of the two perturbed transitions is presented in Figure 4.11. Similar resonance perturbation with the [404] level of the same (280) bending state resulted in the distortion of the (obs.-calc.) tendency for the [404] energy level of the (312) state (see Figure 4.10).

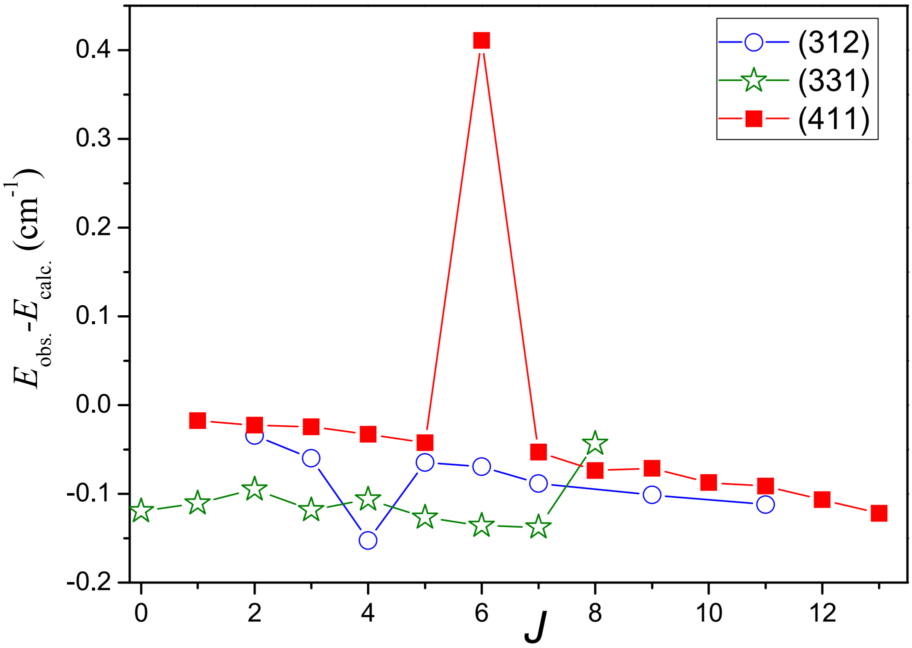

Figure 4.10. Variation of the differences between the observed and calculated [28] values for the $D_2{}^{16}O$ energy levels of the (331), (411), and (312) vibrational states with $K_a = 0$, 1 as a function of the J rotational quantum number.

Another example of deviation from the (obs.-calc.) tendency has been encountered in the case of (411) [11 2 9] calculated energy level at 14716.43 cm^{-1}, which deviates from the observed value by 0.31 cm^{-1}, again due to a resonance interaction with the (181) highly excited bending state. However, in that case, the observed energy level was derived from a single line and has to be treated with caution.

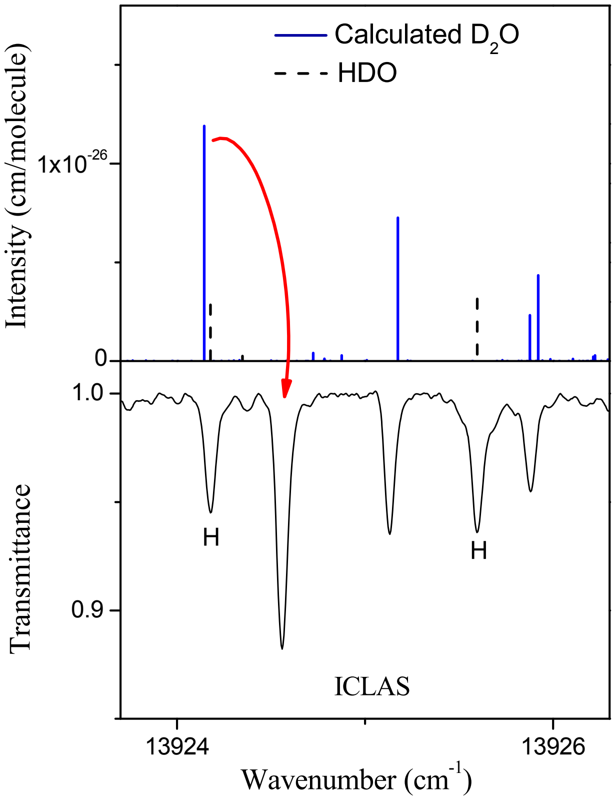

Figure 4.11. The $D_2^{16}O$ spectrum near 13924 cm^{-1} showing the (411) [616]-(000) [515] perturbed transition. *Upper panel:* Stick spectrum obtained by the superposition of the $D_2^{16}O$ predictions of Ref. [28] and the $HD^{16}O$ experimental line list of Refs. [33], [34]. Note that the ordinate scale corresponds to the $D_2^{16}O$ line strengths while the $HD^{16}O$ line strengths have been divided by a factor of 125 in order to take into account the relative concentration of the $D_2^{16}O$ and $HD^{16}O$ species. *Lower panel:* ICLAS spectrum (P= 16.1 hPa, l_{eq}= 24 km).

3.4 Vibrational problem for $D_2^{16}O$ and normal mode labelling

Labelling of vibrational states is an important problem for $H_2^{16}O$ and its isotopologues. Both local mode [46] and normal mode notations can be used. Typically, at high vibrational excitation, the local mode states are closer to the molecular eigenstates while the normal mode notations become ambiguous because of strong anharmonic mixings. Nevertheless, the normal mode labelling is traditionally used in the literature and accepted in the most popular spectroscopic databanks like HITRAN [47] and GEISA [48].

It is then important to find a consistent way to attach normal mode labels to the $D_2^{16}O$ vibrational states. The procedure of vibrational labelling adopted in Ref. [28] is based on theoretical considerations developed in Refs. [49], [50], and is not fully satisfactory in our energy region. Following Refs. [49], [50], the vibrational energies of the $(\upsilon_1\upsilon_2\upsilon_3)$ states were calculated using a simple formula:

$$E = \upsilon_1\omega_1 + \upsilon_2\omega_2 + \upsilon_3\omega_3 \,, \tag{4.1}$$

where ω_1, ω_2, and ω_3 are the usual harmonic frequencies. The vibrational label of a given level was chosen according to the best coincidence between the calculated and experimental energies. However, the approximate Eq. (4.1) leads to important discrepancies between the observed and calculated energies in particular at high energy. Consequently, Zobov et al. [49] applied additional corrections to the calculated energies to obtain a better agreement with the experiment and to fix the vibrational label. It seems that these corrections were determined phenomenologically and that the obtained results are not fully satisfactory.

We present here a more consistent approach to obtain the normal mode vibrational labels of the $D_2{}^{16}O$ states. This approach is based on the effective vibrational Hamiltonian model. It was first developed for the $H_2{}^{16}O$ molecule [51], and later applied to the H_2S vibrational states [52]. As shown in Section 4 of Chapter III, vibrational energies are obtained as a result of diagonalization of the matrix of the effective vibrational Hamiltonian.

We reviewed all the literature data concerning the $D_2{}^{16}O$ vibrational band origins [18]-[26], [39], [41], [42], [45], [53]. When the experimental value of the $J = 0$ level of a given vibrational state was not available in the literature, we estimated the vibrational energies either by fitting the experimental energy levels with low J and K_a quantum numbers in the effective Hamiltonian approach or by extrapolation at $J \to 0$ of the (obs.-calc.) tendencies using predicted values obtained from variational calculations [28]. In case of the EH fitting, the uncertainty on the vibrational level was taken equal to that provided by the fit. In case of extrapolation of E_v value from the variational calculations, the experimental value was obtained from the calculated value after correction by the average value of the (obs.-calc.) deviations for the energy levels with $K_a = 0$. The accuracy of such estimations may vary from 0.005 to 0.1 cm^{-1}. More details about the energy values derived in such a way are included in the footnotes of Table 4.10. For instance, we found that the vibrational energy of the (022) state (7826.38 cm^{-1} in Ref. [45]) should be lowered to 7826.30 cm^{-1} in agreement with the variational predictions of Ref. [28].

Table 4.10. Experimental and calculated vibrational levels of $D_2{}^{16}O$ (in cm^{-1}).

E_{obs} ,cm^{-1}	Reference	obs.-calc.$_{EH}$	obs.-calc.$_{VAR}$	P_1	W_1	P_2	W_2	$(v_1v_2v_3)_{VAR}$
1178.379	[41]	-0.051	-0.069	1.000	0 1 0	0.000	0 1 0	
2336.839	[42]	0.012	-0.045	0.998	0 2 0	0.002	1 0 0	
2671.645	[42]	0.057	0.008	0.998	1 0 0	0.002	0 2 0	
2787.718	[42]	0.036	0.007	1.000	0 0 1	0.000	0 0 1	
3474.319	[56]	0.031	-0.004	0.995	0 3 0	0.005	1 1 0	
3841.428**	[27](This work), [45]	0.006	-0.002	0.995	1 1 0	0.005	0 3 0	
3956.013	[56]	-0.019	-0.029	1.000	0 1 1	0.000	0 1 1	
4589.28*	[27] (This work), [50]	0.018	0.006	0.992	0 4 0	0.008	1 2 0	
4990.827	[54]	0.004	0.023	0.987	1 2 0	0.008	0 4 0	
5105.385	[54]	0.022	0.005	0.997	0 2 1	0.003	1 0 1	
5291.723	[54]	0.016	-0.011	0.962	2 0 0	0.033	0 0 2	
5373.903	[54]	-0.017	-0.011	0.997	1 0 1	0.003	0 2 1	
5529.438	[54]	0.011	-0.006	0.966	0 0 2	0.033	2 0 0	
5679.56*	[27] (This work), [50]	-0.003	-0.023	0.988	0 5 0	0.012	1 3 0	
6119.039**	[45], [53]	-0.051	0.018	0.977	1 3 0	0.012	2 1 0	
6235.082	[53]	0.002	0.023	0.992	0 3 1	0.008	1 1 1	
6452.980	[53]	-0.006	0.010	0.954	2 1 0	0.034	0 1 2	
6533.236	[53]	0.005	-0.020	0.992	1 1 1	0.008	0 3 1	
6686.993	[45]	-0.049	-0.018	0.966	0 1 2	0.034	2 1 0	
7343.91**	[27] (This work), [45]	-0.008	-0.019	0.987	0 4 1	0.013	1 2 1	
7593.267	6	0.014	0.019	0.938	2 2 0	0.034	0 2 2	
7672.918	[22], [55]	0.017	-0.001	0.979	1 2 1	0.013	0 4 1	

E_{obs} ,cm^{-1}	Reference	obs.-calc.$_{\text{EH}}$	obs.-calc.$_{\text{VAR}}$	P_1	W_1	P_2	W_2	$(\upsilon_1\upsilon_2\upsilon_3)_{\text{VAR}}$
7826.30*	[27] (This work), [45]	-0.039	0.017	0.957	0 2 2	0.035	2 2 0	
7852.928	[22]	-0.075	-0.020	0.835	3 0 0	0.154	1 0 2	
7899.826**	[27] (This work), [45]	-0.066	-0.006	0.935	2 0 1	0.057	0 0 3	
8054.074	[22]	0.022	-0.019	0.839	1 0 2	0.156	3 0 0	
8220.178	[22]	0.002	-0.018	0.943	0 0 3	0.057	2 0 1	
8792.63*	[21] (This work)	-0.030	-0.035	0.963	1 3 1	0.019	2 1 1	
9005.50*	[21] (This work)	-0.023	0.005	0.819	3 1 0	0.157	1 1 2	
9050.349	[21] (This work)	0.019	0.000	0.924	2 1 1	0.057	0 1 3	
9202.716	[21] (This work)	0.044	0.010	0.828	1 1 2	0.160	3 1 0	
9366.313	[21] (This work)	0.004	-0.004	0.943	0 1 3	0.057	2 1 1	
10180.116	[21] (This work)	0.020	0.005	0.895	2 2 1	0.056	0 2 3	
10341.01*	[24]	0.028	-0.011	0.526	4 0 0	0.327	2 0 2	
10358.563	[18]	-0.029	0.016	0.791	3 0 1	0.191	1 0 3	
10679.69*	[24]	-0.039	-0.007	0.801	1 0 3	0.191	3 0 1	
11483.639	[25] (This work)	0.047	-0.017	0.540	4 1 0	0.383	2 1 2	
11500.247	[25] (This work)	0.042	0.006	0.766	3 1 1	0.194	1 1 3	
11605.79*	[25] (This work)	0.052	0.032	0.930	0 3 3	0.053	2 3 1	
11679.389	[25] (This work)	0.082	0.117	0.482	2 1 2	0.425	4 1 0	
11816.637	[25] (This work)	0.061	0.052	0.790	1 1 3	0.192	3 1 1	
12618.912	4	-0.070	-0.009	0.707	3 2 1	0.187	1 2 3	
12698.46*	[27] (This work)	-0.017	-0.060	0.924	0 4 3	0.047	2 4 1	
12737.397	[28]	-0.025	-0.019	0.587	3 0 2	0.263	5 0 0	5 0 0
12743.035	[19], [28]	0.107	0.008	0.575	4 0 1	0.363	2 0 3	
12799.25*	[28]	-0.018	0.111	0.471	2 2 2	0.399	4 2 0	
12934.20*	[26] (This work)	-0.077	0.098	0.767	1 2 3	0.184	3 2 1	
12988.432	[26] (This work)	-0.005	0.114	0.661	5 0 0	0.167	1 0 4	3 0 2
13088.307	[26] (This work)	-0.043	0.118	0.512	2 0 3	0.374	4 0 1	
13263.902	[26] (This work)	0.009	0.097	0.716	1 0 4	0.237	3 0 2	
13717.264	[27] (This work)	0.069	-0.120	0.654	3 3 1	0.182	1 3 3	
13869.26*	[27] (This work)	-0.076	-0.115	0.575	3 1 2	0.193	5 1 0	5 1 0
13876.021	[27] (This work)	-0.028	-0.025	0.537	4 1 1	0.361	2 1 3	
		***rms*=0.055**	***rms*=0.048**					

Notes:

(obs.-calc.$_{\text{EH}}$) is the difference of the energy value calculated with the EH model and the experimental value

(obs.-calc.$_{\text{VAR}}$) is the difference of the energy value obtained by variational calculations [28] and the experimental value

P_1 and P_2 indicate the largest, and the second largest mixing coefficients, respectively, of the vibrational eigenvector (see text).

W_1 and W_2 indicate the corresponding vibration normal mode quantum numbers, $(v_1\, v_2\, v_3)$.

In the last column, $(\upsilon_1\upsilon_2\upsilon_3)_{VAR}$, the vibrational label of the corresponding level as provided in Ref. [28], is given only when it differs from our assignment.

Vibrational energies marked by * have been estimated from the (obs.-calc.$_{\text{VAR}}$) tendencies for low J and K_a rotational levels (see Text). The corresponding accuracy is estimated to be 0.01-0.1 cm^{-1}.

Vibrational energies marked by ** have been accurately estimated from the EH fitting of the observed rovibrational energies.

The approximate vibrational energies which could be derived or corrected in this study are the followings:

The energies of the (040) and (050) states were derived at 4589.28 ±0.01, 5679.56 ±0.03 cm^{-1}, respectively, from the corresponding energy levels of Ref. [39], and differ slightly from the estimates given in that reference.

The vibrational energy of the (022) state was estimated at 7826.30±0.02 cm^{-1} using data of Ref. [45], but differs noticeably from the value given in [45] (7826.38 cm^{-1}).

The (400) and (103) energies were accurately estimated in Ref. [24] at 10341.01±0.02 and 10679.69 ±0.01 cm^{-1}, respectively. For the (043) state, we derived a rough estimation: 12698.46 ±0.1 cm^{-1} for the vibrational energy from an average (obs-calc$_{\text{VAR}}$) deviations of all the energy levels observed for this state in Ref. [20], since there was a lack of the energy levels with J=0, 1. Despite the limited accuracy of the obtained value, the (043) energy value was included into the vibrational fitting in order to improve the predictive ability of the model.

The (041) energy at 7343.91±0.01 cm^{-1} was derived from the EH fitting of the energy levels with low J and K_a values from Ref. [45], and is slightly less than that of Ref. [45] (7343.93 cm^{-1}).

Accurate vibrational energies for the (110), (130) and (201) states at 3841.428 ±0.005, 6119.039 ±0.005, 7899.826 ±0.005 cm^{-1}, respectively, were evaluated from the EH fitting to the observed energies from Ref. [57] for (110), Ref. [53] for (130), and Refs. [22] for the (201) state. These estimates agree well with those from Ref. [45] (Note, that in [45] the vibrational label of the (201) and (003) states are interchanged compared to ours).

We used this literature data set together with the band origins presently determined, as input data in a fit of the effective vibrational parameters (Eqs. (3.2)–(3.5)). An *rms* deviation of 0.055 cm^{-1} was achieved by varying 24 parameters listed in Table 4.11. The comparison of the 53 experimental band origins with the fitted values is presented in Table 4.10 where the relevant references of the experimental data are included. The full list of vibrational energies calculated with the obtained EH up to 18000 cm^{-1} is provided as Supplementary Material of Ref. [27].

Table 4.11. Spectroscopic constants of the effective vibrational Hamiltonian of $D_2^{16}O$ molecule.

Parameter	Value (in cm^{-1})	Parameter	Value (in cm^{-1})
ω_1	2762.870(240)	y_{223}	0.4748(820)
ω_2	1207.313(240)	y_{233}	-0.2876(600)
ω_3	2890.426(420)	y_{333}	0.1142(240)
x_{11}	-22.322(110)	z_{1122}	-0.02315(520)
x_{12}	-9.3700(940)	z_{1222}	0.01459(500)
x_{13}	-86.463(140)	z_{2222}	-0.02580(100)
x_{22}	-9.6528(720)	z_{2223}	0.04031(820)
x_{23}	-10.099(260)	z_{2233}	-0.0329(130)
x_{33}	-27.319(190)	F	10.609(220)
y_{111}	0.0432(130)	Γ_{DD}	-21.8499(880)
y_{113}	0.6514(360)	γ_1	0.2540(220)
y_{123}	-0.7106(300)	γ_2	0.0595(100)

The quoted errors correspond to two standard deviations. The fit includes 53 band origins and 24 adjusted parameters (for the definition of parameters, see Section 4 of Chapter III).

The band origins obtained by variational calculations [28] are also included in Table 4.10. The variational *rms* deviation (0.048 cm^{-1}) is very close to that obtained with the EH model (0.055 cm^{-1}) but variational calculations are much more accurate in predicting the band origins, especially for the highly excited bending states. The accuracy achieved with our simple EH model is sufficient to unambiguously associate our calculated energy levels both with the observed band origins, and with the variational energies at least up to 16066 cm^{-1} which is the highest energy value calculated in Ref. [28].

On the basis of these EH calculations, it is possible to propose consistent normal mode labels for the highly excited $D_2^{16}O$ vibrational states. In the considered procedure, the approximate vibrational quantum numbers u_1, u_2, u_3 are chosen to coincide with those of the $|\upsilon_1\upsilon_2\upsilon_3\rangle$ basis function (Eq. (3.37)) which has the maximal value of the mixing coefficient P_1. The first and the second largest mixing coefficients (or fractions) denoted as P_1 and P_2, respectively, are included in Table 4.10 and plotted in Figure 4.12 as a function of the corresponding vibrational energy for all states up to 18000 cm^{-1}. Up to 12600 cm^{-1}, the vibrational eigenstates show a clear normal mode behavior, with a dominant fraction no less than 68% (except for four levels). Vibrational mixings become more important between 12600 and

15000 cm^{-1} and increase with the energy leading to maximal fractions of less than 20% for separate states above 15000 cm^{-1}. Note however, that a few highly excited vibrational states, mostly with prevailing ν_2 or ν_3 excitation, still show a clearly dominant normal mode character.

Up to 12700 cm^{-1}, our labels coincide with those from Ref. [28]. Above this value, some discrepancies are noted. A few of the conflicting labels concern states that have a clearly dominant normal mode character in our calculations. For example, we label as (500) (maximal fraction of 66%) the vibrational state at 12988.432 cm^{-1} [26], while this state is labeled as (302) in [28]. In the region under study, we preferred the vibrational label (312) (58% contribution) for the state at 13869.26 cm^{-1}, which was assigned to (510) in [28]. In fact, the (510) state (65% contribution) corresponds to a state predicted at 14121.74 cm^{-1} by variational calculations [28]. Thus, in spite of a higher excitation of the ν_3 mode, which exceeds in energy that of the ν_1 mode, the (312) vibrational state has a lower energy than the (510) state.

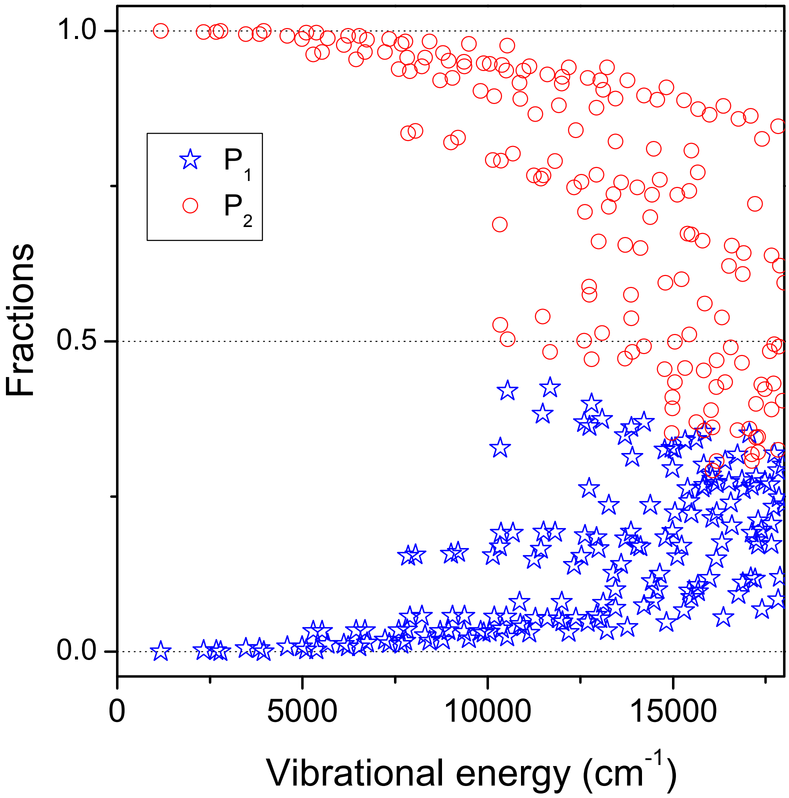

Figure 4.12. The two largest fractions (P_1 and P_2) of the vibrational wave function obtained from the diagonalization of the vibrational effective Hamiltonian matrix, versus the calculated energy value up to 18000 cm^{-1}.

4. Intracavity laser absorption spectroscopy of HD^{16}O between 9100 and 14115 cm^{-1}

4.1 Introduction

Monodeuterated water, HDO, is of great interest for the study of planetary atmospheres. For instance, HDO is an important species in the determination of the isotopic D/H ratio, which is necessary to understand the origin and source of the atmospheric water. It is also used to compare water found in comets or in other solar system bodies with terrestrial water [58].

This Section is devoted to the investigation of the weak HDO absorption spectrum by high sensitivity ICLAS in two regions 9100-9640 cm^{-1} and 13020-14115 cm^{-1} [59]-[60]. Figure 4.13 shows an overview comparison of HDO spectra obtained from our ICLAS recordings with the FTS spectrum of Ref. [33].

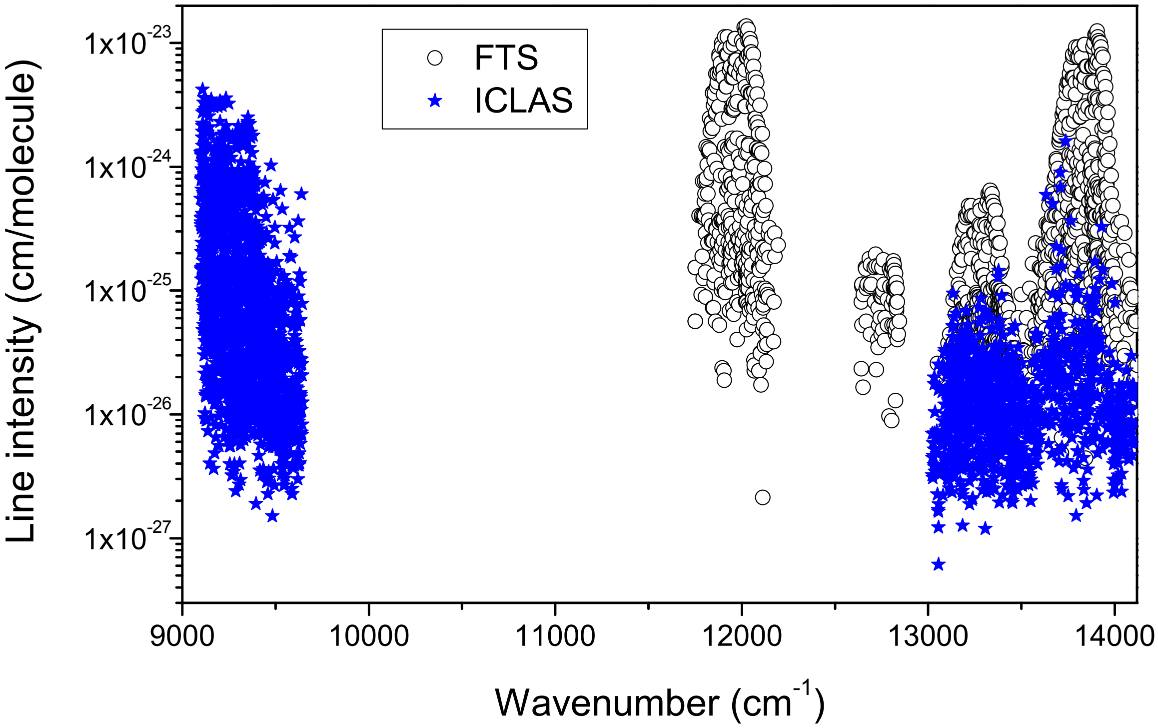

Figure 4.13. Overview comparison of the HD^{16}O line lists presently analyzed by ICLAS and FTS [33].

The HDO molecule possesses an absorption spectrum significantly different from that of the parent H_2O species. It is due to the decrease in symmetry from C_{2V} to C_S and a considerable change in harmonic frequencies. In particular, the ω_3 harmonic frequency (3887 cm^{-1}) corresponding to OH stretch is much larger than the ω_1 for the OD stretch (2823 cm^{-1}) and ω_2 for the bending vibration (1444 cm^{-1}). This results in a series of well isolated $(00\upsilon_3)$ vibrational states [61], [62]. However, the close coincidence between the ω_1 and $2\omega_2$ harmonic frequencies combined with abnormal centrifugal distortion effects gives rise to strong high-order resonance interactions in HDO, examined in the present work.

An exhaustive list and experts review of all published HD^{16}O rovibrational transitions in the 0-23000 cm^{-1} spectral range has been recently reported by an international IUPAC-sponsored

Task Group [21]. Numerous studies of the $HD^{16}O$ high resolution vibrational-rotational spectrum in the visible and near-infrared spectral ranges were performed by FTS [63]-[64] and ICLAS [61]-[62], [65]-[69]. A review (up to 2003) of the absorption bands of HDO recorded between 9600 and 18350 cm^{-1} using different ICLAS spectrometers (VeCSEL, Ti:Sapphire, dyes) is presented in Fig. 1 of Ref. [62]. As concerns our region of interest, ten years ago the HDO absorption spectra in the 13570-14300 [67] and 13160-13500 [68] cm^{-1} regions were studied by ICLAS using dye lasers. Since 2003, the analysis of the absorption spectrum of HDO above 9000 cm^{-1} has been extended by a few additional contributions: the FTS study of the 8900-9600 cm^{-1} [70] and 10110-12215 cm^{-1} [64] regions, obtained with a 123 m path length and 0.02 cm^{-1} resolution; the full coverage of the FTS absorption spectrum between 11500 and 23000 cm^{-1}, recorded with a 600 m path length [71], [33]; ICLAS-Ti: Sapphire study of the 11645-12330 cm^{-1} region [72] which lowered by more than one order of magnitude the FTS detection limit of Refs. [64], [71]. Finally, the HDO absorption spectrum between 9387-9449 cm^{-1} was recorded by ICLAS using an Nd glass laser at 800K [73].

One of the two presently investigated spectral regions 9100-9640 cm^{-1} shown in Figure 4.14 corresponds to a “transparency window” for both the main isotopologue, $H_2{}^{16}O$, and HDO. It lies between the much stronger $\nu_2 + 2\nu_3$ and $3\nu_3$ bands of HDO at 8611.095 and 10631.683 cm^{-1} respectively. As it will be shown in the next Section, the high sensitivity of the ICLAS technique used in our study provided a much deeper knowledge of this spectral region.

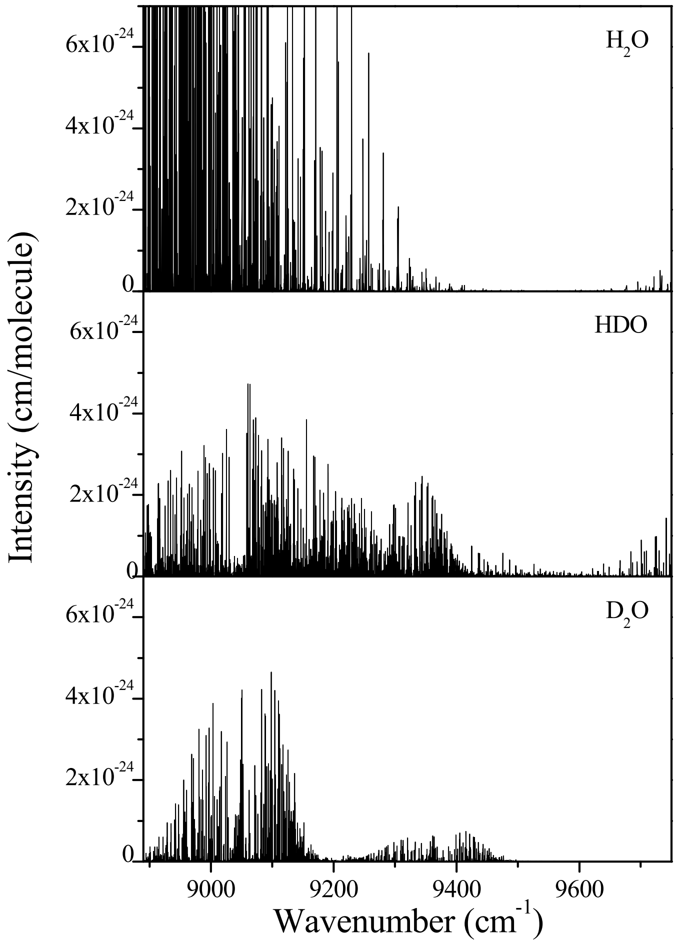

Figure 4.14. Overview of the H_2O, HDO and D_2O spectrum as calculated by Schwenke and Partridge [29], [30]. Note that the intensity scale corresponds to the pure species.

As concerns the 13020-14115 cm^{-1} spectral range, a sensitivity higher than 2×10^{-26} cm/molecule obtained in previous studies for pure HDO [67], [68], [71] was achieved using a titanium sapphire laser instead of dye lasers for ICLAS. It allowed (*i*) to complete the previous measurements by new observations of weak transitions beyond the FTS sensitivity; (*ii*) to replace the first ICLAS line lists [67], [68] by a more complete dataset where the calibration problem (of the order of 0.01 cm^{-1}) evidenced [33] for the 13100-13500 cm^{-1} region [68] was corrected. The increased sensitivity of the new recordings is demonstrated in Figure 4.13, where the new ICLAS observations are superimposed to the FTS [33] spectrum.

4.2 Experimental details and line list construction

The spectra were recorded with the ICLAS spectrometer based on a VeCSEL and Ti: Sapphire laser in the 9100-9640 cm^{-1} and 13020-14115 cm^{-1} spectral regions, respectively. The experimental setup was described in Section 2. Deuterated water was obtained by mixing liquid H_2O and D_2O. Two D_2O:H_2O mixing ratios were used for the recordings: in the 9100-9640 cm^{-1} range and below 13550 cm^{-1}, D_2O and H_2O were mixed in equal quantities leading to a 1:2:1 proportion for H_2O:HDO:D_2O in the gas phase. Above 13550 cm^{-1}, a higher deuterium enrichment was used in order to decrease the absorption of the strong $\Delta V_{OH} = 4$ stretching overtone of $H_2{}^{16}O$ which may obscure many HDO lines. The D_2O absorption in this region being very weak, as shown in Figure 4.3, a 5:1 mixing ratio for D_2O and H_2O in the liquid phase was used. It led to a factor of 10 for the HDO:H_2O relative concentration in the gas phase which helped to detect very weak HDO lines. The contribution of the intracavity air (oxygen A band below 13160 cm^{-1} and water vapor) was minimized by continuously flowing dry nitrogen into the box containing the Ti:Sapphire laser.

The line list construction was nearly the same as for the D_2O absorption spectrum described above in Section 3. Each of the 12 cm^{-1} wide individual spectrum was calibrated independently using reference line positions. When possible, the HDO line positions measured by FTS [70] and [33] were adopted as reference in the 9100-9640 cm^{-1} and 13020-14115 cm^{-1} spectral regions, respectively. In some spectral sections, the line list of Ref. [33] was too sparse and we used the $H_2{}^{16}O$ line positions of Ref. [74]. In the 13020-13160 cm^{-1} region, $H_2{}^{16}O$ and HDO lines are very weak and we took advantage of the transitions of the oxygen A band (due to residual oxygen inside the Ti:Sapphire cavity) to calibrate the spectra.

The accuracy of the ICLAS line positions for well-isolated lines of intermediate intensities in the 9100-9640 cm^{-1} and 13020-14115 cm^{-1} spectral regions was estimated to be of the order of 0.002 cm^{-1} and 0.005 cm^{-1}, respectively. It is confirmed below by the uncertainty obtained for the energy levels retrieved from several transitions. Our measurements were mostly devoted to weak lines, since strong lines were previously analysed [33], [70]−[71].

An important concern is the retrieval of line intensities: contrary to ICLAS based on dye or Ti:Sapphire lasers, the specific laser dynamics of VeCSELs prevents its systematic use for absolute quantitative measurements from ICLAS-VeCSEL spectra. For instance, in Ref. [75] it was shown, that in some experimental conditions (high pumping rate, very long generation times, high line intensity etc.) the absorption profile of the stronger lines can be strongly asymmetric in the ICLAS-VeCSEL spectrum and in some extreme conditions, replaced by emission lines. Despite the fact that in the present recordings we took much care in choosing experimental conditions that lead to symmetric line profile, relative intensities are not trustable. The absorption line intensity depends on the location of the line relative to the central frequency of the VeCSEL emission profile. The comparison with the FTS spectrum of Ref. [70] indicates that the absorption is systematically underestimated when the line appears on the wings of the emission profile.

Moreover, in the ICLAS set up (both ICLAS-Ti:Sapphire and ICLAS-VeCSEL) it is difficult to estimate accurately the HDO partial pressure in the ICLAS cell, which leads to the uncertainty in the absolute line intensity values. In such circumstances, it was not reasonable to try to retrieve accurate line intensities from our spectra.

However, the complete assignment of the spectrum relies greatly on the intensity criterion i.e. the reasonable matching between observed and calculated intensities [29], [30]. Indeed, the quality of the calculated intensity values was tested in many different spectral regions and was found, in most cases, close to the experimental accuracy. Thus, efforts were undertaken to normalize the experimental intensities against those calculated by Schwenke and Partridge [30] in both spectral regions under consideration. As a result, a satisfactory agreement with the calculation was achieved for middle and weak lines, while the situation was less satisfactory for the strongest lines, which were frequently saturated in the ICLAS spectra.

In consequence of the difficult and laborious process followed in the line list construction, the obtained intensity values should be used with caution. The obtained intensity values proved to be of great help for identification of the weakest lines not included into CD relations, and in the case of blended lines. The weakest detected lines have an intensity value of the order of 10^{-27} cm/molecule. As the ICLAS intensity values of the strongest lines were frequently distorted due to saturation effects, we have transferred the FTS [33] intensities values for the 234 lines with intensities larger than 2.0×10^{-25} cm/molecule in the 13020-14115 cm^{-1} spectral region.

4.3 Spectrum analysis and results

The 9100-9640 cm^{-1} spectral region

The line list obtained in the 9100-9640 cm^{-1} spectral region includes a total of 2250 transitions corresponding to the superposition of the HDO, H_2O and D_2O contributions. 195 $H_2{}^{16}O$ lines were identified on the basis of the line list attached to Ref. [76], while 349 D_2O lines were discriminated by comparison with the ICLAS-VeCSEL D_2O spectrum recorded in the same region [21]. Overall 1706 lines were attributed to the HDO species. The spectrum assignment was performed on the basis of the *ab initio* calculations by Schwenke and Partridge [29], [30].

The rovibrational assignments were assessed by taking into account both CD relations and the fact that the (obs.-calc.) deviations of the energy levels depend smoothly on J and K_a rotational quantum numbers. This is illustrated for instance in Figure 4.15 for the $K_a = 0-5$ levels of the different investigated vibrational states. However, as we proceeded with our assignments, both theoretical predictions and experimental accuracy degraded for the weakest lines corresponding to the highly excited transitions that resulted in less reliable assignments, in particular, in the case of single line not involved in lower sate combination relations. The upper energy levels were derived by adding the lower energy values [77] to the observed transitions. A set of 746 energy levels was derived from transitions assigned to 13 upper vibrational states, 300 of them being reported for the first time.

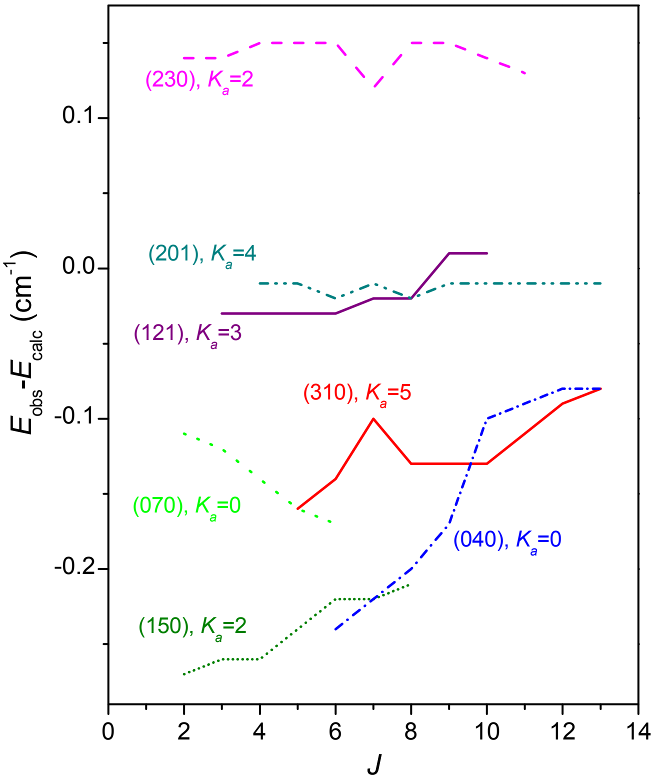

Figure 4.15. Variation of the differences between the experimental and calculated [29], [30] energy levels of HDO as a function of *J*. The experimental energy levels are obtained from the analysis of ICLAS-VeCSEL spectrum of HDO between 9100 and 9640 cm^{-1}. K_a= 0, 2–5 sublevels of seven of the analyzed vibrational states are given.

The presently obtained results along with the state-by-state comparison with those of Ref. [70] are summarized in Table 4.12. As expected, most of the new energy levels were obtained for the highly excited (041), (150), (230), and (070) states corresponding to the weakest bands. We could also reach higher *J* and K_a values for the three strongest bands, namely (201)-(000), (121)-(000), and (310)-(000). From the (obs.-calc.) extrapolation for energy levels with K_a = 0, we estimate at 9032.11±0.1 and 9086.32 ±0.05 cm^{-1}, the origin of the (041)-(000) and (070)-(000) bands respectively (see Figure 4.15). The $HD^{16}O$ energy levels derived from ICLAS-VeCSEL spectrum in the 9100-9640 cm^{-1} are partly presented in Table 4.13. They agree with that of Ref. [70] within 0.0036 cm^{-1} on average with a largest discrepancy of 0.026 cm^{-1} for the (230) [321] level at 9596.5320 cm^{-1}. We believe that in many cases our energy level values are more precise since they are often derived from a larger number of lines reaching the same upper level and that our program for automatic spectrum assignment allows for discarding the less accurate line positions among all the lines included into CD relations. For the complete set of the derived $HD^{16}O$ energy levels the reader is referred to the relevant article [59].)

Table 4.12. Summary of the information obtained from the ICLAS-VeCSEL spectrum of HDO recorded between 9100 and 9640 cm^{-1}. The count of the newly observed levels considers not only the results of Ref. [70] but also the levels determined in Refs. [62], [64] thus reducing the number of newly observed levels.

Vibrational state	$E_v{}^a$, cm^{-1}	This work			Ref. [70]			
		N levels	J_{max}	$K_{a\,max}$	N levels	J_{max}	$K_{a\,max}$	New levels
060	7914.317 ^{b}	1						1
012	8611.102 ^{c}	2						2
041	9032.31 ^{d}	102	13	7	23	8	4	82
201	9047.068	128	13	9	117	13	7	25
070	9086.32 ^{d}	55	12	3	24	7	2	31
121	9155.817	108	15	6	62	9	6	47
150	9381.792	52	13	4	19	6	2	29
310	9292.999	148	16	8	101	14	6	42
230	9487.915	80	12	5	29	7	2	36
102	9967.023 ^{e}	51						4
080	10119.36 ^{g}	1						1
022	9934.789 ^{e}	15						
003	10631.683 ^{f}	3						
Total:		746			375			300

^{a}Vibrational term value

^{b} Experimental value from Ref. [78], see also this reference for additional levels of the (060) state.

^{c} Experimental value from Ref. [79], see also this reference for additional levels of the (012) state.

^{d} Extrapolated value (see Text).

^{e} Experimental value from Ref. [62], see also this reference for additional levels of the (102) and (022) states.

^{f} Experimental value from Ref. [64], see also this reference for additional levels of the (003) state.

^{g} Predicted value [29], [30].

Table 4.13. The experimental energy levels of the (230), (070), and (150) vibrational states of HD^{16}O newly derived by ICLAS-VeCSEL in the 9100–9640 cm^{-1} spectral region.

$J\,K_a\,K_c$	**(230)**			**(070)**			**(150)**		
	E_{obs} (cm^{-1})	σ	N	E_{obs} (cm^{-1})	σ	N	E_{obs} (cm^{-1})	σ	N
0 0 0	9487.9156		1				9381.7921	1.0	2
1 0 1	9503.2835	1.2	4				9397.0303	1.0	2
1 1 1	9528.8008	2.2	4	9174.2609	1.8	2	9427.9568	0.2	3
1 1 0	9532.0413	0.8	3	9177.7155	1.8	2	9431.4219	1.6	3
2 0 2	9533.6490	1.0	4	9133.3657		1	9427.2931	1.3	3
2 1 2	9556.3596	0.6	4	9203.8195	1.2	4	9454.9554	0.3	3
2 1 1	9566.0735	1.4	3	9212.7616	1.4	3	9465.3384	3.3	3
2 2 1	9549.3421	1.3	4	9399.1347	1.8	2	9645.4923	0.8	2
2 2 0	9549.6927	2.2	3	9399.2591	0.7	4	9645.7522	6.5	4
3 0 3	9578.3410	1.8	5	9179.1221		1	9472.1203	0.4	3
3 1 3	9597.5547	1.2	5	9240.8737	0.1	2	9495.2707	1.8	4
3 1 2	9616.9051	2.9	4	9264.7087	1.4	3	9515.9703	1.1	5
3 2 2	9594.8784	3.8	6	9445.5663	1.4	6	9691.9465	1.1	4
3 2 1	9596.5320	2.4	4	9446.3482	1.4	4	9693.2713	1.5	4
3 3 1	9735.4903		1	9682.3587	2.7	2	9842.5387		1
3 3 0	9735.5095		1	9682.3607		1	9842.5537	0.4	2
4 0 4	9636.6233	1.2	4	9238.7725		1	9531.1106	1.8	5
4 1 4	9651.9966	2.5	5	9295.8320	0.9	2	9548.7055	1.6	5
4 1 3	9684.2212	1.2	5	9333.1813	0.4	2	9582.9911	0.8	4
4 2 3	9655.3407	0.3	4	9512.2502	1.8	7	9753.6437	3.8	5
4 2 2	9660.1148	2.7	5	9509.1344	1.4	8	9757.5040	6.8	2
4 3 2	9797.3540	1.7	4	9744.3360	2.8	2	9905.4627		1
4 3 1	9797.4674	1.0	3	9744.4298	2.7	3	9905.5301	0.4	2
4 4 1	9928.6481	2.8	4				10037.1799 T		1
4 4 0	9928.6528	4.5	3				10037.1782 T		1
5 0 5	9707.8820	0.4	3	9311.8475		1	9604.7898	1.8	4
5 1 5	9719.6464	2.1	4	9363.8575	0.8	2	9615.0467	1.1	3
5 1 4	9767.6088	1.1	4	9433.9199	0.2	2	9665.8424	1.4	9
5 2 4	9730.5456	1.2	3	9589.5115	0.3	4	9830.3904	1.3	3
5 2 3	9740.6111	1.0	4	9587.5678	2.2	6	9838.9880	2.7	2
5 3 3	9874.7981	4.3	2	9821.8093	1.7	3	9984.153 I		
5 3 2	9875.2208	0.5	2	9822.1677	2.0	2	9984.467 I		
5 4 2	10004.3031	4.3	2						
5 4 1	10004.2968	3.9	3						
5 5 1	10195.0767		1						
5 5 0	10195.0766		1						

$J K_a K_c$	(230)			(070)			(150)		
	E_{obs} (cm^{-1})	σ	N	E_{obs} (cm^{-1})	σ	N	E_{obs} (cm^{-1})	σ	N
6 0 6	9791.6291	0.9	3	9398.1472		1	9677.7722	1.1	4
6 1 6	9800.2387	0.0	2	9444.8721	0.5	2	9694.0639	0.2	3
6 1 5	9866.4750	5.6	3	9534.6849		1	9764.2777	1.1	3
6 2 5	9820.3343	0.4	3	9682.6139	2.5	4	9921.9308		1
6 2 4	9838.2738	1.2	3	9696.7517	0.8	3	9938.0057	3.8	2
6 3 4	9967.7883	0.0	2	9914.6897	4.2	2	10078.600 I		
6 3 3	9969.0549	2.2	2	9915.7978	1.4	2			
6 4 3	10095.2157	8.5	2						
6 4 2	10095.2596	2.7	2						
6 5 2	10285.4333		1						
6 5 1	10285.4323		1						
7 0 7	9887.5450	0.5	3				9775.2560		1
7 1 7	9893.5060	2.2	3	9538.7007	0.2	2	9785.7449	0.5	2
7 1 6	9980.1225	3.7	2	9650.4604	3.0	3	9877.0264	0.2	3
7 2 6	9922.3800	2.5	5	9791.0651		1	10028.0605		1
7 2 5	9953.0546	2.3	2	9808.5496	1.3	3	10054.540 I		
7 3 5	10076.2923	1.5	2	10022.9117		1	10188.712 I		
7 3 4	10079.2542		1	10025.5715		1	10190.958 I		
7 4 4	10201.4760	7.5	2						
7 4 3	10201.6592	5.5	3						
8 0 8	9995.5424		1	9609.9425		1	9881.3728	2.8	3
8 1 8	9999.3033	3.7	2	9645.2177	1.7	2	9888.5792	0.5	2
8 1 7	10003.3587	5.4	2	9788.7495	3.7	2	10107.7002		1
8 2 7	10040.7419	1.8	2	9914.9494		1	10148.130 I		
8 2 6	10084.5880	1.8	2	9938.2804	0.4	2	10188.256 I		
8 3 6	10200.1792		1	10146.2681		1			
8 3 5	10206.1692		1	10152.2310		1			
8 4 5	10323.1420		1						
9 0 9	10116.1548		1				9999.8839		1
9 1 9	10117.5310		1				10004.9036	1.1	3
9 1 8	10142.3058		1	9937.1275		1	10248.530 I		

For completeness, the set of levels presently derived from the analysis of the ICLAS-VeCSEL spectrum between 9100 and 9640 cm^{-1}, has been combined with the levels determined in Ref. [62] which are marked by *"I"*. *"T"* marks tentative assignments.

N is the number of lines used for the upper energy level determination and σ denotes the corresponding experimental uncertainty in 10^{-3} cm^{-1} units.

For the complete set of the presently derived $HD^{16}O$ energy levels, the reader is referred to the relevant article [59].

The 13020-14115 cm^{-1} spectral region

The rovibrational assignment of the HDO absorption spectrum in the 13020-14115 cm^{-1} region was based on the results of the high accuracy SP variational calculations [29], [30], [80] as well as recent calculations using a new potential energy surface performed by Voronin, Tolchenov and Tennyson [81], [82]. The 1877 absorption lines of our list were assigned to 21 upper vibrational states of $HD^{16}O$ and to the (004) state of $HD^{18}O$. Taking into account multiple assignments, they correspond to 2157 transitions.

A number of new high J and K_a energy levels has been derived for the three strongest bands (023) - (000), (103) - (000) and (004) - (000), while only small J and K_a transitions have been assigned to the three new very weak absorption bands: (510)-(000), (401)-(000) and (132)-(000) at 14147.50, 14024.58 and 13960.08 cm^{-1}, respectively. The summary of the obtained information is presented in Table 4.14. As transitions reaching the [000] rotational level were not detected, the pure vibrational energies of the (510), (401) and (132) vibrational $HD^{16}O$ states were estimated from an extrapolation at K_a = 0 of the (obs.-calc.) differences between the derived and calculated energy levels.

Table 4.14. Summary of the information obtained by ICLAS in the 13020–14115 cm^{-1} region and comparison of the experimental and calculated values of the vibrational terms.

Vibrational band	Upper state energy (cm^{-1})			Levels		Transitions	Intensity ratio VTT /SP [b]
	Experimental	VTT[81], [82]	SP [29], [30],[80]	Total	New		
HD^{16}O							
042-000		12516.40	12516.63	2	2	3	1.19
071-000		12694.32	12694.53	1	1	1	5.83
500-000	12767.141	12767.15	12766.72	2	0	2	0.89
180-000		12852.34	12852.95	2	1	2	2.80
311-000	12919.938	12920.00	12919.77	5	2	5	1.17
151-000		12986.78	12986.67	7	6	13	1.40
420-000		13108.45	13108.33	1	1	1	1.02
340-000		13218.55	13218.09	4	4	10	1.73
023-000	13278.35	13278.33	13278.44	138	22	600	1.03
0110-000		13326.84	13327.59	6	3	9	0.50
103-000	13331.603	13331.58	13331.73	126	20	531	1.15
052-000		13716.46	13716.98	5	1	9	0.83
081-000		13797.37	13797.53	1	0	5	1.01
004-000	13853.628	13853.63	13853.93	183	26	777	1.01
190-000			13884.52	1	1	2	0.49
212-000		13889.58	13890.01	5	5	7	0.73
132-000	13960.08 ± 0.05[a]	13960.04	13960.20	18	18	19	1.53
401-000	14024.58 ± 0.05[a]	14024.70	14024.25	16	16	17	0.75
510-000	14147.50 ± 0.05[a]	14147.42	14147.51	29	25	44	1.09
033-010		14563.08	14563.55	3	3	3	0.92
014-010	15166.104	15166.09	15166.52	16	0	18	1.00
Total				571	157	2078	1.06
HD^{18}O							
004-000	13814.526		13814.75	48	48	79	

[a] Vibrational energies are evaluated by extrapolation of the (obs.–calc.) values for the $K_a = 0$ series (see text).

[b] Ratio of the sum of the VTT and SP calculated values limited to the observed transitions.

Overall, 571 rovibrational energy levels have been derived, 157 of them being reported for the first time. Figure 4.16 shows the (obs.-calc.) deviations of the HD^{16}O energy levels plotted versus $J + K_a / J$ for SP [29], [30] and VTT [81], [82] calculations. The recent VTT calculations are clearly more accurate: the *rms* deviations are 0.06 and 0.23 cm^{-1} for VTT and SP, respectively, while the largest deviations reach a value of 0.80 cm^{-1} for SP to be compared to 0.22 cm^{-1} for VTT. As an example, the deviations for the (004) and (401) energy levels are highlighted with different symbols on Figure 4.16. We have performed a detailed comparison of the energy levels of the (004), (023) and (103) vibrational states in common with the FTS set of Ref. [33]. The obtained values are comparable in terms of accuracy for most of the levels but the accuracy of the high *J* and K_a energy levels corresponding to the weakest transitions in the FTS line list is generally improved by the present measurements.

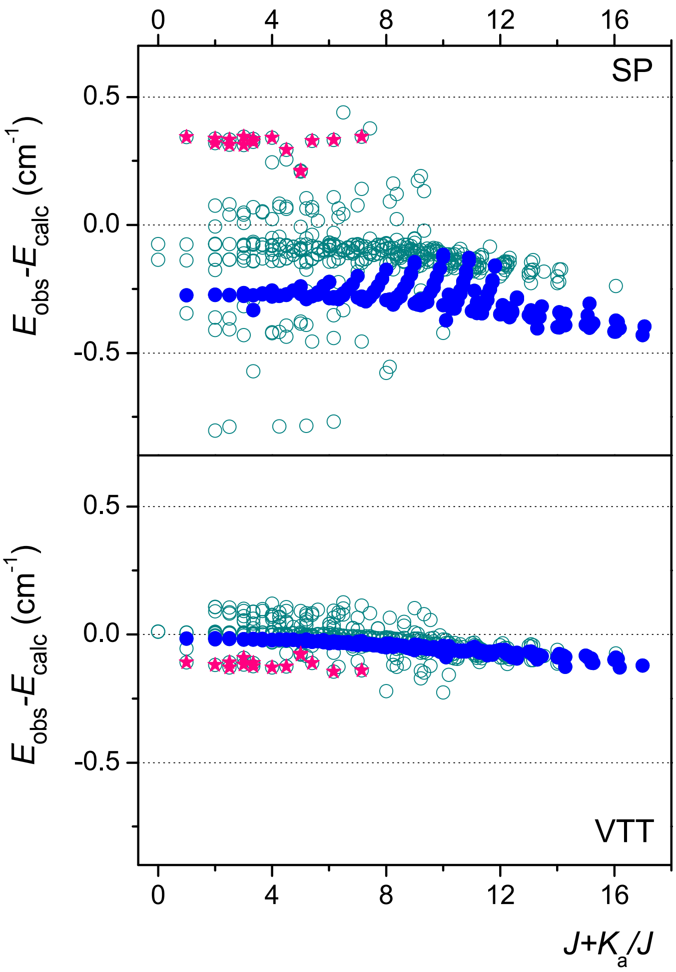

Figure 4.16. Variation of the differences between the observed and calculated values for the HDO energy levels determined from the ICLAS spectrum between 13020 and 14115 cm^{-1}: *Upper panel:* variational calculations of Schwenke and Partridge [29], [30]; Lower panel: variational calculations of VTT [81], [82]. As examples, the deviations corresponding to the (004) and (401) vibrational levels have been highlighted with full circles and stars, respectively.

Intensity information provides another approach to support the assignments. The comparison presented in Figure 4.17 shows that the two sets of calculated intensities agree better with each other than with the experiment. It is probably a consequence of the difficulty of retrieving accurate intensity of a weak line in a strong absorbing region. However, as evidenced in the Ref. [33], in some specific cases connected with the resonance redistributions of the intensities, VTT results were found to match better with the experiment.

We have included in Table 4.14 the values of ratios of the sums of VTT and SP calculated intensities limited to the observed transitions. Important disagreements are noted for the weakest bands: compared to SP values, VTT intensities are weaker by up to a factor of 2-3 for part of the transitions of the (212)-(000) band, by 25-30% for the transitions of the (401) -(000) band while the VTT intensities of the (132)-(000) band exceed by about 40-50% the SP values. The intensities of the very weak (151)-(000) and (340)-(000) bands have a clear resonance origin and also vary significantly from VTT to SP. As these differences concern mostly the weakest observed transitions with measured intensities with large uncertainties, it is difficult to judge definitely, which calculations are more accurate.

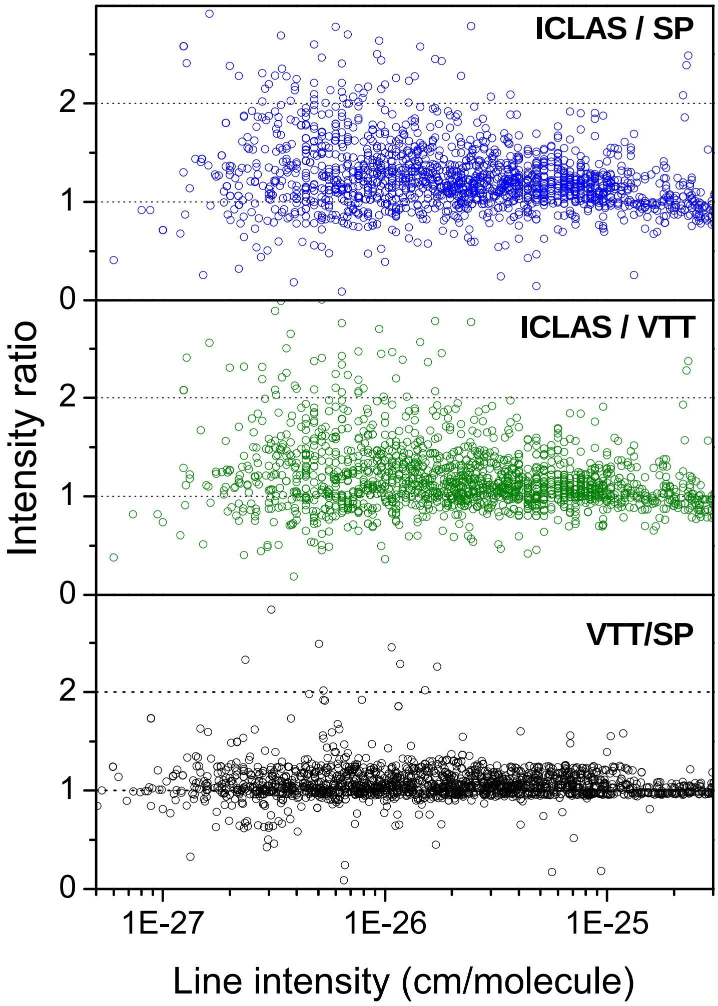

Figure 4.17. Ratios of the experimental and calculated line intensities. The experimental values are compared to the intensity values calculated by Schwenke and Partridge [30] (upper panel) and VTT [81], [82] (middle panel) while the lower panel shows the comparison between the two calculations.

At the final stage of analysis, seventy-nine weak transitions of the $4\nu_3$ band of the HD^{18}O isotopologue were assigned. It leads to the derivation of 48 new energy levels that are the most excited ones reported so far for this isotopologue. The vibrational term value of the well isolated (004) state of HD^{18}O (E_v = 13814.526 cm^{-1}) has been accurately evaluated from the fit using a Watson–type rotational Hamiltonian.

For the complete energy levels set of the HD^{16}O and HD^{18}O molecules derived from the analysis of ICLAS spectra in the 9100-9640 cm^{-1} and 13020-14115 cm^{-1} regions the reader is referred to the relevant articles [59], [60].)

4.4 High-order resonance interactions and rovibrational labelling

The HDO molecule is known to undergo strong centrifugal distortion effects connected with the excitation of large amplitude ν_2 bending vibration (see [33], [61], for example). It induces high–order resonance interactions with highly excited bending states resulting in intensity transfers, which make the corresponding transitions observable. The high sensitivity of the present recordings allowed detecting very weak transitions reaching some of these "dark" states. Thus due to intensity transfer from stronger lines – resonance counterparts, some transitions involving the (150), (070), (151), (052), (071), (081), (180), (190), and (0 11 0) (SP labelling) upper states could be identified. As the SP vibrational labels are sometimes erroneous or ambiguous and as no labels are provided by VTT calculations [82], these labellings were checked and sometimes corrected on the basis of EH calculations.

In the course of the analysis of the 9100−9640 cm^{-1} spectral region, two bands – (150)-(000) and (070)-(000) were found to have a resonance origin. The (150)-(000) band steals its intensity *via* a distant resonance interaction with the (230)-(000) band. The interaction seems to be so strong, that it leads to nearly equal transition intensities for both bands. Interestingly, the observation of the (070)−(000) band arises from resonance coupling with three vibrational bands depending on K_a values: (041)-(000) (for K_a = 0 levels), (121)-(000) (for K_a= 1 levels), and (310)-(000) (for K_a = 2 levels). Three lines belonging to the $6\nu_2$ and $8\nu_2$ bands were also observed due to a resonance interaction with the much stronger (121)-(000) and (111)-(000) bands respectively. As stressed in Ref. [62], SP rovibrational assignments for the (230) and (150) states are often ambiguous. The new information on the experimental energy levels derived in this study and in Ref. [70] confirms this observation. In particular, for the (230) state, the energy in the J-multiplet does not increase with K_a increasing from 1 to 2 as expected (Table 4.13). We attempted a rough fitting within the Effective Hamiltonian approach to relabel the energy levels of the (150) and (230) states considering them as isolated, but the results were not satisfactory. Further analysis is then required to solve this problem.

In the higher energy region 13020-14115 cm^{-1} analysis, the labellings of the levels of the (103) and (023) dyad were the most problematic. Using the EH approach, we could obtain an approximate global EH fitting of these two interacting states with an *rms* value of 0.08 cm^{-1}. The effective Hamiltonian used in the calculation was based on the Padé-Borel approximants [83]. The maximal normal mode contribution to the wave function provided unambiguous rovibrational labelling for most of the levels. Some of the SP labels had to be corrected as a different normal mode state was clearly dominant in the expansion of the EH wavefunction.

The labelling of the highly excited bending vibrational states was very difficult too. These states are involved in series of resonance interactions that may lead to large shifts (up to several tens of cm^{-1}) in their rotational energy levels compared to the unperturbed values. For this reason, a number of EH calculations were performed to confirm that the series of the presently observed $K_a = 1$ energy levels with $J = 1 - 4$ belong to the (0 11 0) pure bending state.

The corresponding transitions borrow their intensities from much stronger lines of the $4\nu_3$ band. The vibrational labelling of this (0 11 0) state predicted [82] at 13326.84 cm^{-1} has been confirmed by the results of Ref. [33]. However, the $K_a = 1$ energy levels are by more than 500 cm^{-1} higher than those with $K_a = 0$, that hindered the straightforward assignment even in case of the [111] and [110] rotational levels. The upper states differing by one bending excitation, the (004)-(0 11 0) interaction shows a great similarity with the previously analysed (014)-(0 12 0) resonance interaction [33], [61]. A careful comparison of the $K_a = 1$ rotational sublevels derived for the (0 12 0) state in Refs. [33], [61] confirmed our labelling of the transitions reaching the [110], [211] and [414] sublevels of the (0 11 0) state (see Table 2 in the relevant article [60]). These considerations also made it clear that the (052) vibrational labelling given in Refs. [33], [68] for the [312], [515] and [616] levels at 13964.294, 14065.157 and 14150.219 cm^{-1}, respectively, had to be changed to (0 11 0). Our new identifications are also confirmed by the fact that all these (0 11 0) energy levels show similar (obs.-calc.) deviations for both VTT and SP calculations.

5. The high resolution ICLAS spectra of $H_2^{18}O$ in the 12580-14100 cm^{-1} spectral range

5.1 Introduction

$H_2^{18}O$ is considered to be the fifth main contributor to the atmospheric absorption of solar radiation with natural abundance about 0.02%. Knowledge of the line positions and strengths of the $H_2^{18}O$ isotopologue is then of importance for an accurate atmospheric modelling, in particular in the near-infrared and visible spectral regions. The exhaustive critical evaluation of all $H_2^{18}O$ rovibrational line positions and energy levels available in the literature was released by an international IUPAC-sponsored Task Group [85] and recently updated in Ref. [86]. It covers the 0-17125 cm^{-1} range. Hereafter, we will call "IUPAC TG levels and transitions", the 5133 levels and 31730 lines which were critically evaluated and recommended in Refs. [85], [86] for $H_2^{18}O$. In particular, the IUPAC-TG review showed a lack of high sensitivity investigations of the $H_2^{18}O$ spectrum in the high energy region above 12500 cm^{-1} (see Fig. 3 of Ref. [85]).

Indeed, the previous analyses of the $H_2^{18}O$ spectrum in our region of interest 12580-14100 cm^{-1} are limited. In studies [87]-[89] spectra of isotopically enriched water (73% $H_2^{18}O$) recorded by Chevillard and co-workers in the early 1980's using McMath Fourier-transform spectrometer at the National Solar Observatory (Kitt Peak, AZ) are analyzed. Bykov and co-workers [87] analyzed the $H_2^{18}O$ enriched spectrum recorded between 11300 and 13600 cm^{-1}. These authors were able to obtain 315 accurate rotational energy levels for six interacting vibrational states by means of the effective Hamiltonian approach. Later, Tanaka et al. [88], [89] used variational calculations to reanalyze these FTS spectra in the 12400-14520 cm^{-1} region covering the $3\nu+\delta$ and 4ν polyads. All the transitions of $H_2^{18}O$ provided in Ref. [89], were included into the HITRAN2004, 2008 [47], [91] databases. More recently, ICLAS was used to investigate the 11520-12810 cm^{-1} [90] spectral region. Compared to FTS, ICLAS allows an important gain in sensitivity, which makes it particularly suitable for the characterization of spectral regions with weak absorption features. Rovibrational assignment based on results of high accuracy variational calculations [29], [30], [92] allowed 386 new energy levels belonging to 16 vibrational states to be derived from the measurement of 1712 $H_2^{18}O$ transitions.

In the present work, the $H_2^{18}O$ spectra were investigated by ICLAS in the ranges 12580-13550 [93] and 13540-14100 [94], hereafter referred to as first and second regions, respectively. The 12580-13550 cm^{-1} spectral region, which is known as one of the transparency windows of water vapour, covers the $3\text{v}+\delta$ polyad of very weak absorption. On the contrary, the 13540-14100 cm^{-1} range [94] corresponds to a relatively strong 4ν polyad. Figure 4.18 shows an overview comparison of the ICLAS line lists ([90] and present work) with the HITRAN line list. The ICLAS sensitivity allows lowering the detection limit by more than two orders of magnitude in comparison with previous FTS studies [87]-[89]: while HITRAN intensity cut off is of the order of 1×10^{-25} cm/molecule (for pure species), line intensities as low as 5×10^{-28} cm/molecule are measured by ICLAS. The gain was particularly significant in the wide 12707-13364 cm^{-1} interval where no $H_2{}^{18}O$ lines were previously reported.

After the presentation of the line list construction, we will describe the spectrum assignments performed with the aid of variational calculations and compare our results to literature data.

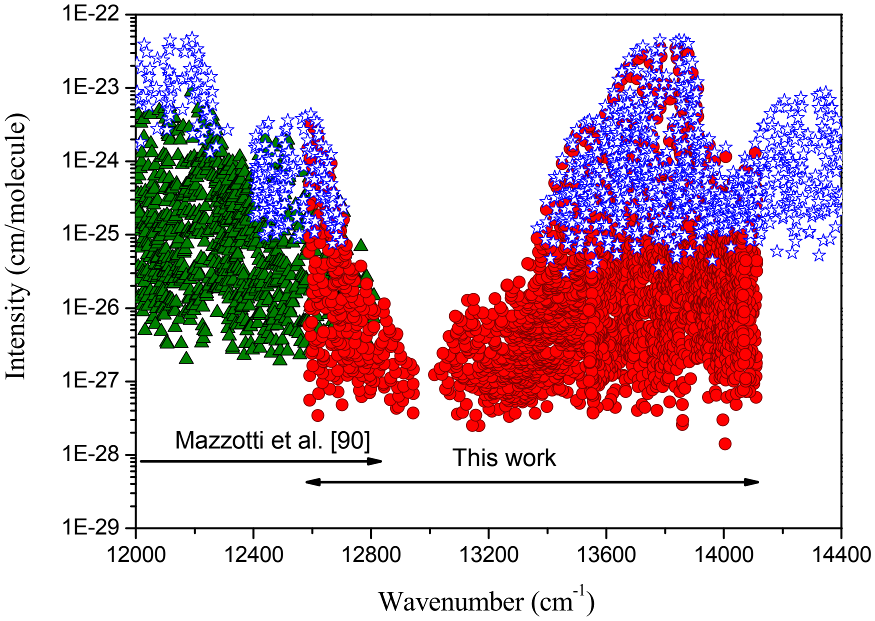

Figure 4.18. Overview of the $H_2{}^{18}O$ spectra in the 12000-14400 cm^{-1} region. The spectral regions previously [90] and presently analyzed by ICLAS are indicated together with the data available in the HITRAN-2008 database [91] (stars).

5.2 Experimental details and line list construction

The high sensitivity experimental setup used to record the weak absorption spectrum in presently studied region (12580-14100 cm^{-1}) was described in Section 2 of the current Chapter. Detailed description of our ICLAS spectrometer can be found in Refs. [95]–[96]. The ICLAS spectrum was recorded in successive 14 cm^{-1} wide spectral window. The wavenumber calibration of each of these individual spectra requires: *(i)* the correction of the non-linear dispersion of the grating spectrograph, which was achieved by means of a frequency comb provided by an intracavity etalon to linearize the frequency scale; *(ii)* reference line positions for the accurate calibration of the wavenumber scale. In the 12580–12810 cm^{-1} region, $H_2{}^{18}O$ and $H_2{}^{16}O$ lines provided in the line list attached to Ref. [90] were used for calibration. Above 13360 cm^{-1}, the $H_2{}^{18}O$ line positions available in the HITRAN database [91] were adopted as reference lines. Moreover, for the 12900-13165 cm^{-1} spectral range where the transitions are the weakest, A-band transitions of molecular oxygen were used. In the other intervals where $H_2{}^{18}O$ reference lines were unknown or too sparse, additional reference positions were calculated using ground state combination difference relations and the IUPAC-TG energy levels [86]. The average experimental accuracy of wavenumber calibration is estimated to be 0.005 cm^{-1} and 0.008 cm^{-1} for the first and second regions, respectively. The estimated isotopic composition of our samples was the following: $H_2^{18}O$: 93.6%, $H_2^{16}O$: 4.1%, $H_2^{17}O$: 1.9%, $HD^{18}O$: 0.40 %, and $H_2^{18}O$: 93.4%, $H_2^{16}O$: 4.1%, $H_2^{17}O$: 1.5%, $HD^{18}O$: 0.40 % for the 1st and 2nd considered regions, respectively.

In the first region, for each individual spectrum the line centres and the corresponding relative line intensities were determined using a least squares multi-line fitting program FITYK[6] assuming a Voigt profile. The absolute intensities of $H_2^{18}O$ transitions were obtained by scaling the relative line intensities against the values predicted in Ref. [92].

The second region corresponds to a relatively strong absorption for $H_2^{18}O$ and for the main isotopologue $H_2^{16}O$ as well. Considering the congestion of the spectrum and the saturation of many lines with intensities larger than 1.0×10^{-25} cm/molecule, we did not undertake a systematic retrieval of the absolute line intensities over the whole 13550-14100 cm^{-1} region, unlike 12580-13550 cm^{-1}. The line centres and peak depths were automatically determined using software that was specially developed. Rough values of the absolute line intensities were then derived by scaling the peak depths using the variational intensity values [92]. In spite of their large uncertainty, these estimated intensity values were highly valuable in the assignment process.

The complete line list in both regions was created by gathering the lists corresponding to each 14 cm^{-1} wide elementary spectrum. In the overlapping regions between successive recordings, the positions and intensities were averaged. The saturation of the $H_2^{18}O$ lines with intensities larger than 1×10^{-24} cm/molecule was so large that their line centres could not be determined precisely. In order to provide a "complete" line list in the second region, we decided to adopt the IUPAC-TG line positions for 271 strongly saturated lines. The resulting total line list contains 4112 lines belonging to four water isotopologues: $H_2^{18}O$, $H_2^{17}O$, $H_2^{16}O$ and $HD^{18}O$. The line lists limited to the $H_2^{18}O$, $H_2^{17}O$ and $HD^{18}O$ species are provided as Supplementary Material of Ref. [93], [94].

5.3 Spectrum analysis and results

5.3.1 Spectrum assignment and energy levels derivation

The identification of lines coming on new upper levels was based on the results of the high accuracy variational calculations performed by Shirin et al [92]. As already mentioned, the main criteria for establishing correspondence between the experimental and predicted lines are the

---

[6] FITYK program version v0.8.6, http://sourceforge.net/projects/fityk/

agreement of positions and intensities, combination difference relations and smooth dependence of the difference between the experimental and calculated energy level on the rotational and vibrational quantum numbers. Figure 4.19 shows the comparison between the experimental spectrum, variational calculations of Shirin et al. [92] and Schwenke and Partridge [30].

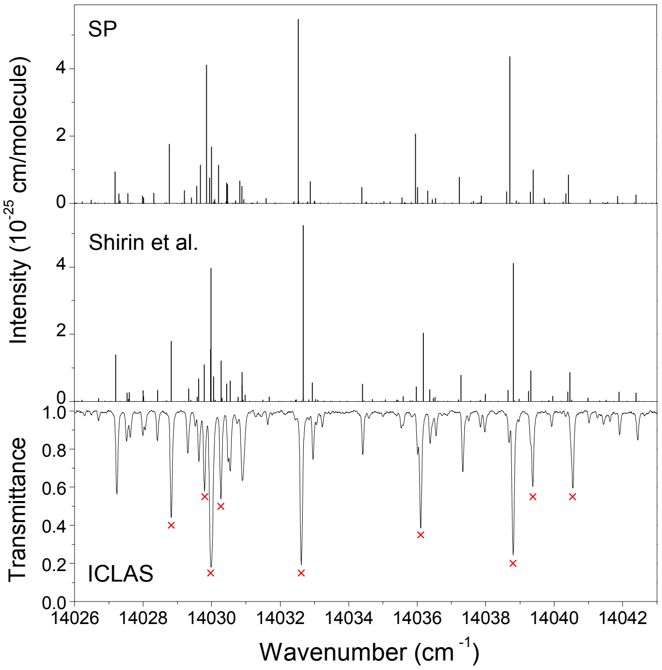

Figure 4.19. The spectrum of $H_2{}^{18}O$ around 14034 cm^{-1}: *Upper panel:* variational calculations of Schwenke and Partridge [29], [30]; *Middle panel:* variational calculations of Shirin et al. [92]; *Lower panel:* ICLAS spectrum recorded at a total pressure of about 5.9 Torr with an equivalent absorption pathlength of 24 km. The $H_2{}^{18}O$ transitions included in the HITRAN database are marked by a red cross.

In the displayed spectral interval, a very satisfactory agreement is observed for both calculations. Nevertheless, the overall comparison of the energy levels (Figure 4.20) shows that a significantly better agreement was achieved by Shirin et al [92]: the *rms* is 0.07 cm^{-1} and the maximal (obs.-calc.) value is only 0.38 cm^{-1} while SP calculations [29] start to diverge sharply at $J \geq 12$, with the maximum (obs.-calc.) deviations up to 4 cm^{-1}.

As a result, 1306 $H_2{}^{18}O$ upper energy levels belonging to 30 vibrational states were determined from the assigned experimental transitions by adding the (000) or (010) lower state energies from IUPAC TG database [85], [86], 780 of these levels are new.

The summary of the observed information is presented in Table 4.15, the (141)-(000), (042)-(000), (240)-(000), (311)-(010) and (231)-(010) bands are newly observed. Experimental information on the (023)-(000), (122)-(000), (221)-(000), (301)-(000), (202)-(000), (103)-(000) and (400)-(000) bands was significantly extended. The vibrational energies estimated from the (obs.-calc.) trend of the energy levels with $K_a = 0$ are marked by '*', the accuracy of these estimations is about ±0.05 cm^{-1}.

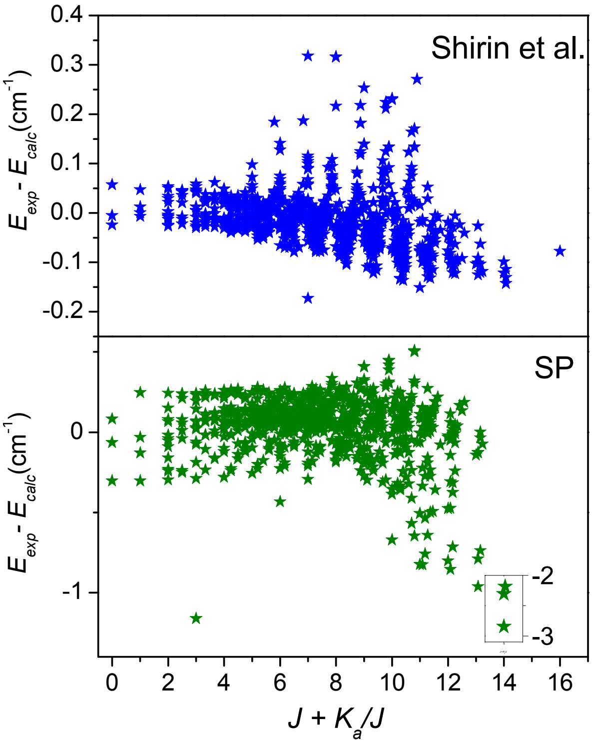

Figure 4.20. Variation of the differences between the experimental $H_2{}^{18}O$ energy levels determined from the ICLAS spectrum between 12580 and 13550 cm^{-1} and variational values. *Upper panel:* calculated data were taken from Shirin et. al. [92]; *Lower panel:* calculated data were taken from Schwenke and Partridge [29], [30].

Our energy levels, determined from the analysis of $H_2{}^{18}O$ spectrum in the 12580-13550 cm^{-1} and 13540-14100 cm^{-1} spectral regions, agree with those from IUPAC TG database with *rms* deviations of 0.0052 cm^{-1} and 0.0068 cm^{-1}, respectively. The obtained *rms* deviation is consistent with the estimated accuracy of our line positions: 0.005 cm^{-1} for not-very-weak isolated lines and up to 0.015–0.020 cm^{-1} for very weak or highly blended lines.

Table 4.15. Summary of the spectroscopic information obtained from the ICLAS spectrum of a highly ^{18}O enriched sample of water in the 12580–14100 cm^{-1} region.

Isotopologue	Vibrational band	Vibrational energy, cm^{-1}		Total number of levels	Number of new levels
		Predicted	Experimental		
$H_2{}^{18}O$	(080)-(000)	11213.30		2	2
	(230)-(000)	11734.51	11734.5250	1	1
	(131)-(000)	11774.71	11774.7076	3	2
	(032)-(000)	11963.53	11963.5371	10	4
	(310)-(000)	12106.93	12106.9776	10	1
	(211)-(000)	12116.74	12116.7970	24	9
	(160)-(000)	12337.59		6	6
	(112)-(000)	12372.66	12372.7056	72	18
	(090)-(000)	12488.06		2	2
	(013)-(000)	12520.12	12520.1229	115	22
	(061)-(000)	12538.46		20	18
	(240)-(000)	13167.72	13167.7184	87	87
	(141)-(000)	13212.70	13212.6782	83	78
	(042)-(000)	13403.73	13403.71*	41	39
	(320)-(000)	13602.66	13602.71*	95	78
	(221)-(000)	13612.66	13612.7102	113	42
	(170)-(000)	13617.64		6	6
	(071)-(000)	13784.21	13784.2461	12	11

	(400)-(000)	13793.27	13793.2607	119	59
	(301)-(000)	13795.41	13795.3982	134	50
	(0 10 0)-(000)	13798.55		1	1
	(122)-(000)	13870.46	13870.4855	79	70
	(023)-(000)	14015.48	14015.5107	71	60
	(202)-(000)	14187.97	14187.9824	68	30
	(103)-(000)	14276.34	14276.3360	82	34
	(004)-(000)	14488.21		7	7
	(231)-(010)	15073.92	15073.9747	22	22
	(212)-(010)	15303.01		1	1
	(311)-(010)	15305.79	15305.8057	19	19
	(113)-(010)	15784.27		1	1
			Total	1306	780
$HD^{18}O$	(023)-(000)	13235.52	13235.497	40	40
	(103)-(000)	13286.85		8	8
	(004)-(000)	13814.75	13814.526	68	28
			Total	116	76
$H_2^{17}O$	(080)-(000)	11232.31		1	1
	(310)-(000)	12122.16		1	
	(112)-(000)	12389.06		9	5
	(240)-(000)	13185.20		1	1
	(013)-(000)	12541.24	12541.227	50	14
	(141)-(000)	13233.16		6	4
	(042)-(000)	13427.15		1	
	(320)-(000)	13620.56		14	11
	(221)-(000)	13631.45	13631.501	67	17
	(071)-(000)	13808.24	13808.301	3	2
	(400)-(000)	13809.74		40	16
	(301)-(000)	13812.17	13812.158	85	17
	(122)-(000)	13889.43		7	7
	(023)-(000)	14039.33		5	5
	(202)-(000)	14203.54		21	15
	(103)-(000)	14296.29	14296.279	9	5
			Total	320	95

Experimental vibrational energies marked by asterisk have been estimated with the accuracy of about ±0.05 cm^{-1} using the (obs.-calc.) trend of levels with $K_a = 0$.

In Table 4.16 the energy levels for the highly excited bending states – (160), (061), (071), (170), (090) and (0 10 0) of $H_2^{18}O$ newly derived from the analysis of ICLAS spectra between 12580–14100 cm^{-1} are partly presented. The complete set of new experimental energy levels of $H_2^{18}O$ and $H_2^{17}O$ obtained in present study is given as Supplementary Material in relevant articles [93], [94].

Table 4.16. New experimental energy levels for the (160), (061), (071), (170), (080), (090) and (0 10 0) highly excited bending states of $H_2^{18}O$ derived by ICLAS in the 12580–14100 cm^{-1} region.

$V_1V_2V_3$	J	K_a	K_c	E_{obs}(cm^{-1})	$\sigma\times10^3$cm^{-1}	N	δ (cm^{-1})
160	6	4	3	13791.5683	4.7	2	-0.067
160	9	3	7	14029.4484		1	-0.064
160	9	7	3	15379.7638		1	0.200
160	9	7	2	15379.2530		1	0.157
160	11	0	11	13776.6283		1	-0.151
160	12	1	12	13995.4260		1	-0.062

$V_1V_2V_3$	J	K_a	K_c	$E_{obs}(cm^{-1})$	$\sigma \times 10^3 cm^{-1}$	N	δ (cm^{-1})
061	4	4	1	13569.1137	4.1	2	0.098
061	5	4	2	13692.3255	1.6	2	0.184
061	5	5	1	14000.6491		1	-0.024
061	5	5	0	14000.5012	1.4	2	0.077
061	6	1	5	13170.1263		1	-0.023
061	6	5	1	14149.2852		1	0.186
061	6	6	1	14470.7795		1	0.318
061	6	6	0	14470.7791		1	0.318
061	7	5	2	14320.5926		1	0.092
061	7	7	1	14951.5390		1	0.315
061	7	7	0	14951.5396		1	0.316
061	8	5	3	14513.6902		1	0.157
061	8	7	2	15143.2045	2.9	2	0.278
061	8	7	1	15143.2041	2.7	2	0.277
061	9	7	3	15357.1112		1	0.216
061	9	7	2	15357.1192		1	0.222
061	10	7	3	15592.8018		1	0.164
061	11	7	5	15849.7639		1	0.112
071	0	0	0	13784.2461		1	0.033
071	1	0	1	13807.3353		1	0.033
071	2	0	2	13853.2201	3.8	2	0.020
071	3	1	3	14060.5359		1	0.041
071	3	1	2	14101.2987		1	-0.023
071	4	0	4	14010.9650	2.3	2	-0.007
071	5	0	5	14120.2390		1	-0.014
071	5	2	3	14815.0772		1	-0.055
071	6	0	6	14254.7867		1	-0.066
071	8	0	8	14571.9893		1	-0.051
071	10	1	10	15025.2551		1	-0.003
170	3	0	3	13757.0668		1	0.059
170	4	0	4	13851.4268		1	0.017
170	4	1	4	14030.5657		1	0.008
170	5	1	5	14130.0135		1	0.015
170	7	1	6	14567.2036		1	-0.140
170	9	0	9	14638.1887		1	-0.221
080	7	6	1	14645.6816*	3.1	2	0.107
080	11	8	3	15359.6035*		1	0.344
090	7	0	7	13130.6372		1	-0.172
090	8	3	6	14840.8460*		1	0.290
0 10 0	7	0	7	14522.5109		1	-0.019

The assignment (and labelling) of the three levels marked by asterisk (*) are tentative.

σ denotes experimental uncertainty of the level derived from the CD of 2 and more transitions. N represents the number of transitions used to derive the energy level. $\delta = E_{obs} - E_{calc}$ where E_{calc} corresponds to variational data from Ref. [92]. The complete set of energy levels derived in this study for $H_2^{18}O$ and $H_2^{17}O$ isotopologues is given as Supplementary Material of Ref. [93], [94] and available from the authors upon request.

The high sensitivity provided by ICLAS allowed for the detection of a large number of transitions involving highly excited upper rovibrational states, which resulted in complicated labelling problems. As mentioned in Chapter III, the effective Hamiltonian approach is the most reliable for determining appropriate rovibrational labelling, though in certain cases strong resonance couplings or very high excitation of the bending vibration may lead to ambiguities. Thus, in order to establish reasonable rotational and vibrational labellings, approximate calculations in the framework of an effective Hamiltonian approach were performed. Among the 1306 experimental energy levels derived in this study, rovibrational labellings have been changed for 599 levels compared to those provided by Partridge and Schwenke [29]. It is worth mentioning that in Ref. [92] the labelling procedure did not consider the known dependence of transition intensity on vibrational and rotational quantum numbers of the lower and upper states. As a result, a lot of strong transitions are erroneously labelled as belonging to very weak bands, or have unrealistic large values of $\Delta K_a = |K'_a - K''_a|$ and $\Delta K_c = |K'_c - K''_c|$.

5.3.2 High-order resonance interactions

In the water molecule, high order resonance interactions arise from strong centrifugal distortion effect leading to line intensity borrowing and consequently, to the observation of transitions involving highly excited bending states [84]. Similarly to the effective Hamiltonian approach, the resonance intensity redistribution in variational calculations depends on the rovibrational wave functions of the interacting upper states and is then very sensitive to the details of the potential energy surface [33]. As mentioned in Section 5 of Chapter III, in case of close resonances, the uncertainty on the resulting variational wavefunctions may lead to important errors (up to several orders of magnitude) in the transition intensities of the weaker (extra) lines. That is why it is desirable to determine all possible resonance interactions which can influence the quality of variational intensities.

In Table 4.17, several transitions that were observed in our study as a result of a resonance intensity transfer are listed together with their much stronger resonance counterparts. They all reach levels of highly excited bending states such as (160), (061) and (090) and correspond to ΔK_a values up to 3, while the strong resonance partners correspond to $\Delta K_a = 0,1$. We found that not only close, but also distant resonances, with energy differences up to 60 cm^{-1} between interacting levels, can induce important intensity transfer to otherwise weak transitions (Table 4.17). Interestingly, those high-order resonances always involve highly excited bending states.

Table 4.17. Some examples of high-order resonances in the $H_2{}^{18}O$ molecule.

$\upsilon_1 \upsilon_2 \upsilon_3$	$J K_a K_c$ upper	$J K_a K_c$ lower	Predicted frequency, cm^{-1}	Predicted intensity, cm/molecule	Measured frequency, cm^{-1}	Measured intensity, cm/molecule
160	11 0 11	10 1 10	12666.97	3.1E-27	12666.826	2.5E-27
013	11 1 11	10 1 10	12663.78	8.7E-26	12663.714	7.9E-26
090	7 0 7	6 1 6	12685.46	8.5E-27	12685.291	5.7E-27
112	7 2 5	6 1 6	12686.94	2.9E-26	12686.904	3.5E-26
061	5 1 4	4 3 1	12634.30	3.8E-27	12634.291	3.3E-27

$\upsilon_1\upsilon_2\upsilon_3$	$J\,K_a\,K_c$ upper	$J\,K_a\,K_c$ lower	Predicted frequency, cm^{-1}	Predicted intensity, cm/molecule	Measured frequency, cm^{-1}	Measured intensity, cm/molecule
013	5 3 2	4 3 1	12632.47	2.8E-25	12632.465	2.1E-25*
061	8 1 7	7 3 4	12708.70	1.3E-26	12708.620	1.9E-26
013	8 3 5	7 3 4	12707.13	1.6E-25	12707.060	1.3E-25*
0 10 0	7 0 7	8 3 6	13520.82	1.6E-26	13520.8051	1.4E-26
400	7 2 5	8 3 6	13520.34	2.4E-25	13520.2730	1.4E-25*
061	7 7 1	7 7 0	13376.56	1.47E-27	13376.861	1.8E-27
301	7 7 1	7 7 0	13431.40	1.74e-26	13431.594	2.4E-26

5.3.3 Comparison with HITRAN-2008 database

In course of the analysis, we evidenced some important and systematic deviations between the HITRAN line intensities and the variational values of Ref. [92]. This observation was unexpected as variational calculations are generally believed to agree reasonably with the experimental values. We compared the line intensities provided by the HITRAN database with their variational values obtained by Shirin et al. [92] and Schwenke and Partridge [30]. The comparison was performed for the 10000-14520 cm^{-1} region. Lines of the various line lists were automatically associated using the rovibrational assignment and line centre coincidences as criteria. Above 12400 cm^{-1}, the spectroscopic parameters provided in HITRAN originate from the work of Tanaka et al. [89]. Figure 4.21 shows the variation of the intensity ratios versus the wavenumber both for the variational values of Refs. [30] and [92] and the values of HITRAN and Ref. [92]. While the average ratio is close to 1 for the variational calculations and for the HITRAN values below 12400 cm^{-1}, a systematic overestimation by 25% and a higher dispersion are noted for the HITRAN values transferred from Tanaka et al. [89].

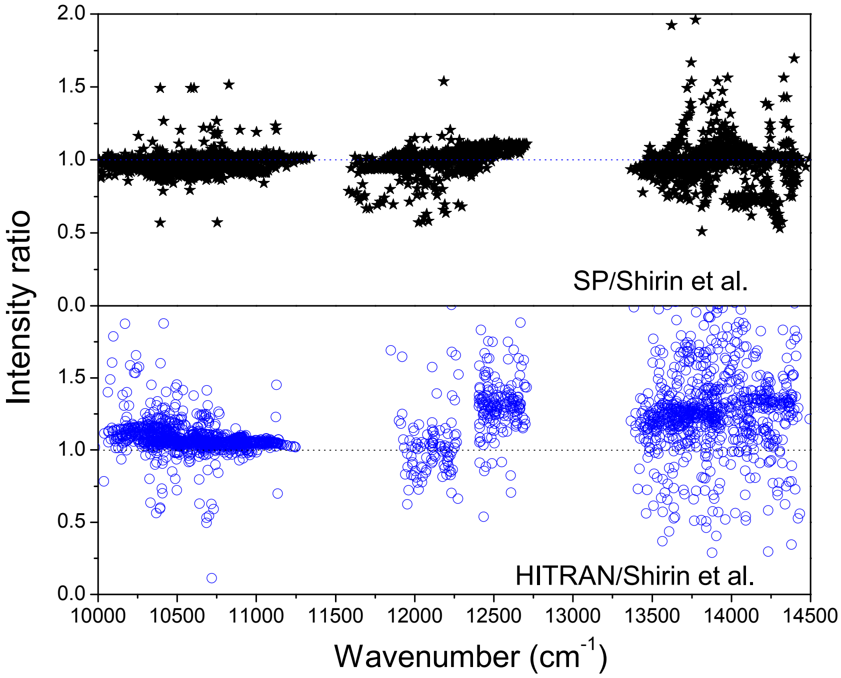

Figure 4.21. Ratios of the $H_2^{18}O$ transition intensities in the 10000 – 14500 cm^{-1} spectral region *versus* the line positions. *Upper panel*: variational intensities provided by Schwenke and Partridge [30] and Shirin et al. [92]; *Lower panel:* HITRAN intensity values [91] and variational intensities from Shirin et al. [92]. The HITRAN intensity values above 12400 cm^{-1} originate from Ref. [89].

In order to clarify the origin of this discrepancy, a 30 cm^{-1} spectral interval around 14030 cm^{-1} was selected to derive absolute line intensity values from our ICLAS spectra and to compare to HITRAN and variational values. Figure 4.22 shows the comparison of the four line lists around 14020 cm^{-1}. Our measurements confirm that HITRAN values are strongly overestimated. Even the relative intensities provided in HITRAN appear to be inaccurate as further illustrated by the large dispersion of the intensity ratios displayed on Figure 4.21. No details about the intensity retrieval were given in the original papers of Tanaka et al. [88], [89] and it is difficult to trace the origin of this overestimation, the spectra used by Tanaka et al. being those recorded twenty five years ago by Chevillard et al. [97], [98]. We believe that a significant improvement of the HITRAN line list for $H_2^{18}O$ in the 12400-14520 cm^{-1} region would be obtained by replacing the intensity values of Ref. [89] by the variational values of Ref. [92].

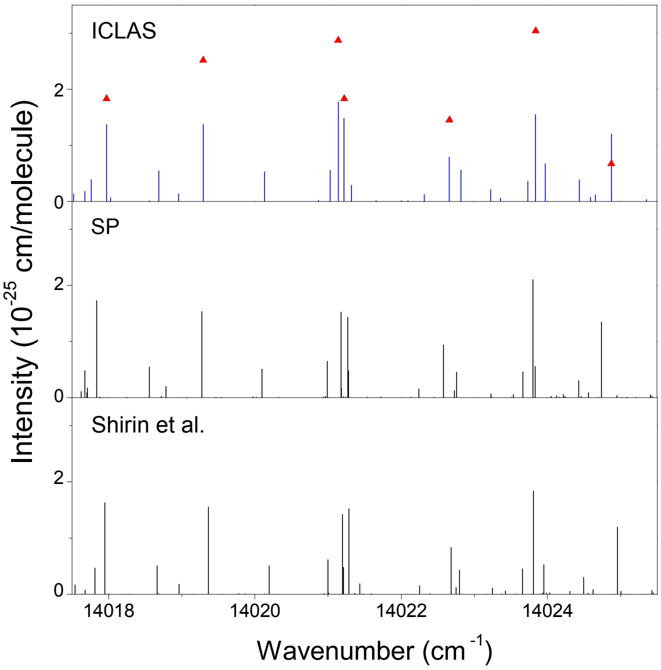

Figure 4.22. Comparison of the $H_2^{18}O$ line lists near 14021 cm^{-1}: *Upper panel:* stick spectrum obtained by ICLAS. Intensity values provided in HITRAN are marked (full triangle); *Middle panel:* variational calculations of Schwenke and Partridge [30]; *Lower panel:* variational calculations of Shirin et al. [92].

Note that it is difficult to decide whether the good agreement observed below 12400 cm^{-1} between HITRAN and variational values (Figure 4.21) is significative or not. Between 10000 and 11500 cm^{-1}, the main experimental source for HITRAN is Ref. [98] but as described in Ref. [99] the experimental intensities of Ref. [98] were scaled according to the early variational calculations of Partridge and Schwenke [29], which were later corrected in Ref. [30].

Thus, we conclude that the IUPAC-TG line list of $H_2^{18}O$ [85], [86] which includes variational intensities values should be preferably used in the studied region. The large amount of new information obtained by ICLAS in the present work will be valuable to complete the IUPAC-TG line list of Refs. [85], [86] by using the MARVEL procedure [100], [101].

5.3.4 $H_2^{17}O$ and $HD^{18}O$

Despite the small relative concentration of $H_2^{17}O$ in our samples (less than 2%), $H_2^{17}O$ lines could be detected in the studied spectra and new information was obtained for this isotopologue as well. As for $HD^{18}O$, the rovibrational assignments were based on the variational calculations of Ref. [92]. The obtained energy level set agrees with the available published data [85], [86], within the *rms* deviation of 0.007 cm^{-1} for 320 energy levels in common, the remaining 95 energy levels being newly reported (see Table 4.15).

Moreover, very weak absorption lines of $HD^{18}O$ present with a 0.4% relative concentration in the cell could be identified. The rovibrational assignments used the predicted spectrum of Ref. [80] which was based on the PS potential energy and dipole moment surfaces [29]−[30]. New information concerns mainly the (023) and (004) vibrational states at 13235.497 cm^{-1} and

13814.526 cm^{-1}, respectively (see Table 4.15). The overview of the $2\nu_2+3\nu_3$ band is given in Figure 4.23.

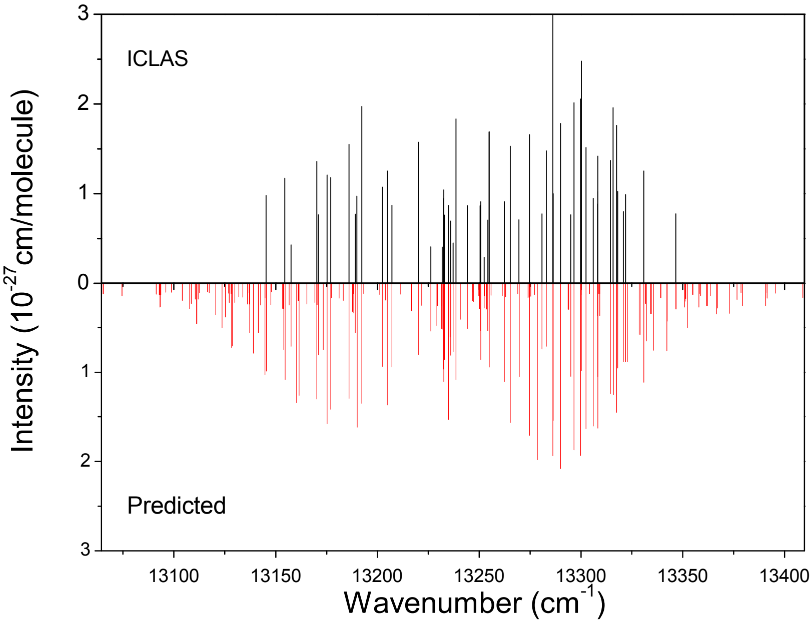

Figure 4.23. Comparison of the weak $2\nu_2+3\nu_3$ absorption band of $HD^{18}O$ measured by ICLAS (*upper panel*) to the variational calculation based on Schwenke and Partridge potential energy and dipole moment surfaces [80] (*lower panel*).

5.4 *Vibrational problem for $H_2^{18}O$ and normal mode labelling*

Vibrational energies of $H_2^{18}O$ molecule newly derived from the present study of the 12500-14200 cm^{-1} region together with all available literature data have been used to determine the parameters of the vibrational Hamiltonian described in Section 4 of Chapter III. In total, 51 vibrational energy levels have been introduced in the fitting, and 26 vibrational parameters have been retrieved which reproduce the input data within the *rms* deviation of 0.17 cm^{-1}. Table 4.18 lists the retrieved parameters, while Table 4.19 illustrates the quality of the fitting. The two largest mixing coefficients of the resulting wave function are also given in Table 4.19. For majority of the vibrational energies (76%) presented in Table 4.19, the leading mixing coefficient is well above 50% and exceeds by more than two times the second contribution to the resulting wave function, providing reasonable vibrational labelling of the corresponding states. In the two last columns of Table 4.19 the vibrational labelling of Refs. [30], [92] is given for comparison, when it differs from our label attached to the maximal contribution to the wavefunction.

Table 4.18. Spectroscopic parameters of effective vibrational Hamiltonian of $H_2^{18}O$ molecule

Parameter	Value (cm^{-1})	Parameter	Value (cm^{-1})
ω_1	3822.884(486)	z_{1112}	-0.07179(874)
ω_2	1642.220(412)	z_{1222}	0.06710(483)
ω_3	3925.783(384)	z_{2222}	-0.06181(655)
x_{11}	-42.349(187)	z_{2223}	0.3308(142)
x_{12}	-16.487(147)	z_{2233}	0.2732(492)
x_{13}	-163.539(294)	z_{2333}	0.1483(382)
x_{22}	-18.385(141)	p_{11223}	0.0517(120)

Parameter	Value (cm^{-1})	Parameter	Value (cm^{-1})
x_{23}	-16.261(462)	p_{22222}	-0.005996(605)
x_{33}	-46.336(102)	p_{22233}	-0.071882(913)
y_{113}	1.3214(808)	Γ_{DD}	-39.803(115)
y_{123}	-2.271(126)	F	11.904(235)
y_{233}	-2.017(250)	γ_1	0.5884(387)
z_{1111}	0.01339(435)	γ_2	-0.1393(184)

The quoted errors correspond to one standard deviation. The fit included 51 band origins and 26 adjusted parameters (for the definition of parameters, see Section 3 and Section 4 of Chapter III).

There are seven differences between our labels and those of SP [30] and Shirin et al. [92]. Still, the SP labelling is more consistent with ours: (*i*) differences concern states with nearly equal first and second mixing coefficients, which leads to an ambiguity in labelling; (*ii*) from time to time the SP label has $\upsilon_1 \pm 1$ value compared to our υ_1, such states are separated by about 3800 cm^{-1}, and there is no other reasonable explanation to this effect, than definite technical defect of the labelling procedure in [30] at a high degree of vibrational excitation. If we correct these artefacts, we conclude that all seven SP labels formally differing from ours, actually coincide with our results. On the contrary, six of the seven labels of Shirin et al. [92], different from ours, seem to be inadequate, as they correspond to obviously lesser component of the wave function. The most illustrative cases concern the (071) and (301) labels, which are interchanged in [92] compared to ours. As a result, the transitions involving the (071) [000] and (301) [000] upper levels have in [92] the intensities of 1.95E-23 and 4.75E-26 cm/molecule, respectively, what is not realistic, as the (071)-(000) band is much weaker than the strong (301)-(000) band. The labelling recommended by the IUPAC TG [85], [86] coincides with that obtained in this study for all, but four states: (400), (202), (320) and (122).

Table 4.19. Experimental and calculated vibrational energy levels of $H_2{}^{18}O$ (in cm^{-1}).

E_{obs} (cm^{-1})	obs.-calc.$_{EH}$	P_1	W_1	P_2	W_2	$(\upsilon_1\upsilon_2\upsilon_3)_{VAR}$ [30]	$(\upsilon_1\upsilon_2\upsilon_3)_{VAR}$[92]
1588.277	-0.119	1.000	0 1 0	0.000	0 0 0		
3139.051	0.093	0.999	0 2 0	0.001	1 0 0		
3649.688	0.234	0.999	1 0 0	0.001	0 2 0		
3741.567	0.206	1.000	0 0 1	0.000	0 0 0		
4648.463	0.009	0.997	0 3 0	0.003	1 1 0		
5221.242	-0.007	0.997	1 1 0	0.003	0 3 0		
5310.466	-0.070	1.000	0 1 1	0.000	0 0 0		
6110.403	0.057	0.996	0 4 0	0.004	1 2 0		
6755.510	0.073	0.993	1 2 0	0.004	0 4 0		
6844.598	0.102	0.998	0 2 1	0.002	1 0 1		
7185.877	0.024	0.869	2 0 0	0.128	0 0 2		
7228.884	-0.107	0.998	1 0 1	0.002	0 2 1		
7418.733	0.013	0.872	0 0 2	0.128	2 0 0		
8249.036	-0.261	0.988	1 3 0	0.006	2 1 0		
8341.108	-0.113	0.996	0 3 1	0.004	1 1 1		
8739.526	-0.152	0.858	2 1 0	0.135	0 1 2		
8779.719	-0.056	0.996	1 1 1	0.004	0 3 1		
8967.565	-0.070	0.864	0 1 2	0.135	2 1 0		
9795.330	-0.024	0.993	0 4 1	0.007	1 2 1		
10256.580	0.100	0.847	2 2 0	0.138	0 2 2		
10295.630	0.189	0.987	1 2 1	0.007	0 4 1		
10483.221	0.065	0.857	0 2 2	0.138	2 2 0		
10573.910	-0.174	0.526	3 0 0	0.468	1 0 2		
10585.280	-0.148	0.870	2 0 1	0.124	0 0 3		
10839.955	-0.123	0.528	1 0 2	0.469	3 0 0	3 0 0	

E_{obs} (cm^{-1})	obs.-calc.$_{EH}$	P_1	W_1	P_2	W_2	$(\upsilon_1\upsilon_2\upsilon_3)_{VAR}$ [30]	$(\upsilon_1\upsilon_2\upsilon_3)_{VAR}$[92]
10993.680	-0.039	0.876	0 0 3	0.124	2 0 1		
11734.525	0.181	0.840	2 3 0	0.135	0 3 2		
11774.680	0.002	0.978	1 3 1	0.013	2 1 1		
11963.537	-0.012	0.855	0 3 2	0.136	2 3 0		
12106.978	0.325	0.504	3 1 0	0.482	1 1 2		
12116.797	-0.076	0.859	2 1 1	0.128	0 1 3		
12372.706	0.114	0.508	1 1 2	0.484	3 1 0	3 1 0	
12520.124	-0.038	0.872	0 1 3	0.128	2 1 1		
13167.718	-0.043	0.840	2 4 0	0.127	0 4 2		
13212.678	0.040	0.972	1 4 1	0.018	2 2 1		
13403.710	-0.011	0.860	0 4 2	0.128	2 4 0		
13602.710	-0.186	0.482	3 2 0	0.480	1 2 2		
13612.711	-0.256	0.834	2 2 1	0.128	0 2 3		
13784.246	-0.004	0.991	0 7 1	0.009	1 5 1		3 0 1-
13793.261	0.017	0.677	2 0 2	0.238	4 0 0	3 0 2	4 0 0-
13795.398	0.236	0.634	3 0 1	0.346	1 0 3		0 7 1-
13870.486	-0.079	0.499	1 2 2	0.481	3 2 0	3 2 0	
14015.511	0.034	0.866	0 2 3	0.128	2 2 1		
14187.986	-0.002	0.712	4 0 0	0.157	2 0 2		2 0 2-
14276.336	0.072	0.646	1 0 3	0.349	3 0 1		
15073.975	0.108	0.815	2 3 1	0.126	0 3 3		
15303.015	-0.071	0.673	2 1 2	0.204	4 1 0	3 1 2	4 1 0-
15305.804	0.126	0.611	3 1 1	0.352	1 1 3		
16775.381	-0.023	0.511	3 2 1	0.309	1 2 3		
16854.772	0.024	0.575	3 0 2	0.199	1 0 4	4 0 2	5 0 0-
16854.991	-0.113	0.472	2 0 3	0.358	4 0 1	4 0 1	4 0 1

Notes:

(obs.-calc.$_{EH}$) is the difference of the energy value calculated with the EH model and the experimental value

P_1 and P_2 indicate the largest, and the second largest mixing coefficients, respectively, of the vibrational eigenvector.

W_1 and W_2 indicate the corresponding vibration normal mode quantum numbers, (v_1 v_2 v_3).

Vibrational labels from SP [30] and Shirin et al. [92] are given in the two last columns, if different from ours corresponding to maximal contribution. "–" is attached to those labels in the last two columns which are believed to disagree with ours, as they either do not coincide with our label corresponding to 2nd contribution, or they coincide with it, but the 2nd contribution to the wavefunction is importantly less than the first one.

Note that the SP labels [30] which differ from ours by +1 or -1 in υ_1 are considered as being distorted by a technical defect in the assigning procedure exploited in SP, and then accepted to be identical with ours.

Despite the poor levels/parameters ratio (it equals to 2), the predictive ability of the EH model used [51] seems to be quite reasonable as shown for D_2O molecule in Section 3 of the current Chapter. We compared vibrational energies predicted with our parameters to variational values [Shirin et al. [92] below 20000 cm^{-1}, and SP [30] above 20000 cm^{-1}] that are believed to be more accurate than the EH predictions. The *rms* deviation between the EH and variational vibrational energies equals to 11 cm^{-1} for 96 compared levels with maximal discrepancy being of 36 cm^{-1}. This comparison is presented in Figure 4.24. As it was anticipated, the worst EH predictions concern the states with the highly excited bending mode (only states with $\upsilon_2 \leq 5$ were compared, the EH prediction for states with larger υ_2 being strongly distorted). The total list of the EH predicted vibrational energies is given in Appendix A.2.

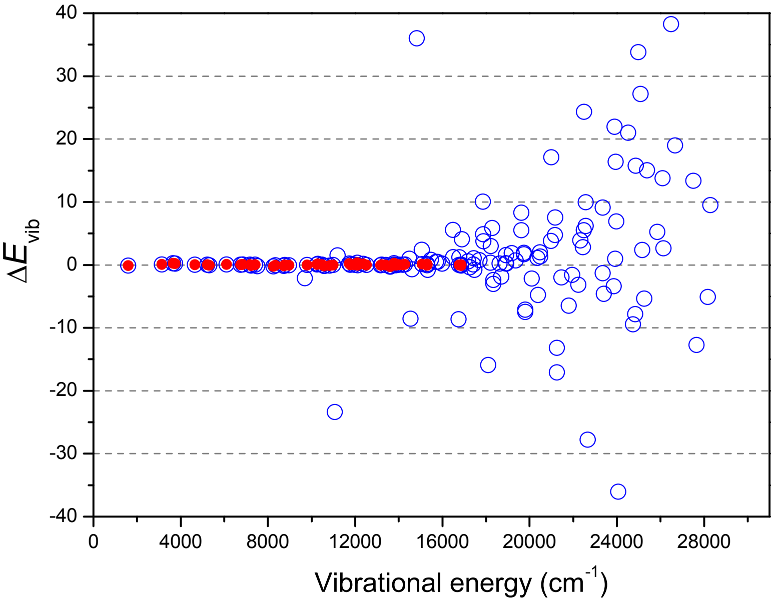

Figure 4.24. Differences between observed, variational and EH calculated vibrational energies of $H_2^{18}O$. The deviations in red concern observed - EH calculated [102] vibrational energies; differences between variational and EH predicted energies [102] are shown in blue for Ref. [92] data below 20000 cm^{-1} and for the SP calculation above 20000 cm^{-1} [30].

As the input data of EH fitting were limited in energy up to 16810 cm^{-1}, the long extrapolation up to energies of 28000 cm^{-1} with the average accuracy of 11 cm^{-1} seems to be satisfactory, at least for establishing the reasonable labelling. Let us stress, that in the whole region from 0 to 28000 cm^{-1} most part (90%) of our vibrational labels attached to the first or second leading mixing coefficient of the wavefunctions coincide with the SP labels [30], confirming the correctness of our results, while the agreement with [92] is much poorer. At the same time, for a number of the highly excited states the EH-wavefunctions seem to be greatly mixed without pronounced maximum, what prevents establishing the unambiguous labelling, still we can trace, which basic functions contribute to the resulting wave function.

6. Modelling of the rovibrational energy levels of water isotopologues in the frame of the effective Hamiltonian approach and consistent labelling

In the course of spectra identification, the high accuracy variational calculations [28]–[30], [39], [82], [92] have been used. However, the rovibrational labelling provided by all the variational calculations is inadequate in a number of cases. In the variational calculations of Schwenke and Partridge [29]–[30] the same labels can be ascribed to several levels having different energy values. In the variational computations [28], [39], [92] the rovibrational labelling is unique, however it does not account for the dependence of the transition intensities on the rotational and the vibrational quantum numbers of upper and lower states predicted by the rovibrational theory: the larger is the difference between the upper and lower K_a or K_c values, the weaker is the transition intensity. Likewise, the higher is the bending excitation, the weaker is the corresponding vibrational band. Nevertheless, the relatively strong variational transitions in [28], [39], [92] can have rovibrational labels corresponding to conventionally weak and very weak lines with very large ΔK_a and ΔK_a up to 12. In the recent high-accuracy variational calculations of the HDO line positions and intensities – VTT [82], the rovibrational labelling is importantly incomplete.

Variational calculations do not involve the concept of resonance interactions, which is one of the corner stones in the effective Hamiltonian approach. However, large distortions of the variational intensities have been evidenced [33], [72] and appeared to be frequently connected with strong resonance perturbations of the corresponding upper levels. The (obs.-calc.) tendencies for the energy levels can be, likewise, distorted by the resonance interactions. Therefore, the inspection of the resonance interactions between the considered vibrational states based on the EH scheme is of importance, as it can help to explain abrupt decrease of the accuracy of the variational line positions and intensities.

In the frame of the EH approach the rovibrational labelling comes straightforwardly from inspecting the resulting wavefunction. It corresponds to the rovibrational label of the basis state with maximal contribution. Despite the high accuracy of variational calculations, their predictive abilities are limited, and the (obs.-calc.) deviations may reach up to 1 cm^{-1} and larger in case of long extrapolation, which hinders the assignment process. In these circumstances, calculations in the EH framework can provide the additional criterion for establishing reasonable rovibrational labelling and identification. That is why the fitting based on the EH approach was performed for all the experimental energy levels derived in this study. It is worth noting, that these experimental energy levels correspond to the highly excited rovibrational states, which leads to additional problems with reasonable labelling. On the one hand, the variational labels become inadequate in many cases, on the other hand, proper realization of the EH scheme seems to be problematic due to numerous strong resonance interactions including high-order interpolyad mixing, and lack of the experimental energy levels for a number of vibrational states included in the considered polyad. Therefore, our fittings in the EH framework are approximate, and their results are used, mostly, for the labelling purpose and tracing the resonance coupling.

As an example, we briefly present below the modelling of the $D_2{}^{16}O$, $H_2{}^{18}O$ energy levels belonging to the 2nd decade and the 1st pentadecade. The problems that arise in performing the $HD^{16}O$ energy levels fitting are also discussed. As the water molecule experiences the strong centrifugal distortion effect, the rotational Hamiltonian presented through Padé-Borel approximants (3.29) has been applied in the EH calculations described below. In addition to the conventional Fermi and Coriolis–type constants: F_0, F_k, F_j, F_y, C_y, C_xz [103], the other resonance parameters included in Equations (3.24), (3.26) are involved. Note that, the F_0 parameter was not varied, as it correlates strongly with E_v, which makes the fitting unstable.

$D_2{}^{16}O$ (in the 8800-9520 cm^{-1} spectral range)

The experimental energy levels of the 2nd decade of resonating states were obtained from the combined analysis of the FTS and ICLAS spectra in the 8800–9520 cm^{-1} region and are described in Section 3. Formally, the 2nd decade includes 10 vibrational states listed in Table 4.20, of which (051), (150), and (070) states are the so-called "dark" states, as no experimental energy levels were attributed for them. The (051) and (070) dark states were found not to influence the observed states, and were then excluded from the fit. All the possible rovibrational and anharmonic resonances between the states introduced into the least squares fitting have been accounted for in the form given in Section 3 of Chapter III. The energy levels of the (131) state with $K_a = 0,\ 1$ seemed to be perturbed by the highly excited bending state (080) at 8760.26 cm^{-1}, which was also included into the fitting.

Table 4.20. Energy levels (cm^{-1}) of the 2nd decade of $D_2{}^{16}O$ and $H_2{}^{18}O$ included in the EH fitting.

$\upsilon_1\ \upsilon_2\ \upsilon_3$	**$D_2{}^{16}O$**					**$H_2{}^{18}O$**			
	E_var [28]	E_obs	N_lev	J_max	K_amax	E_var [92]	E_obs	N_lev	K_amax
0 7 0	7771.948					10052.171			
1 5 0	8305.537					11064.603			
0 5 1	8430.285					11199.380		6	7
2 3 0	8712.060		11	10	6	11734.507	11734.525	63	7
0 8 0	8760.673								
1 3 1	8792.665	8792.630	81	12	9	11774.707	11774.707	78	8
0 3 2	8947.015		14	9	5	11963.533	11963.537	64	8
3 1 0	9005.495	9005.500	99	14	8	12106.935	12106.978	70	7
2 1 1	9050.349	9050.349	171	16	9	12116.743	12116.797	79	8
1 1 2	9202.706	9202.716	138	17	9	12372.662	12372.706	78	7
0 1 3	9366.317	9366.313	156	16	9	12520.120	12520.124	74	6
Total N_lev					670				512
N_param					100				93
***rms* (cm^{-1})**					0.035				0.075

The (080) state belonging to the higher polyad is included, as it interacts with the (131) state.

Finally, all the observed 670 energy levels could be reproduced with the *rms* deviation of 0.035 cm^{-1} and maximal deviation of 0.18 cm^{-1} by varying 60 diagonal and 40 resonance parameters. The resulting observed and calculated energy levels followed by the mixing coefficients of the wavefunctions are partly given in Appendix A.3. The complete set of the calculated energy levels and spectroscopic resonance parameters obtained are available from the author upon request. Figure 4.25 shows the average resonance mixing for seven out of the ten vibrational states as a function of the rotational quantum number *J*. As evident from Figure 4.25, the resonance mixing rapidly increases with *J*, which decreases the quality of the fitting and the prediction.

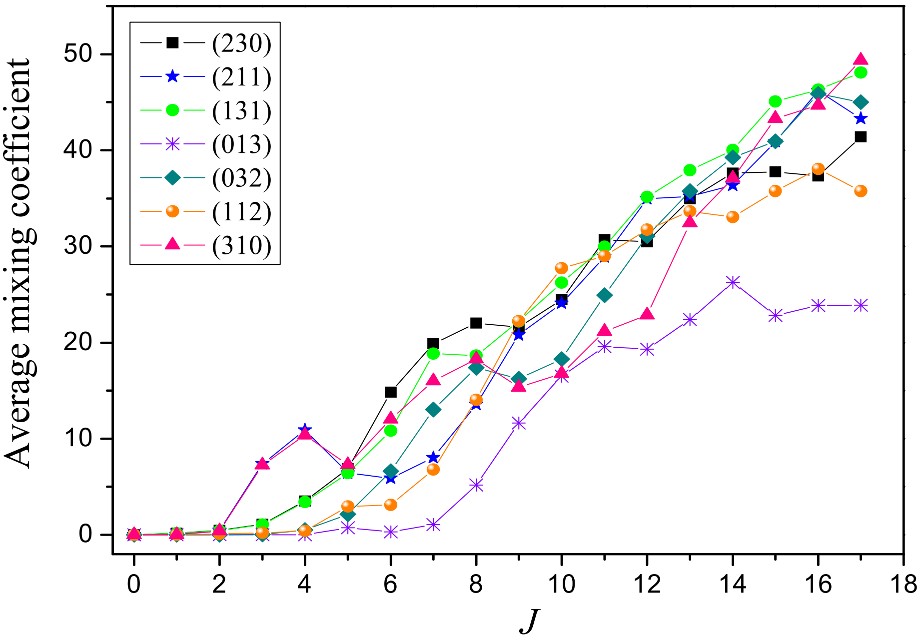

Figure 4.25. Average mixing (%) of the wavefunctions for the 2nd decade of resonating vibrational states of $D_2{}^{16}O$ versus the rotational quantum number *J*.

Figure 4.26 shows the (obs.-calc.) deviations versus $J + K_a / J$ value for the EH, SP [29]–[30] and Ref. [28] calculations. The EH deviations are symmetric with respect to zero, and have no expressed dependence on rotational quantum numbers: they just rapidly increase with *J*. Moreover, these EH deviations are greatly dispersed due to outliers caused by accidental resonances. Both variational calculations demonstrate clear dependence of the (obs.-calc.) deviations on the K_a values within the same *J*–multiplet. No noticeable outliers are seen for more recent calculations [28], with (obs.-calc.) deviations being less dispersed compared to the EH case.

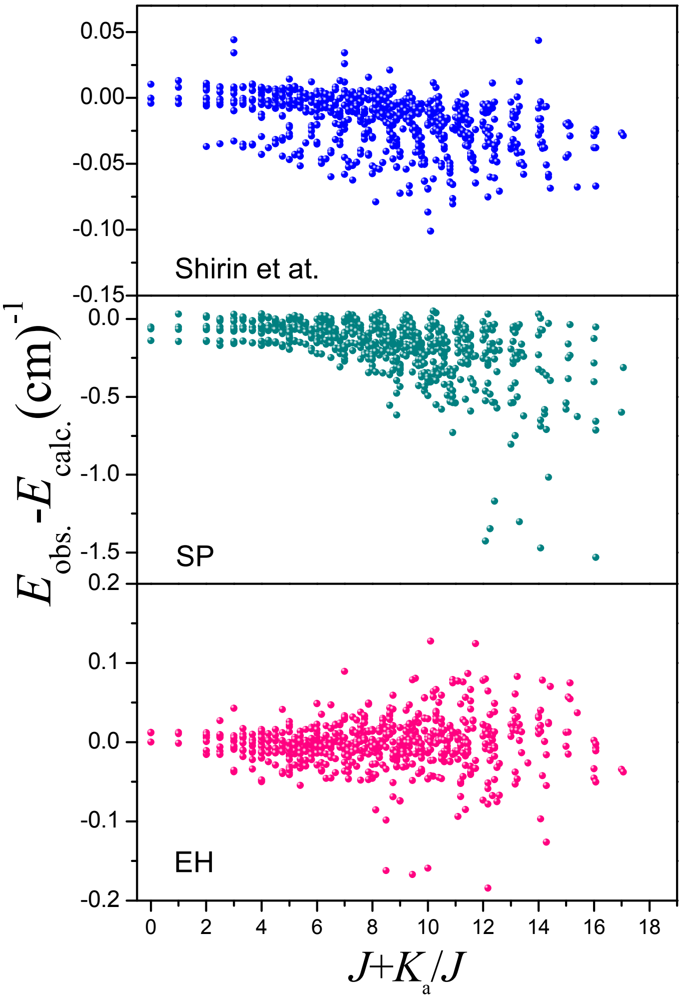

Figure 4.26. Variation of the differences between the observed and calculated values of the $D_2{}^{16}O$ energy levels of the 2nd decade of resonating states determined from the combined analysis of the FTS and ICLAS spectra in the 8800–9520 cm^{-1} region: *Upper panel:* variational calculations of Shirin et al. [28]; *Middle panel*: variational calculations of Schwenke and Partridge [29], [30]; *Lower panel*: calculation in the frame of Effective Hamiltonian approach.

Obviously, the results of the EH calculation are much closer to the experimental values than the SP calculations [29]–[30] that clearly diverge at $J > 10$. On the contrary, the new variational calculations [28] seem to be more accurate than the calculation in the EH framework, with *rms* and maximal (obs.-calc.) deviation of 0.027 and 0.10 cm^{-1}, respectively. The impressive improvement of the variational calculations from the SP [29]–[30] to the ones [28] is based on the optimization of the D_2O PES to the newly reported energy levels including those derived from the transitions falling into the 8800–9520 cm^{-1} spectral range. However, as it was already discussed, the rovibrational labelling in Refs. [28], [39] should be used with caution. In this respect, the results of the EH fitting obtained in the present study can be helpful.

$H_2{}^{18}O$

The experimental energy levels of the (211), (013), (230), (032), (310), and (112) states belonging to the 2nd decade have been partly derived in the course of the 12800–13500 cm^{-1} spectral range analysis performed in this study. These energy levels combined with Ref. [87]–

[90] data were introduced in the least squares fitting, they are listed in Table 4.20, where the three "dark" states: (150), (051), and (070) are included as well. The set of EH parameters derived in [87] was adopted as the initial approximation, and then was refined from the fitting. The $H_2{}^{18}O$ molecule suffers from the strong centrifugal distortion effect in much larger extent than the $D_2{}^{16}O$ molecule, which directly results in strengthening of resonance interactions and increasing their number. Therefore, we limited our fitting by the levels with $J \leq 8$. The *rms* deviation obtained was 0.075 cm^{-1} with 93 varied parameters for 512 energy levels. Average mixing of the wavefunctions of the observed vibrational states is shown in Figure 4.27, it reaches up to 27% already at $J = 8$. Though being approximate, this fitting provided the reasonable rovibrational labelling for the majority of the observed experimental energy levels that belong to the 2nd decade with *J* as large as fourteen.

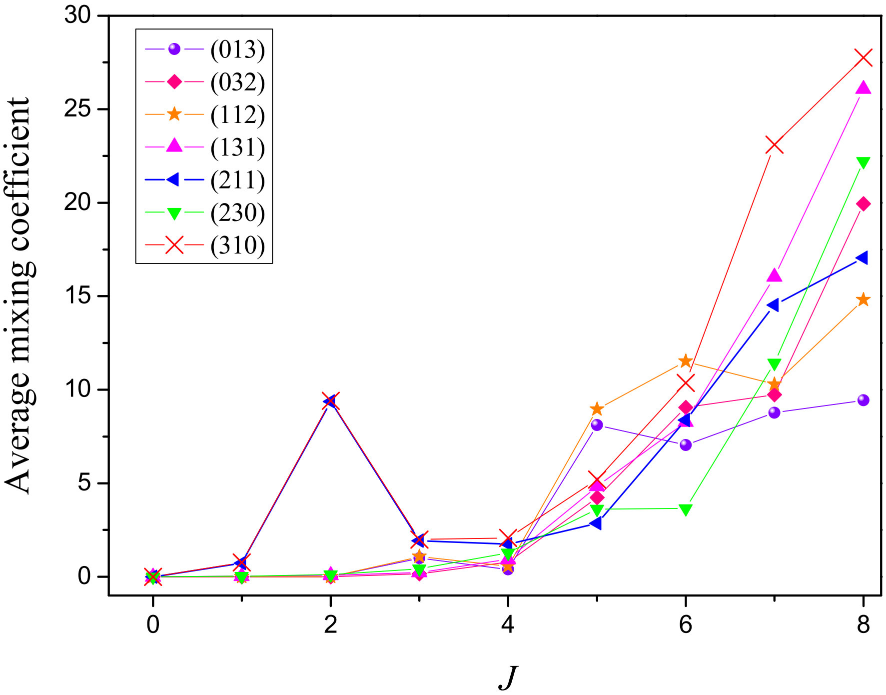

Figure 4.27. Average mixing (%) of the wavefunctions for the 2nd decade of resonating vibrational states of $H_2{}^{18}O$ versus the rotational quantum number *J*.

The most difficult case was the modelling of the vibrational states derived from the analysis of the 12800–14100 cm^{-1} spectral region. These states belong to the polyad of 15 resonating vibrational states, listed in Table 4.21, which we refer to as the first ”pentadecade”. As the experimental energy for many of studied states were sparse, the approximate fitting has been performed for variational [92] energy levels of eleven vibrational states of the 15 resonating ones (Table 4.21). Due to difficulties, which arise in modelling of the highly excited bending states, the (160), (061) and (080) states were not included into consideration. The (004) state was also excluded, as being well above in energy from other polyad members.

Table 4.21. Vibrational states of the first pentadecade of $H_2{}^{18}O$ included in the EH fitting.

$\upsilon_1\ \upsilon_2\ \upsilon_3$	E_{var} [92]	E_{obs}	
2 4 0	13167.723	13167.718	
1 4 1	13212.702	13212.678	
0 4 2	13403.732	13403.71	
3 2 0	13602.655	13602.71	
2 2 1	13612.662	13612.710	
2 0 2	13793.274	13793.260	
3 0 1	13795.413	13795.398	
1 2 2	13870.456	13870.485	
0 2 3	14015.478	14015.510	
4 0 0	14187.975	14187.982	
1 0 3	14276.340	14276.336	
Total N_{lev}			865
N_{param}			75
***rms* (cm^{-1})**			1.1

Only variational [92] energy levels are introduced into the EH fitting.

We were able to fit the 865 energy levels up to $J \le 8$ within *rms* of 1 cm^{-1} by varying 56 diagonal and 19 resonance parameters. This poor accuracy, however, was satisfactory for the unambiguous labelling of the majority of the fitted levels and the ones predicted on the base of the EH fitting. This labelling was then transferred to the experimental energy levels of the $H_2{}^{18}O$ and $H_2{}^{17}O$ molecules obtained in our study with J as large as sixteen. In Table 4.22 the energy levels of the first pentadecade are given for $J = 5$ followed by the (obs.-calc.) (EH) deviations and the leading mixing coefficient of the wavefunction which provides the libelling. In the last two columns labels from Ref. [92] are given, if different from ours. It is seen from the Table 4.22 that in 35 cases out of 120 our labelling differs from that of Ref. [92]. Part of the energy levels are unreasonably labelled in [92] as belonging to (160), (061), (170), (071), (080), (090), and even (0 10 0). In fact, transitions involving the energy levels of these highly excited bending states are predicted by conventional theory to be very weak and may be strengthened only in very rare cases of the close resonance interactions.

Table 4.22. The energy levels of the first pentadecade of interacting vibrational states of $H_2{}^{18}O$.

J K_a K_c	E_{VAR} (cm^{-1})	($E_{VAR.}$-E_{EH})	P_1	($\upsilon_1\upsilon_2\upsilon_3$) [92]	J K_a K_c [92]	J K_a K_c	E_{VAR} (cm^{-1})	($E_{VAR.}$-E_{EH})	P_1	($\upsilon_1\upsilon_2\upsilon_3$) [92]	J K_a K_c [92]
	301						**122**				
5 0 5	14097.01	-0.16	98.7			5 3 3	14123.23	1.07	93.5	0 7 1	5 0 5
5 1 5	14097.34	-0.22	99.0			5 3 2	14127.55	1.00	94.9		
5 1 4	14167.13	-0.36	90.7			5 4 2	14249.56	-1.28	82.5	3 0 1	5 3 2
5 2 4	14177.89	-0.27	94.2			5 4 1	14249.82	-0.84	72.4	0 7 1	5 1 5
5 2 3	14210.13	-0.32	96.6			5 5 1	14397.99	1.15	50.3		
5 3 3	14253.79	-0.84	79.9	1 4 1	5 5 1	5 5 0	14398.39	1.46	49.3		
5 3 2	14260.07	-0.41	94.5	1 4 1	5 5 0		**042**				
5 4 2	14343.90	-0.06	94.6			5 0 5	13724.97	1.17	99.8		
5 4 1	14344.25	-0.05	94.7			5 1 5	13731.56	0.05	99.5		
5 5 1	14461.44	-1.37	81.9			5 1 4	13826.24	2.02	98.1		
5 5 0	14461.44	-1.37	81.9			5 2 4	13873.59	-1.49	99.5		
	221					5 2 3	13901.19	0.52	96.6	3 2 0	5 0 5
5 0 5	13921.24	-0.18	99.7			5 3 3	14020.66	-0.35	68.6		
5 1 5	13922.96	0.00	98.7			5 3 2	14025.71	1.09	62.4		
5 1 4	14004.81	-0.24	87.1	3 2 0	5 2 4	5 4 2	14200.86	1.10	96.3		
5 2 4	14029.80	-0.46	47.1	1 4 1	5 4 2	5 4 1	14200.98	1.10	96.0	4 0 0	5 2 3
5 2 3	14059.51	-0.34	95.2			5 5 1	14414.55	-1.96	59.0		
5 3 3	14130.17	0.32	94.4			5 5 0	14414.55	-1.97	59.0		
5 3 2	14134.65	0.27	95.1				**202**				
5 4 2	14254.30	0.40	91.2	4 0 0	5 3 2	5 0 5	14094.89	0.01	99.2		

J K_a K_c	E_{VAR} (cm^{-1})	($E_{VAR.}$-E_{EH})	P_1	($\upsilon_1\upsilon_2\upsilon_3$) [92]	J K_a K_c [92]
5 4 1	14254.57	0.05	85.8		
5 5 1	14403.02	-0.28	82.3		
5 5 0	14403.02	-0.29	82.3		
	141				
5 0 5	13531.90	-0.20	100.0		
5 1 5	13539.65	-0.40	100.0		
5 1 4	13632.60	-0.68	100.0		
5 2 4			100.0		
5 2 3	13712.53	0.46	99.6	0 8 0	5 5 1
5 3 3	13838.92	1.12	99.7	0 9 0	5 2 3
5 3 2	13841.13	0.91	99.5		
5 4 2	14021.74	-0.02	65.2	2 2 1	5 2 4
5 4 1	14026.50	0.61	67.7		
5 5 1	14243.96	0.24	90.7	3 2 0	5 4 1
5 5 0	14243.94	0.21	90.3	3 2 0	5 4 2
	103				
5 0 5	14578.70	0.13	99.8	0 7 1	5 2 3
5 1 5	14578.84	-0.12	98.0		
5 1 4	14650.39	-0.13	99.8		
5 2 4	14663.40	-0.28	74.9		
5 2 3	14694.45	-0.30	99.0		
5 3 3	14725.98	0.10	58.5	2 0 2	5 4 1
5 3 2	14746.06	0.31	65.6		
5 4 2	14814.53	0.84	94.1	1 7 0	5 3 2
5 4 1	14815.00	0.84	94.0		
5 5 1	14920.62	1.00	99.8		
5 5 0	14920.61	0.99	99.8		
	023				
5 0 5	14326.08	0.02	99.9		
5 1 5	14328.00	0.09	94.9		
5 1 4	14411.08	-0.06	100.0		
5 2 4	14429.45	0.21	99.0		
5 2 3	14464.40	0.01	99.8		
5 3 3	14528.50	0.56	86.1		
5 3 2	14533.65	0.47	93.6		
5 4 2	14640.81	0.01	98.2	2 0 2	5 3 2
5 4 1	14641.09	0.01	98.2	2 0 2	5 3 3
5 5 1	14781.92	-0.23	100.0		
5 5 0	14781.93	-0.22	100.0		
	122				
5 0 5	13911.72	-1.19	95.9	0 4 2	5 2 3
5 1 5	13913.77	-0.09	99.4		
5 1 4	13995.98	-0.68	96.0	1 6 0	5 5 0
5 2 4	14019.87	1.20	85.5	0 6 1	5 5 0
5 2 3	14050.92	0.06	96.8	3 2 0	5 2 3
5 1 5	14095.21	-0.04	98.4		
5 1 4	14165.46	-0.17	95.0		
5 2 4	14176.41	-0.08	89.9		
5 2 3	14208.21	-0.33	96.8	0 4 2	5 4 1
5 3 3	14252.14	0.12	85.5		
5 3 2	14258.21	-0.28	93.2	2 2 1	5 4 2
5 4 2	14342.21	0.39	94.2	0 7 1	5 1 4
5 4 1	14342.55	0.37	94.3		
5 5 1	14459.49	-1.93	73.5		
5 5 0	14459.50	-1.92	73.5		
	320				
5 0 5	14179.37	0.13	99.7	0 10 0	5 0 5
5 1 5	14181.30	0.43	99.9		
5 1 4	14264.30	-0.36	98.1		
5 2 4	14286.21	0.97	99.7		
5 2 3	14318.13	-0.49	94.7		
5 3 3	14389.82	1.09	98.4		
5 3 2	14393.79	0.36	94.2		
5 4 2	14515.27	-0.12	93.2		
5 4 1	14514.75	-0.17	85.7		
5 5 1	14672.19	-2.94	97.8		
5 5 0	14672.21	-2.92	97.8		
	400				
5 0 5	14488.92	0.00	100.0	1 7 0	5 2 3
5 1 5	14489.59	0.01	100.0		
5 1 4	14560.09	0.01	100.0	0 7 1	5 2 4
5 2 4	14570.80	0.13	99.8		
5 2 3	14604.02	0.08	97.8		
5 3 3	14646.44	0.43	98.6	0 2 3	5 4 1
5 3 2	14649.28	0.09	74.7	0 2 3	5 4 2
5 4 2	14729.98	0.24	65.4		
5 4 1	14742.84	0.47	58.5	1 0 3	5 3 3
5 5 1	14848.99	0.04	94.2		
5 5 0	14848.96	0.02	94.3		
	240				
5 0 5	13485.68	-1.01	100.0		
5 1 5	13496.07	0.54	100.0		
5 1 4	13588.53	0.55	100.0		
5 2 4	13650.31		100.0	1 6 0	5 4 2
5 2 3	13671.87	1.10	99.8		
5 3 3	13807.62	0.65	99.7		
5 3 2	13809.03	0.24	98.0		
5 4 2	14004.25	0.37	98.8		
5 4 1	14004.50	0.55	98.9	0 6 1	5 5 1
5 5 1	14230.19	-0.49	96.5		
5 5 0	14230.19	-0.49	96.5		

($E_{VAR.}$-E_{EH})is the difference between the variational energy value and that calculated with the EH model.
P_1 indicates the leading mixing coefficient of the wavefunction, which provides the labelling.
Rovibrational labels from Shirin et al. [92] are given in the two last columns, if different from ours.

The Tables with observed and calculated energy levels followed by the mixing coefficients for the states of the 2nd decade and the 1st pentadecade are partly given in Appendix A.4 and A.5, respectively, and are fully available from the author upon request.

HDO

The HDO molecule has lower symmetry (C_s) compared to $H_2{}^{18}O$ and $D_2{}^{16}O$ (C_{2V}). This leads to important changes in the harmonic frequencies (see Section 1 of the current Chapter), and then in formation of the resonance polyads. Due to the close coincidence between the ω_1 and $2\omega_2$, the anharmonic high-order resonances in HDO are very strong. This implies that the polyad size increases starting already from the low lying vibrational states. For example, in [104] four vibrational states of HDO: (011), (200), (120), and (040) are fitted together, while in symmetrical water isotopologues these states belong to different polyads: (011) relates to the second triad, and (200), (120), (040) are included in the first hexad. At the same time, in HDO there is a sequence of well-isolated vibrational states of the (00*υ*) type, which can be fitted separately [65], [68], [105]–[106].

The experimental energy levels of the HDO molecule derived in our study correspond to the highly excited vibrational states, for which the full-size EH fitting becomes problematic, as it should include the strong interactions with the high bending states like (070), (170), (071), (180), (081), (090) and even (0 11 0). That is why we did not attempt the full-size EH fitting for our set of the HDO experimental energy levels: only Fermi–dyad has been analyzed for the (103) and (023) states, other vibrational states were approximately fitted as the isolated states with the *rms* deviations varying from 0.03 to 1 cm^{-1}.

We were able to reproduce 262 energy levels with J as high as 16 and K_a as high as 8 of the (103)–(023) Fermi–dyad with *rms* of 0.047 cm^{-1} by varying 27 parameters, including 8 Fermi and Coriolis–type resonance constants, which is noticeably better than our previous fitting [60] with *rms* of 0.083 cm^{-1}. The spectroscopic parameters obtained in the fitting are given in Table 4.23 followed by 68% confidential intervals. The new version of the mixing coefficients for the (103)-(023) states is given, partly, in Appendix A.6, and is fully available from the author upon request.

The fitting of the (004) energy levels as an isolated state resulted in a satisfactory *rms* of 0.032 cm^{-1} for 176 energy levels with J and K_a up to 17 and 9, respectively, obtained in this study and in Ref. [68]. Only 9 energy levels were excluded from the fitting process, as being strongly perturbed by the resonances interactions with the other states. The parameters obtained are included in Table 4.23. Spectroscopic constants of the (103) and (004) states are close in values, while those of the (023) state (especially parameters related to J_z sequence in Hamiltonian) can differ significantly because of the strong centrifugal distortion effect, for example, H_k for the (023) state is more than 30 times larger than H_k for the (103).

Though for the most cases the EH fittings performed were found to be satisfactory as far as the rovibrational labelling is concerned, we could not obtain reliable EH prediction for the (150) and (230) states considering them as isolated. Further analysis is then required to solve this problem.

Table 4.23. Spectroscopic parameters (cm^{-1}) for the (103)–(023) Fermi–dyad and (004) vibrational state.

Parameters	**(023)**	**(103)**	**(004)**
E_v	13278.3588	13331.6121	13853.62698(864)
A	23.61267(250)	20.58608(180)	19.44556(140)
B	9.323153(760)	8.948009(810)	9.05663(350)
C	6.002981(420)	6.069867(410)	6.09106(240)
D_k	4.56885(880)E-02	7.6936(760)E-03	9.1406(540)E-03
D_{jk}		6.709(490)E-04	3.838(260)E-04
D_j	5.4052(150)E-04	3.4809(160)E-04	4.14965(820)E-04
d_k	4.9333(770)E-03	7.711(520)E-04	1.5669(140)E-03
d_j	2.1694(120)E-04	1.1859(150)E-04	1.47844(510)E-04
H_k	1.43202(990)E-03	3.9E-05	3.2045(820)E-05
H_{kj}			-8.676(530)E-06
H_{jk}			2.901(190)E-06
h_k	1.794(360)E-05		
L_k	-2.0267(360)E-05		
l_k			-1.866(310)E-07
P_k	1.3566(330)E-07		
p_k			4.494(550)E-09
Coupling parameters	**(023)-(103)**		
F_k	-9.78067(960)E-01		
F_j	-7.873(320)E-02		
F_{xy}	-6.5001(540)E-02		
F_{xyk}	-8.205(360)E-04		
C_{ykk}	2.518(310)E-04		
C_{xzk}	-1.462(270)E-03		
C_{yk}	1.2660(630)E-02		
C_{xz}	-1.1442(450)E-01		

For the definition of parameters, see Section 3 of Chapter III.

7. "Reference" spectra of water isotopologues in the 6000-15500 cm^{-1} spectral region

For a number of fundamental problems and applications, the accurate and detailed linelists of water vapour isotopologues are necessary. All the experimental energy levels derived in this study together with the available literature data for the $D_2{}^{16}O$ molecule [17]-[27], [45], [53], [55] and with the IUPAC TG energy levels for $H_2{}^{18}O$ and $HD^{16}O$ [85]-[86] were used to generate transition wavenumbers as a difference between the upper and lower energy level. These transition wavenumbers were augmented with the variational intensities [28], [82], [92] to obtain detailed lists of the $D_2{}^{16}O$, $H_2{}^{18}O$ and $HD^{16}O$ absorption lines with the intensity cutoff of 2×10^{-28} cm/molecule falling into the 6100–15500 cm^{-1} spectral region, which covers the transitions involving presently obtained upper energy levels.

As rovibrational labels for the experimental energy levels adopted in this study and other publications may differ from the variational labels, the comparison between the experimental energy levels and variational transitions set was performed in several steps. The main criteria for comparison were coincidence of the rotational quantum number J and rovibrational symmetry, as well as the acceptable difference ΔE between the experimental and calculated energy for the upper rovibrational state in the variational transitions. Variational labels for the lower states were found to coincide reasonably well with those accepted in the experimental studies, and the substitution of variational lower energy levels for the experimental values was performed straightforwardly. As soon as the correspondence with the experiment was established for the variational upper energy level for at least one transition, variational wavenumbers of all other transitions having the same upper level were promptly corrected.

The variation interval of ΔE for the upper energy levels was chosen from the extensive comparisons of variational calculations with the experimental data (see, for example, [85], [86]). For the considered spectral region, the variational upper energy levels differ from the experimental values from 0.01 up to 0.5 cm^{-1}. Therefore, at the first step ΔE was set to 0.05 cm^{-1}, and a number of the experimental and calculated energy levels were compared. At the next steps, the comparison has been continued for yet non-compared experimental energy levels with successive increasing of the ΔE up to 0.5 cm^{-1}. Thus, the resulting constructed linelists include 10853, 7800, and 54852 transitions for the $D_2{}^{16}O$, $H_2{}^{18}O$ and $HD^{16}O$ molecules, respectively, and are available from the author upon request.

The wavenumbers of the extensive sets of the water isotopologue transitions constructed as described above, have the best to date experimental accuracy. This is because their upper and lower energy levels were averaged over all the published experimental transitions taking into account the associated experimental errors. Rovibrational intensities provided by variational computations [28], [82], [92] were tested in a number of papers (see, for example, [29]-[30], [107]), and they are believed to have satisfactory accuracy. Then, the constructed linelists of $D_2{}^{16}O$, $H_2{}^{18}O$ and $HD^{16}O$ can be considered as “reference” spectra.

The results obtained for the HDO molecule are summarized in Figure 4.28 where the reference transitions involving all the available energy levels provided by the IUPAC TG [21] (our included) are shown (in gray) in comparison with the directly observed transitions from the literature (in green), and the reference transitions calculated from our total (in blue) and new (in red) energy levels set. It is worth noting, that the $HD^{16}O$ energy levels derived from the study of the 9100 – 9640 cm^{-1} region, give rise to relatively strong reference transitions up to 6100 cm^{-1}. The majority of the reference transitions based on our energy levels and falling into the 6100-8500 cm^{-1} region represent the hot transitions.

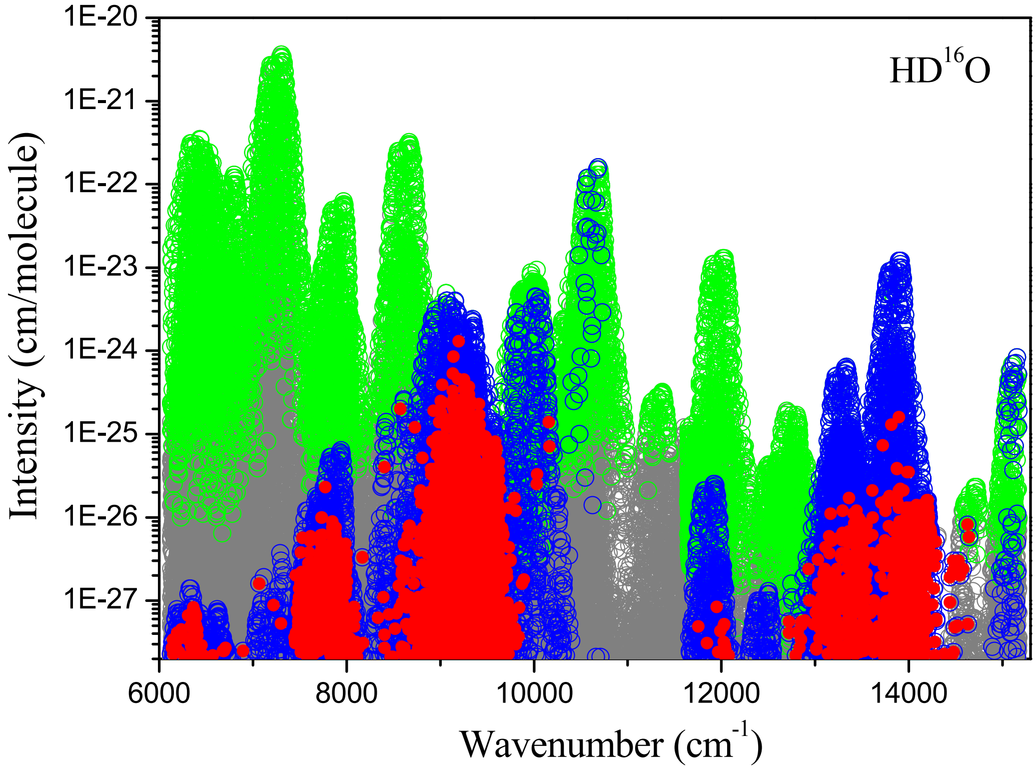

Figure 4.28. $HD^{16}O$ observed and “reference” transitions. In gray- reference transitions involving the IUPAC TG [21] energy levels; in green - experimentally observed transitions from the IUPAC TG database [21]; in blue - reference transitions involving 1317 energy levels derived in our studies [59], [60]; in red – reference transitions related to the 458 newly observed energy levels [59], [60]. Intensity cutoff is 2×10^{-28} cm/molecule.

Figure 4.29 illustrates the contribution of reference transitions of $D_2{}^{16}O$ in comparison with the pure variational prediction [28]. It is obvious that above 8800 cm^{-1}, most of reference transitions (in blue and red) are generated using our $D_2{}^{16}O$ energy levels. Unlike $HD^{16}O$, the $D_2{}^{16}O$ reference transitions do not extend so long, as the D_2O experimental energy set corresponds to more higher excitation than in HDO, resulting in attenuation of the transition intensities.

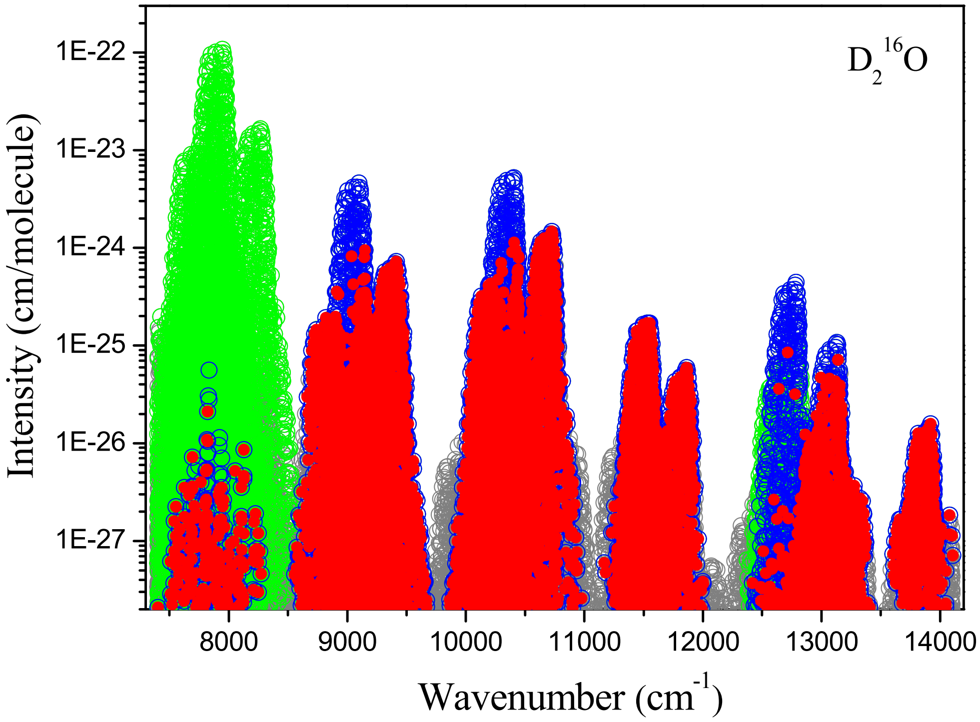

Figure 4.29. $D_2^{16}O$ variational and “reference” transitions. In gray- pure variational prediction; in green - reference transitions involving all available in literature energy levels, including ours [21], [24]-[27]; in blue - reference transitions involving 2630 upper energy levels derived in our studies [21], [24]-[27]; in red – reference transitions related to the 1924 newly observed energy levels [21], [24]-[27]. Intensity cutoff is 2×10^{-28} cm/molecule.

The list of all the rovibrational transitions reaching the 1306 energy levels of $H_2^{18}O$ derived in this study (intensity cut off of 2×10^{-28} cm/molecule) is also generated. The line positions were calculated from the experimental upper energy levels and the lower experimental energy levels provided by the IUPAC TG [85], [86], the intensities being the variational intensities of Ref. [92]. This line list, provided as supplementary material of Ref. [93]−[94], extends from 10000 to 15500 cm^{-1}, much beyond the range of the present recordings. The transitions calculated from the new levels are highlighted in Figure 4.30 in order to illustrate the impact of the newly derived experimental upper levels.

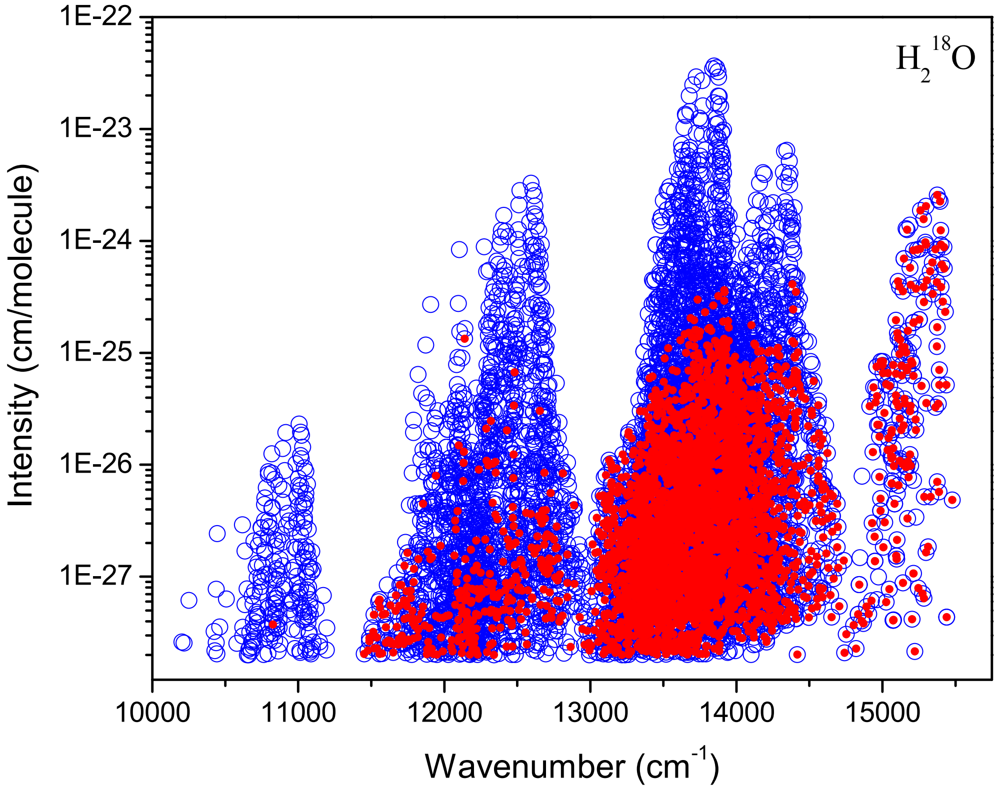

Figure 4.30. $H_2{}^{18}O$ transitions reaching the 1036 energy levels derived from the analysis of the ICLAS spectrum between 12580 and 14100 cm^{-1}. The variational intensities of Ref. [92] were attached to the line positions calculated from the experimental energy values. The transitions reaching the 780 newly derived energy levels are highlighted (red dot).

The reference spectra generated in this study can be used: (*i*) for so called trivial assignments of the experimental hot and cold spectra, as well as for calibration purposes, since their positions are of experimental accuracy; (*ii*) for line shape studies as they provide all the possible components of the quasi-degenerated experimental lines; (*iii*) for atmospheric calculations, as they exceed the HITRAN data in a number and in accuracy; (*iv*) for planning the future experiments, as they include all the presently measured and accurately evaluated transitions.

8. Conclusions

The high resolution spectra of various water isotopologues were recorded by ICLAS and FTS in wide spectral region from 8800 to 14100 cm^{-1}. The high sensitivity of experimental methods presently implemented provided a much deeper characterisation of considered of line position and strengths of considered water isotopologues in this spectral region. The spectrum analysis based on the results of high accuracy variational calculations [28]-[30], [80], [82], [92] provided an immense amount of new energy levels for each of the isotopologues under consideration. The experimental information obtained in the present study is summarized in Table 4.24. The experimental energy levels derived in this study and available in the literature allowed us to calculate the line positions at the level of experimental accuracy in a region which extends much further the range of the present recordings. These line positions augmented with variational intensities provide very useful information for many applications. As one example, these high accuracy ("reference") line lists could be used for the purpose of spectrum calibration.

It is worth noting, that the large amount of new experimental information obtained in our study could be used for further improvement of the mass-dependent H_2O PES.

Table 4.24. Summary of the experimental information obtained in the present study of the high resolution spectra of various water isotopologues by ICLAS and FTS from 8800 to 14100 cm^{-1}.

Isotopologue	Spectral range (cm^{-1})	Experimental technique	Number of new rovibrational energy levels
$D_2{}^{16}O$	8800–9520 [21]	ICLAS-VeCSEL, FTS	577
	10000–13200 [24]	FTS	436
	11400–11900 [25]	ICLAS	530
	12850–13380 [26]	ICLAS	422
	13600–14020 [27]	ICLAS	177
$HD^{16}O$	9100–9640 [59]	ICLAS-VeCSEL	300
	13020–14115 [60]	ICLAS	157
$H_2{}^{18}O$	12580–13550 [93]	ICLAS	438
	13540–14100 [94]	ICLAS	342

For the complete set of $D_2{}^{16}O$, $HD^{16}O$ and $H_2{}^{18}O$ experimental energy levels newly derived in the present study over the whole spectral region under consideration, the reader is referred to the relevant papers [21], [25]-[27], [59]-[60], [93]-[94]. The energy levels of $D_2{}^{16}O$ obtained from the analysis of FTS spectrum between 10000 and 13200 cm^{-1} [24] have not been published yet and so are given in Appendix A.1.

D_2O

The absorption spectra of dideuterated water, D_2O, were recorded by various high sensitivity techniques and theoretically treated in the 8800-14020 cm^{-1} spectral region.

The 8800-9520 cm^{-1} spectral section was recorded with the FTS spectrometer with a 600 m path length in Reims and by ICLAS-VeCSEL in Grenoble. The combination of two high sensitive absorption spectra recorded independently in different experimental conditions improved the reliability of the experimental data obtained.

The stronger part of D_2O absorption between 10000 and 13200 cm^{-1} was recorded with the same FTS spectrometer by the Reims-Brussels collaboration [24]. Weaker lines above 11400 cm^{-1} were measured by the high-sensitivity ICLAS-Ti:Sapphire technique in Grenoble. The D_2O

spectra above 12800 cm^{-1} have been the highest energy range reported so far. The performance of the ICLAS-Ti:Sapphire technique combined with the use of a highly enriched sample containing 98 % of deuterium yielded a detailed D_2O absorption spectrum for the 11400–14020 cm^{-1} spectral range, including regions where the HDO or H_2O transitions are much stronger than those of D_2O for pure species (Figure 4.3). As a result, a detailed list of 1962 lines was constructed in 11400–14020 cm^{-1} region enlarging considerably the previous set of 304 lines observed by FTS in the same region [24].

The spectrum assignment was performed using recent results of variational calculations based on an optimized potential energy surface of D_2O [28], [39] and Schwenke and Partridge DMS [30]. At the time of spectra assignment, available variational calculations have been examined. In particular, when analysing the 8800 – 9520 cm^{-1} spectral region, it was evidenced that the PS calculation starts to diverge at $J \geq 10$, leading to irregular (obs.-calc.) deviations as large as 1.53 cm^{-1}. At the same time, variational calculations based on PES of Ref. [39] of and DMS of Ref. [30] showed regular and smooth (obs.-calc.) tendencies up to $J = 17$ (Figure 4.5).

However, variational wavenumbers [39] could deviate from the experimental values by up to 1.00 cm^{-1}, in the high frequency end of the presently investigated D_2O spectrum, which certainly prevented performing unambiguous assignment. The experimental energy levels derived from our studies [21], [24], [25] as well as the data obtained from the analysis of the 12450–12850 cm^{-1} region [20] were then used in [28] to further refine the PES of the D_2O molecule. This PES [28] was successfully applied for the assignment of the ICLAS spectra above 11400 cm^{-1} with *rms* deviation varying within 0.09–0.13 cm^{-1}. Much larger deviations – up to 0.4 cm^{-1}, though, were evidenced for separate transitions involving upper energy levels perturbed by high-order resonance interactions (see Figure 4.10). Variational intensities provided by the PES [28] and DMS [30] were found to agree very satisfactory with the experimental values in the whole presently investigated spectral region. Still, significant deviations between the calculated and experimental intensities were identified for lines involving the (091) and (203) upper levels in close resonance, also showing some small deficiencies of the PES of Ref. [28].

In total, 4360 rovibrational lines of the D_2O molecule were assigned leading to derivation of 2086 new experimental energy levels belonging to 42 vibrational states. The new information includes 20 rovibrational bands, among which are the highest in energy observed so far: (203)–(000) at 13088.307, (104)–(000) at 13263.902, (331)–(000) at 13717.264, (411)–(000) at 13876.021 cm^{-1}. New information obtained in our series of studies together with a detailed and exhaustive analysis of the literature data allowed us to construct the most complete set of 53 vibrational energy levels for $D_2{}^{16}O$. This list has been used to determine the vibrational Hamiltonian parameters in order to propose consistent vibrational labels of the $D_2{}^{16}O$ states up to

18000 cm^{-1}. Our analysis has shown that above 15000 cm^{-1}, normal mode labels have to be used with caution as the resulting wave functions become greatly mixed for most of the vibrational states for this isotopologue.

Due to the change in atomic masses of D_2O compared to H_2O, the D_2O variational calculations are sensitive to adiabatic and nonadiabatic corrections to the H_2O PES obtained in the Born-Oppenheimer approximation. Thus, the results obtained in this study both extend our knowledge about the energy levels structure of the D_2O molecule and may be of importance for further improvement of the mass dependent PES of the H_2O molecule.

HDO

The high resolution absorption spectrum of monodeterated water HDO was recorded by ICLAS-VeCSEL and ICLAS-Ti:Sapphire in the 9100-9640 cm^{-1} and 13020-14115 cm^{-1} regions, respectively. These high sensitivity ICLAS investigations improved by more than one order of magnitude the FTS detection limit of Refs. [33], [70] and then allowed to observe numerous weak lines. The observed transitions have been assigned by using the high accuracy SP [29], [30], [80] and VTT [81], [82] variational calculations.

The analysis of the 9100–9640 cm^{-1} spectral region resulted in a complete assignment of the observed transitions and the derivation of 300 new accurate energy levels for the (201), (310), (121), (041), (230), (070), and (150) states. An unexpectedly high number of 55 rotational energy levels of the highly excited bending (070) state could be derived as a consequence of a strong resonance strengthening of the $7\nu_2$ band. This confirms that centrifugal distortion effect in HDO is abnormally strong and leads to considerable perturbation of its rovibrational spectrum at a high excitation of bending vibration [61], [84].

The noise equivalent absorption of the order of $\alpha_{\min} \sim 10^{-9}$ cm^{-1} achieved in the 13020–14115 cm^{-1} spectra recordings allowed detecting transitions with line strengths as small as 2×10^{-27} cm/molecule. It is about 10 times lower than the smallest line intensities previously detected in this spectral region. 2157 transitions involving 21 upper vibrational states were assigned to $HD^{16}O$ while only four bands were previously reported in this range. The obtained set of 619 rovibrational energy levels includes 157 and 48 newly reported ones for $HD^{16}O$ and $HD^{18}O$, respectively. Transitions of the very weak (510)–(000), (132)–(000) and (401)–(000) absorption bands of $HD^{16}O$ were identified and the corresponding band origins were accurately evaluated from the (obs.-calc.) extrapolation at $J = 0$ of the $K_a = 0$ series of energy levels. The new results include 48 energy levels of the (004) vibrational state of the $HD^{18}O$ isotopologue at 13814.526 cm^{-1} which is the most excited vibrational state reported so far for this species.

Transitions reaching the $K_a = 1$ energy levels of the (0 11 0) bending state of $HD^{16}O$ at 13326.84 cm^{-1} were observed due to intensity transfers from the (004) state via high-order resonance interactions. The quality of the new VTT variational calculations [81], [82] was confirmed for the $HD^{16}O$ line positions. For the derived energy levels, the *rms* value of the (obs.-calc.) deviations has been decreased to 0.06 cm^{-1} compared to 0.23 cm^{-1} for SP results. In addition, VTT calculations provide more accurate intensities for the transitions in close resonance. Significant discrepancies between SP and VTT calculated intensities were evidenced for the weak (212)-(000), (132)-(000) and (401)-(000) bands which are mostly free of resonance interactions, but the accuracy of the experimental intensity values of the corresponding very weak lines is not sufficient to decide which of the two calculations is more accurate.

The experimental information provided in this work makes a marked improvement in the knowledge of the HDO absorption spectrum. The generated line list may be helpful for discriminating between weak HDO lines and trace species absorption in the 9100–9640 cm^{-1} transparency region.

The most complete and accurate identification list in the 13020-14115 cm^{-1} region could be generated by combining the present ICLAS results with the FTS data of Ref. [33] for the stronger transitions. It will significantly improve and replace the previous ICLAS measurements [67]. The newly reported transitions are included into the exhaustive $HD^{16}O$ and $HD^{18}O$ datasets used by the IUPAC task group [21] to determine a consistent set of energy levels for these two isotopologues.

$H_2{}^{18}O$

The high resolution rovibrational spectrum of a highly ^{18}O enriched water sample was recorded by ICLAS-Ti:Sapphire in the wide 12580–13550 cm^{-1} spectral range corresponding to a transparency window of water and in the 13350–14100 cm^{-1} covering the relatively strong 4*v* polyad. Four isotopologues of water –$H_2{}^{18}O$, $H_2{}^{16}O$, $H_2{}^{17}O$, $HD^{18}O$–were found to contribute to the spectra.

In course of the 12580-13550 cm^{-1} spectral range analysis, the 1293 absorption lines belonging to the $H_2{}^{18}O$, $H_2{}^{17}O$ and $HD^{18}O$ isotopologues were assigned on the basis of variational calculations [29]-[30], [80], [92] yielding 524 new accurate rovibrational energy levels belonging to a total of 40 vibrational states (Table 4.15). Reasonable labelling for the highly excited rovibrational energy levels was established using an effective Hamiltonian approach. It has been found that not only close, but distant resonances, with energy differences up to 60 cm^{-1} between interacting levels, can induce important intensity transfer to otherwise weak transitions. Interestingly, those high-order resonances always involve highly excited bending states.

As a result of the 13540-14100 cm^{-1} spectral range investigation, 342, 84 and 26 levels were newly derived for the $H_2{}^{18}O$, $H_2{}^{17}O$ and $HD^{18}O$ isotopologues, respectively. A large amount of new energy levels were obtained for the (023), (122) and (311) vibrational states and levels of highly excited bending states as (061), (160), (071), (170), (080) and (090) could be determined.

An important overestimation of the HITRAN line intensities of $H_2{}^{18}O$ over the wide 12400-14520 cm^{-1} region has been evidenced by comparison to variational calculations [30], [92] and to ICLAS absolute intensity values. The IUPAC-TG line list of $H_2{}^{18}O$ [85], [86] which includes variational intensities values should be preferably used in the studied region. We believe that this conclusion applies also at lower energies. The large amount of new information obtained by ICLAS in the present work will be valuable to complete the IUPAC-TG line list of Refs. [85], [86] by using the MARVEL procedure [100], [101].

References for Chapter IV

[1] L. A. Pakhomycheva et al. Line structure of generation spectra of lasers with inhomogeneous broadening of the amplification line. JETP Lett. 12, 1970; 43.

[2] H. J. Kimble. Calculated enhancement for intracavity spectroscopy with single-mode laser. IEEE J. Quantum Electron. QE-16 4, 1980; 455.

[3] K. J. Boller and T. Schroeder. Demonstration of broadband intracavity spectroscopy in a pulsed optical parametric oscillator of beta-barium borate. J. Opt. Soc. Am. B 10, 1993; 1778.

[4] A. Kachanov A. Charvat, F. Stoeckel. Intracavity laser spectroscopy with vibronic solid-state lasers: I. Spectro-temporal transient behaviour of a Ti:sapphire laser. J. Opt. Soc. Am. B 11, 1994; 2412.

[5] V. M. Baev. Laser intracavity absorption spectroscopy. Appl. Phys. B 69, 1999; 171.

[6] A. Garnache et al. High-sensitivity intracavity laser absorption spectroscopy with vertical-external-cavity surface-emitting semiconductor lasers. Opt. Lett. 24, 1999; 826.

[7] J. Cheng et al. Infrared intracavity laser absorption spectroscopy with a continuous-scan Fourier-transform interferometer. Appl. Opt. 39, 2000; 2221.

[8] Encyclopedia of Laser Physics and Technology, http://www.rp-photonics.com/

[9] A. A. Kachanov, V. R. Mironenko, I. K. Pashkovich. Quantum threshold of the sensitivity of an intracavity traveling-wave laser spectrometer. Sov. J. Quantum Electron. 19, 1989; 95.

[10] A. Garnache, A. A. Kachanov, F. Stoeckel, R. Houdré. Diode-pumped broadband vertical-external-cavity surface-emitting semiconductor laser applied to high-sensitivity intracavity absorption spectroscopy. J. Opt. Soc. Am. B, 17, 2000; 1589.

[11] Charvat, A.A. Kachanov, A. Campargue, D. Permogorov, F. Stoeckel. High sensitivity intracavity absorption spectroscopy of CHD_3 in the near infrared with a titanium:sapphire laser. Chem. Phys. Lett. 14, 1993; 495.

[12] F. Mazzotti, O.V. Naumenko, S. Kassi, A.D. Bykov and A. Campargue. ICLAS of weak transitions of water between 11300 and 12850 cm^{-1}: comparison with FTS databases. J Mol Spectrosc. 239, 2006; 174.

[13] A. Campargue, F. Stoeckel and M. Chenevier. High sensitive intracavity laser spectroscopy: application to the study of overtone transitions in the visible range, Spectrochim Acta Rev. 13, 1990; 69.

[14] E. Bertseva, A. A. Kachanov, and A. Campargue. Intracavity laser absorption spectroscopy of N_2O with a vertical external cavity surface emitting laser. Chem. Phys. Letters*,* 351, 2002; 18.

[15] Y. Ding, V.I. Perevalov, S.A. Tashkun, J.-L. Teffo, S. Hu, E. Bertseva, A. Campargue. J. Mol. Spectrosc. Weak overtone transitions of N_2O around 1.05 µm by ICLAS-VECSEL. 220, 2003; 80.

[16] E. Bertseva, V. Perevalov, S.A. Tashkun, A. Campargue. New observations of weak overtone transitions of N_2O by ICLAS-VeCSEL near 1.07 µm. J. Mol. Spectrosc. 226, 2004; 196.

[17] J.-J. Zheng, O. N. Ulenikov, G. A. Onopenko et al. High-resolution vibration-rotation spectrum of D_2O in the region near the $2v_1+v_2+v_3$ absorption band. Mol. Phys. 99, 2001; 931.

[18] O. N. Ulenikov, S.-M. Hu, E. S. Bekhtereva et al. High-resolution Fourier transform spectrum of D_2O in the region near 0.97 µm. J. Mol. Spectrosc. 210, 2001; 18.

[19] S.-M. Hu, O. N. Ulenikov, E. S. Bekhtereva et al. High-resolution Fourier-transform intracavity laser absorption spectroscopy of D_2O in the region of the $4v_1+v_3$ band. J. Mol. Spectrosc. 212, 2002; 89.

[20] A. Campargue, F. Mazzotti, S. Béguier, O.L. Polyansky, I.A. Vasilenko, O.V. Naumenko. High sensitivity ICLAS of D_2O between 12450 and 12850 cm^{-1}. J. Mol. Spectrosc. 245, 2007; 89.

[21] O. V. Naumenko, O. M. Leshchishina, S. Shirin, A. Jenouvrier, S. Fally, A.C. Vandaele, E. Bertseva, A. Campargue. Combined analysis of the high sensitivity Fourier transform and ICLAS-VeCSEL absorption spectra of D_2O between 8800 and 9520 cm^{-1}. J. Mol. Spectrosc. 238, 2006; 79.

[22] O. N. Ulenikov, S.-G. He, G. A. Onopenko, E. S. Bekhtereva et al. High-resolution study of the $(v_1+1/2v_2+v_3 = 3)$ polyad of strongly interacting vibrational bands of D_2O. J. Mol. Spectrosc. 204, 2000; 216.

[23] A.D. Bykov, O. V. Naumenko, E. R. Polovtseva, S.-M. Hu, A.-W. Liu. Fourier transform absorption spectrum of D_2O in 7360–8440 cm^{-1} spectral region. J. Quant. Spectrosc. Radiat. Transfer. 111, 2010; 2197.

[24] A. Jenouvrier, S. Fally, A.C. Vandaele, O.V. Naumenko, O.Leshchishina, S.V. Shirin The Fourier Transform absorption spectrum of the $D_2{}^{16}O$ molecule in the 10000−13200 cm^{-1} spectral region. Proceedings of XV Symposium on HRMS, Nigniy Novgorod, 2006.

[25] O.V. Naumenko, F. Mazzotti, O. M. Leshchishina, J. Tennyson, and A. Campargue, Intracavity laser absorption spectroscopy of D_2O between 11400 and 11900 cm^{-1}. J. Mol.

Spectrosc. 242, 2007; 1.

[26] O. V. Naumenko, O. M. Leshchishina, S. Béguier, and A. Campargue. Intracavity Laser Absorption Spectroscopy of D_2O between 12850 and 13380 cm^{-1}. J. Mol. Spectrosc. 252, 2008; 52.

[27] A. Campargue, O.M. Leshchishina, O.V. Naumenko, $D_2{}^{16}O$: ICLAS between 13600 and 14020 cm^{-1} and normal mode labeling of the vibrational states, J. Mol. Spectrosc. 254, 2009; 1.

[28] S. V. Shirin, N. F. Zobov and O. L. Polyansky. Theoretical line list of $D_2{}^{16}O$ up to 16000 cm^{-1} with an accuracy close to experimental. J. Quant. Spectrosc. Radiat. Transfer. 109, 2008; 549.

[29] H. Partridge, D. W. Schwenke. The determination of an accurate isotope dependent potential energy surface for water from extensive ab initio calculations and experimental data. J. Chem. Phys. 106, 1997; 4618.

[30] D. W. Schwenke, H. Partridge Convergence testing of the analytic representation of an ab initio dipole moment function for water: improved fitting yields improved intensities. J Chem Phys 113, 2000; 6592.

[31] A. Campargue, E. Bertseva, O. Naumenko. The Absorption Spectrum of HDO in the 16300-16670 and 18000-18350 cm^{-1} Spectral Regions*,* J. Mol. Spectrosc. 204, 2000; 94.

[32] O.V. Naumenko, B.A. Voronin, F. Mazzotti, J. Tennyson, A. Campargue. Intracavity laser absorption spectroscopy of HDO between 12145 and 13160 cm^{-1}. J. Mol. Spectrosc. 248, 2008; 122.

[33] B.A. Voronin, O.V. Naumenko, M. Carleer, P.-F. Coheur, S. Fally, A. Jenouvrier, R.N. Tolchenov, A.C. Vandaele, J. Tennyson. HDO absorption spectrum above 11500 cm^{-1}: Assignment and dynamic. J. Mol. Spectrosc. 244, 2007; 87.

[34] M. Bach, S. Fally, P.-F. Coheur, M. Carleer, A. Jenouvrier, A. C. Vandaele. Line parameters of HDO from high-resolution Fourier transform spectroscopy in the 11500-23000 cm^{-1} spectral region. J. Mol. Spectrosc. 232, 2005; 341.

[35] A. Jenouvrier, M. F. Mérienne, M. Carleer, R. Colin, A.- C. Vandaele, P. F. Bernath, O. L. Polyansky, and J. Tennyson. The Visible and Near Ultraviolet Rotation-Vibration Spectrum of HOD. J. Mol. Spectrosc. 209, 2001; 165.

[36] P.-F. Coheur, S. Fally, M. Carleer, C. Clerbaux, R. Colin, A. Jenouvrier, M. -F. Mérienne, C. Hermans, A. C. Vandaele New water vapor line parameters in the 26000–13000 cm^{-1} region. J. Quant. Spectrosc. Radiat. Transfer 74**,** 2002; 493.

[37] S. Fally, P. -F. Coheur, M. Carleer, C. Clerbaux, R. Colin, A. Jenouvrier, M. -F. Mérienne, C. Hermans, A.C. VandaeleWater vapor line broadening and shifting by air in the 26000–13000 cm^{-1} region. J. Quant. Spectrosc. Radiat. Transfer 82**,** 2003; 119.

[38] M.-F. Mérienne, A. Jenouvrier, M. Carleer, P. -F. Coheur, R. Colin, S. Fally, C. Hermans, A. C. Vandaele, M. Bach. Water vapor line parameters in the 13000–9250 cm^{-1} region. J. Quant. Spectrosc. Radiat. Transfer 89**,** 2003; 99.

[39] S. V. Shirin, N. F. Zobov, O. L. Polyansky, J. Tennyson, T. Parekunnel and P.F. Bernath. Analysis of hot D_2O emission using spectroscopically determined potentials. J. Chem. Phys. 120, 2004; 206.

[40] S. A. Tashkun, private communication.

[41] G. Ch. Mellau, S. N. Mikhailenko, E. N. Starikova, S. A. Tashkun, H. Over, and Vl. G. Tyuterev. Rotational levels of the (000) and (010) states of $D_2{}^{16}O$ from hot emission spectra in the 320-860 cm^{-1} region. J. Mol. Spectrosc. 224**,** 2004; 32.

[42] S. N. Mikhailenko, G. Ch. Mellau, E. N. Starikova, S. A. Tashkun, Vl. G. Tyuterev. Analysis of the first triad of interacting states (020), (100), and (001) of $D_2{}^{16}O$ from hot emission spectra. J. Mol. Spectrosc. 233**,** 2005; 32.

[43] N. Papineau, J.M. Flaud, C. Camy-Peyret, G. Guelachvili. The $2\nu_2$, ν_1, and ν_3 bands of $D_2{}^{16}O$. The ground state (000) and the triad of interacting states (020), (100), (001)}. J. Mol. Spectrosc. 87, 1981; 219.

[44] R. A. Toth. $D_2{}^{16}O$ and $D_2{}^{18}O$ transition frequencies and strengths in the ν_2 bands. J. Mol. Spectrosc. 162, 1993; 41.

[45] N. F. Zobov, R. I. Ovsannikov, S. V. Shirin, O. L. Polyansky, J. Tennyson, A. Janka and P. F. Bernath. Infrared emission spectrum of hot D_2O. J. Mol. Spectrosc. 240, 2006; 112.

[46] L. Halonen, T. Carrington. Fermi resonances and local modes in water, hydrogen sulfide, and hydrogen selenide. J. Chem. Phys. 88,1998; 4171.

[47] L. S. Rothman, D. Jacquemart, A. Barbe, D. C. Benner, M. Birk, L. R. Brown, et al. The HITRAN 2004 molecular spectroscopic database. J. Quant. Radiat. Transfer. 96, 2005; 139.

[48] N. Jacquinet-Husson, N.A. Scott, A. Chédin, L. Crépeau, R. Armante, V. Capelle, J. Orphal, A. Coustenis, C. Boonne, N. Poulet-Crovisier, A. Barbe, M. Birk, L.R. Brown, C. Camy-Peyret, C. Claveau, K. Chance, N. Christidis, C. Clerbaux, P.F. Coheur, V. Dana, et al. The GEISA spectroscopic database: Current and future archive for Earth and planetary atmosphere studies. J. Quant. Spectrosc. Radiat. Transfer. 109, 2008; 1043.

[49] N. F. Zobov, O. L. Polyansky, V. A. Savin, and S. V. Shirin. Atmos. Assignment of quantum numbers to calculated highly exited energy levels of water molecule. Oceanic Opt. 13, 2000; 1024.

[50] N. F. Zobov, R. I. Ovsyannikov, S. V. Shirin, and O. L. Polyansky. The assignment of quantum numbers in the theoretical spectra of the $H_2\ ^{16}O$, $H_2\ ^{17}O$, and $H_2\ ^{18}O$ molecules calculated by variational methods in the region 0–26000 cm^{-1}. Optics and Spectroscopy 102, 2007; 394.

[51] A. D. Bykov, Yu. S. Makushkin, and O. N. Ulenikov. The vibrational analysis of $H_2{}^{16}O$. J. Mol. Spectrosc. 99, 1983; 221.

[52] O. V. Naumenko and A. Campargue. $H_2{}^{32}S$: First observation of the $(70^{\pm},0)$ local mode pair and updated global effective vibrational Hamiltonian. J. Mol. Spectrosc. 210, 2001; 224.

[53] P. S. Ormsby, K. N. Rao, M. Winnewisser, B. P. Winnewisser, A. D. Bykov, O. V. Naumenko, L. N. Sinitsa. The $3\nu_2 + \nu_3$, $\nu_1 + \nu_2 + \nu_3$, $\nu_1 + 3\nu_2$, $2\nu_1 + \nu_2$, and $\nu_2 + 2\nu_3$ bands of $D_2{}^{16}O$: The second hexade of interacting states. J. Mol. Spectrosc. 158, 1993; 109.

[54] X.-H. Wang, O.N. Ulenikov, G.A. Onopenko, E.S. Bekhtereva, S.-G. He, S.-M. Hu, H. Lin, Q.-S. Zhu. High-resolution study of the first hexad of D_2O. J. Mol. Spectrosc. 200, 2000; 25.

[55] A. D. Bykov, O. V. Naumenko, L. N. Sinitsa, B. P. Winnewisser, M. Winnewisser, P.S. Ormsby, K.N. Rao The hot band $v_1+2v_2+v_3-v_2$ of $D_2{}^{16}O$. J. Mol. Spectrosc.166, 1994; 169.

[56] A. Bykov, O. V. Naumenko, L. Sinitsa, B. Voronin, B. P. Winnewisser. The $3\nu_2$ band of $D_2{}^{16}O$. J. Mol. Spectrosc. 199, 2000; 158.

[57] S.-G. He, O. N. Ulenikov, G.A. Onopenko, E.S. Bekhtereva, X.-H. Wang, S.-M. Hu, H. Lin, Q.-S. Zhu. High-Resolution Fourier Transform Spectrum of the D_2O Molecule in the Region of the Second Triad of Interacting Vibrational States. J. Mol. Spectrosc. 200, 2000; 34.

[58] R. Meier, T. C. Owen, H.E. Matthews, D.C. Jewitt, D. Bockelée-Morvan, N. Biver, J. Crovisier, D. Gautier. A determination of the HDO/H2O ratio in Comet C/1995 O1 (Hale-Bopp). Science. 279, 1998; 842.

[59] O.V. Naumenko, O. Leshchishina, A. Campargue. High sensitivity absorption spectroscopy of HDO by ICLAS-VeCSEL between 9100 and 9640 cm^{-1}. J. Mol. Spectrosc. 236, 2006; 58.

[60] O.V. Naumenko, S. Béguier, O.M. Leshchishina, A. Campargue. ICLAS of HDO between 13020 and 14115 cm^{-1}. J. Quant. Spectrosc. Radiat. Transfer. 111, 2010; 36.

[61] O. Naumenko, A. Campargue. High-order resonance interactions in HDO: Analysis of the absorption spectrum in the 14980–15350 cm^{-1} spectral region. J. Mol. Spectrosc. 199, 2000; 59.

[62] E. Bertseva, O. Naumenko, A. Campargue. The absorption spectrum of HDO around 1.0 mkm by ICLAS-VECSEL. J. Mol. Spectrosc. 221, 2003; 38.

[63] A. Jenouvrier, M.-F. Merienne, M. Carleer, R. Colin, A.C. Vandaele, P. Bernath, O. Polyansly, J. Tennyson. The Visible and Near Ultraviolet Rotation-Vibration Spectrum of HOD. J. Mol.Spectrosc. 209, 2001; 165.

[64] O. Naumenko, S.-M. Hu, S.-G. He, A. Campargue. Rovibrational analysis of the absorption spectrum of HDO between 10 110 and 12 215 cm^{-1}. Phys. Chem. Chem. Phys. 6, 2004; 910.

[65] E. Bertseva, O. Naumenko, A. Campargue. The $5V_{OH}$ Overtone Transition of HDO. J. Mol. Spectrosc. 203, 2000; 28.

[66] S. Hu, H. Lin, S. He, J. Cheng, Q. Zhu. Fourier-transform intra-cavity laser absorption spectroscopy of HOD v_{OD} overtone = 5. Phys. Chem. Chem. Phys. 1, 1999; 3727.

[67] O. Naumenko, E. Bertseva, A. Campargue, D.W. Schwenke. Experimental and ab initio studies of the HDO absorption spectrum in the 13165-13500 cm^{-1} spectral region. J. Mol. Spectrosc. 201, 2000; 297.

[68] O. Naumenko, E. Bertseva, A. Campargue. The $4V_{OH}$ absorption spectrum of HDO. J. Mol. Spectrosc. 197, 1999; 122.

[69] A. Campargue, E. Bertseva, O. Naumenko. The absorption spectrum of HDO in the 16300-16670 and 18000-18350 cm^{-1} spectral regions. J. Mol. Spectrosc. 204, 2000; 94.

[70] O. N. Ulenikov, S.-M. Hu, E. S. Bekhtereva and Q.-S. Zhu. High-resolution ro−vibrational spectroscopy of HDO in the region 8900-9600 cm^{-1}. J. Mol. Spectrosc. 231, 2005; 57.

[71] M. Bach, S. Fally, P.−F. Coheur, M. Carleer, A. Jenouvrier, and A. C. Vandaele. Line parameters of HDO from high-resolution Fourier transform spectroscopy in the 11500−23000 cm^{-1} spectral region. J. Mol. Spectrosc. 232, 2005; 329.

[72] A. Campargue, I. Vasilenko and O. Naumenko. Intracavity laser absorption spectroscopy of HDO between 11 645 and 12 330 cm^{-1}. J. Mol. Spectrosc. 234, 2005; 216.

[73] T. M. Petrova, L. N. Sinitsa, A. M. Solodov. H_2O lines shifts measurements in 1:06 μm region. SPIE 2008; 6936, 93602.

[74] R. Tolchenov, J. Tennyson. Water line parameters from refitted spectra constrained by empirical upper state levels: Study of the 9500–14 500 cm^{-1} region. J. Quant. Radiat. Transfer. 109, 2008; 559.

[75] E. Bertseva, A. Campargue. Spectral condensation near molecular transitions in ICLAS-VECSEL. Optics Com. 232, 2004; 251.

[76] R. N. Tolchenov, J. Tennyson, S. V. Shirin, N. F. Zobov, O. L. Polyansky and A. N. Maurellis. Water line parameters for weak lines in the range 9000-12700 cm^{-1}. J. Mol. Spectrosc. 221, 2003; 99.

[77] R. Toth. $HD^{16}O$, $HD^{18}O$, and $HD^{17}O$ transition frequencies and strengths in the ν_2 bands. J. Mol. Spectrosc. 162, 1993; 20.

[78] O. V. Naumenko, S. Voronina, S.−M. Hu, High resolution Fourier transform spectrum of HDO in the 7500-8200 cm^{-1} region: revisited. J. Mol. Spectrosc. 227, 2004;151.

[79] S.–M. Hu, S. He, J. Zheng, X. Wang, Y. Ding and Q. Zhu Qing-shi. High-resolution analysis of the $\nu_2+2\nu_3$ band of HDO. Chinese Physics, 10, 2001; 1021.

[80] http://spectra.iao.ru/ (Schwenke/Partridge 296K).

[81] S. N. Yurchenko, B. A. Voronin, R. N. Tolchenov, N. Doss, O. V. Naumenko, W. Thiel, Tennyson J, Potential energy surface of HDO up to 25000 cm^{-1}. J Chem Phys. 128, 2008; 044312.

[82] B. A. Voronin, J. Tennyson, R. N. Tolchenov, A. A. Lugovskoy, S. N. Yurchenko. A high accuracy computed line list for the HDO molecule. Monthly Notices of the Royal Astronomical Society. 402, 2010; 492.

[83] J. M. Flaud, C. Camy-Peyret, A. Bykov, O.V. Naumenko, T. Petrova, A. Shcherbakov, L. N. Sinitsa. The High-resolution spectrum of water vapor between 11600 and 12750 cm^{-1}. J Mol Spectrosc. 183, 1997; 300.

[84] A. Bykov, O. Naumenko, L. Sinitsa, B. Voronin, J. M. Flaud, C. Camy–Peyret, R. Lanquetin. High-Order Resonances in the Water Molecule. J Mol Spectrosc. 205, 2001; 1.

[85] J. Tennyson, P. F. Bernath, L. R. Brown, A. Campargue, M. R. Carleer, A. G. Császár, et al. Critical evaluation of the rotational-vibrational spectra of water vapor. Part I. Energy levels and transition wavenumbers for $H_2{}^{17}O$ and $H_2{}^{18}O$. J Quant Radiat Transfer. 110, 2009; 573.

[86] J. Tennyson, P. F.Bernath, L. R. Brown, A. Campargue, M. R. Carleer, A. G. Császár et al. IUPAC Critical Evaluation of the Rotational-Vibrational Spectra of Water Vapor. Part II. Energy Levels and Transition Wavenumbers for $HD^{16}O$, $HD^{17}O$ and $HD^{18}O$. J. Quant . Radiat. Transfer. 111, 2010; 2160.

[87] A. Bykov, O. Naumenko, T. Petrova, A. Shcherbakov, L. Sinitsa, J.-Y. Mandin, et al. The second decade of $H_2{}^{18}O$: line positions and energy levels. J. Mol. Spectrosc. 172, 1995; 243.

[88] M. Tanaka, J. W. Brault, J. Tennyson. Absorption spectrum of $H_2{}^{18}O$ in the range 12 400–14 520 cm^{-1}. J Mol Spectrosc. 216, 2002; 77.

[89] M. Tanaka, O. Naumenko, J. W. Brault, J. Tennyson. Fourier transform absorption spectra of $H_2{}^{18}O$ and $H_2{}^{17}O$ in the $3\nu+\delta$ and 4ν polyad region. J Mol Spectrosc. 234, 2005; 1.

[90] F. Mazzotti, R. N. Tolchenov, A. Campargue. High sensitivity ICLAS of $H_2{}^{18}O$ in the region of the second decade (11520-12810 cm^{-1}). J Mol Spectrosc. 243, 2007; 78.

[91] L. S. Rothman, I. E. Gordon, A. Barbe, D. C. Benner, P.F. Bernath, M. Birk, et al. The HITRAN 2008 molecular spectroscopic database. J Quant Spectrosc. Radiat Transfer. 110, 2009; 533.

[92] S. V. Shirin, R. I. Ovsyannikov, N. F. Zobov, O. L. Polyansky, J. Tennyson. Water line lists close to experimental accuracy using a spectroscopically determined potential energy surfaces for $H_2{}^{16}O$, $H_2{}^{17}O$ and $H_2{}^{18}O$. J Chem Phys. 128, 2008; 2243061.

[93] O. M. Leshchishina, O.V. Naumenko, A. Campargue. High sensitivity ICLAS of $H_2{}^{18}O$ in the 12580–13550 cm^{-1} transparency window. J. Quant. Spectrosc. Radiat. Transfer 112, 2011; 913.

[94] O. M. Leshchishina, O.V. Naumenko, A. Campargue. High Sensitivity ICLAS of $H_2{}^{18}O$ between 13540 and 14100 cm^{-1}. J Mol Spectrosc. 2011, accepted.

[95] A. Campargue, S. N. Mikhailenko, A. W. Liu. ICLAS of water in the 770 nm transparency window (12746-13558 cm^{-1}). Comparison with FTS databases. J Quant Radiat Transfer 109, 2008; 2832.

[96] A. Campargue, F. Stoeckel, M. Chenevier. High sensitive intracavity laser spectroscopy: Application to the study of overtone transitions in the visible range. Spectrochimica Acta Reviews 13, 1990; 69.

[97] J.-P. Chevillard, J.-Y. Mandin, J.-M. Flaud, C. Camy-Peyret. The first hexad {(040), (120), (021), (200), (101), (002)} of $H_2{}^{18}O$: experimental energy levels and line intensities. Can. J. Phys. 64, 1986; 746.

[98] J.-P. Chevillard, J.-Y. Mandin, J.-M. Flaud, C. Camy-Peyret. $H_2{}^{18}O$: line positions and intensities between 9500 and 11 500 cm^{-1}. The (041), (220), (121), (201), (102), and (003) interacting states. Can. J. Phys. 65, 1987; 777.

[99] L.R. Brown, R.A. Toth, M. Dulick. Empirical line parameters of $H_2{}^{16}O$ near 0.94 µm: positions, intensities and air-broadening coefficients. J.Mol.Spectrosc. 212, 2002: 57.

[100] T. Furtenbacher, A. G. Császár, J. Tennyson. MARVEL: measured active rotational–vibrational energy levels. J Mol Spectrosc 245, 2007; 115.

[101] A. G. Császár, G. Czakó, T. Furtenbacher T, E. Mátyus. Chapter 9 An Active Database Approach to Complete Rotational–Vibrational Spectra of Small Molecules. Ann Rep Comput. Chem. 3, 2007; 155.

[102] O. M. Leshchishina, O. V. Naumenko, A. Campargue. High Sensitivity ICLAS of $H_2{}^{18}O$ between 13540 and 14100 cm^{-1}. Proceedings of XVII International Symposium “Atmospheric and Ocean Optics. Atmospheric Physics”, Tomsk, 2010.

[103] Y. Y. Kwan. The interacting states of an asymmetric top molecule XY_2 of the group C_{2V}. J Mol Spectrosc. 71, 1978; 260.

[104] A. D. Bykov, B. A.Voronin, O. V. Naumenko, T. M. Petrova, L. N. Sinitsa. Spectroscopic constants of the (011), (200), (120), and (040) states of the $HD^{16}O$ molecule. Atmosph. and Oceanic optics J. 12, 1999; 786.

[105] A. D. Bykov, O. V. Naumenko, T. M. Petrova, L. N. Sinitsa. Theoretical analysis of the $2\nu_3$ absorption band of $HD^{16}O$. Atmosph. and Oceanic optics J. 11, 1998; 1099.

[106] A. D. Bykov, V. A. Kapitanov, S. M. Kobtsev, O. V. Naumenko. Detection and analysis of the $5\nu_3$ absorption band in $HD^{16}O$. Atmosph. and Oceanic optics J. 3, 1990; 133.

[107] L. Anwen, O. Naumenko, S. Kassi, A. Campargue. High sensitivity CW-CRDS of ^{18}O enriched water near 1.6 μm. J Quant Radiat Transfer. 110, 2009; 1781.

Conclusion

The investigations presented in this thesis allowed us to obtain important and original results for two major atmospheric species – water and oxygen – for which the current status of knowledge is not sufficient to fulfil the needs of atmospheric sciences.

The study of the very weak $a^1\Delta_g - X^3\Sigma_g^-$ system of molecular oxygen was initially motivated by the first detection of electric quadrupole transitions in the atmospheric solar spectrum, showing the necessity to improve the spectral parameters of the $a^1\Delta_g - X^3\Sigma_g^-$ band of molecular oxygen from the new laboratory measurements. The very high sensitivity CW-Cavity Ring Down Spectroscopy technique was used to record the absorption spectrum of the $a^1\Delta_g - X^3\Sigma_g^-$ band of six oxygen isotopologues near $1.27\ \mu\text{m}$ at room temperature and at 80 K. The spectra were obtained between 7640 and 7917 cm^{-1} with “natural” oxygen and with samples highly enriched in ^{18}O and ^{17}O. The magnetic dipole-allowed $a^1\Delta_g - X^3\Sigma_g^-$ (0-0) band was observed for $^{16}O_2$, $^{16}O^{18}O$, $^{16}O^{17}O$, $^{17}O^{18}O$, $^{18}O_2$ and $^{17}O_2$ species. The achieved experimental sensitivity (noise equivalent absorption $\alpha_{\min} \sim 5\times10^{-11}$ cm^{-1}) allowed for the first laboratory detection of

- *(i)* the $a^1\Delta_g - X^3\Sigma_g^-$ (1-1) hot band of $^{16}O_2$, $^{18}O_2$, $^{16}O^{17}O$ and $^{17}O_2$ which has a relative intensity of about 5×10^{-4} compared to the (0-0) band,
- *(ii)* extremely weak quadrupole transitions in the $a^1\Delta_g - X^3\Sigma_g^-$ (0-0) band of $^{18}O_2$, $^{16}O^{17}O$ and $^{17}O_2$,
- *(iii)* the partly resolved hyperfine structure of the $a^1\Delta_g - X^3\Sigma_g^-$ transitions of the three ^{17}O containing isotopologues – $^{16}O^{17}O$, $^{17}O^{18}O$ and $^{17}O_2$.

The results presented here provide valuable information for improving the HITRAN line list both in terms of accuracy and completeness. Indeed, the intensities of the $a^1\Delta_g - X^3\Sigma_g^-$ (1-1) band of $^{16}O_2$ and the $a^1\Delta_g - X^3\Sigma_g^-$ (0-0) band of $^{16}O^{17}O$ measured in this work are comparable with those of the $^{16}O_2$ electric quadrupole transitions that, as recently shown, are important for improving atmospheric retrievals and also need to be accounted for. The parameters measured in this study can be used to generate line lists and update and extend the present HITRAN line list by including bands just discussed above and lowering the intensity cut off.

The line intensities for $^{16}O^{18}O$ measured here, constitute an important contribution to the HITRAN database, where so far their values required improvements. The lack of proper experimental input parameters for $^{16}O^{18}O$ was the main reason for the limited quality of line intensities in the $a^1\Delta_g - X^3\Sigma_g^-$ band for this species in HITRAN.

The spectroscopic fit of the line positions measured in this work, combined with microwave and Raman measurements available in the literature provides the best to date set of spectroscopic constants for the $a^1\Delta_g$ and $X^3\Sigma_g^-$ states. For the $^{17}O^{18}O$ species, the $a^1\Delta_g$ parameters were determined for the first time. Moreover, improved ground state constants (in particular centrifugal distortion) were obtained for the $^{16}O^{17}O$ and $^{17}O^{18}O$ isotopologues. The spectroscopic constants of the $a^1\Delta_g$ $(\upsilon = 0,1)$ states of $^{17}O_2$ including hyperfine coupling parameter are derived for the first time.

The accuracy of the spectroscopic parameters of the $a^1\Delta_g$ state of ^{17}O containing isotopologues obtained in our study has been recently experimentally verified. The research team of B. Drouin at Jet Propulsion Laboratory has very recently measured microwave transitions in the $a^1\Delta_g$ state of ^{17}O containing isotopologues of oxygen. According to them, the predictions of the hyperfine transitions using our constants were much better than they expected in view of the partly resolved hyperfine structure observed in our CRDS spectra. Despite the fact that they could actually resolve all the hyperfine components, they could not really improve much the *a* coupling constant we reported, they could only reduce the uncertainty on that parameter.

The second main topic of this thesis was the study of the spectrum of the minor isotopologues of water- $H_2{}^{18}O$, $HD^{16}O$ and $D_2{}^{16}O$.

Theoretical analysis of the weak absorption lines of water isotopologues $D_2{}^{16}O$, $HD^{16}O$ and $H_2{}^{18}O$ has been performed over a wide spectral region between 8800 and 14100 cm^{-1} based on the high accuracy variational calculations. The D_2O and $H_2{}^{18}O$ spectra in the 12800-14100 cm^{-1} and 12707-13364 cm^{-1} ranges, respectively, have been investigated for the first time. It is worth noting that the 13500-14200 cm^{-1} range is the most excited spectral region reported so far for the $D_2{}^{16}O$ species.

Extensive sets of experimental energy levels have been derived: 2356 for $D_2{}^{16}O$, 1317 for $HD^{16}O$ and 1306 for $H_2{}^{18}O$. 2086, 457 and 780 of them are new respectively. New information concerns rotational structure of the 17 vibrational states reported for the first time, and, in total, transitions coming on 123 highly excited upper states have been identified.

The modelling of the derived experimental energy levels within the frame of the effective Hamiltonian approach has been undertaken to establish the correct rovibrational labelling. The effective rotational Hamiltonian in the Padé-Borel form has been used to avoid the divergence problem. The newly determined energy levels for the $D_2{}^{16}O$ molecules have been used for optimization of $D_2{}^{16}O$ PES (Shirin et al., 2008). Despite the high accuracy of variational computations used in the assignment process, a number of the experimental energy levels presently derived deviate from their variational estimates by up to 0.4 cm^{-1}. This discrepancy is well above the *rms* deviation achieved in global variational calculations (0.02-0.04 cm^{-1}) and therefore the newly obtained energy levels can serve for further refinement of variational linelists.

Due to a high sensitivity of the experimental setup used, 264 and 517 transitions belonging to $HD^{18}O$ and $H_2{}^{17}O$ molecules present in small concentration in the cell have also been detected and identified leading to the determination of 124 and 95 new energy levels for $HD^{18}O$ and $H_2{}^{17}O$, respectively, including those of the highest in energy (004) vibrational state of $HD^{18}O$ at 13814.526 cm^{-1}.

All the newly derived vibrational energies of the $D_2{}^{16}O$ and $H_2{}^{18}O$ molecules combined with available literature data were introduced in a least squares fit to refine the parameters of spectroscopic vibrational Hamiltonian, and the consistent vibrational labelling has been established for vibrational states up to 20000 cm^{-1}. The limit of validity of the normal mode notations has been estimated for the $D_2{}^{16}O$ molecule. It turned out that the normal mode labelling becomes ambiguous and should be used with caution above 15000 cm^{-1}. Comparison of the resulting EH pure vibrational and rovibrational labels with those provided by variational calculations has shown that variational labels are often either ambiguous (SP 1997, 2000) or unreasonable (Shirin et al., 2008). According to variational calculations performed by Shirin et al., relatively strong transitions may be attributed to the highly excited bending states, or may involve upper and lower states with large difference in K_a and K_c values (up to 12). However, intensities of such transitions are predicted by conventional theory to be negligibly small. More than 25% of rovibrational labels have been corrected in comparison with variational data (Shirin et al., 2008) for $D_2{}^{16}O$ molecule.

Intramolecular dynamics of the water isotopologues of interest has been investigated based on extensive set of experimental energy levels and assigned transitions. The resonance interactions which are the corner stone of the EH approach, are not explicitly accounted for in variational approach. However, perturbations affecting both positions and intensities were found to be linked to EH high-order close resonances and the agreement proved to depend mainly on the PES employed. Not only close, but also distant (with the energy difference as large as 60 cm^{-1}) high-order resonance interactions in the EH scheme explain important redistribution of variational intensity from the stronger lines to their otherwise negligibly weak lines– resonance- counterparts. A number of transitions attributed to the highly excited bending states like (160), (061), (170), (071), (080), (090), and even (0 10 0), (0 11 0) could be assigned in the experimental spectra of $HD^{16}O$ and $H_2{}^{18}O$, as they were strengthened due to close and distant resonances with stronger vibrational bands. In particular, a remarkable set of 55 experimental energy levels has been obtained for the (070) energy levels of $HD^{16}O$ molecule from transitions stealing intensities from the $\nu_1 + 2\nu_2 + \nu_3$, $4\nu_2 + \nu_3$ and $3\nu_1 + \nu_2$ bands.

Finally, large sets of synthetic transitions have been generated for all considered isotopologues in the 6100–15200 cm^{-1} spectral region. Accurate transition wavenumbers obtained as a difference between the experimental energies of upper and lower rovibrational states derived in this study and available from the literature, were augmented with variational intensities. These sets of transitions can serve (*i*) as reference spectra for calibration and trivial assignment, as they have the best accuracy in wavenumbers presently achieved; (*ii*) for investigation of the line shape, as they include all components of the quasidegenerate lines which cannot be resolved experimentally; (*iii*) for further optimization of the variational PES, as they incorporate all published experimental energy levels; (*iv*) for atmospheric and astrophysics applications, as they exceed the HITRAN-2008 and IUPAC-TG line lists of the considered isotopologues both in completeness and in accuracy.

Appendix A.1. Rovibrational energy levels of the $D_2^{16}O$ molecule derived from analysis of the FT spectrum between 10000 and 13200 cm^{-1} [24].

Note: ΔE means the RMS uncertainty of the level derived from a CD of 2 and more lines in 10^{-3} cm^{-1}. ΔE sets to 0.0 in case of the energy level derived from one line.

VIB	J	Ka	Kc	Energy	ΔE	N
				cm^{-1}	10^{-3} cm^{-1}	
103	1	0	1	10691.3898	0.01	2
103	1	1	0	10700.5634	0.66	2
103	2	0	2	10714.2283	0.00	1
103	2	1	2	10719.0534	0.34	2
103	2	1	1	10726.4332	0.09	2
103	2	2	1	10746.5013	0.00	1
103	2	2	0	10747.0629	0.28	2
103	3	0	3	10747.2423	0.35	2
103	3	1	3	10750.1512	0.22	2
103	3	1	2	10764.8082	0.04	2
103	3	2	2	10781.6512	0.00	1
103	3	2	1	10784.2783	0.79	3
103	3	3	1	10821.3187	0.00	1
103	3	3	0	10821.4038	0.54	2
103	4	0	4	10789.5984	0.22	2
103	4	1	4	10791.1280	0.00	1
103	4	1	3	10815.0741	0.16	2
103	4	2	3	10828.0322	0.00	1
103	4	2	2	10835.0319	0.00	1
103	4	3	2	10869.1794	0.35	3
103	4	3	1	10869.7386	1.95	2
103	4	4	1	10922.9564	1.21	2
103	4	4	0	10922.9597	7.81	2
103	5	0	5	10840.9739	0.74	2
103	5	1	5	10841.6037	3.85	2
103	5	1	4	10876.3248	0.20	2
103	5	2	4	10885.2665	0.29	3
103	5	2	3	10899.1704	0.12	2
103	5	3	2	10931.0205	0.00	1
103	5	4	2	10983.0618	0.22	2
103	5	4	1	10983.1504	0.08	2
103	5	5	1	11051.1405	0.00	1
103	5	5	0	11051.1462	0.00	1
103	6	0	6	10901.3878	0.22	2
103	6	1	6	10901.6139	0.00	1
103	6	1	5	10947.5091	0.00	1
103	6	2	5	10952.9382	0.00	1
103	6	2	4	10976.0003	0.52	2
103	6	3	4	11000.5356	2.03	2
103	6	3	3	11005.9646	2.13	2
103	6	4	3	11055.3502	0.45	2
103	6	4	2	11055.7591	1.11	2
103	6	5	2	11123.6489	0.00	1
103	6	5	1	11123.6432	0.00	1
103	6	6	1	11205.4342	1.97	2
103	6	6	0	11205.4344	1.77	2
103	7	0	7	10970.9649	0.74	2
103	7	1	7	10970.9422	0.07	2
103	7	1	6	11027.8697	0.28	2
103	7	2	6	11030.6666	1.15	2
103	7	3	5	11083.4526	1.91	2
103	7	3	4	11094.7552	0.69	2
103	7	4	4	11139.7695	0.00	1
103	7	4	3	11141.1155	0.68	3
103	7	5	3	11208.3118	0.00	1
103	7	5	2	11208.1724	0.48	2
103	7	6	2	11291.1369	0.00	1
401	5	3	2	12992.2697	1.20	3
401	5	4	1	13047.4843	2.86	2
401	5	5	1	13120.4634	0.00	1
401	5	5	0	13120.4629	0.00	1
401	6	0	6	12960.8967	2.03	2
401	6	1	6	12961.2801	1.87	2
401	6	1	5	13003.9505	6.73	2
401	6	2	5	13011.6448	2.92	2
401	6	2	4	13033.8852	0.00	1
401	6	3	4	13060.0986	0.15	2
401	6	3	3	13064.9186	0.00	1
401	6	4	3	13117.4922	0.00	1
401	6	5	2	13190.4285	0.54	2
401	6	5	1	13190.4260	2.57	2
401	6	6	1	13227.0389	0.00	1
401	6	6	0	13227.0388	0.00	1
401	7	0	7	13028.9571	2.74	2
401	7	1	7	13029.0694	0.00	1
401	7	1	6	13086.2778	2.46	2
401	7	2	6	13087.8450	2.20	2
401	7	2	5	13120.4225	2.84	2
401	7	3	5	13140.8817	0.00	1
401	7	3	4	13151.0946	2.76	2
401	7	4	3	13200.5798	0.00	1
401	8	0	8	13106.1362	6.57	2
401	8	1	8	13106.2548	1.51	2
401	8	1	7	13173.1890	0.00	1
401	8	2	7	13173.7944	0.00	1
401	8	3	6	13232.5364	0.00	1
401	8	3	5	13250.9163	0.00	1
401	8	4	5	13293.2135	0.00	1
401	8	8	1	13649.9674	0.00	1
401	8	8	0	13649.9675	0.00	1
401	9	0	9	13192.1844	0.00	1
401	9	1	8	13269.9180	0.00	1
401	9	2	8	13269.2757	0.00	1
401	9	3	7	13334.6527	0.00	1
401	10	0	10	13287.4731	0.00	1
401	10	1	10	13287.4624	0.00	1
401	10	2	9	13373.3432	0.00	1
401	11	0	11	13391.5929	7.13	2
401	11	1	11	13391.6073	2.65	2
221	0	0	0	10180.1165	0.00	1
221	1	0	1	10191.9118	0.91	2
221	1	1	1	10201.4213	0.00	1
221	1	1	0	10204.0985	0.31	2
221	2	0	2	10214.9911	0.79	2
221	2	1	2	10222.6563	0.52	3
221	2	1	1	10230.4683	0.68	3
221	2	2	1	10258.7477	4.61	2
221	2	2	0	10259.2303	0.46	2
221	3	0	3	10248.4653	0.70	2
221	3	1	3	10251.4536	3.33	2
221	3	1	2	10269.5465	0.01	2
221	3	2	2	10293.5684	0.11	2
221	3	2	1	10295.8253	0.10	3
221	3	3	1	10347.8282	0.00	1

Appendix A.1 (continued)

VIB	J	Ka	Kc	Energy	ΔE	N
				cm^{-1}	$10^{-3}\ \mathrm{cm}^{-1}$	
103	7	6	1	11291.1365	0.00	1
103	7	7	1	11385.2753	0.00	1
103	7	7	0	11385.2754	0.00	1
103	8	0	8	11049.9916	1.82	2
103	8	1	8	11049.6243	0.08	2
103	8	1	7	11117.2243	0.19	2
103	8	2	7	11118.1272	0.48	2
103	8	2	6	11161.3817	0.00	1
103	8	3	6	11177.3307	0.00	1
103	8	3	5	11197.0524	0.00	1
103	8	4	5	11236.1555	0.14	2
103	8	4	4	11239.9635	0.68	2
103	8	5	3	11305.8844	0.00	1
103	8	6	3	11388.9308	0.00	1
103	8	7	2	11487.1006	0.00	1
103	8	7	1	11487.1003	0.00	1
103	9	0	9	11134.4190	0.00	1
103	9	1	9	11138.3899	1.04	2
103	9	1	8	11216.1982	0.00	1
103	9	2	8	11215.1917	0.00	1
103	9	3	7	11281.5582	0.00	1
103	9	3	6	11311.9738	0.00	1
103	9	4	6	11344.2126	0.00	1
103	9	4	5	11352.3045	0.00	1
103	9	5	5	11414.0510	2.12	2
103	9	6	4	11499.7074	0.00	1
103	9	7	3	11598.6462	1.34	2
103	9	7	2	11598.6462	1.68	2
103	9	8	2	11691.6034	0.00	1
103	9	8	1	11691.6030	0.00	1
103	10	0	10	11233.5622	0.00	1
103	10	1	10	11232.7243	0.05	2
103	10	1	9	11314.9921	0.00	1
103	10	3	8	11395.8791	3.19	2
103	10	4	7	11463.5060	0.00	1
103	10	4	6	11478.5749	0.00	1
103	10	5	6	11534.9432	0.00	1
103	10	6	4	11620.1628	0.00	1
103	10	8	3	11807.0036	0.00	1
103	10	8	2	11807.0037	0.00	1
103	11	0	11	11339.3750	0.00	1
103	11	1	11	11339.2319	0.00	1
103	11	3	9	11518.7342	0.00	1
103	11	3	8	11574.3947	0.00	1
103	11	4	7	11617.9360	0.00	1
103	12	0	12	11454.5750	0.00	1
103	12	1	12	11454.5774	0.00	1
103	12	1	11	11556.5345	0.00	1
103	12	4	8	11770.3351	0.00	1
103	12	6	7	11895.8382	0.00	1
103	13	0	13	11578.9030	0.00	1
103	13	1	13	11578.8746	0.00	1
103	13	1	12	11692.2998	0.00	1
103	13	2	11	11790.6714	0.00	1
103	13	5	8	11984.6102	0.00	1
103	14	2	13	11835.1974	0.00	1
103	14	3	11	12037.8835	0.00	1
103	14	4	11	12051.2291	0.00	1
103	15	0	15	11854.7686	0.00	1
301	0	0	0	10358.5603	0.00	1
301	1	0	1	10370.2138	0.57	2
301	1	1	1	10377.3159	0.81	2
301	1	1	0	10379.7271	0.03	2
301	2	0	2	10392.9448	0.74	3
301	2	1	2	10397.8497	0.13	2
301	2	1	1	10404.2312	1.33	3
221	3	3	0	10347.8853	0.06	2
221	4	0	4	10291.3991	0.27	2
221	4	1	4	10293.6319	0.38	2
221	4	1	3	10320.8032	0.41	2
221	4	2	3	10339.7747	0.02	2
221	4	2	2	10345.6843	1.61	2
221	4	3	2	10395.3258	0.77	2
221	4	3	1	10395.7155	0.27	2
221	4	4	1	10468.6939	1.48	2
221	4	4	0	10468.7507	3.74	2
221	5	0	5	10343.2639	5.46	2
221	5	1	5	10344.4540	0.04	2
221	5	1	4	10383.4626	0.44	2
221	5	2	4	10397.1714	1.99	2
221	5	2	3	10408.3995	0.40	2
221	5	3	3	10454.8017	0.02	2
221	5	3	2	10456.2756	0.47	2
221	5	4	2	10528.1354	0.02	2
221	5	4	1	10528.2827	0.21	2
221	5	5	1	10620.6049	2.52	2
221	5	5	0	10620.6075	0.59	2
221	6	0	6	10403.9659	0.00	1
221	6	1	6	10404.5284	1.07	2
221	6	2	5	10465.4775	2.07	2
221	6	2	4	10493.2689	1.07	2
221	6	3	4	10526.1363	0.05	2
221	6	3	3	10530.1796	0.43	2
221	6	4	3	10599.5820	0.65	2
221	6	4	2	10600.0687	0.66	2
221	6	5	2	10691.9304	0.00	1
221	6	5	1	10691.9247	0.00	1
221	6	6	1	10802.1772	0.93	2
221	6	6	0	10802.1774	1.13	2
221	7	0	7	10473.5638	1.65	2
221	7	1	7	10473.8089	1.26	2
221	7	1	6	10538.9842	0.02	2
221	7	2	6	10544.2575	1.64	2
221	7	2	5	10582.1700	0.64	2
221	7	3	5	10609.0602	0.59	3
221	7	3	4	10617.9197	0.13	2
221	7	4	4	10682.6354	0.90	2
221	7	4	3	10684.3846	0.07	2
221	7	5	3	10775.3852	0.00	1
221	7	5	2	10775.4231	0.23	2
221	7	6	2	10885.0525	0.00	1
221	7	6	1	10885.1703	0.65	3
221	7	7	1	11011.3414	0.00	1
221	7	7	0	11011.3415	0.00	1
221	8	1	8	10552.2167	0.00	1
221	8	1	7	10630.1903	0.66	2
221	8	2	7	10633.0367	0.27	2
221	8	2	6	10683.1599	0.00	1
221	8	3	6	10704.6944	2.63	2
221	8	3	5	10719.4693	0.67	2
221	8	4	5	10778.1106	0.73	2
221	8	4	4	10781.6315	3.28	3
221	8	5	3	10871.7406	1.17	2
221	8	6	3	10980.2768	0.00	1
221	8	6	2	10980.2524	0.00	1
221	8	7	2	11105.4190	0.00	1
221	8	7	1	11105.4194	0.00	1
221	9	0	9	10639.6536	0.88	2
221	9	1	9	10639.7320	0.00	1
221	9	1	8	10729.9578	0.60	2
221	9	2	8	10731.4297	1.15	2
221	9	2	7	10798.6846	0.59	2

Appendix A.1 (continued)

VIB	J	Ka	Kc	Energy	ΔE	N
				cm^{-1}	10^{-3} cm^{-1}	
301	2	2	1	10426.7609	0.03	2
301	2	2	0	10427.2777	0.00	1
301	3	0	3	10425.8242	0.31	3
301	3	1	3	10428.6258	0.08	2
301	3	1	2	10443.5560	0.27	2
301	3	2	2	10461.1673	0.62	3
301	3	2	1	10463.5827	0.42	3
301	3	3	1	10503.3981	0.15	2
301	3	3	0	10503.4689	0.29	2
301	4	0	4	10468.0159	0.74	3
301	4	1	4	10469.3529	0.09	2
301	4	1	3	10492.2049	0.17	3
301	4	2	3	10506.7016	0.32	3
301	4	2	2	10513.1164	0.09	2
301	4	3	2	10550.1450	0.20	3
301	4	3	1	10550.6269	0.22	3
301	4	4	1	10607.6523	0.51	2
301	4	4	0	10607.6558	6.61	2
301	5	0	5	10519.1640	0.59	2
301	5	1	5	10519.7126	0.09	2
301	5	1	4	10555.5723	0.14	2
301	5	2	4	10563.1258	0.42	3
301	5	2	3	10575.7526	0.85	3
301	5	3	3	10608.6482	0.66	2
301	5	3	2	10610.4469	0.69	4
301	5	4	2	10666.1852	0.47	3
301	5	4	1	10666.2589	0.85	3
301	5	5	1	10739.3118	2.22	2
301	5	5	0	10739.3144	0.89	2
301	6	0	6	10579.2721	0.80	3
301	6	1	6	10579.4680	0.78	3
301	6	1	5	10625.8792	0.27	2
301	6	2	5	10630.1680	0.33	3
301	6	2	4	10650.6966	0.96	4
301	6	3	4	10678.7604	0.85	4
301	6	3	3	10683.5633	0.60	2
301	6	4	3	10736.6702	1.00	3
301	6	4	2	10737.0118	0.27	3
301	6	5	2	10809.5415	0.21	2
301	6	5	1	10809.5160	14.52	2
301	6	6	1	10898.1290	0.68	2
301	6	6	0	10898.1291	0.88	2
301	7	0	7	10648.4197	0.63	3
301	7	1	7	10648.4655	0.36	2
301	7	1	6	10705.5344	1.78	4
301	7	2	6	10707.4896	1.15	3
301	7	2	5	10736.5849	0.90	3
301	7	3	5	10760.2352	0.70	2
301	7	3	4	10770.3098	0.01	2
301	7	4	4	10819.1193	0.05	2
301	7	4	3	10820.2743	2.40	3
301	7	5	3	10891.7044	0.75	2
301	7	5	2	10891.8769	0.42	2
301	7	6	2	10980.0906	1.62	2
301	7	6	1	10980.0925	0.70	2
301	7	7	1	11084.2787	1.04	2
301	7	7	0	11084.2789	0.96	2
301	8	0	8	10726.6609	0.36	2
301	8	1	8	10726.6746	2.75	2
301	8	1	7	10794.0373	0.25	2
301	8	2	7	10794.7047	0.45	3
301	8	2	6	10843.7654	0.13	2
301	8	3	6	10852.7885	0.49	2
301	8	3	5	10869.8885	0.52	3
301	8	4	5	10913.4507	0.13	2
301	8	4	4	10916.6520	0.67	2
221	9	3	7	10809.9520	0.88	2
221	9	3	6	10834.0258	0.00	1
221	9	4	6	10889.7921	2.47	2
221	9	4	5	10892.3117	2.29	2
221	9	5	5	10979.1794	0.00	1
221	9	5	4	10978.7343	0.57	2
221	9	6	3	11087.4857	0.00	1
221	9	9	1	11439.0593	0.00	1
221	9	9	0	11439.0593	0.00	1
221	10	0	10	10736.2660	5.10	2
221	10	1	10	10736.3263	0.16	2
221	10	2	9	10838.7352	0.00	1
221	10	2	8	10917.6735	0.00	1
221	10	4	7	11008.3916	0.00	1
221	10	4	6	11016.8075	0.00	1
221	10	7	4	11330.3258	1.37	2
221	10	7	3	11330.3222	0.00	1
221	10	8	3	11525.6835	0.00	1
221	10	8	2	11525.6836	0.00	1
221	11	0	11	10841.9127	0.00	1
221	11	1	11	10841.9369	0.00	1
221	11	1	10	10955.6124	0.00	1
221	11	4	8	11139.0909	0.00	1
221	11	5	7	11189.5163	2.08	2
221	12	0	12	10956.7587	1.36	2
221	12	1	12	10957.2203	0.00	1
221	12	1	11	11081.7921	0.00	1
221	12	2	11	11082.1886	0.00	1
221	12	3	9	11263.2968	0.00	1
221	13	1	12	11217.0960	0.00	1
221	13	6	7	11639.1452	0.00	1
221	14	0	14	11212.5905	0.00	1
221	14	1	14	11212.5929	0.00	1
400	1	0	1	10352.6129	0.00	1
400	1	1	1	10360.1815	0.13	2
400	2	0	2	10375.3291	9.47	2
400	2	1	2	10380.9028	0.00	1
400	2	1	1	10388.3659	1.35	2
400	3	0	3	10408.2607	6.79	2
400	3	1	3	10411.7496	0.00	1
400	3	1	2	10426.6179	0.00	1
400	3	2	2	10439.6127	0.50	3
400	3	3	1	10683.2957	0.00	1
400	3	3	0	10485.1172	0.00	1
400	4	0	4	10450.5913	0.88	2
400	4	1	4	10452.4661	0.00	1
400	4	1	3	10476.9440	0.00	1
400	4	2	3	10485.8845	0.00	1
400	4	2	2	10493.1317	0.00	1
400	4	3	2	10532.5557	0.00	1
400	4	4	1	10590.7466	2.60	2
400	4	4	0	10590.7501	1.37	2
400	5	0	5	10501.8845	0.00	1
400	5	1	5	10502.7783	0.81	2
400	5	2	4	10542.9032	1.25	3
400	5	3	3	10592.0541	6.24	2
400	5	3	2	10593.0911	0.00	1
400	5	4	2	10650.0239	0.00	1
400	5	4	1	10650.0643	3.41	2
400	5	5	1	10723.7053	0.00	1
400	5	5	0	10723.7052	0.00	1
400	6	0	6	10562.0672	0.00	1
400	6	1	6	10759.7025	0.00	1
400	6	1	5	10603.4276	0.00	1
400	6	2	5	10610.3189	0.00	1
400	6	3	4	10663.6714	0.00	1

Appendix A.1 (continued)

VIB	J	Ka	Kc	Energy cm^{-1}	ΔE 10^{-3} cm^{-1}	N
301	8	5	4	10985.8759	0.05	2
301	8	5	3	10986.1874	0.32	2
301	8	6	3	11073.9755	3.74	2
301	8	6	2	11073.9832	8.24	2
301	8	7	2	11178.2608	0.08	2
301	8	7	1	11178.2608	0.26	2
301	8	8	1	11300.0245	2.15	2
301	8	8	0	11300.0248	2.31	2
301	9	0	9	10814.0195	0.23	2
301	9	1	9	10814.0434	0.07	2
301	9	1	8	10891.3977	1.25	2
301	9	2	8	10891.4906	0.56	2
301	9	2	7	10951.1168	0.00	1
301	9	3	7	10956.1170	0.54	4
301	9	3	6	10983.7557	0.50	3
301	9	4	6	11019.4672	0.06	2
301	9	4	5	11026.5670	0.09	2
301	9	5	5	11092.0803	0.03	2
301	9	5	4	11092.8894	0.10	2
301	9	6	4	11179.8954	1.80	2
301	9	6	3	11179.8554	0.08	2
301	9	7	3	11283.5964	0.00	1
301	9	7	2	11283.6458	0.00	1
301	9	8	2	11365.1582	0.00	1
301	9	8	1	11365.1581	0.00	1
301	9	9	1	11503.5926	0.00	1
301	9	9	0	11503.5926	0.00	1
301	10	0	10	10910.4641	2.05	2
301	10	1	10	10910.4729	0.06	2
301	10	1	9	10997.8640	0.47	2
301	10	2	9	10997.6244	4.58	2
301	10	2	8	11066.2092	1.13	2
301	10	3	8	11068.7763	0.28	3
301	10	4	7	11136.8681	0.10	2
301	10	4	6	11150.3672	4.67	2
301	10	5	6	11210.2796	0.15	2
301	10	5	5	11212.3120	0.97	2
301	10	6	5	11298.1282	0.07	2
301	10	6	4	11297.8190	0.00	1
301	11	0	11	11016.0408	7.08	2
301	11	1	11	11016.0552	2.70	2
301	11	1	10	11112.8639	0.27	2
301	11	2	10	11113.1161	2.76	2
301	11	2	9	11191.9020	0.00	1
301	11	3	9	11191.4241	0.00	1
301	11	3	8	11256.5493	1.37	2
301	11	4	8	11265.2729	0.00	1
301	11	4	7	11287.6947	1.66	2
301	11	5	7	11340.3560	0.56	2
301	11	5	6	11344.9385	0.36	3
301	11	6	6	11428.6975	0.00	1
301	11	6	5	11428.0267	0.00	1
301	11	7	5	11531.2495	0.00	1
301	11	7	4	11531.2872	0.00	1
301	12	0	12	11130.7057	0.00	1
301	12	1	12	11130.7081	0.00	1
301	12	1	11	11232.1992	0.00	1
301	12	2	11	11238.0958	0.00	1
301	12	2	10	11326.9433	0.00	1
301	12	3	10	11327.2495	0.00	1
301	12	4	9	11403.8897	0.00	1
301	12	4	8	11437.6779	0.00	1
301	12	5	8	11481.8759	0.00	1
301	12	6	7	11568.7791	0.00	1
301	12	7	6	11673.0722	0.00	1
301	13	0	13	11254.5369	0.41	2
400	6	3	3	10666.4339	0.34	2
400	6	4	3	10721.2970	0.91	2
400	6	4	2	10721.4919	0.52	3
400	6	5	2	10794.7338	0.00	1
400	6	5	1	10794.7330	0.44	2
400	6	6	1	10883.7735	0.00	1
400	6	6	0	10883.7792	0.00	1
400	7	0	7	10631.3373	0.00	1
400	7	1	7	10631.4838	6.42	2
400	7	1	6	10885.3379	0.00	1
400	7	2	6	10888.7240	0.00	1
400	7	3	4	10753.2928	0.00	1
400	7	4	4	10804.5848	0.73	2
400	7	4	3	10805.2369	0.00	1
400	7	5	3	10877.7063	0.16	2
400	7	5	2	10877.6221	3.76	2
400	7	6	2	10966.6652	0.00	1
400	7	6	1	10966.6566	0.00	1
400	7	7	1	11070.0466	0.00	1
400	8	0	8	10709.9945	0.00	1
400	8	1	8	10907.0143	0.00	1
400	8	2	6	10819.7326	0.00	1
400	8	3	6	10832.0032	8.62	2
400	8	3	5	10853.6411	0.00	1
400	8	4	5	10899.8522	0.00	1
400	8	4	4	10901.5049	0.04	2
400	8	5	4	11170.8108	0.00	1
400	8	5	3	10971.6467	0.00	1
400	8	7	2	11165.2349	0.00	1
400	8	7	1	11163.5768	0.00	1
400	9	2	8	10871.5777	0.00	1
400	9	3	7	10936.8128	1.45	2
400	9	3	6	10966.9973	0.00	1
400	9	4	6	11007.0440	0.00	1
400	9	4	5	11011.5981	0.00	1
400	9	5	5	11079.4901	8.32	2
400	9	6	4	11167.8756	0.00	1
400	9	6	3	11168.1265	0.00	1
400	9	7	3	11272.9035	0.12	2
400	9	8	2	11394.7739	0.00	1
400	10	0	10	10893.1179	0.00	1
400	10	1	10	10893.0626	0.00	1
400	10	4	7	11125.9750	10.38	2
400	10	5	6	11383.3365	1.06	2
400	10	7	4	11390.9872	0.00	1
400	11	0	11	10998.5349	0.00	1
400	11	1	11	11198.2420	0.69	2
400	11	4	8	11241.9446	0.77	2
400	11	4	7	11271.6995	0.00	1
400	11	5	7	11509.7021	0.00	1
400	11	7	5	11519.1894	0.00	1
400	12	6	7	11560.0633	0.00	1
320	3	2	1	10255.6779	0.00	1
320	3	3	1	10308.0118	0.00	1
320	4	2	2	10304.7358	1.53	2
320	4	3	2	10356.5973	0.06	2
320	4	3	1	10356.4142	0.00	1
320	5	2	4	10355.2550	0.00	1
320	5	3	3	10418.0473	0.39	2
320	6	3	4	10482.5140	0.32	2
320	7	3	5	10567.0867	0.00	1
320	7	4	3	10648.8764	0.00	1
320	7	5	3	10743.0250	3.19	2
320	8	5	4	10839.4033	0.00	1
320	9	4	6	10854.3207	0.00	1
320	9	5	5	10947.6751	0.33	2

Appendix A.1 (continued)

VIB	J	Ka	Kc	Energy	ΔE	N
				cm^{-1}	10^{-3} cm^{-1}	
301	13	1	13	11254.4521	5.57	2
301	13	1	12	11371.2124	0.67	2
301	13	2	12	11365.5735	4.40	2
301	13	2	11	11470.1371	2.02	2
301	13	3	10	11558.9211	0.00	1
301	13	4	9	11599.0966	0.00	1
301	14	0	14	11387.2101	1.20	2
301	14	1	14	11387.2114	2.33	2
301	14	2	13	11514.2274	0.27	2
301	14	3	12	11621.5035	0.00	1
301	14	4	11	11716.2793	0.00	1
301	15	0	15	11529.0158	0.21	2
301	15	1	15	11529.0157	0.93	2
301	15	1	14	11660.0226	0.00	1
301	15	2	13	11780.7234	0.00	1
301	16	1	15	11820.2829	0.00	1
301	16	2	15	11820.3049	0.00	1
301	16	3	14	11949.8096	0.00	1
301	17	0	17	11839.6171	0.00	1
301	17	1	17	11839.6169	0.00	1
203	0	0	0	13088.3239	0.00	1
203	1	0	1	13099.8580	2.21	2
203	1	1	1	13106.5233	5.31	2
203	1	1	0	13108.9789	2.51	2
203	2	0	2	13122.3664	0.00	1
203	2	1	2	13127.1788	2.72	2
203	2	1	1	13134.5117	0.00	1
203	2	2	1	13154.4636	1.83	2
203	2	2	0	13155.0390	0.00	1
203	3	0	3	13154.9179	0.00	2
203	3	1	2	13172.3801	0.19	2
203	3	2	1	13191.7943	1.82	3
203	3	3	1	13228.6171	0.00	1
203	3	3	0	13228.6996	0.00	1
203	4	0	4	13196.7097	4.32	2
203	4	1	4	13198.1874	1.41	2
203	4	1	3	13221.9322	0.00	1
203	4	2	3	13234.9997	0.23	2
203	4	2	2	13241.9110	0.24	2
203	4	3	2	13276.1901	0.00	1
203	4	4	1	13329.4129	0.00	1
203	4	4	0	13329.4072	0.00	1
203	5	0	5	13247.5629	2.16	2
203	5	1	5	13248.0176	0.00	1
203	5	1	4	13282.1351	0.00	1
203	5	3	3	13335.3390	0.00	1
203	5	3	2	13337.3454	0.00	1
203	5	5	1	13456.6864	0.00	1
203	5	5	0	13456.6859	0.00	1
203	6	1	6	13307.2112	0.00	1
203	6	1	5	13351.7661	0.00	1
203	6	2	5	13358.3851	0.00	1
203	6	3	4	13406.1801	0.00	1
203	6	6	1	13610.2628	0.00	1
203	6	6	0	13610.2627	0.00	1
203	7	0	7	13374.0709	0.00	1
203	7	1	7	13376.2125	0.00	1
203	7	1	6	13430.2147	0.00	1
203	7	2	6	13435.2684	0.00	1
203	7	2	5	13468.4562	0.00	1
203	7	3	5	13488.2172	0.00	1
203	8	1	8	13450.8624	0.00	1
203	8	2	7	13521.9140	0.00	1
203	8	4	5	13641.6040	0.00	1
203	9	0	9	13538.0653	0.00	1
203	9	1	8	13613.6779	0.00	1
320	10	5	6	11069.8697	0.00	1
311	1	0	1	11511.9560	0.78	2
311	1	1	1	11520.0365	0.00	1
311	1	1	0	11522.5860	0.61	2
311	2	0	2	11534.7757	0.00	1
311	2	1	2	11540.5899	0.24	2
311	2	1	1	11548.0991	0.32	2
311	2	2	1	11572.7660	0.00	1
311	2	2	0	11573.2780	0.00	1
311	3	0	3	11567.7714	0.40	2
311	3	1	3	11571.2749	1.53	2
311	3	1	2	11585.7636	0.74	2
311	3	2	1	11609.7956	0.24	2
311	3	3	1	11654.6711	0.00	1
311	3	3	0	11654.7425	0.00	1
311	4	0	4	11610.0597	1.02	2
311	4	1	4	11611.8182	2.06	2
311	4	1	3	11634.4576	0.00	1
311	4	2	3	11653.1591	0.77	2
311	4	2	2	11659.6802	0.00	1
311	4	3	2	11701.7127	5.27	2
311	4	3	1	11702.1505	1.22	2
311	4	4	1	11766.1777	0.00	1
311	4	4	0	11766.1720	0.00	1
311	5	0	5	11661.2686	0.96	2
311	5	1	5	11662.0035	0.00	1
311	5	1	4	11700.3150	0.00	1
311	5	2	4	11709.8347	2.85	2
311	5	2	3	11722.8455	2.96	2
311	5	3	3	11760.5197	0.00	1
311	5	3	2	11762.1668	6.32	2
311	5	4	1	11825.1366	0.00	1
311	5	5	1	11907.0357	0.00	1
311	5	5	0	11907.0352	0.00	1
311	6	0	6	11721.2063	2.41	2
311	6	1	6	11721.5239	0.02	2
311	6	1	5	11771.1796	0.00	1
311	6	2	5	11777.0968	1.37	2
311	6	3	4	11830.9448	0.00	1
311	6	6	1	12077.0512	0.00	1
311	6	6	0	12077.0511	0.00	1
311	7	0	7	11790.1201	0.45	2
311	7	1	7	11790.2439	0.00	1
311	7	1	6	11851.5137	0.11	2
311	7	2	5	11887.2843	0.00	1
311	8	0	8	11868.0063	3.93	2
311	8	1	8	11868.0552	2.56	2
311	8	1	7	11940.6560	0.00	1
311	8	2	7	11942.0616	0.00	1
311	8	3	6	12005.8055	0.00	1
311	9	1	9	11954.9600	0.00	1
311	9	1	8	12038.4531	0.00	1
311	11	0	11	12155.6237	0.00	1
311	11	1	11	12155.6479	0.00	1
023	2	0	2	10530.0936	0.00	1
023	2	2	1	10570.4558	0.00	1
023	4	0	4	10606.8178	0.00	1
023	5	1	5	10659.8410	0.00	1
023	5	1	4	10698.9893	0.00	1
023	5	2	3	10726.3926	0.00	1
023	5	3	3	10765.5076	0.00	1
023	5	4	2	10832.6508	0.00	1
023	5	4	1	10832.6565	0.00	1
023	6	3	4	10838.5344	0.00	1
023	7	5	3	11076.7908	0.00	1
023	7	5	2	11076.7965	0.00	1

Appendix A.1 (continued)

VIB	J	Ka	Kc	Energy	ΔE	N	VIB	J	Ka	Kc	Energy	ΔE	N
				cm^{-1}	10^{-3} cm^{-1}						cm^{-1}	10^{-3} cm^{-1}	
203	12	1	12	13851.3575	0.00	1	023	8	1	8	10868.8420	0.00	1
203	13	0	13	13626.6863	0.00	1	023	8	3	5	11038.4863	0.00	1
203	13	1	13	13626.6910	0.00	1	023	10	2	8	11232.5097	0.00	1
401	0	0	0	12743.0491	0.00	1	023	10	4	7	11321.8923	0.00	1
401	1	0	1	12754.2708	0.16	2	122	2	2	1	10412.7112	0.00	1
401	1	1	1	12761.5235	2.08	2	122	2	2	0	10413.1072	0.00	
401	1	1	0	12763.9215	1.26	2	122	3	2	2	10448.3217	2.47	2
401	2	0	2	12777.6337	0.00	1	122	3	2	1	10450.2319	0.00	1
401	2	1	2	12781.9407	0.98	3	122	4	1	3	10469.7815	0.00	1
401	2	1	1	12789.0905	2.87	2	122	4	2	2	10500.9487	0.56	2
401	2	2	1	12810.2989	3.26	2	122	5	2	4	10550.9318	0.50	2
401	2	2	0	12810.8084	2.96	2	122	6	1	5	10611.2150	0.00	1
401	3	0	3	12809.7199	1.10	2	122	6	2	5	10619.6785	0.21	2
401	3	1	3	12812.3318	0.63	2	122	7	2	6	10698.4974	0.00	1
401	3	1	2	12826.4483	0.29	2	122	7	3	5	10763.5579	0.00	1
401	3	2	2	12844.4887	1.16	2	122	7	6	2	11032.4154	0.86	2
401	3	2	1	12846.9120	0.75	3	122	8	1	7	10785.3995	0.00	1
401	3	3	1	12886.1445	0.00	1	122	8	2	7	10787.1923	0.00	1
401	3	3	0	12886.2099	0.74	2	122	8	2	6	10835.8084	0.00	1
401	4	0	4	12851.2104	8.17	2	122	8	6	3	11130.2405	0.00	1
401	4	1	4	12852.4679	2.68	2	122	8	6	2	11130.2408	0.00	1
401	4	1	3	12875.3874	0.00	1	122	8	7	2	11255.5432	0.00	1
401	4	2	3	12889.6488	0.95	3	122	8	7	1	11255.5431	0.00	1
401	4	2	2	12896.1653	0.96	2	122	9	1	9	10788.6889	0.00	1
401	4	3	2	12932.2634	1.97	2	122	9	7	3	11347.7735	0.00	1
401	4	3	1	12932.7327	0.00	1	122	10	2	9	10994.2929	0.00	1
401	4	4	1	12989.2037	0.00	1	122	10	2	8	11071.3174	0.00	1
401	4	4	0	12989.1980	0.00	1	122	11	1	10	11107.1828	0.00	1
401	5	0	5	12901.6211	0.64	2	122	11	2	10	11104.2796	2.32	2
401	5	1	5	12902.1221	2.75	2	122	12	1	11	11232.9664	4.00	2
401	5	1	4	12934.9715	2.99	2	122	13	2	12	11365.3826	1.17	2
401	5	2	4	12945.4809	0.99	2	122	14	1	13	11508.1285	1.83	2
401	5	2	3	12958.4354	0.14	2	122	15	2	14	11668.1766	0.00	1

Appendix A.2. Vibrational energies of the $H_2^{18}O$ molecule predicted from the effective Vibrational Hamiltonian and provided by variational calculations.

Evar	var-EH	Coef_1	P1	P2	P3	Coef_2	Q1	Q2	Q3	R1	R2	R3	S1	S2	S3
cm^{-1}	cm^{-1}									SP[29,30]			SHIRIN [92]		
1	2	3		4		5		6			7			8	
7514.200	0.103	0.995	0	5	0	0.005	1	3	0						
9694.600	-2.142	0.984	1	4	0	0.010	2	2	0						
11064.600	-23.119	0.981	1	5	0	0.013	2	3	0						
11199.400	1.861	0.991	0	5	1	0.008	1	3	1						
14488.200	0.938	0.810	0	0	4	0.155	2	0	2						
14538.900	-8.272	0.848	2	5	0	0.115	0	5	2						
14600.200	-0.318	0.968	1	5	1	0.022	2	3	1						
14768.600	-26.099	0.870	0	5	2	0.115	2	5	0	1	8	0-	1	8	0-
15065.100	2.387	0.471	3	3	0	0.471	1	3	2						
15332.200	-0.847	0.509	1	3	2	0.439	3	3	0	3	3	0			
15478.400	0.673	0.861	0	3	3	0.126	2	3	1						
15703.400	0.437	0.710	4	1	0	0.145	2	1	2				2	1	2-
15784.300	0.468	0.633	1	1	3	0.355	3	1	1						
15991.700	0.167	0.802	0	1	4	0.158	2	1	2						
16487.100	5.541	0.475	3	4	0	0.455	1	4	2						
16496.600	1.291	0.803	2	4	1	0.126	0	4	3						
16742.500	-8.678	0.476	3	4	0	0.400	1	4	2						
16776.700	1.216	0.496	2	2	2	0.202	4	2	0	4	2	0-	0	12	0-
16905.600	4.018	0.859	0	4	3	0.122	2	4	1						
17182.700	0.511	0.691	4	2	0	0.137	2	2	2				2	2	2-
17258.800	-0.403	0.614	1	2	3	0.349	3	2	1	3	2	1			
17416.700	0.052	0.625	5	0	0	0.355	1	0	4				3	0	2-
17448.300	1.052	0.531	4	0	1	0.286	2	0	3				2	0	3
17465.700	-0.870	0.795	0	2	4	0.156	2	2	2						
17698.300	0.726	0.417	1	0	4	0.333	3	0	2	5	0	0-	1	0	4
17861.100	10.385	0.494	3	5	0	0.434	1	5	2						
17874.400	5.312	0.801	2	5	1	0.126	0	5	3						
17888.800	3.687	0.795	0	0	5	0.167	2	0	3						
18108.100	-15.586	0.490	1	5	2	0.451	3	5	0						
18216.000	2.977	0.544	2	3	2	0.191	4	3	0	3	3	2	4	3	0
18214.700	0.292	0.487	3	3	1	0.310	1	3	3						
18284.000	6.311	0.858	0	5	3	0.118	2	5	1						
18341.500	-3.006	0.561	3	1	2	0.203	1	1	4				5	1	0-
18342.700	-2.359	0.472	2	1	3	0.338	4	1	1	4	1	1	4	1	1
18625.000	0.070	0.669	4	3	0	0.135	2	3	2				2	3	2-
18700.000	-1.963	0.600	1	3	3	0.342	3	3	1	3	3	1			
18902.700	0.067	0.327	0	3	4	0.265	5	1	0	5	1	0	3	1	2-
18916.200	1.389	0.462	0	3	4	0.340	5	1	0						
18936.600	0.147	0.526	4	1	1	0.271	2	1	3				2	1	3
19186.900	1.796	0.393	1	1	4	0.329	3	1	2	5	1	0-	1	1	4
19367.200	0.550	0.792	0	1	5	0.168	2	1	3						
19622.500	8.338	0.544	2	4	2	0.189	4	4	0				4	4	0-
19623.100	5.612	0.491	3	4	1	0.276	1	4	3						
19733.000	1.783	0.461	4	0	2	0.343	2	0	4	3	0	2	6	0	0-
19733.000	1.576	0.527	3	0	3	0.221	5	0	1	5	0	1-	5	0	1
19808.500	-6.973	0.502	3	2	2	0.187	1	2	4	4	2	2	5	2	0-
19808.800	-7.323	0.430	2	2	3	0.298	4	2	1	4	2	1	4	2	1
20105.500	-2.148	0.592	1	4	3	0.337	3	4	1	3	4	1			
20364.700	0.956	0.542	5	2	0	0.322	1	2	4						
20384.700	-4.855	0.470	4	2	1	0.241	2	2	3						
20483.000	1.975	0.345	2	0	4	0.340	6	0	0	6	0	0			
20489.000	1.268	0.526	5	0	1	0.352	1	0	5						
20993.100	17.547	0.502	3	5	1	0.312	1	5	3						
20980.000	3.736	0.470	1	0	5	0.349	3	0	3	3	0	3			
21170.300	7.392	0.361	4	1	2	0.264	2	1	4	3	1	2			
21168.100	4.635	0.412	3	1	3	0.175	5	1	1	5	1	1-			
21254.200	-12.988	0.403	3	3	2	0.159	4	1	2	4	3	2			
21251.100	-16.890	0.351	2	3	3	0.239	4	3	1	4	3	1			
21466.400	-1.526	0.590	1	5	3	0.336	3	5	1	3	5	1			

Appendix A.2 (continued)

Evar	var-EH	Coef_1	P1	P2	P3	Coef_2	Q1	Q2	Q3	R1	R2	R3	S1	S2	S3
cm^{-1}	cm^{-1}									SP[29,30]			SHIRIN [92]		
1	2	3	4			5	6			7			8		
21804.900	-6.621	0.444	4	3	1	0.227	2	3	3						
21955.200	-1.655	0.498	5	1	1	0.350	1	1	5						
22237.600	-3.765	0.766	0	3	5	0.160	2	3	3						
22330.400	3.754	0.545	6	1	0	0.238	4	1	2						
22440.700	2.718	0.453	1	1	5	0.344	3	1	3	3	1	3			
22498.200	24.063	0.471	3	0	4	0.347	5	0	2	4	0	2			
22479.400	5.220	0.519	4	0	3	0.260	2	0	5	3	0	3			
22572.200	10.007	0.284	3	4	2	0.228	4	2	2	3	2	2			
22569.800	6.269	0.258	3	2	3	0.248	2	4	3	5	2	1-			
22671.600	-27.420	0.312	3	2	3	0.259	2	4	3	4	2	3			
23354.200	8.856	0.246	5	0	2	0.194	1	0	6	7	0	0-			
23347.900	-1.522	0.377	6	0	1	0.305	2	0	5						
23410.900	-4.620	0.381	5	2	1	0.269	1	2	5						
23864.300	-3.581	0.413	1	2	5	0.313	3	2	3	5	2	1-			
23892.300	21.753	0.307	4	1	3	0.158	3	3	3	5	1	3			
23921.900	0.914	0.600	7	0	0	0.271	1	0	6	2	10	1-			
23952.700	16.725	0.264	2	5	3	0.228	4	1	3	4	5	1-			
23975.900	6.836	0.322	4	0	3	0.321	6	0	1	6	0	1			
24072.300	-35.518	0.397	3	3	3	0.164	2	5	3	4	3	3			
24515.600	21.071	0.502	5	5	0	0.338	1	5	4						
24745.000	-9.748	0.288	6	1	1	0.222	2	1	5						
24865.800	15.675	0.194	6	3	0	0.181	5	1	2						
24847.100	-7.867	0.294	5	3	1	0.204	1	3	5						
24987.300	33.808	0.738	0	5	5	0.172	2	5	3						
25093.800	26.751	0.448	5	0	3	0.400	3	0	5	4	0	3			
25167.700	2.050	0.463	6	3	0	0.217	4	3	2	4	0	2-			
25262.400	-5.676	0.393	1	3	5	0.300	3	3	3	0	4	5-			
25382.600	14.762	0.554	7	1	0	0.280	1	1	6						
25860.800	4.679	0.731	0	1	7	0.187	2	1	5	1	1	7			
26097.400	13.412	0.285	7	0	1	0.200	3	0	5						
26137.700	2.513	0.246	5	4	1	0.209	1	4	5	7	0	1-			
26494.700	37.923	0.410	5	1	3	0.366	3	1	5	3	1	3-			
26676.500	19.260	0.349	4	3	3	0.171	2	3	5	5	3	3			
27518.900	13.287	0.247	7	1	1	0.180	3	1	5						
27655.500	-12.623	0.305	6	3	1	0.287	2	3	5						
28179.800	-5.511	0.237	7	1	1	0.151	4	3	3	7	1	1			
28295.800	9.294	0.231	7	1	1	0.211	1	1	7	7	1	1			

96 levels RMS deviation 11.2 cm^{-1}

Notes:

Columns are as follows.

1 - variational energies from Ref. [92] below 20000 cm^{-1}
and from Ref. [29,30] above 20000 cm^{-1};
2 - difference between variational energies and those
extrapolated from the EH parameters;
3 - leading contribution to the resulting wavefunction;
4 - $V_1V_2V_3$ label of the basis function corresponding to the leading contribution;
5 - second in value contrution to the resulting wavefunction
6 - $V_1V_2V_3$ label of the basis function corresponding to the second in value contribution;
7 - the corresponding $V_1V_2V_3$ label from [29,30], if different from ours
attached to the leading contribution;
8 - the corresponding $V_1V_2V_3$ label from [92], if different from ours
attached to the leading contribution;

.

"-" is attached to those labels in the last two columns which are believed to disagree with ours, as they either do not coincide with our label corresponding to 2nd contribution, or they coincide with it, but the 2nd contribution to the resulting wavefunction is importantly (more than 2 times) less than the first one.
Mind that the SP labels that differ from ours by +1 or -1 in V_1 are considered as being distorted by the technical defect in the assigning procedure exploited in SP, and then are believed to be identical with ours.

Appendix A.3. Observed and EH-calculated energy levels of the $D_2{}^{16}O$ molecule (example).

J	Ka	Kc	Ecalc cm^{-1}	Eobs cm^{-1}	Obs-calc $10^{-4}\ \text{cm}^{-1}$	MIXING COEFFICIENTS, %								
				(211)		(211)	(013)	(131)	(310)	(112)	(230)	(032)	(150)	(080)
8	0	8	9422.7204	9422.7354	14995.77		0.01	1.45	0.17	2.40	0.18	0.01	0.00	0.00
8	1	8	9422.8344	9422.8304	-3997.19		0.01	0.05	0.31	2.44	0.01	0.00	0.00	0.00
8	1	7	9495.6652	9495.6623	-2898.03		0.00	0.09	0.38	1.50	0.01	0.00	0.00	0.00
8	2	7	9497.3911	9497.4044	13394.91		0.00	0.07	3.40	1.60	0.00	0.01	0.00	0.00
8	2	6	9546.1020	9546.0868	-15195.66		0.01	0.08	2.56	1.65	0.02	0.01	0.00	0.00
8	3	6	9561.2778	9561.3073	29585.59		0.00	0.18	10.43	3.77	0.01	0.01	0.00	0.00
8	3	5	9577.6565	9577.6590	2452.68		0.01	0.47	15.58	0.51	0.17	30.54	0.04	0.00
8	4	5	9629.5595	9629.5719	12487.07		0.01	0.38	8.36	4.14	0.01	0.04	0.00	0.00
8	4	4	9632.5106	9632.5266	16088.76		0.01	0.45	9.11	1.60	0.02	0.05	0.00	0.00
8	5	4	9712.4852	9712.4989	13689.26		0.02	0.29	6.06	4.35	0.01	0.01	0.00	0.00
8	5	3	9712.3011	9712.3182	17090.81		0.01	0.30	6.11	2.76	0.01	0.01	0.00	0.00
8	6	3	9811.1254	9811.1374	11990.37		0.03	0.61	4.19	4.76	0.02	0.01	0.00	0.00
8	6	2	9811.1178	9811.1372	19490.39		0.01	0.61	4.19	4.77	0.02	0.01	0.00	0.00
8	7	2	9926.4162	9926.4057	-10486.48		0.03	1.35	2.54	9.27	0.24	0.03	0.06	0.00
8	7	1	9926.4169	9926.4055	-11386.48		0.03	1.35	2.54	9.27	0.24	0.03	0.06	0.00
8	8	1	10056.8888	10056.8914	2570.38		0.42	3.15	0.49	25.52	0.00	0.00	0.00	0.03
8	8	0	10056.8889	10056.8915	2670.39		0.42	3.15	0.49	25.52	0.00	0.00	0.00	0.03
				(013)										
8	0	8	9741.0122	9741.0051	-70	0.05	98.96	0.00	0.00	0.98	0.00	0.00	0.00	0.00
8	1	8	9740.9523	9740.9440	-83	0.02	99.63	0.00	0.00	0.34	0.00	0.00	0.00	0.00
8	1	7	9813.6437	9813.6350	-87	0.06	98.73	0.00	0.01	1.19	0.00	0.00	0.00	0.00
8	2	7	9815.4205	9815.4151	-54	0.06	99.64	0.00	0.00	0.29	0.00	0.00	0.00	0.00
8	2	6	9861.9450	9861.9395	-55	1.98	52.80	0.01	0.55	44.64	0.01	0.01	0.00	0.00
8	3	6	9879.8788	9879.8800	12	0.02	99.57	0.00	0.00	0.41	0.00	0.00	0.00	0.00
8	3	5	9899.8765	9899.8743	-22	0.02	99.76	0.00	0.00	0.21	0.00	0.00	0.00	0.00
8	4	5	9944.6882	9944.7026	144	0.04	99.13	0.00	0.00	0.83	0.00	0.00	0.00	0.00
8	4	4	9948.1446	9948.1522	76	0.04	99.25	0.00	0.00	0.71	0.00	0.00	0.00	0.00
8	5	4	10020.8467	10020.8560	92	0.06	98.01	0.00	0.10	1.82	0.00	0.00	0.00	0.00
8	5	3	10021.0822	10021.0917	95	0.06	98.03	0.00	0.10	1.80	0.00	0.00	0.00	0.00
8	6	3	10112.4397	10112.4398	0	0.22	95.48	0.00	0.00	4.28	0.00	0.00	0.00	0.00
8	6	2	10112.4476	10112.4378	-97	0.22	95.49	0.00	0.00	4.28	0.00	0.00	0.00	0.00
8	7	2	10218.7432	10218.7196	-236	0.02	88.79	0.00	0.00	11.19	0.00	0.00	0.00	0.00
8	7	1	10218.7433	10218.7193	-240	0.02	88.79	0.00	0.00	11.19	0.00	0.00	0.00	0.00
8	8	1	10335.0822	10335.1032	210	0.06	99.86	0.00	0.00	0.08	0.00	0.00	0.00	0.00
8	8	0	10335.0822	10335.1033	211	0.06	99.86	0.00	0.00	0.08	0.00	0.00	0.00	0.00
				(131)										
8	0	8	9169.5208	9169.5456	248	0.04	0.00	88.52	0.02	0.00	10.27	0.00	0.11	1.03
8	1	8	9170.0763	9170.0739	-23	0.04	0.00	85.79	0.02	0.00	10.41	0.01	0.00	3.73
8	1	7	9253.8856	9253.8065	-790	0.05	0.00	94.90	0.01	0.00	5.01	0.01	0.00	0.01
8	2	7	9258.1325			0.06	0.00	80.28	0.04	0.00	19.50	0.03	0.03	0.05
8	2	6	9308.3549	9308.3718	168	0.06	0.00	97.64	0.00	0.00	0.68	1.61	0.00	0.00
8	3	6	9337.1858	9337.2220	362	0.11	0.00	70.06	0.10	0.01	26.61	2.73	0.37	0.02
8	3	5	9361.2610			0.04	0.00	65.14	0.07	0.00	33.76	0.39	0.22	0.37
8	4	5	9425.0926	9424.9408	-1518	0.21	0.00	84.53	0.11	0.01	12.15	2.74	0.24	0.02
8	4	4	9426.2412			1.74	0.00	85.05	0.08	0.04	12.09	0.75	0.23	0.02
8	5	4	9529.6101	9529.6289	187	0.47	0.00	91.28	0.04	0.01	5.76	2.07	0.34	0.03
8	5	3	9529.6130			0.41	0.00	91.17	0.04	0.00	5.74	2.26	0.33	0.03
8	6	3	9653.0576	9653.0110	-465	1.02	0.00	85.88	0.07	0.47	2.16	10.02	0.34	0.04
8	6	2	9653.0290	9653.0114	-176	0.96	0.00	86.16	0.05	0.02	2.17	10.25	0.34	0.04
8	7	2	9804.5852	9804.5583	-268	0.80	0.00	56.79	1.07	0.01	0.31	40.69	0.20	0.14
8	7	1	9804.5839	9804.5580	-259	0.80	0.00	56.80	1.07	0.01	0.31	40.68	0.20	0.14
8	8	1	9957.7310	9957.7204	-105	3.67	0.00	90.24	0.04	0.02	0.01	5.95	0.03	0.03
8	8	0	9957.7310	9957.7205	-104	3.67	0.00	90.24	0.04	0.02	0.01	5.95	0.03	0.03
				(310)										
8	0	8	9377.3855	9377.3749	-105	0.05	0.00	0.00	99.76	0.00	0.14	0.05	0.00	0.00
8	1	8	9377.5081	9377.4965	-116	0.07	0.00	0.00	99.75	0.00	0.12	0.05	0.00	0.00
8	1	7	9450.2463	9450.2366	-96	0.12	0.00	0.05	99.55	0.00	0.16	0.12	0.00	0.00
8	2	7	9453.3245	9453.3256	11	0.38	0.00	0.01	99.33	0.00	0.15	0.13	0.00	0.00
8	2	6	9499.2445			0.78	0.00	0.01	98.87	0.04	0.15	0.14	0.00	0.00
8	3	6	9519.4331			3.54	0.00	0.01	95.82	0.02	0.19	0.42	0.00	0.00
8	3	5	9537.7565	9537.7266	-299	4.11	0.00	0.02	95.23	0.13	0.19	0.32	0.00	0.00
8	4	5	9595.3518	9595.3181	-33716.67		0.00	3.32	36.11	0.45	38.93	1.75	2.76	0.00
8	4	4	9596.8612	9596.7881	-731	5.59	0.00	1.93	44.32	0.30	44.46	0.25	3.15	0.00
8	5	4	9674.9740	9675.0124	384	4.89	0.00	4.71	46.58	0.68	0.22	42.77	0.14	0.00
8	5	3	9675.1951	9675.2442	490	4.87	0.00	4.75	45.62	0.55	0.22	43.85	0.15	0.00
8	6	3	9777.3335			2.21	0.16	0.68	71.83	18.93	0.59	5.50	0.09	0.00
8	6	2	9777.8136	9777.7965	-171	3.08	0.04	0.77	78.32	10.92	0.65	6.11	0.10	0.00
8	7	2	9898.0258	9898.0059	-199	4.20	0.03	0.11	92.34	0.57	1.14	1.45	0.17	0.00
8	7	1	9898.0237	9898.0055	-182	4.20	0.03	0.11	92.35	0.56	1.14	1.45	0.17	0.00
8	8	1	10032.2702			1.67	0.07	0.04	95.14	0.07	2.16	0.36	0.48	0.00
8	8	0	10032.2701			1.67	0.07	0.04	95.15	0.07	2.16	0.36	0.48	0.00

Appendix A.3 (continued)

J	Ka	Kc	Ecalc cm^{-1}	Eobs cm^{-1}	Obs-calc 10^{-4} cm^{-1}	MIXING COEFFICIENTS, %								
				(211)		(211)	(013)	(131)	(310)	(112)	(230)	(032)	(150)	(080)
				(112)										
8	0	8	9576.0426	9576.0025	-401	3.82	0.01	0.07	1.83	90.07	0.06	4.15	0.01	0.00
8	1	8	9576.1934	9576.1511	-422	3.50	0.01	0.00	0.06	96.42	0.01	0.01	0.00	0.00
8	1	7	9649.0670	9649.0638	-32	3.71	0.01	0.47	0.94	94.67	0.03	0.17	0.00	0.00
8	2	7	9651.5257	9651.5067	-190	2.61	0.03	0.00	0.10	97.24	0.01	0.01	0.00	0.00
8	2	6	9698.3239	9698.3389	149	2.94	0.31	0.01	0.13	96.60	0.01	0.01	0.00	0.00
8	3	6	9717.1136	9717.1099	-36	2.69	1.11	0.00	0.33	95.83	0.01	0.02	0.00	0.00
8	3	5	9735.3043	9735.3275	232	1.56	0.31	0.00	0.11	97.99	0.01	0.02	0.00	0.00
8	4	5	9785.6873	9785.6992	119	5.83	1.35	0.49	13.49	76.52	0.16	2.01	0.03	0.12
8	4	4	9788.2513	9788.1512	-1000	4.42	0.48	1.68	5.61	84.00	0.12	3.63	0.04	0.02
8	5	4	9866.5058	9866.5187	129	2.07	47.94	0.01	0.75	49.20	0.01	0.01	0.00	0.00
8	5	3	9864.4790	9864.5083	293	3.99	0.98	0.01	1.29	93.67	0.03	0.02	0.00	0.00
8	6	3	9961.1717	9961.2333	616	8.82	1.94	0.08	0.43	88.69	0.03	0.00	0.00	0.00
8	6	2	9961.1592	9961.2034	442	8.82	1.95	0.08	0.43	88.69	0.03	0.00	0.00	0.00
8	7	2	10074.2958	10074.2845	-1122	4.81	4.09	0.79	0.13	70.15	0.03	0.00	0.00	0.00
8	7	1	10074.2952	10074.2866	-85	24.81	4.09	0.79	0.13	70.15	0.03	0.00	0.00	0.00
8	8	1	10196.3486	10196.2738	-747	0.03	11.06	0.00	0.00	88.89	0.02	0.00	0.00	0.00
8	8	0	10196.3486	10196.2741	-744	0.03	11.06	0.00	0.00	88.89	0.02	0.00	0.00	0.00
				(230)										
8	0	8	9088.8354			0.00	0.00	10.24	0.10	0.01	89.59	0.00	0.06	0.00
8	1	8	9089.2567			0.00	0.00	10.23	0.10	0.01	89.61	0.00	0.05	0.00
8	1	7	9172.9382			0.00	0.00	4.75	0.10	0.01	76.78	0.04	18.33	0.00
8	2	7	9180.4529			0.01	0.00	5.70	0.13	0.01	94.10	0.00	0.06	0.00
8	2	6	9226.1571			0.01	0.00	3.98	0.13	0.01	95.81	0.00	0.07	0.00
8	3	6	9262.5632			0.02	0.00	2.83	0.17	0.01	96.83	0.00	0.15	0.00
8	3	5	9277.3049			0.01	0.00	16.12	0.13	0.01	83.54	0.00	0.10	0.09
8	4	5	9347.2983			0.08	0.00	34.97	0.17	0.01	64.10	0.16	0.50	0.02
8	4	4	9358.3117			0.02	0.00	25.69	0.17	0.01	73.50	0.13	0.47	0.02
8	5	4	9465.7290			0.02	0.00	11.35	0.33	0.01	85.81	0.43	2.05	0.01
8	5	3	9465.8097			0.02	0.00	11.20	0.35	0.01	86.21	0.15	2.05	0.00
8	6	3	9596.7714	9596.6980	-734	12.89	0.00	2.15	32.35	0.38	48.62	0.16	3.45	0.00
8	6	2	9595.4107	9595.4145	38	5.75	0.00	3.53	42.13	0.31	43.02	2.21	3.05	0.00
8	7	2	9746.8029			0.04	0.00	1.91	1.01	0.02	82.16	0.79	14.07	0.00
8	7	1	9746.8029			0.04	0.00	1.91	1.01	0.02	82.16	0.79	14.07	0.00
8	8	1	9915.6993			0.37	0.00	0.58	2.01	0.05	70.47	3.05	23.46	0.00
8	8	0	9915.6993			0.37	0.00	0.58	2.01	0.05	70.47	3.05	23.46	0.00
				(032)										
8	0	8	9325.3062			0.00	0.00	2.37	0.04	0.00	0.39	97.18	0.01	0.00
8	1	8	9326.1796			0.00	0.00	1.59	0.05	0.01	0.00	98.33	0.02	0.00
8	1	7	9408.4531			0.00	0.00	2.17	0.09	0.00	0.21	97.53	0.00	0.00
8	2	7	9414.1854			0.00	0.00	0.49	0.14	0.00	0.01	99.36	0.00	0.00
8	2	6	9463.3984			0.00	0.00	0.10	0.14	0.01	0.01	99.72	0.02	0.00
8	3	6	9492.6275			0.00	0.00	0.95	0.43	0.01	0.14	98.44	0.03	0.00
8	3	5	9508.6688			0.00	0.00	0.42	0.34	0.01	0.03	99.16	0.04	0.00
8	4	5	9575.6146	9575.6110	-36	17.49	0.00	1.19	15.00	0.07	0.70	65.42	0.12	0.00
8	4	4	9578.2754			0.80	0.00	1.29	0.99	4.40	0.87	91.50	0.16	0.00
8	5	4	9681.3019	9681.3446	427	4.01	0.00	5.25	43.20	0.35	0.38	46.74	0.08	0.00
8	5	3	9681.4341	9681.4500	159	4.11	0.00	5.10	44.36	0.21	0.38	45.75	0.08	0.00
8	6	3	9789.3583			1.44	0.01	38.59	7.05	0.18	0.24	50.74	0.41	1.35
8	6	2	9789.3790			1.75	0.01	37.36	8.36	2.00	0.21	48.56	0.39	1.34
8	7	2	9930.7140			0.32	0.00	5.73	1.65	0.01	0.18	90.82	1.29	0.00
8	7	1	9930.7141			0.32	0.00	5.73	1.65	0.01	0.18	90.82	1.29	0.00
8	8	1	10086.2820			0.00	0.00	0.04	0.73	0.00	0.75	95.28	3.19	0.00
8	8	0	10086.2820			0.00	0.00	0.04	0.73	0.00	0.75	95.28	3.19	0.00

Full list of the mixing coefficients for the 2nd decade states of the $D_2{}^{16}O$ is available from the author upon request.

Appendix A.4. Observed and calculated energy levels for the 2nd decade of the $H_2^{18}O$ molecule (example).

JKaKc	Ecalc cm^{-1}	Eobs cm^{-1}	Obs-calc cm^{-1}	MIXING COEFFICIENTS, %								
				131	211	013	051	230	032	310	112	150
		(131)										
8 0 8	12489.2416	12489.3123	0.0707	98.6	0.1	0.0	0.6	0.7	0.0	0.0	0.0	0.0
8 1 8	12490.5112	12490.4063	-0.1049	96.7	0.1	0.0	2.5	0.7	0.0	0.0	0.0	0.0
8 1 7	12668.3963	12668.4974	0.1011	98.8	0.0	0.0	0.6	0.6	0.0	0.0	0.0	0.0
8 2 7	13001.4853	13001.5304	0.0451	97.7	1.4	0.0	0.1	0.3	0.5	0.0	0.0	0.0
8 2 6	12783.4647	12783.3674	-0.0973	90.8	2.4	0.0	1.0	4.9	0.0	0.8	0.0	0.1
8 3 6	12837.7948	12837.7245	-0.0703	96.7	2.5	0.0	0.3	0.4	0.0	0.0	0.0	0.0
8 3 5	12874.3668	12874.3221	-0.0447	83.0	0.8	0.0	0.8	0.6	14.8	0.0	0.0	0.0
8 4 5	13402.3844	13402.3296	-0.0548	81.8	9.6	0.0	4.6	0.3	3.2	0.4	0.1	0.0
8 4 4	13004.1769	13004.1825	0.0056	92.6	1.8	0.0	0.1	0.2	5.2	0.1	0.0	0.0
8 5 4	13192.6445	13192.6440	-0.0005	49.8	1.0	0.0	0.4	0.3	37.2	10.9	0.3	0.1
8 5 3	13190.4259	13190.3296	-0.0963	66.5	1.6	0.0	0.6	0.3	11.3	18.4	1.3	0.0
8 6 3	13792.5296	13792.5570	0.0274	49.2	17.3	0.6	21.8	3.2	6.5	1.0	0.4	0.1
8 6 2	13402.3808	13402.3284	-0.0524	82.0	9.6	0.0	4.6	0.3	3.1	0.4	0.0	0.0
8 7 2	13627.9182			39.1	43.5	0.2	15.9	0.4	0.8	0.1	0.0	0.0
8 7 1	13627.9188			39.1	43.5	0.2	15.9	0.4	0.8	0.1	0.0	0.0
8 8 1	13977.2618			44.1	14.4	2.0	38.5	0.0	0.2	0.0	0.8	0.0
8 8 0	13792.5296	13792.5572	0.0276	49.2	17.3	0.6	21.8	3.2	6.5	1.0	0.4	0.1
		(211)										
8 0 8	12817.5926	12817.5851	-0.0075	1.6	72.1	0.0	0.0	2.0	0.1	24.1	0.0	0.1
8 1 8	12816.5828	12816.5639	-0.0189	1.9	71.7	0.0	0.0	0.2	0.0	26.2	0.0	0.0
8 1 7	12961.7936	12961.8286	0.0350	0.4	82.8	0.0	0.1	5.4	0.0	11.2	0.0	0.0
8 2 7	12963.3335	12963.2655	-0.0680	0.9	85.0	0.0	0.0	0.1	0.0	14.0	0.0	0.0
8 2 6	13066.2497	13066.4103	0.1606	2.0	94.7	0.0	0.0	0.0	0.1	2.5	0.8	0.0
8 3 6	13087.6760	13087.7020	0.0260	0.1	98.1	0.0	0.0	0.0	0.0	1.0	0.8	0.0
8 3 5	13135.4430	13135.2550	-0.1880	0.5	99.3	0.0	0.0	0.0	0.0	0.1	0.0	0.0
8 4 5	13206.5694	13206.5846	0.0152	0.2	97.7	0.1	0.0	0.0	0.0	0.1	1.9	0.0
8 4 4	13217.1303	13217.2435	0.1132	0.1	98.5	1.1	0.2	0.0	0.0	0.0	0.0	0.0
8 5 4	13341.9936	13342.0682	0.0746	1.6	97.3	0.2	0.0	0.1	0.0	0.0	0.7	0.0
8 5 3	13342.6962	13342.7902	0.0940	1.6	97.7	0.5	0.0	0.1	0.0	0.0	0.1	0.0
8 6 3	13505.5589	13505.6141	0.0552	9.3	89.3	0.6	0.5	0.1	0.0	0.0	0.2	0.1
8 6 2	13505.6185	13505.6733	0.0548	9.3	89.3	0.6	0.5	0.1	0.0	0.0	0.2	0.1
8 7 2	13710.3125	13710.3771	0.0646	36.7	53.8	1.7	7.0	0.2	0.0	0.0	0.6	0.0
8 7 1	13710.3223	13710.3730	0.0507	36.7	53.8	1.6	7.0	0.2	0.0	0.0	0.6	0.0
8 8 1	13865.8476	13865.8490	0.0014	0.5	64.8	0.7	33.3	0.3	0.2	0.0	0.2	0.0
8 8 0	13865.8478	13865.8493	0.0015	0.5	64.8	0.7	33.3	0.3	0.2	0.0	0.2	0.0
		(013)										
8 0 8	13224.3652	13224.4047	0.0395	1.2	1.1	77.7	18.9	0.9	0.0	0.0	0.1	0.0
8 1 8	13224.3949	13224.3903	-0.0046	0.0	0.0	99.8	0.0	0.0	0.0	0.0	0.1	0.0
8 1 7	13368.1275	13368.1706	0.0431	0.0	0.2	99.4	0.0	0.0	0.0	0.0	0.3	0.0
8 2 7	13368.8333	13368.8088	-0.0245	0.1	0.0	93.6	0.0	0.0	2.7	0.0	3.5	0.0
8 2 6	13475.9848	13476.0021	0.0173	0.0	0.1	99.7	0.0	0.0	0.0	0.0	0.2	0.0
8 3 6	13494.7624	13494.7208	-0.0416	0.1	0.1	83.1	0.3	0.5	0.4	6.2	9.2	0.1
8 3 5	13546.6486	13546.6107	-0.0379	0.0	0.1	99.4	0.0	0.0	0.0	0.0	0.5	0.0
8 4 5	13612.6532	13612.6710	0.0178	0.0	0.3	65.1	0.0	0.0	0.2	0.3	34.1	0.0
8 4 4	13622.4709	13622.6139	0.1430	0.0	0.2	86.6	0.0	0.3	0.1	0.1	12.7	0.0
8 5 4	13723.6857	13723.6350	-0.0507	0.1	0.4	86.2	0.1	0.0	0.4	0.3	12.5	0.0
8 5 3	13724.9528	13724.9190	-0.0338	0.0	0.3	85.6	0.1	0.0	0.5	0.3	13.2	0.0
8 6 3	13869.5280	13869.4813	-0.0467	0.1	0.6	95.8	0.2	0.0	0.9	0.1	2.3	0.0
8 6 2	13869.5950	13869.5487	-0.0463	0.1	0.6	95.8	0.2	0.0	0.9	0.1	2.3	0.0
8 7 2	14031.3313			0.0	0.8	84.1	0.0	2.3	6.1	2.5	3.6	0.5
8 7 1	14031.3328			0.0	0.8	84.1	0.0	2.3	6.1	2.5	3.6	0.5
8 8 1	14212.6740			0.2	2.0	96.8	0.8	0.0	0.0	0.0	0.1	0.0
8 8 0	14212.6740			0.2	2.0	96.8	0.8	0.0	0.0	0.0	0.1	0.0
		(051)										
8 0 8	11928.4482			0.2	0.0	0.0	97.5	2.4	0.0	0.0	0.0	0.0
8 1 8	11932.9454			0.2	0.0	0.0	97.4	2.4	0.0	0.0	0.0	0.0
8 1 7	12157.2589			0.1	0.0	0.0	98.1	1.8	0.0	0.0	0.0	0.0
8 2 7	12200.0879			0.0	0.0	0.0	97.6	2.4	0.0	0.0	0.0	0.0
8 2 6	12298.3653			0.4	0.0	0.0	98.1	1.5	0.0	0.0	0.0	0.0
8 3 6	12432.3106			2.4	0.0	0.0	95.2	2.4	0.0	0.0	0.0	0.0
8 3 5	12453.2392			0.6	0.0	0.0	97.4	2.0	0.0	0.0	0.0	0.0

Appendix A.4 (continued)

JKaKc	Ecalc cm^{-1}	Eobs cm^{-1}	Obs-calc cm^{-1}	MIXING COEFFICIENTS, % 131	211	013	051	230	032	310	112	150
8 4 5	12666.8278			47.1	0.0	0.0	51.6	1.3	0.0	0.0	0.0	0.0
8 4 4	12675.9163			1.4	0.0	0.0	94.8	2.7	1.0	0.0	0.0	0.0
8 5 4	12940.1786			1.5	0.0	0.0	95.5	2.9	0.0	0.0	0.0	0.0
8 5 3	12940.4813			2.0	0.0	0.0	94.8	2.9	0.0	0.2	0.0	0.0
8 6 3	12685.2269	12685.2538	0.0269	52.8	0.0	0.0	45.2	1.9	0.0	0.0	0.0	0.0
8 6 2	13224.6409			4.4	0.0	21.2	70.7	3.4	0.0	0.1	0.0	0.0
8 7 2	13520.3621			22.3	0.6	0.2	68.8	4.7	0.0	3.3	0.1	0.1
8 7 1	13520.3486			22.3	0.6	0.2	68.8	4.7	0.0	3.3	0.1	0.1
8 8 1	13224.5793			5.6	0.0	0.0	89.6	4.4	0.0	0.2	0.0	0.0
8 8 0	13977.2618			44.1	14.4	2.0	38.5	0.0	0.2	0.0	0.8	0.0
		(230)										
8 0 8	12447.0646	12446.9920	-0.0726	0.6	0.0	0.0	2.3	96.8	0.0	0.3	0.0	0.1
8 1 8	12447.9473	12448.1648	0.2175	0.8	0.0	0.0	2.3	96.6	0.0	0.3	0.0	0.1
8 1 7	12626.9487	12626.9562	0.0076	0.0	0.0	0.0	2.0	97.5	0.1	0.3	0.0	0.1
8 2 7	12641.5971	12641.5206	-0.0766	0.6	0.0	0.0	1.9	85.5	0.1	0.3	0.0	11.6
8 2 6	12742.5961			0.1	0.0	0.0	1.1	97.1	0.7	0.7	0.0	0.3
8 3 6	12800.1153	12799.8820	-0.2333	6.1	0.5	0.0	1.7	70.7	0.2	19.4	0.0	1.3
8 3 5	12833.2336			0.3	0.0	0.0	1.1	90.6	4.5	0.6	0.0	2.9
8 4 5	12973.4560	12973.5331	0.0771	0.4	1.3	0.0	1.5	83.4	0.5	12.2	0.0	0.7
8 4 4	12969.8604			0.1	0.0	0.0	1.0	53.2	43.8	1.4	0.0	0.4
8 5 4	13166.7159	13166.7002	-0.0157	0.2	0.0	0.0	3.9	91.3	0.6	3.4	0.0	0.5
8 5 3	13167.4439			0.2	0.0	0.0	3.9	90.0	0.6	4.7	0.1	0.5
8 6 3	13388.6284			0.2	0.0	0.0	3.7	83.5	0.6	11.3	0.1	0.6
8 6 2	13388.6494			0.2	0.0	0.0	3.7	83.5	0.6	11.3	0.1	0.6
8 7 2	13626.7747			0.2	0.0	0.4	2.4	54.3	0.2	31.7	0.8	10.0
8 7 1	13626.7615			0.2	0.0	0.0	2.4	54.5	0.2	31.7	0.8	10.0
8 8 1	13967.8367			0.0	0.0	0.1	1.1	53.2	16.3	12.0	10.6	6.8
8 8 0	13967.8367			0.0	0.0	0.1	1.1	53.2	16.3	12.0	10.6	6.8
		(032)										
8 0 8	12680.6950			0.0	0.0	0.0	0.0	0.3	99.5	0.2	0.0	0.0
8 1 8	12681.2338			0.0	0.0	0.0	1.0	0.1	98.7	0.2	0.0	0.0
8 1 7	12859.8325			0.0	0.0	0.0	0.0	3.8	95.8	0.1	0.0	0.2
8 2 7	12865.3203	12865.4558	0.1355	14.7	0.1	0.0	0.1	0.1	84.9	0.0	0.0	0.0
8 2 6	12981.2101			0.2	0.0	0.0	0.6	42.2	55.9	0.7	0.1	0.3
8 3 6	13025.4465	13025.5151	0.0686	4.8	0.2	0.0	0.0	0.4	93.8	0.4	0.3	0.0
8 3 5	13064.2347			0.4	0.0	0.0	0.0	0.7	97.6	1.1	0.1	0.0
8 4 5	13178.4410	13178.5098	0.0688	20.0	0.4	0.0	0.3	0.1	75.0	3.0	1.2	0.0
8 4 4	13182.6089	13182.6204	0.0115	44.3	0.7	0.0	0.6	0.1	52.9	1.3	0.2	0.0
8 5 4	13364.5465			3.0	0.2	0.0	0.3	1.0	88.0	4.7	2.7	0.0
8 5 3	13364.2491			3.0	0.2	2.0	0.3	1.3	84.1	7.5	1.6	0.0
8 6 3	13570.6192	13570.5118	-0.1074	0.4	0.1	0.0	0.6	1.7	92.4	3.0	1.7	0.1
8 6 2	13570.6422			0.4	0.1	0.0	0.6	1.7	92.4	3.0	1.7	0.1
8 7 2	13798.7239	13798.7139	-0.0099	4.5	1.3	0.3	3.7	2.4	78.8	3.8	5.1	0.2
8 7 1	13798.7238	13798.7084	-0.0154	4.5	1.3	0.3	3.7	2.4	78.8	3.8	5.1	0.2
8 8 1	14045.2183	14045.2335	0.0152	0.0	0.1	13.7	0.3	12.1	55.0	8.1	9.2	1.4
8 8 0	14045.2181	14045.2335	0.0154	0.0	0.1	13.7	0.3	12.1	55.0	8.1	9.2	1.4
		(310)										
8 0 8	12806.0783			0.8	25.6	0.0	0.0	0.5	0.2	72.8	0.0	0.0
8 1 8	12808.0322	12808.0584	0.0262	0.3	24.9	0.0	0.4	17.9	0.2	55.8	0.0	0.5
8 1 7	12952.1386			0.4	13.8	0.0	0.0	0.7	0.0	84.8	0.0	0.3
8 2 7	12952.5392	12952.6149	0.0757	0.6	15.0	0.0	0.3	6.9	0.1	77.0	0.0	0.0
8 2 6	13057.0928	13056.9875	-0.1053	0.0	0.7	0.0	0.0	1.1	0.2	95.1	2.8	0.0
8 3 6	13081.5802	13081.6558	0.0756	0.0	3.3	0.0	0.0	0.8	0.1	85.6	10.1	0.0
8 3 5	13125.6121	13125.6559	0.0438	0.1	0.0	0.0	0.0	1.9	1.2	96.5	0.3	0.1
8 4 5	13201.9979			9.9	0.1	0.0	0.1	1.0	12.1	71.8	2.0	2.9
8 4 4	13212.4040			2.0	0.0	0.0	0.0	2.1	6.5	53.7	0.2	35.4
8 5 4	13331.9256	13331.9158	-0.0098	0.0	0.0	0.0	0.0	1.7	7.5	71.9	18.4	0.3
8 5 3	13334.7846			0.0	0.0	0.1	0.0	2.2	7.7	87.2	2.3	0.4
8 6 3	13501.1105	13501.0595	-0.0510	1.0	0.1	0.1	4.3	8.3	3.5	77.0	4.3	1.7
8 6 2	13501.7541	13501.7760	0.0219	0.9	0.1	4.3	4.0	7.6	3.1	70.3	8.3	1.5
8 7 2	13709.2563	13709.3011	0.0448	0.6	0.1	0.0	1.7	35.3	6.3	46.5	4.5	5.0
8 7 1	13709.2579			0.6	0.1	0.0	1.7	35.3	6.3	46.5	4.5	5.0
8 8 1	13778.4716			0.0	0.0	0.0	0.4	6.0	0.1	59.0	3.1	31.3
8 8 0	13778.4717			0.0	0.0	0.0	0.4	6.0	0.1	59.0	3.1	31.3
		(112)										

Appendix A.4 (continued)

JKaKc	Ecalc cm^{-1}	Eobs cm^{-1}	Obs-calc cm^{-1}	MIXING COEFFICIENTS, %								
				131	211	013	051	230	032	310	112	150
8 0 8	13073.0200	13072.9421	-0.0779	0.0	1.0	0.0	0.0	0.1	0.0	2.4	96.4	0.0
8 1 8	13071.9399	13071.9933	0.0534	0.0	0.1	0.0	0.0	0.1	0.4	10.4	89.0	0.0
8 1 7	13218.6459	13218.6477	0.0018	0.0	1.8	0.0	0.1	0.0	0.1	0.4	97.6	0.0
8 2 7	13221.6746	13221.7282	0.0536	0.0	0.1	0.0	0.0	0.1	0.5	3.6	95.5	0.2
8 2 6	13324.4587	13324.4944	0.0357	0.0	0.6	0.2	0.0	0.0	0.1	0.3	98.7	0.0
8 3 6	13347.7919	13347.6875	-0.1044	0.1	0.1	0.2	0.0	0.8	0.2	18.7	79.9	0.1
8 3 5	13396.0588	13396.0061	-0.0527	0.2	0.0	4.4	0.0	0.0	1.1	0.6	93.7	0.0
8 4 5	13463.1220	13463.0101	-0.1119	0.0	0.1	0.9	0.0	0.1	0.5	2.0	96.3	0.0
8 4 4	13470.5672	13470.6827	0.1155	0.0	0.0	12.7	0.0	0.2	0.5	2.5	84.0	0.1
8 5 4	13593.8801			0.0	0.1	13.1	0.0	0.0	0.7	0.8	85.2	0.1
8 5 3	13590.6773	13590.5902	-0.0871	0.0	0.1	34.8	0.0	0.0	0.5	0.6	63.9	0.1
8 6 3	13759.8601	13759.8858	0.0257	0.2	0.9	13.4	0.1	0.0	1.9	1.8	81.4	0.2
8 6 2	13759.7647	13759.7863	0.0216	0.2	0.9	12.7	0.1	0.0	2.0	1.8	82.2	0.2
8 7 2	13938.9121	13938.9547	0.0426	0.5	0.0	3.1	0.7	0.0	6.9	2.8	86.0	0.0
8 7 1	13938.9118	13938.9492	0.0374	0.5	0.0	3.1	0.7	0.0	6.9	2.8	86.0	0.0
8 8 1	14146.6454			0.0	0.0	0.7	0.0	0.0	22.5	3.7	72.9	0.2
8 8 0	14146.6454			0.0	0.0	0.7	0.0	0.0	22.5	3.7	72.9	0.2

Full list of the mixing coefficients for the 2nd decade states of the $H_2{}^{18}O$ is available from the author upon request.

Appendix A.5. Observed and calculated energy levels for the 1st pentadecade of the $H_2^{18}O$ molecule (example).

JKaKc	Ecalc cm^{-1}	Eobs cm^{-1}	Obs-calc cm^{-1}	MIXING COEFFICIENTS, %										
				301	221	141	103	023	320	042	202	122	400	240
		(301)												
8 0 8	14484.1476	14484.2793	0.1317	99.7	0.0	0.1	0.0	0.0	0.0	0.0	0.1	0.0	0.0	0.0
8 1 8	14484.2497	14484.3157	0.0660	99.8	0.0	0.0	0.0	0.0	0.0	0.0	0.1	0.0	0.0	0.0
8 1 7	14613.1261	14613.4737	0.3476	76.9	0.5	0.1	0.0	0.0	0.1	0.0	22.5	0.0	0.0	0.0
8 2 7	14614.1398	14613.8331	-0.3067	96.0	0.2	0.3	0.0	0.0	0.0	0.0	3.5	0.0	0.0	0.0
8 2 6	14709.6475	14708.9375	-0.7100	83.4	1.8	0.1	0.0	0.0	0.1	0.0	14.5	0.0	0.0	0.0
8 3 6	14722.6987	14723.9300	1.2313	82.2	0.3	3.9	0.0	0.0	0.0	0.6	12.9	0.0	0.0	0.0
8 3 5	14774.8072	14773.4927	-1.3145	88.7	0.8	3.2	0.0	0.0	0.3	0.0	7.0	0.0	0.0	0.0
8 4 5	14826.8050	14827.8400	1.0350	86.7	2.5	0.3	0.0	0.0	0.2	0.0	10.3	0.0	0.0	0.0
8 4 4	14839.4492	14840.2200	0.7708	90.2	1.9	0.3	0.0	0.0	0.1	0.0	7.5	0.1	0.0	0.0
8 5 4	14947.7469	14950.2800	2.5331	72.4	17.0	1.7	0.0	0.0	1.6	0.0	6.9	0.3	0.0	0.0
8 5 3	14948.7389	14951.2500	2.5111	73.3	16.5	1.7	0.0	0.0	1.5	0.0	6.6	0.3	0.0	0.0
8 6 3	15048.0914	15047.7800	-0.3114	51.0	36.7	2.7	0.0	0.0	4.4	0.0	4.5	0.7	0.0	0.0
8 6 2	15048.1496	15047.8400	-0.3096	51.0	36.7	2.7	0.0	0.0	4.4	0.0	4.5	0.7	0.0	0.0
8 7 2	15192.4583	15191.0600	-1.3983	78.9	3.8	10.7	0.0	0.0	1.2	0.7	4.6	0.1	0.0	0.0
8 7 1	15192.4599	15191.0700	-1.3899	78.9	3.8	10.7	0.0	0.0	1.2	0.7	4.6	0.1	0.0	0.0
8 8 1	15364.6273	15363.5700	-1.0573	86.2	3.0	2.5	0.0	0.0	6.3	0.1	0.7	0.0	0.0	1.2
8 8 0	15364.6273	15363.5700	-1.0573	86.2	3.0	2.5	0.0	0.0	6.3	0.1	0.7	0.0	0.0	1.2
		(221)												
8 0 8	14311.8313	14312.7700	0.9387	0.0	98.3	0.8	0.0	0.0	0.7	0.0	0.0	0.1	0.0	0.0
8 1 8	14310.2026	14310.2100	0.0074	0.0	94.1	5.7	0.0	0.0	0.2	0.0	0.0	0.1	0.0	0.0
8 1 7	14471.8995	14470.9500	-0.9495	0.1	98.6	0.6	0.0	0.0	0.4	0.0	0.0	0.4	0.0	0.0
8 2 7	14473.3259	14473.2000	-0.1259	0.1	91.6	2.3	0.0	0.0	5.5	0.1	0.0	0.4	0.0	0.0
8 2 6	14583.1765	14583.5500	0.3735	0.2	83.4	3.0	0.0	0.0	11.7	0.4	0.1	1.1	0.0	0.0
8 3 6	14611.4433	14611.5600	0.1167	0.4	85.2	0.4	0.0	0.0	12.9	0.2	0.1	0.8	0.0	0.0
8 3 5	14656.4335	14656.5100	0.0765	0.9	89.4	0.8	0.0	0.0	7.4	0.5	0.1	0.9	0.0	0.0
8 4 5	14745.6591	14746.5500	0.8909	2.4	83.9	0.2	0.0	0.0	11.3	0.0	0.5	1.6	0.0	0.2
8 4 4	14754.7523	14755.7100	0.9577	3.5	86.2	0.2	0.0	0.0	8.7	0.1	0.2	1.1	0.0	0.1
8 5 4	14893.4913	14892.6300	-0.8613	17.4	70.2	0.1	0.0	0.0	8.7	0.1	2.3	1.2	0.0	0.0
8 5 3	14894.4736	14893.7500	-0.7236	17.1	70.9	0.1	0.0	0.0	8.5	0.1	2.1	1.2	0.0	0.0
8 6 3	15119.6355	15122.9900	3.3545	32.0	50.2	9.7	0.0	0.0	5.1	0.1	2.0	0.9	0.0	0.0
8 6 2	15119.6559	15123.1300	3.4741	32.0	50.2	9.7	0.0	0.0	5.1	0.1	2.0	0.9	0.0	0.0
8 7 2	15356.5056			13.6	40.4	35.5	0.0	0.1	3.4	0.1	0.2	6.7	0.0	0.0
8 7 1	15356.5047			13.6	40.4	35.5	0.0	0.1	3.4	0.1	0.2	6.7	0.0	0.0
8 8 1	15531.7398	15530.7300	-1.0098	1.8	72.0	16.7	0.0	0.1	3.9	0.0	0.3	5.1	0.0	0.0
8 8 0	15531.7398	15530.7300	-1.0098	1.8	72.0	16.7	0.0	0.1	3.9	0.0	0.3	5.1	0.0	0.0
		(141)												
8 0 8	13932.0086	13932.5000	0.4914	0.0	0.1	99.9	0.0	0.0	0.0	0.0	0.0	0.0	0.0	0.0
8 1 8	13933.9942			0.0	0.1	99.9	0.0	0.0	0.0	0.0	0.0	0.0	0.0	0.0
8 1 7	14129.5019	14128.4700	-1.0319	0.0	0.0	100	0.0	0.0	0.0	0.0	0.0	0.0	0.0	0.0
8 2 7	14148.5254			0.0	0.0	99.9	0.0	0.0	0.0	0.0	0.0	0.0	0.0	0.0
8 2 6	14251.0601	14251.9400	0.8799	0.0	0.7	99.0	0.0	0.0	0.2	0.0	0.0	0.0	0.0	0.0
8 3 6	14333.5777	14333.4100	-0.1677	0.1	5.6	93.6	0.0	0.0	0.6	0.1	0.0	0.0	0.0	0.0
8 3 5	14361.3854	14359.8600	-1.5254	0.1	0.5	97.2	0.0	0.0	0.3	1.9	0.0	0.0	0.0	0.0
8 4 5	14525.0633	14527.2600	2.1967	0.6	2.1	94.0	0.0	0.0	0.1	3.1	0.0	0.0	0.0	0.0
8 4 4	14528.1792	14528.0500	-0.1292	0.3	2.6	79.0	0.0	0.0	1.5	16.2	0.0	0.4	0.0	0.0
8 5 4	14745.8907	14744.0300	-1.8607	4.7	2.3	72.0	0.0	0.0	18.6	0.1	2.3	0.1	0.0	0.0
8 5 3	14748.0727	14748.4500	0.3773	3.1	4.6	59.3	0.0	0.0	24.8	5.9	1.0	1.3	0.0	0.0
8 6 3	14988.6250	14986.9900	-1.6350	8.6	1.9	85.0	0.0	0.0	0.2	0.5	3.7	0.0	0.0	0.0
8 6 2	14988.6397	14986.9900	-1.6497	8.7	1.9	85.0	0.0	0.0	0.1	0.5	3.6	0.0	0.0	0.0
8 7 2	15261.6292	15262.2200	0.5908	0.8	44.2	50.3	0.0	0.0	3.7	0.1	0.3	0.5	0.0	0.0
8 7 1	15261.6298	15262.0100	0.3802	0.8	44.2	50.3	0.0	0.0	3.7	0.1	0.3	0.5	0.0	0.0
8 8 1	15686.6771			5.6	14.4	79.3	0.0	0.0	0.5	0.0	0.0	0.0	0.0	0.0
8 8 0	15686.6771			5.6	14.4	79.3	0.0	0.0	0.5	0.0	0.0	0.0	0.0	0.0
		(103)												
8 0 8	14967.1495	14967.3100	0.1605	0.0	0.0	0.0	99.9	0.0	0.0	0.0	0.0	0.0	0.1	0.0
8 1 8	14967.0855	14967.3600	0.2745	0.0	0.0	0.0	99.8	0.0	0.0	0.0	0.0	0.0	0.2	0.0
8 1 7	15096.0900	15096.0500	-0.0400	0.0	0.0	0.0	99.5	0.0	0.0	0.0	0.0	0.0	0.5	0.0
8 2 7	15096.8032	15096.1000	-0.7032	0.0	0.0	0.0	98.5	0.0	0.0	0.0	0.0	0.0	1.5	0.0
8 2 6	15195.4584	15196.8600	1.4016	0.0	0.0	0.0	99.5	0.0	0.0	0.0	0.0	0.0	0.5	0.0
8 3 6	15201.5224	15201.4500	-0.0724	0.0	0.0	0.0	84.5	0.0	0.0	0.0	0.0	0.0	15.5	0.0
8 3 5	15262.6090	15262.3100	-0.2990	0.0	0.0	0.0	96.6	0.0	0.0	0.0	0.0	0.0	3.4	0.0
8 4 5	15297.6166	15296.6800	-0.9366	0.0	0.0	0.0	80.6	0.0	0.0	0.0	0.0	0.0	19.4	0.0
8 4 4	15310.9150	15310.7800	-0.1350	0.0	0.0	0.0	64.4	0.0	0.0	0.0	0.0	0.0	35.6	0.0
8 5 4	15404.8158	15403.4000	-1.4158	0.0	0.0	0.0	89.9	0.0	0.0	0.0	0.0	0.0	10.1	0.0
8 5 3	15406.6882	15407.2300	0.5418	0.0	0.0	0.0	89.6	0.0	0.0	0.0	0.0	0.0	10.4	0.0
8 6 3	15531.6905	15530.7500	-0.9405	0.0	0.0	0.0	94.5	0.0	0.0	0.0	0.0	0.0	5.5	0.0
8 6 2	15531.7906	15530.7500	-1.0406	0.0	0.0	0.0	94.5	0.0	0.0	0.0	0.0	0.0	5.5	0.0
8 7 2	15682.1624	15681.2400	-0.9224	0.0	0.0	0.0	97.2	0.0	0.0	0.0	0.0	0.0	2.8	0.0
8 7 1	15682.1649	15681.2500	-0.9149	0.0	0.0	0.0	97.2	0.0	0.0	0.0	0.0	0.0	2.8	0.0
8 8 1	15856.4033	15858.5300	2.1267	0.0	0.0	0.0	99.4	0.0	0.0	0.0	0.0	0.0	0.6	0.0

Appendix A.5 (continued)

JKaKc	Ecalc cm^{-1}	Eobs cm^{-1}	Obs-calc cm^{-1}	MIXING COEFFICIENTS, %										
				301	221	141	103	023	320	042	202	122	400	240
8 8 0	15856.4033	15858.5300	2.1267	0.0	0.0	0.0	99.4	0.0	0.0	0.0	0.0	0.0	0.6	0.0
		(023)												
8 0 8	14719.2905	14719.2600	-0.0305	0.0	0.0	0.0	0.0	99.9	0.0	0.0	0.0	0.0	0.0	0.0
8 1 8	14719.3850	14719.3700	-0.0150	0.0	0.0	0.0	0.0	99.9	0.0	0.0	0.0	0.1	0.0	0.0
8 1 7	14877.6005	14877.3300	-0.2705	0.0	0.0	0.0	0.0	99.9	0.0	0.0	0.0	0.1	0.0	0.0
8 2 7	14879.7988	14879.7600	-0.0388	0.0	0.0	0.0	0.0	98.3	0.1	0.1	0.0	1.5	0.0	0.0
8 2 6	14991.6828	14991.5000	-0.1828	0.0	0.0	0.0	0.0	99.9	0.0	0.0	0.0	0.1	0.0	0.0
8 3 6	15009.6145	15008.7600	-0.8545	0.0	0.3	0.0	0.0	62.2	0.0	0.0	0.1	37.2	0.0	0.2
8 3 5	15067.5548	15067.5200	-0.0348	0.0	0.0	0.0	0.0	99.1	0.0	0.0	0.0	0.9	0.0	0.0
8 4 5	15139.9412	15139.7400	-0.2012	0.0	0.2	0.0	0.0	90.8	0.0	0.0	0.0	9.0	0.0	0.0
8 4 4	15150.1343	15149.3100	-0.8243	0.0	0.3	0.0	0.0	81.6	0.0	0.0	0.0	18.1	0.0	0.0
8 5 4	15282.5447	15283.0000	0.4553	0.0	0.1	0.0	0.0	97.1	0.0	0.0	0.0	2.7	0.0	0.0
8 5 3	15283.5455	15284.2100	0.6645	0.0	0.1	0.0	0.0	97.1	0.0	0.0	0.0	2.8	0.0	0.0
8 6 3	15446.1396	15446.2400	0.1004	0.0	0.0	0.0	0.0	98.8	0.0	0.0	0.0	1.1	0.0	0.0
8 6 2	15446.1859	15446.3000	0.1141	0.0	0.0	0.0	0.0	98.8	0.0	0.0	0.0	1.1	0.0	0.0
8 7 2	15625.8132	15624.6800	-1.1332	0.0	0.3	0.0	0.0	80.1	17.2	0.7	1.5	0.2	0.0	0.1
8 7 1	15625.8142	15624.6800	-1.1342	0.0	0.3	0.0	0.0	80.1	17.2	0.7	1.5	0.2	0.0	0.1
8 8 1	15805.8517	15806.0200	0.1683	0.0	0.0	0.0	0.0	99.9	0.0	0.0	0.0	0.1	0.0	0.0
8 8 0	15805.8517	15806.0200	0.1683	0.0	0.0	0.0	0.0	99.9	0.0	0.0	0.0	0.1	0.0	0.0
		(320)												
8 0 8	14302.6204	14301.5600	-1.0604	0.0	0.2	0.6	0.0	0.0	98.0	1.2	0.0	0.0	0.0	0.0
8 1 8	14303.0984	14305.5200	2.4216	0.0	0.8	0.2	0.0	0.0	97.8	1.2	0.0	0.0	0.0	0.0
8 1 7	14461.2350	14461.8500	0.6150	0.0	5.0	0.0	0.0	0.0	93.3	1.6	0.1	0.0	0.0	0.0
8 2 7	14465.6676	14463.6400	-2.0276	0.0	1.2	0.2	0.0	0.0	97.3	1.1	0.1	0.0	0.0	0.0
8 2 6	14572.4474	14575.4500	3.0026	0.0	9.2	0.0	0.0	0.0	89.6	0.4	0.2	0.5	0.0	0.0
8 3 6	14605.0562	14605.2500	0.1938	0.1	16.6	0.1	0.0	0.0	81.5	1.1	0.5	0.2	0.0	0.0
8 3 5	14649.8180	14648.0000	-1.8180	0.1	7.7	0.0	0.0	0.0	90.2	0.2	1.7	0.1	0.0	0.0
8 4 5	14740.8779	14742.2000	1.3221	2.1	7.9	33.1	0.0	0.0	50.3	2.2	1.8	2.6	0.0	0.0
8 4 4	14753.3151	14752.1400	-1.1751	0.9	8.7	19.1	0.0	0.0	64.3	4.3	2.6	0.1	0.0	0.0
8 5 4	14889.6790	14890.1200	0.4410	2.7	7.8	0.1	0.0	0.0	60.1	10.6	16.6	1.7	0.0	0.4
8 5 3	14890.1889	14887.8200	-2.3689	2.1	7.7	0.1	0.0	0.2	59.7	13.7	15.4	0.7	0.0	0.5
8 6 3	15117.5556	15120.9500	3.3944	1.4	5.6	0.2	0.0	0.0	54.4	14.8	21.0	0.6	0.0	2.0
8 6 2	15117.5885	15121.0700	3.4815	1.4	5.5	0.2	0.0	0.0	54.4	14.8	21.0	0.6	0.0	2.0
8 7 2	15354.6041	15353.4300	-1.1741	3.8	7.0	0.2	0.0	0.0	68.5	0.2	10.7	0.7	0.0	8.9
8 7 1	15354.6045	15353.4300	-1.1745	3.8	7.0	0.2	0.0	0.0	68.5	0.2	10.7	0.7	0.0	8.9
8 8 1	15624.4068	15624.6800	0.2732	0.1	0.7	0.1	0.0	19.5	70.2	3.0	5.5	0.5	0.0	0.4
8 8 0	15624.4066	15624.6800	0.2734	0.1	0.7	0.1	0.0	19.6	70.2	3.0	5.5	0.5	0.0	0.4
		(042)												
8 0 8	14124.9337	14125.9800	1.0463	0.0	0.0	0.0	0.0	0.0	1.1	98.7	0.0	0.1	0.0	0.1
8 1 8	14126.8546	14127.7200	0.8654	0.0	0.0	0.0	0.0	0.0	1.1	98.7	0.0	0.1	0.0	0.0
8 1 7	14328.1457	14329.1600	1.0143	0.0	0.0	0.0	0.0	0.0	0.3	53.7	0.0	0.0	0.0	45.9
8 2 7	14341.9851	14338.5200	-3.4651	0.0	0.0	2.0	0.0	0.0	0.9	97.0	0.0	0.0	0.0	0.1
8 2 6	14442.1735			0.0	0.0	0.0	0.0	0.0	0.3	98.8	0.0	0.2	0.0	0.6
8 3 6	14518.8249	14514.6800	-4.1449	0.1	0.2	17.3	0.0	0.0	0.6	80.8	0.0	1.0	0.0	0.1
8 3 5	14550.3009	14551.6000	1.2991	0.0	0.1	2.8	0.0	0.0	1.4	95.3	0.0	0.2	0.0	0.1
8 4 5	14702.9938	14703.1400	0.1462	0.0	1.6	1.4	0.0	0.0	3.8	88.0	0.0	4.6	0.0	0.6
8 4 4	14708.1969	14709.1600	0.9631	3.1	0.1	2.6	0.0	0.0	1.0	77.6	14.7	0.4	0.0	0.5
8 5 4	14920.3439	14920.0400	-0.3039	1.8	0.4	1.3	0.0	0.0	2.7	77.7	12.4	1.7	0.0	1.9
8 5 3	14915.0147	14914.2000	-0.8147	1.2	0.6	0.7	0.0	0.9	3.8	41.8	8.8	41.2	0.0	1.1
8 6 3	15155.2708	15156.8800	1.6092	0.3	2.0	0.2	0.0	0.0	13.1	75.7	2.4	0.3	0.0	6.0
8 6 2	15155.2789	15156.9000	1.6211	0.3	2.0	0.2	0.0	0.0	13.1	75.7	2.4	0.3	0.0	6.0
8 7 2	15414.9083	15415.3900	0.4817	0.3	0.4	0.0	0.0	0.0	5.7	50.9	0.2	0.1	0.0	42.3
8 7 1	15414.9084	15415.3900	0.4816	0.3	0.4	0.0	0.0	0.0	5.7	50.9	0.2	0.1	0.0	42.3
8 8 1	15493.7579			0.0	0.1	0.0	0.0	0.0	3.0	90.4	1.6	0.1	0.0	4.9
8 8 0	15493.7579			0.0	0.1	0.0	0.0	0.0	3.0	90.4	1.6	0.1	0.0	4.9
		(202)												
8 0 8	14482.3154	14482.2000	-0.1154	0.1	0.0	0.0	0.0	0.0	0.1	0.0	99.8	0.0	0.0	0.0
8 1 8	14482.3485	14482.2000	-0.1485	0.1	0.0	0.0	0.0	0.0	0.1	0.0	99.8	0.0	0.0	0.0
8 1 7	14610.7507	14610.6200	-0.1307	3.1	0.1	0.0	0.0	0.0	1.5	0.0	95.2	0.0	0.0	0.0
8 2 7	14611.7848	14611.2400	-0.5448	22.5	0.4	0.0	0.0	0.0	0.2	0.0	76.8	0.0	0.0	0.0
8 2 6	14707.2774	14706.4600	-0.8174	7.5	0.5	0.0	0.0	0.0	4.4	15.7	71.7	0.0	0.0	0.1
8 3 6	14722.5674	14722.5600	-0.0074	16.6	0.1	0.1	0.0	0.1	0.6	0.0	82.5	0.1	0.0	0.0
8 3 5	14772.0708	14771.6800	-0.3908	6.4	0.0	0.0	0.0	0.0	0.5	0.0	93.0	0.2	0.0	0.0
8 4 5	14825.6399	14826.2100	0.5701	10.5	0.1	0.4	0.0	0.0	2.8	0.0	85.9	0.2	0.0	0.0
8 4 4	14837.5747	14837.2500	-0.3247	6.2	0.1	0.2	0.0	0.0	1.9	0.1	84.4	7.1	0.0	0.0
8 5 4	14946.8429	14948.3800	1.5371	6.0	3.1	0.9	0.0	0.0	24.8	6.0	58.8	0.3	0.0	0.1
8 5 3	14947.6980	14949.4400	1.7420	5.9	3.0	1.0	0.0	0.0	24.1	5.4	60.2	0.3	0.0	0.1
8 6 3	15045.0298	15046.4000	1.3702	6.9	2.7	0.1	0.0	0.0	21.5	0.4	68.0	0.0	0.0	0.3
8 6 2	15045.0978	15046.5400	1.4422	6.9	2.7	0.1	0.0	0.0	21.5	0.4	68.1	0.0	0.0	0.3
8 7 2	15205.5243	15205.3600	-0.1643	5.4	1.2	0.0	0.0	0.0	9.9	0.4	82.9	0.1	0.0	0.1
8 7 1	15205.5258	15205.3600	-0.1658	5.4	1.2	0.0	0.0	0.0	9.9	0.4	82.9	0.1	0.0	0.1
8 8 1	15391.4113	15392.7100	1.2987	1.4	0.8	0.0	0.0	0.0	7.8	0.5	89.4	0.2	0.0	0.0
8 8 0	15391.4113	15392.7100	1.2987	1.4	0.8	0.0	0.0	0.0	7.8	0.5	89.4	0.2	0.0	0.0

Appendix A.5 (continued)

JKaKc	Ecalc cm^{-1}	Eobs cm^{-1}	Obs-calc cm^{-1}	MIXING COEFFICIENTS, %										
				301	221	141	103	023	320	042	202	122	400	240
		(122)												
8 0 8	14569.5926	14567.6700	-1.9226	0.0	0.2	0.0	0.0	0.0	0.3	0.3	0.0	99.2	0.0	0.0
8 1 8	14570.1136	14569.6100	-0.5036	0.0	0.7	0.1	0.0	0.0	0.0	1.5	0.0	97.7	0.0	0.0
8 1 7	14729.9934	14731.4500	1.4566	0.0	0.6	0.0	0.0	0.0	0.1	0.2	0.1	97.9	0.0	1.0
8 2 7	14734.4526	14733.1900	-1.2626	0.0	0.7	0.0	0.0	0.0	5.1	2.6	0.4	91.2	0.0	0.0
8 2 6	14844.6559	14843.0700	-1.5859	0.5	0.2	0.0	0.0	0.1	0.2	0.3	6.3	92.3	0.0	0.0
8 3 6	14871.8171	14870.3000	-1.5171	0.0	0.8	0.0	0.0	0.1	0.5	2.6	0.1	95.8	0.0	0.1
8 3 5	14926.5205	14925.7800	-0.7405	0.6	0.2	0.6	0.0	0.7	0.7	35.8	4.2	56.2	0.0	0.8
8 4 5	15009.4843	15011.1600	1.6757	0.0	0.9	0.0	0.0	1.1	0.0	0.1	0.1	97.3	0.0	0.5
8 4 4	15024.4870	15024.9700	0.4830	0.0	0.4	0.0	0.0	37.8	0.0	0.1	0.1	61.4	0.0	0.2
8 5 4	15172.0681	15169.9900	-2.0781	0.0	1.0	0.0	0.0	18.5	0.0	0.1	0.1	80.1	0.0	0.0
8 5 3	15171.5159	15170.1600	-1.3559	0.0	1.1	0.0	0.0	9.2	0.0	0.1	0.2	89.3	0.0	0.0
8 6 3	15346.3086	15348.2000	1.8914	1.2	3.4	2.8	0.0	2.8	0.5	0.1	0.5	88.8	0.0	0.0
8 6 2	15346.3196	15348.2200	1.9004	1.2	3.4	2.8	0.0	2.8	0.5	0.1	0.5	88.8	0.0	0.0
8 7 2	15554.6760	15555.6900	1.0140	0.0	6.0	1.3	0.0	1.1	0.0	0.0	0.3	91.2	0.0	0.0
8 7 1	15554.6763	15555.7000	1.0237	0.0	6.0	1.3	0.0	1.1	0.0	0.0	0.3	91.2	0.0	0.0
8 8 1	15840.1605	15840.5000	0.3395	0.0	1.1	0.0	0.0	0.2	0.1	0.0	0.4	98.2	0.0	0.0
8 8 0	15840.1605	15840.5000	0.3395	0.0	1.1	0.0	0.0	0.2	0.1	0.0	0.4	98.2	0.0	0.0
		(400)												
8 0 8	14875.5751	14875.5200	-0.0551	0.0	0.0	0.0	0.0	0.0	0.0	0.0	0.0	0.0	100	0.0
8 1 8	14875.6224	14875.9500	0.3276	0.0	0.0	0.0	0.0	0.0	0.0	0.0	0.0	0.0	100	0.0
8 1 7	15005.1161	15005.2200	0.1039	0.0	0.0	0.0	0.1	0.0	0.0	0.0	0.0	0.0	99.9	0.0
8 2 7	15006.2566	15004.5100	-1.7466	0.0	0.0	0.0	0.1	0.0	0.0	0.0	0.0	0.0	99.9	0.0
8 2 6	15103.5290	15103.7000	0.1710	0.0	0.0	0.0	0.3	0.0	0.0	0.0	0.0	0.0	99.7	0.0
8 3 6	15116.2166	15116.0000	-0.2166	0.0	0.0	0.0	0.7	0.0	0.0	0.0	0.0	0.0	99.3	0.0
8 3 5	15167.8677	15166.2800	-1.5877	0.0	0.0	0.0	2.0	0.0	0.0	0.0	0.0	0.0	98.0	0.0
8 4 5	15216.6820	15216.7800	0.0980	0.0	0.0	0.0	4.5	0.0	0.0	0.0	0.0	0.0	95.5	0.0
8 4 4	15236.3312	15236.6300	0.2988	0.0	0.0	0.0	16.1	0.0	0.0	0.0	0.0	0.0	83.9	0.0
8 5 4	15340.8041	15340.6000	-0.2041	0.0	0.0	0.0	36.5	0.0	0.0	0.0	0.0	0.0	63.5	0.0
8 5 3	15338.9208	15339.4500	0.5292	0.0	0.0	0.0	19.8	0.0	0.0	0.0	0.0	0.0	80.2	0.0
8 6 3	15470.1035	15468.8600	-1.2435	0.0	0.0	0.0	10.5	0.0	0.0	0.0	0.0	0.0	89.5	0.0
8 6 2	15470.0782	15469.2400	-0.8382	0.0	0.0	0.0	10.2	0.0	0.0	0.0	0.0	0.0	89.8	0.0
8 7 2	15627.0542	15629.7800	2.7258	0.0	0.0	0.0	5.1	0.0	0.0	0.0	0.0	0.0	94.9	0.0
8 7 1	15627.0540	15630.0800	3.0260	0.0	0.0	0.0	5.1	0.0	0.0	0.0	0.0	0.0	94.9	0.0
8 8 1	15808.2399			0.0	0.0	0.0	1.9	0.0	0.0	0.0	0.0	0.0	98.1	0.0
8 8 0	15808.2399			0.0	0.0	0.0	1.9	0.0	0.0	0.0	0.0	0.0	98.1	0.0
		(240)												
8 0 8	13886.1789	13885.3200	-0.8589	0.0	0.0	0.0	0.0	0.0	0.0	0.0	0.0	0.0	0.0	100
8 1 8	13888.2711	13891.7000	3.4289	0.0	0.0	0.0	0.0	0.0	0.0	0.0	0.0	0.0	0.0	100
8 1 7	14084.0972	14085.3900	1.2928	0.0	0.0	0.0	0.0	0.0	0.0	0.0	0.0	0.0	0.0	100
8 2 7	14106.1195	14100.3400	-5.7795	0.0	0.0	0.0	0.0	0.0	0.0	0.0	0.0	0.0	0.0	100
8 2 6	14206.0858	14206.6000	0.5142	0.0	0.0	0.0	0.0	0.0	0.0	0.1	0.0	0.0	0.0	99.9
8 3 6	14296.3314	14291.5700	-4.7614	0.0	0.0	0.0	0.0	0.0	0.0	0.1	0.0	0.0	0.0	99.8
8 3 5	14318.3544	14314.7000	-3.6544	0.0	0.0	0.0	0.0	0.0	0.3	45.7	0.0	0.0	0.0	54.0
8 4 5	14498.1343	14499.9200	1.7857	0.0	0.0	0.0	0.0	0.0	0.0	0.7	0.0	0.0	0.0	99.3
8 4 4	14501.2098	14499.1600	-2.0498	0.0	0.0	0.0	0.0	0.0	0.0	1.2	0.0	0.0	0.0	98.7
8 5 4	14726.1185	14729.1600	3.0415	0.0	0.0	0.0	0.0	0.0	0.0	2.5	0.0	0.0	0.0	97.4
8 5 3	14726.2471	14727.9600	1.7129	0.0	0.2	0.0	0.0	0.0	0.0	2.6	0.0	0.9	0.0	96.3
8 6 3	14982.8399	14982.7400	-0.0999	0.0	0.1	0.0	0.0	0.0	0.2	8.2	0.0	0.4	0.0	91.1
8 6 2	14982.8713	14982.7600	-0.1113	0.0	0.1	0.0	0.0	0.0	0.2	8.2	0.0	0.2	0.0	91.3
8 7 2	15282.3854	15282.1400	-0.2454	0.1	0.2	0.0	0.0	0.0	2.5	48.2	1.4	0.1	0.0	47.5
8 7 1	15282.3860	15282.1400	-0.2460	0.1	0.2	0.0	0.0	0.0	2.5	48.2	1.4	0.1	0.0	47.5
8 8 1	15874.3434			0.0	0.0	0.0	0.0	0.0	0.1	5.4	0.0	0.0	0.0	94.6
8 8 0	15874.3434			0.0	0.0	0.0	0.0	0.0	0.1	5.4	0.0	0.0	0.0	94.6

Full list of the mixing coefficients for the 1st pentadecade of the $H_2{}^{18}O$ is available from the author upon request.

Appendix A.6. Observed and calculated energy levels for the Fermi-dyad: (103)-(023) of the HD^{16}O molecule (example).

J	Ka	Kc	Ecalc cm^{-1}	Eobs cm^{-1}	Obs-calc 10^{-3}cm^{-1}	MIXING COEFFICIENTS, %	
						103	023
				(103)			
7	0	7	13714.7482	13714.7562	7	99.6	0.4
7	1	7	13715.3323	13715.3348	2	99.5	0.5
7	1	6	13787.8244	13787.8045	-19	96.8	3.2
7	2	6	13797.9182	13797.9102	-7	95.0	5.0
7	2	5	13834.3433	13834.3701	26	90.1	9.9
7	3	5	13879.3897	13879.4615	71	80.1	19.9
7	3	4	13887.7496	13887.7425	-7	79.8	20.2
7	4	4	13980.6385	13980.7060	67	55.4	44.6
7	4	3	13981.2525	13981.3409	88	55.5	44.5
7	5	3	14052.6260	14052.5889	-37	61.4	38.6
7	5	2	14052.6456	14052.6121	-33	61.4	38.6
7	6	2	14186.6660	14186.6710	4	68.7	31.3
7	6	1	14186.6663	14186.6700	3	68.7	31.3
7	7	1	14342.3288	14342.3900	61	71.2	28.8
7	7	0	14342.3288	14342.3900	61	71.2	28.8
				(023)			
7	0	7	13665.5469	13665.5616	14	0.4	99.6
7	1	7	13666.3848	13666.3742	-10	0.4	99.6
7	1	6	13748.0251	13748.0280	2	3.0	97.0
7	2	6	13760.1995	13760.1824	-17	4.9	95.1
7	2	5	13798.8701	13798.8676	-2	7.5	92.5
7	3	5	13846.0802	13846.0803	0	22.1	77.9
7	3	4	13854.1644	13854.1884	24	20.1	79.9
7	4	4	13940.0388	13940.0594	20	44.6	55.4
7	4	3	13940.6530	13940.6716	18	44.5	55.5
7	5	3	14112.1141	14112.0799	-34	38.6	61.4
7	5	2	14112.1325	14112.0879	-44	38.7	61.3
7	6	2	14272.2426	14272.1967	-45	31.3	68.7
7	6	1	14272.2429	14272.1967	-46	31.3	68.7
7	7	1	14457.8385	14457.9166	78	29.0	71.0
7	7	0	14457.8385	14457.9166	78	29.0	71.0
				(103)			
8	0	8	13818.2818	13818.2851	3	99.4	0.6
8	1	8	13818.5638	13818.5709	7	99.4	0.6
8	1	7	13906.4960	13906.4903	-5	95.0	5.0
8	2	7	13912.7784	13912.7627	-15	93.3	6.7
8	2	6	13963.9857	13963.9314	-54	71.4	28.6
8	3	6	14001.6885	14001.6859	-2	75.5	24.5
8	3	5	14017.8252	14017.8151	-10	74.7	25.3
8	4	5	14105.1288	14105.2194	90	51.9	48.1
8	4	4	14106.8709	14106.9475	76	52.0	48.0
8	5	4	14173.6552	14173.6340	-21	63.1	36.9
8	5	3	14173.7376	14173.6860	-51	63.0	37.0
8	6	3	14306.8397	14306.8403	0	69.7	30.3
8	6	2	14306.8416	14306.8341	-7	69.7	30.3
8	7	2	14461.8897	14461.9040	14	72.0	28.0
8	7	1	14461.8897	14461.9040	14	72.0	28.0
8	8	1	14638.4512	14638.4452	-6	72.1	27.9
8	8	0	14638.4512	14638.4452	-6	72.1	27.9
				(023)			
8	0	8	13769.3292	13769.3265	-2	0.6	99.4
8	1	8	13769.7519	13769.7376	-14	0.6	99.4
8	1	7	13868.4320	13868.4406	8	4.9	95.1
8	2	7	13875.9574	13875.9388	-18	6.6	93.4
8	2	6	13930.3847	13930.3866	1	11.7	88.3
8	3	6	13968.5792	13968.5694	-9	41.1	58.9
8	3	5	13983.5003	13983.4966	-3	25.1	74.9
8	4	5	14062.1753	14062.1803	5	48.3	51.7
8	4	4	14063.9205	14063.9121	-8	48.0	52.0
8	5	4	14236.3479	14236.1840	-163	36.9	63.1
8	5	3	14236.4249	14236.3339	-90	36.9	63.1

Appendix A.6 (continued)

J	Ka	Kc	Ecalc cm^{-1}	Eobs cm^{-1}	Obs-calc 10^{-3}cm^{-1}	MIXING COEFFICIENTS, %	
						103	023
8	6	3	14395.9841	14395.9630	-21	30.3	69.7
8	6	2	14395.9858	14395.9650	-20	30.3	69.7
8	7	2	14581.1353	14581.1170	-18	28.1	71.9
8	7	1	14581.1353	14581.1170	-18	28.1	71.9
8	8	1	14790.2942	14790.2630	-31	28.2	71.8
8	8	0	14790.2942	14790.2630	-31	28.2	71.8
				(103)			
9	0	9	13933.7635	13933.7653	1	99.2	0.8
9	1	9	13933.8968	13933.8945	-2	99.2	0.8
9	1	8	14036.8123	14036.7279	-84	92.5	7.5
9	2	8	14040.4936	14040.4831	-10	91.1	8.9
9	2	7	14110.6842	14110.6580	-26	80.3	19.7
9	3	7	14138.5734	14138.6009	27	70.3	29.7
9	3	6	14165.8885	14165.8840	-4	68.4	31.6
9	4	6	14199.5430	14199.5720	28	52.0	48.0
9	4	5	14203.7317	14203.7550	23	51.3	48.7
9	5	5	14310.0234	14310.0006	-22	64.8	35.2
9	5	4	14310.3008			64.7	35.3
9	6	4	14442.1648	14442.1920	27	70.6	29.4
9	6	3	14442.1740	14442.1620	-12	70.6	29.4
9	7	3	14596.4513	14596.4470	-4	72.8	27.2
9	7	2	14596.4515	14596.4460	-5	72.8	27.2
9	8	2	14772.4679			72.9	27.1
9	8	1	14772.4679			72.9	27.1
9	9	1	14970.8105			72.5	27.5
9	9	0	14970.8105			72.5	27.5
				(023)			
9	0	9	13884.9362	13884.9379	1	0.7	99.3
9	1	9	13885.1481	13885.1362	-11	0.8	99.2
9	1	8	14000.0802	14000.0976	17	7.4	92.6
9	2	8	14004.4124	14004.4140	1	8.8	91.2
9	2	7	14075.8637	14075.8593	-4	17.7	82.3
9	3	7	14102.8211	14102.8480	26	31.3	68.7
9	3	6	14130.0718	14130.1320	60	31.1	68.9
9	4	6	14245.3345	14245.2670	-67	48.3	51.7
9	4	5	14249.5238	14249.6040	80	48.6	51.4
9	5	5	14376.3553	14376.3110	-44	35.2	64.8
9	5	4	14376.6125	14376.7230	110	35.2	64.8
9	6	4	14535.2985	14535.4840	185	29.3	70.7
9	6	3	14535.3067	14535.4970	190	29.3	70.7
9	7	3	14719.8377	14719.7780	-59	27.2	72.8
9	7	2	14719.8378	14719.7780	-59	27.2	72.8
9	8	2	14928.2230	14928.2710	47	27.4	72.6
9	8	1	14928.2230	14928.2710	47	27.4	72.6
9	9	1	15163.2022			27.8	72.2
9	9	0	15163.2022			27.8	72.2
				(103)			
10	0	10	14061.2081	14061.2051	-2	99.0	1.0
10	1	10	14061.2703	14061.2590	-11	99.0	1.0
10	1	9	14178.7089	14178.9515	242	89.4	10.6
10	2	9	14180.7756	14180.7877	12	88.4	11.6
10	2	8	14269.0872	14269.0916	4	75.0	25.0
10	3	8	14289.6086	14289.5750	-33	64.8	35.2
10	3	7	14331.3046	14331.3040	0	61.1	38.9
10	4	7	14351.9562	14351.9800	23	56.0	44.0
10	4	6	14360.6532	14360.7010	47	54.4	45.6
10	5	6	14461.7518			66.4	33.6
10	5	5	14462.5407	14462.5460	5	66.3	33.7
10	6	5	14592.6812			71.6	28.4
10	6	4	14592.7168	14592.7550	38	71.6	28.4
10	7	4	14746.0327			73.6	26.4
10	7	3	14746.0335			73.6	26.4
10	8	3	14921.4098			73.7	26.3
10	8	2	14921.4098			73.7	26.3
10	9	2	15119.5994			73.0	27.0

Appendix A.6 (continued)

J	Ka	Kc	Ecalc cm^{-1}	Eobs cm^{-1}	Obs-calc $10^{-3}cm^{-1}$	MIXING COEFFICIENTS, %	
						103	023
10	9	1	15119.5994			73.0	27.0
10	10	1	15343.0446			71.8	28.2
10	10	0	15343.0446			71.8	28.2
				(023)			
10	0	10	14012.4013	14012.4032	1	1.0	99.0
10	1	10	14012.5088	14012.4969	-11	1.0	99.0
10	1	9	14142.8674	14142.8772	9	10.5	89.5
10	2	9	14145.2299	14145.2489	19	11.5	88.5
10	2	8	14233.8966	14233.8682	-28	25.3	74.7
10	3	8	14252.5389	14252.5300	-8	34.5	65.5
10	3	7	14293.0564	14293.1190	62	37.8	62.2
10	4	7	14401.0432	14400.9750	-68	44.8	55.2
10	4	6	14409.8229	14409.8080	-14	45.4	54.6
10	5	6	14532.1463	14532.1680	21	33.5	66.5
10	5	5	14532.8734	14532.9310	57	33.6	66.4
10	6	5	14690.1989			28.2	71.8
10	6	4	14690.2299			28.2	71.8
10	7	4	14873.9188	14873.8710	-47	26.4	73.6
10	7	3	14873.9195	14873.8710	-48	26.4	73.6
10	8	3	15081.2749			26.9	73.1
10	8	2	15081.2749			26.9	73.1
10	9	2	15314.1450			29.6	70.4
10	9	1	15314.1450			29.6	70.4
10	10	1	15584.1070			25.9	74.1
10	10	0	15584.1070			25.9	74.1

Full list of the mixing coefficients for the (103)-(023) dyad of the $HD^{16}O$ is available from the author upon request.